Technical Summary

TS Technical Summary

Coordinating Lead Authors:
Thomas F. Stocker (Switzerland), Qin Dahe (China), Gian-Kasper Plattner (Switzerland)

Lead Authors:
Lisa V. Alexander (Australia), Simon K. Allen (Switzerland/New Zealand), Nathaniel L. Bindoff (Australia), François-Marie Bréon (France), John A. Church (Australia), Ulrich Cubasch (Germany), Seita Emori (Japan), Piers Forster (UK), Pierre Friedlingstein (UK/Belgium), Nathan Gillett (Canada), Jonathan M. Gregory (UK), Dennis L. Hartmann (USA), Eystein Jansen (Norway), Ben Kirtman (USA), Reto Knutti (Switzerland), Krishna Kumar Kanikicharla (India), Peter Lemke (Germany), Jochem Marotzke (Germany), Valérie Masson-Delmotte (France), Gerald A. Meehl (USA), Igor I. Mokhov (Russian Federation), Shilong Piao (China), Venkatachalam Ramaswamy (USA), David Randall (USA), Monika Rhein (Germany), Maisa Rojas (Chile), Christopher Sabine (USA), Drew Shindell (USA), Lynne D. Talley (USA), David G. Vaughan (UK), Shang-Ping Xie (USA)

Contributing Authors:
Myles R. Allen (UK), Olivier Boucher (France), Don Chambers (USA), Jens Hesselbjerg Christensen (Denmark), Philippe Ciais (France), Peter U. Clark (USA), Matthew Collins (UK), Josefino C. Comiso (USA), Viviane Vasconcellos de Menezes (Australia/Brazil), Richard A. Feely (USA), Thierry Fichefet (Belgium), Gregory Flato (Canada), Jesús Fidel González Rouco (Spain), Ed Hawkins (UK), Paul J. Hezel (Belgium/USA), Gregory C. Johnson (USA), Simon A. Josey (UK), Georg Kaser (Austria/Italy), Albert M.G. Klein Tank (Netherlands), Janina Körper (Germany), Gunnar Myhre (Norway), Timothy Osborn (UK), Scott B. Power (Australia), Stephen R. Rintoul (Australia), Joeri Rogelj (Switzerland/Belgium), Matilde Rusticucci (Argentina), Michael Schulz (Germany), Jan Sedláček (Switzerland), Peter A. Stott (UK), Rowan Sutton (UK), Peter W. Thorne (USA/Norway/UK), Donald Wuebbles (USA)

Review Editors:
Sylvie Joussaume (France), Joyce Penner (USA), Fredolin Tangang (Malaysia)

This Technical Summary should be cited as:
Stocker, T.F., D. Qin, G.-K. Plattner, L.V. Alexander, S.K. Allen, N.L. Bindoff, F.-M. Bréon, J.A. Church, U. Cubasch, S. Emori, P. Forster, P. Friedlingstein, N. Gillett, J.M. Gregory, D.L. Hartmann, E. Jansen, B. Kirtman, R. Knutti, K. Krishna Kumar, P. Lemke, J. Marotzke, V. Masson-Delmotte, G.A. Meehl, I.I. Mokhov, S. Piao, V. Ramaswamy, D. Randall, M. Rhein, M. Rojas, C. Sabine, D. Shindell, L.D. Talley, D.G. Vaughan and S.-P. Xie, 2013: Technical Summary. In: *Climate Change 2013: The Physical Science Basis. Contribution of Working Group I to the Fifth Assessment Report of the Intergovernmental Panel on Climate Change* [Stocker, T.F., D. Qin, G.-K. Plattner, M. Tignor, S.K. Allen, J. Boschung, A. Nauels, Y. Xia, V. Bex and P.M. Midgley (eds.)]. Cambridge University Press, Cambridge, United Kingdom and New York, NY, USA.

Table of Contents

Supplementary Material

Supplementary Material is available in online versions of the report.

TS.1 Introduction

Climate Change 2013: The Physical Science Basis is the contribution of Working Group I (WGI) to the Fifth Assessment Report (AR5) of the Intergovernmental Panel on Climate Change (IPCC). This comprehensive assessment of the physical aspects of climate change puts a focus on those elements that are relevant to understand past, document current and project future climate change. The assessment builds on the IPCC Fourth Assessment Report (AR4)[1] and the recent Special Report on Managing the Risk of Extreme Events and Disasters to Advance Climate Change Adaptation (SREX)[2] and is presented in 14 chapters and 3 annexes. The chapters cover direct and proxy observations of changes in all components of the climate system; assess the current knowledge of various processes within, and interactions among, climate system components, which determine the sensitivity and response of the system to changes in forcing; and quantify the link between the changes in atmospheric constituents, and hence radiative forcing (RF)[3], and the consequent detection and attribution of climate change. Projections of changes in all climate system components are based on model simulations forced by a new set of scenarios. The Report also provides a comprehensive assessment of past and future sea level change in a dedicated chapter. Regional climate change information is presented in the form of an Atlas of Global and Regional Climate Projections (Annex I). This is complemented by Annex II: Climate System Scenario Tables and Annex III: Glossary.

The primary purpose of this Technical Summary (TS) is to provide the link between the complete assessment of the multiple lines of independent evidence presented in the 14 chapters of the main report and the highly condensed summary prepared as the WGI Summary for Policymakers (SPM). The Technical Summary thus serves as a starting point for those readers who seek the full information on more specific topics covered by this assessment. This purpose is facilitated by including pointers to the chapters and sections where the full assessment can be found. Policy-relevant topics, which cut across many chapters and involve many interlinked processes in the climate system, are presented here as Thematic Focus Elements (TFEs), allowing rapid access to this information.

An integral element of this report is the use of uncertainty language that permits a traceable account of the assessment (Box TS.1). The degree of certainty in key findings in this assessment is based on the author teams' evaluations of underlying scientific understanding and is expressed as a level of confidence that results from the type, amount, quality and consistency of evidence and the degree of agreement in the scientific studies considered[4]. Confidence is expressed qualitatively. Quantified measures of uncertainty in a finding are expressed probabilistically and are based on a combination of statistical analyses of observations or model results, or both, and expert judgement. Where appropriate, findings are also formulated as statements of fact without using uncertainty qualifiers (see Chapter 1 and Box TS.1 for more details).

The Technical Summary is structured into four main sections presenting the assessment results following the storyline of the WGI contribution to AR5: Section TS.2 covers the assessment of observations of changes in the climate system; Section TS.3 summarizes the information on the different drivers, natural and anthropogenic, expressed in terms of RF; Section TS.4 presents the assessment of the quantitative understanding of observed climate change; and Section TS.5 summarizes the assessment results for projections of future climate change over the 21st century and beyond from regional to global scale. Section TS.6 combines and lists key uncertainties from the WGI assessment from Sections TS.2 to TS.5. The overall nine TFEs, cutting across the various components of the WGI AR5, are dispersed throughout the four main TS sections, are visually distinct from the main text and should allow stand-alone reading.

The basis for substantive paragraphs in this Technical Summary can be found in the chapter sections of the underlying report. These references are given in curly brackets.

---

1 IPCC, 2007: *Climate Change 2007: The Physical Science Basis.* Contribution of Working Group I to the Fourth Assessment Report of the Intergovernmental Panel on Climate Change [Solomon, S., D. Qin, M. Manning, Z. Chen, M. Marquis, K.B. Averyt, M. Tignor and H.L. Miller (eds.)]. Cambridge University Press, Cambridge, United Kingdom and New York, NY, USA, 996 pp.

2 IPCC, 2012: *Managing the Risks of Extreme Events and Disasters to Advance Climate Change Adaptation*. A Special Report of Working Groups I and II of the Intergovernmental Panel on Climate Change [Field, C.B., V. Barros, T.F. Stocker, D. Qin, D.J. Dokken, K.L. Ebi, M.D. Mastrandrea, K.J. Mach, G.-K. Plattner, S.K. Allen, M. Tignor and P. M. Midgley (eds.)]. Cambridge University Press, Cambridge, UK, and New York, NY, USA, 582 pp.

3 Radiative forcing (RF) is a measure of the net change in the energy balance of the Earth system in response to some external perturbation. It is expressed in watts per square metre (W m^{-2}); see Box TS.2.

4 Mastrandrea, M.D., C.B. Field, T.F. Stocker, O. Edenhofer, K.L. Ebi, D.J. Frame, H. Held, E. Kriegler, K.J. Mach, P.R. Matschoss, G.-K. Plattner, G.W. Yohe, and F.W. Zwiers, 2010: *Guidance Note for Lead Authors of the IPCC Fifth Assessment Report on Consistent Treatment of Uncertainties*. Intergovernmental Panel on Climate Change (IPCC).

Box TS.1 | Treatment of Uncertainty

Based on the Guidance Note for Lead Authors of the IPCC Fifth Assessment Report on Consistent Treatment of Uncertainties, this WGI Technical Summary and the WGI Summary for Policymakers rely on two metrics for communicating the degree of certainty in key findings, which is based on author teams' evaluations of underlying scientific understanding:

- Confidence in the validity of a finding, based on the type, amount, quality and consistency of evidence (e.g., mechanistic understanding, theory, data, models, expert judgement) and the degree of agreement. Confidence is expressed qualitatively.
- Quantified measures of uncertainty in a finding expressed probabilistically (based on statistical analysis of observations or model results, or expert judgement).

The AR5 Guidance Note refines the guidance provided to support the IPCC Third and Fourth Assessment Reports. Direct comparisons between assessment of uncertainties in findings in this Report and those in the AR4 and the SREX are difficult, because of the application of the revised guidance note on uncertainties, as well as the availability of new information, improved scientific understanding, continued analyses of data and models and specific differences in methodologies applied in the assessed studies. For some climate variables, different aspects have been assessed and therefore a direct comparison would be inappropriate.

Each key finding is based on an author team's evaluation of associated evidence and agreement. The confidence metric provides a qualitative synthesis of an author team's judgement about the validity of a finding, as determined through evaluation of evidence and agreement. If uncertainties can be quantified probabilistically, an author team can characterize a finding using the calibrated likelihood language or a more precise presentation of probability. Unless otherwise indicated, high or very high confidence is associated with findings for which an author team has assigned a likelihood term.

The following summary terms are used to describe the available evidence: limited, medium, or robust; and for the degree of agreement: low, medium, or high. A level of confidence is expressed using five qualifiers very low, low, medium, high, and very high, and typeset in italics, e.g., *medium confidence.* Box TS.1, Figure 1 depicts summary statements for evidence and agreement and their relationship to confidence. There is flexibility in this relationship; for a given evidence and agreement statement, different confidence levels can be assigned, but increasing levels of evidence and degrees of agreement correlate with increasing confidence.

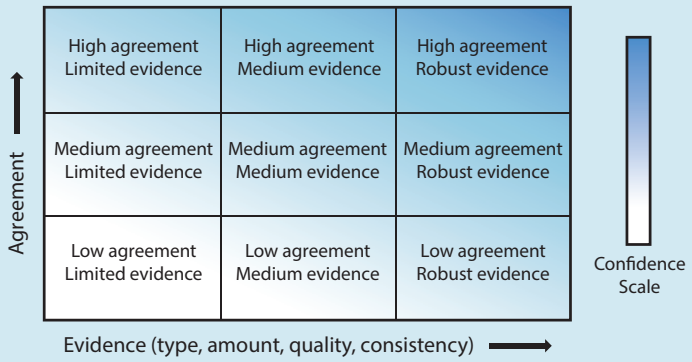

Box TS.1, Figure 1 | A depiction of evidence and agreement statements and their relationship to confidence. Confidence increases toward the top right corner as suggested by the increasing strength of shading. Generally, evidence is most robust when there are multiple, consistent independent lines of high quality. {Figure 1.11}

The following terms have been used to indicate the assessed likelihood, and typeset in italics:

Term*	Likelihood of the outcome
Virtually certain	99–100% probability
Very likely	90–100% probability
Likely	66–100% probability
About as likely as not	33–66% probability
Unlikely	0–33% probability
Very unlikely	0–10% probability
Exceptionally unlikely	0–1% probability

* Additional terms (*extremely likely*: 95–100% probability, *more likely than not*: >50–100% probability, and *extremely unlikely*: 0–5% probability) may also be used when appropriate.

TS.2 Observation of Changes in the Climate System

TS.2.1 Introduction

Observations of the climate system are based on direct physical and biogeochemical measurements, and remote sensing from ground stations and satellites; information derived from paleoclimate archives provides a long-term context. Global-scale observations from the instrumental era began in the mid-19th century, and paleoclimate reconstructions extend the record of some quantities back hundreds to millions of years. Together, they provide a comprehensive view of the variability and long-term changes in the atmosphere, the ocean, the cryosphere and at the land surface.

The assessment of observational evidence for climate change is summarized in this section. Substantial advancements in the availability, acquisition, quality and analysis of observational data sets for the atmosphere, land surface, ocean and cryosphere have occurred since the AR4. Many aspects of the climate system are showing evidence of a changing climate. {2, 3, 4, 5, 6, 13}

TS.2.2 Changes in Temperature

TS.2.2.1 Surface

It is certain that global mean surface temperature (GMST) has increased since the late 19th century (Figures TS.1 and TS.2). Each of the past three decades has been successively warmer at the Earth's surface than any the previous decades in the instrumental record, and the decade of the 2000's has been the warmest. The globally averaged combined land and ocean temperature data as calculated by a linear trend[5], show a warming of 0.85 [0.65 to 1.06] °C[6], over the period 1880–2012, when multiple independently produced datasets exist, about 0.89 [0.69 to 1.08] °C over the period 1901–2012, and about 0.72 [0.49 to 0.89] °C over the period 1951–2012 when based on three independently-produced data sets. The total increase between the average of the 1850–1900 period and the 2003–2012 period is 0.78 [0.72 to 0.85] °C, based on the Hadley Centre/Climatic Research Unit gridded surface temperature data set 4 (HadCRUT4), the global mean surface temperature dataset with the longest record of the three independently-produced data sets. The warming from 1850–1900 to 1986–2005 (reference period for the modelling chapters and the Atlas in Annex I) is 0.61 [0.55 to 0.67] °C, when calculated using HadCRUT4 and its uncertainty estimates. It is also *virtually certain* that maximum and minimum temperatures over land have increased on a global scale since 1950.[7] {2.4.1, 2.4.3; Chapter 2 Supplementary Material Section 2.SM.3}

Despite the robust multi-decadal warming, there exists substantial interannual to decadal variability in the rate of warming, with several periods exhibiting weaker trends (including the warming hiatus since 1998) (Figure TS.1). The rate of warming over the past 15 years (1998–2012; 0.05 [–0.05 to +0.15] °C per decade) is smaller than the trend since 1951 (1951–2012; 0.12[0.08 to 0.14] °C per decade). Trends for short periods are uncertain and very sensitive to the start and end years. For example, trends for 15-year periods starting in 1995, 1996, and 1997 are 0.13 [0.02 to 0.24] °C per decade, 0.14 [0.03 to 0.24] °C per decade and 0.07 [–0.02 to 0.18] °C per decade, respectively. Several independently analysed data records of global and regional land surface air temperature obtained from station observations are in broad agreement that land surface air temperatures have increased. Sea surface temperatures (SSTs) have also increased. Intercomparisons of new SST data records obtained by different measurement methods, including satellite data, have resulted in better understanding of errors and biases in the records. {2.4.1–2.4.3; Box 9.2}

It is *unlikely* that any uncorrected urban heat island effects and land use change effects have raised the estimated centennial globally averaged land surface air temperature trends by more than 10% of the reported trend. This is an average value; in some regions that have rapidly developed urban heat island and land use change impacts on regional trends may be substantially larger. {2.4.1}

There is *high confidence* that annual mean surface warming since the 20th century has reversed long-term cooling trends of the past 5000 years in mid-to-high latitudes of the Northern Hemisphere (NH). For average annual NH temperatures, the period 1983–2012 was *very likely* the warmest 30-year period of the last 800 years (*high confidence*) and *likely* the warmest 30-year period of the last 1400 years (*medium confidence*). This is supported by comparison of instrumental temperatures with multiple reconstructions from a variety of proxy data and statistical methods, and is consistent with AR4. Continental-scale surface temperature reconstructions show, with *high confidence*, multi-decadal periods during the Medieval Climate Anomaly (950–1250) that were in some regions as warm as in the mid-20th century and in others as warm as in the late 20th century. With *high confidence*, these regional warm periods were not as synchronous across regions as the warming since the mid-20th century. Based on the comparison between reconstructions and simulations, there is *high confidence* that not only external orbital, solar and volcanic forcing, but also internal

[5] The warming is reported as an unweighted average based on linear trend estimates calculated from Hadley Centre/Climatic Research Unit gridded surface temperature data set 4 (HadCRUT4), Merged Land–Ocean Surface Temperature Analysis (MLOST) and Goddard Institute for Space Studies Surface Temperature Analysis (GISTEMP) data sets (see Figure TS.2; Section 2.4.3).

[6] In the WGI contribution to the AR5, uncertainty is quantified using 90% uncertainty intervals unless otherwise stated. The 90% uncertainty interval, reported in square brackets, is expected to have a 90% likelihood of covering the value that is being estimated. The upper endpoint of the uncertainty interval has a 95% likelihood of exceeding the value that is being estimated and the lower endpoint has a 95% likelihood of being less than that value. A best estimate of that value is also given where available. Uncertainty intervals are not necessarily symmetric about the corresponding best estimate.

[7] Both methods presented in this paragraph to calculate temperature change were also used in AR4. The first calculates the difference using a best fit linear trend of all points between two years, e.g., 1880 and 2012. The second calculates the difference between averages for the two periods, e.g., 1850 to 1900 and 2003 to 2012. Therefore, the resulting values and their 90% uncertainty intervals are not directly comparable.

variability, contributed substantially to the spatial pattern and timing of surface temperature changes between the Medieval Climate Anomaly and the Little Ice Age (1450–1850). {5.3.5, 5.5.1}

TS.2.2.2 Troposphere and Stratosphere

Based on multiple independent analyses of measurements from radiosondes and satellite sensors, it is *virtually certain* that globally the troposphere has warmed and the stratosphere has cooled since the mid-20th century (Figure TS.1). Despite unanimous agreement on the sign of the trends, substantial disagreement exists between available estimates as to the rate of temperature changes, particularly outside the NH extratropical troposphere, which has been well sampled by radiosondes. Hence there is only *medium confidence* in the rate of change and its vertical structure in the NH extratropical troposphere and *low confidence* elsewhere. {2.4.4}

TS.2.2.3 Ocean

It is *virtually certain* that the upper ocean (above 700 m) has warmed from 1971 to 2010, and *likely* that it has warmed from the 1870s to 1971 (Figure TS.1). There is less certainty in changes prior to 1971 because of relatively sparse sampling in earlier time periods. Instrumental biases in historical upper ocean temperature measurements have been identified and reduced since AR4, diminishing artificial decadal variation in temperature and upper ocean heat content, most prominent during the 1970s and 1980s. {3.2.1–3.2.3, 3.5.3}

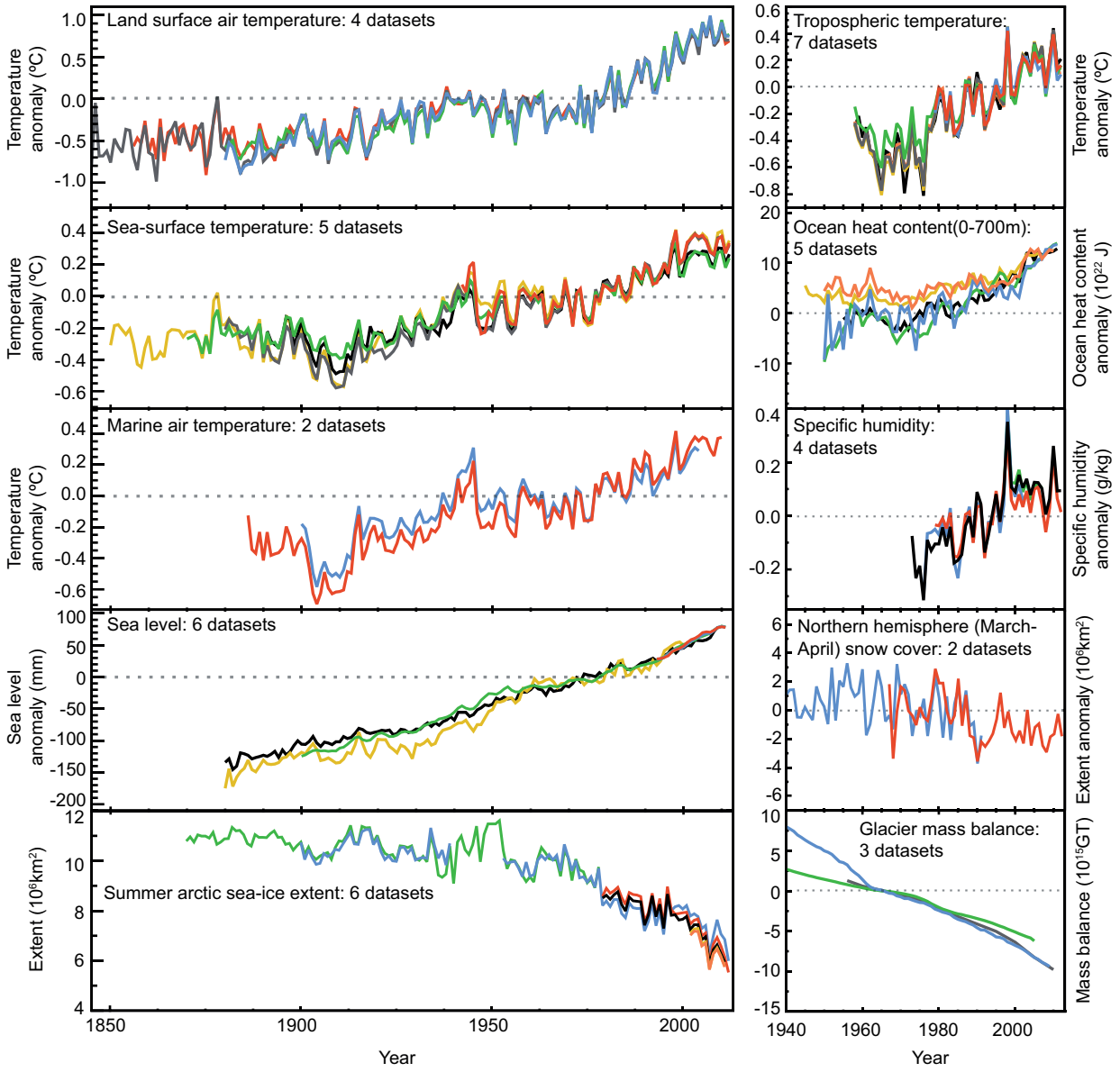

Figure TS.1 | Multiple complementary indicators of a changing global climate. Each line represents an independently derived estimate of change in the climate element. The times series presented are assessed in Chapters 2, 3 and 4. In each panel all data sets have been normalized to a common period of record. A full detailing of which source data sets go into which panel is given in Chapter 2 Supplementary Material Section 2.SM.5 and in the respective chapters. Further detail regarding the related Figure SPM.3 is given in the TS Supplementary Material. {FAQ 2.1, Figure 1; 2.4, 2.5, 3.2, 3.7, 4.5.2, 4.5.3}

It is *likely* that the ocean warmed between 700-2000 m from 1957 to 2009, based on 5-year averages. It is *likely* that the ocean warmed from 3000 m to the bottom from 1992 to 2005, while no significant trends in global average temperature were observed between 2000 and 3000 m depth from circa 1992 to 2005. Below 3000 m depth, the largest warming is observed in the Southern Ocean. {3.2.4, 3.5.1; Figures 3.2b, 3.3; FAQ 3.1}

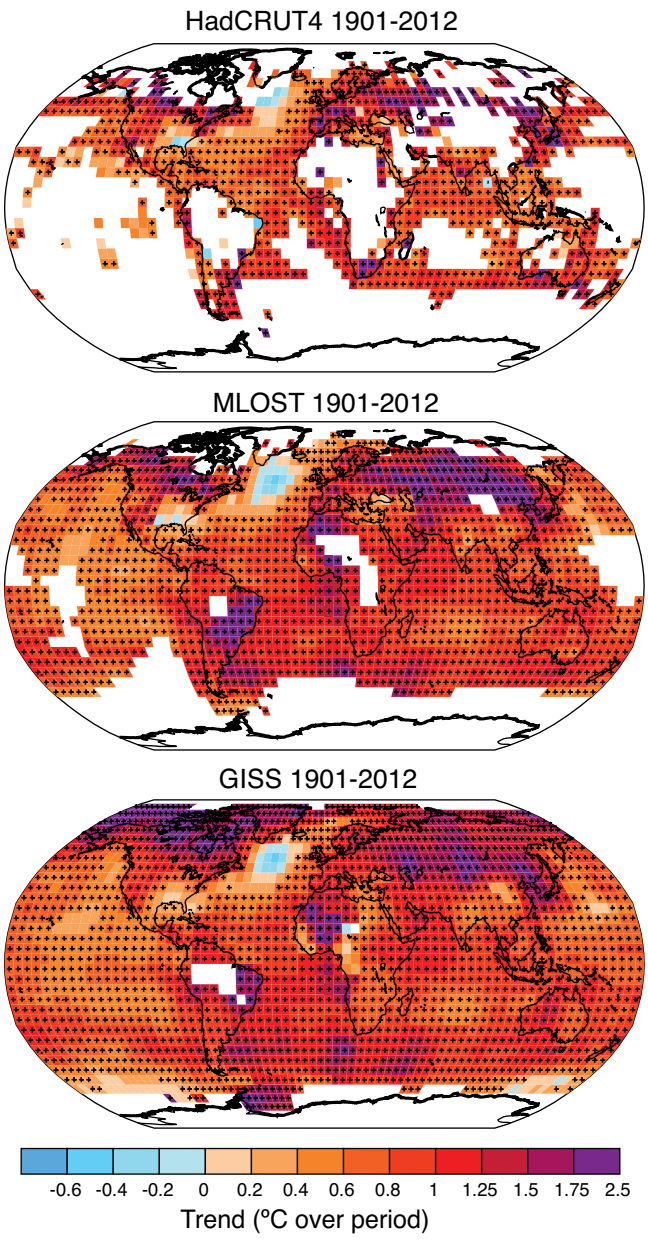

Figure TS.2 | Change in surface temperature over 1901–2012 as determined by linear trend for three data sets. White areas indicate incomplete or missing data. Trends have been calculated only for those grid boxes with greater than 70% complete records and more than 20% data availability in the first and last 10% of the time period. Black plus signs (+) indicate grid boxes where trends are significant (i.e., a trend of zero lies outside the 90% confidence interval). Differences in coverage primarily reflect the degree of interpolation to account for data void regions undertaken by the data set providers ranging from none beyond grid box averaging (Hadley Centre/Climatic Research Unit gridded surface temperature data set 4 (HadCRUT4)) to substantial (Goddard Institute for Space Studies Surface Temperature Analysis (GISTEMP)). Further detail regarding the related Figure SPM.1 is given in the TS Supplementary Material. {Figure 2.21}

TS.2.3 Changes in Energy Budget and Heat Content

The Earth has been in radiative imbalance, with more energy from the Sun entering than exiting the top of the atmosphere, since at least about 1970. It is *virtually certain* that the Earth has gained substantial energy from 1971 to 2010. The estimated increase in energy inventory between 1971 and 2010 is 274 [196 to 351] $\times 10^{21}$ J (*high confidence*), with a heating rate of 213 $\times 10^{12}$ W from a linear fit to the annual values over that time period (see also TFE.4). {Boxes 3.1, 13.1}

Ocean warming dominates that total heating rate, with full ocean depth warming accounting for about 93% (*high confidence*), and warming of the upper (0 to 700 m) ocean accounting for about 64%. Melting ice (including Arctic sea ice, ice sheets and glaciers) and warming of the continents each account for 3% of the total. Warming of the atmosphere makes up the remaining 1%. The 1971–2010 estimated rate of ocean energy gain is 199 $\times 10^{12}$ W from a linear fit to data over that time period, equivalent to 0.42 W m^{-2} heating applied continuously over the Earth's entire surface, and 0.55 W m^{-2} for the portion owing to ocean warming applied over the ocean's entire surface area. The Earth's estimated energy increase from 1993 to 2010 is 163 [127 to 201] $\times 10^{21}$ J with a trend estimate of 275 $\times 10^{15}$ W. The ocean portion of the trend for 1993–2010 is 257 $\times 10^{12}$ W, equivalent to a mean heat flux into the ocean of 0.71 W m^{-2}. {3.2.3, 3.2.4; Box 3.1}

It is *about as likely as not* that ocean heat content from 0–700 m increased more slowly during 2003 to 2010 than during 1993 to 2002 (Figure TS.1). Ocean heat uptake from 700–2000 m, where interannual variability is smaller, *likely* continued unabated from 1993 to 2009. {3.2.3, 3.2.4; Box 9.2}

TS.2.4 Changes in Circulation and Modes of Variability

Large variability on interannual to decadal time scales hampers robust conclusions on long-term changes in atmospheric circulation in many instances. *Confidence* is *high* that the increase of the northern mid-latitude westerly winds and the North Atlantic Oscillation (NAO) index from the 1950s to the 1990s, and the weakening of the Pacific Walker Circulation from the late 19th century to the 1990s, have been largely offset by recent changes. With *high confidence*, decadal and multi-decadal changes in the winter NAO index observed since the 20th century are not unprecedented in the context of the past 500 years. {2.7.2, 2.7.5, 2.7.8, 5.4.2; Box 2.5; Table 2.14}

It is *likely* that circulation features have moved poleward since the 1970s, involving a widening of the tropical belt, a poleward shift of storm tracks and jet streams and a contraction of the northern polar vortex. Evidence is more robust for the NH. It is *likely* that the Southern Annular Mode (SAM) has become more positive since the 1950s. The increase in the strength of the observed summer SAM since 1950 has been anomalous, with *medium confidence*, in the context of the past 400 years. {2.7.5, 2.7.6, 2.7.8, 5.4.2; Box 2.5; Table 2.14}

New results from high-resolution coral records document with *high confidence* that the El Niño-Southern Oscillation (ENSO) system has remained highly variable throughout the past 7000 years, showing no discernible evidence for an orbital modulation of ENSO. {5.4.1}

Recent observations have strengthened evidence for variability in major ocean circulation systems on time scales from years to decades. It is *very likely* that the subtropical gyres in the North Pacific and South Pacific have expanded and strengthened since 1993. Based on measurements of the full Atlantic Meridional Overturning Circulation (AMOC) and its individual components at various latitudes and different time periods, there is no evidence of a long-term trend. There is also no evidence for trends in the transports of the Indonesian Throughflow, the Antarctic Circumpolar Current (ACC) or in the transports between the Atlantic Ocean and Nordic Seas. However, a southward shift of the ACC by about 1° of latitude is observed in data spanning the time period 1950–2010 with *medium confidence*. {3.6}

TS.2.5 Changes in the Water Cycle and Cryosphere

TS.2.5.1 Atmosphere

Confidence in precipitation change averaged over global land areas is *low* prior to 1951 and *medium* afterwards because of insufficient data, particularly in the earlier part of the record (for an overview of observed and projected changes in the global water cycle see TFE.1). Further, when virtually all the land area is filled in using a reconstruction method, the resulting time series shows little change in land-based precipitation since 1901. NH mid-latitude land areas do show a *likely* overall increase in precipitation (*medium confidence* prior to 1951, but *high confidence* afterwards). For other latitudes area-averaged long-term positive or negative trends have *low confidence* (TFE.1, Figure 1). {2.5.1}

It is *very likely* that global near surface and tropospheric air specific humidity have increased since the 1970s. However, during recent years the near-surface moistening trend over land has abated (*medium confidence*) (Figure TS.1). As a result, fairly widespread decreases in relative humidity near the surface are observed over the land in recent years. {2.4.4, 2.5.5, 2.5.6}

Although trends of cloud cover are consistent between independent data sets in certain regions, substantial ambiguity and therefore *low confidence* remains in the observations of global-scale cloud variability and trends. {2.5.7}

TS.2.5.2 Ocean and Surface Fluxes

It is *very likely* that regional trends have enhanced the mean geographical contrasts in sea surface salinity since the 1950s: saline surface waters in the evaporation-dominated mid-latitudes have become more saline, while relatively fresh surface waters in rainfall-dominated tropical and polar regions have become fresher. The mean contrast between high- and low-salinity regions increased by 0.13 [0.08 to 0.17] from 1950 to 2008. It is *very likely* that the inter-basin contrast in freshwater content has increased: the Atlantic has become saltier and the Pacific and Southern Oceans have freshened. Although similar conclusions were reached in AR4, recent studies based on expanded data sets and new analysis approaches provide *high confidence* in this assessment. {3.3.2, 3.3.3, 3.9; FAQ 3.2}

The spatial patterns of the salinity trends, mean salinity and the mean distribution of evaporation minus precipitation are all similar (TFE.1, Figure 1). These similarities provide indirect evidence that the pattern of evaporation minus precipitation over the oceans has been enhanced since the 1950s (*medium confidence*). Uncertainties in currently available surface fluxes prevent the flux products from being reliably used to identify trends in the regional or global distribution of evaporation or precipitation over the oceans on the time scale of the observed salinity changes since the 1950s. {3.3.2–3.3.4, 3.4.2, 3.4.3, 3.9; FAQ 3.2}

TS.2.5.3 Sea Ice

Continuing the trends reported in AR4, there is *very high confidence* that the Arctic sea ice extent (annual, multi-year and perennial) decreased over the period 1979–2012 (Figure TS.1). The rate of the annual decrease was *very likely* between 3.5 and 4.1% per decade (range of 0.45 to 0.51 million km^2 per decade). The average decrease in decadal extent of annual Arctic sea ice has been most rapid in summer and autumn (*high confidence*), but the extent has decreased in every season, and in every successive decade since 1979 (*high confidence*). The extent of Arctic perennial and multi-year ice decreased between 1979 and 2012 (*very high confidence*). The rates are *very likely* 11.5 [9.4 to 13.6]% per decade (0.73 to 1.07 million km^2 per decade) for the sea ice extent at summer minimum (perennial ice) and *very likely* 13.5 [11 to 16] % per decade for multi-year ice. There is *medium confidence* from reconstructions that the current (1980–2012) Arctic summer sea ice retreat was unprecedented and SSTs were anomalously high in the perspective of at least the last 1,450 years. {4.2.2, 5.5.2}

It is *likely* that the annual period of surface melt on Arctic perennial sea ice lengthened by 5.7 [4.8 to 6.6] days per decade over the period 1979–2012. Over this period, in the region between the East Siberian Sea and the western Beaufort Sea, the duration of ice-free conditions increased by nearly 3 months. {4.2.2}

There is *high confidence* that the average winter sea ice thickness within the Arctic Basin decreased between 1980 and 2008. The average decrease was *likely* between 1.3 m and 2.3 m. *High confidence* in this assessment is based on observations from multiple sources: submarine, electromagnetic probes and satellite altimetry; and is consistent with the decline in multi-year and perennial ice extent. Satellite measurements made in the period 2010–2012 show a decrease in sea ice volume compared to those made over the period 2003–2008 (*medium confidence*). There is *high confidence* that in the Arctic, where the sea ice thickness has decreased, the sea ice drift speed has increased. {4.2.2}

It is *very likely* that the annual Antarctic sea ice extent increased at a rate of between 1.2 and 1.8% per decade (0.13 to 0.20 million km^2 per decade) between 1979 and 2012 (*very high confidence*). There was a greater increase in sea ice area, due to a decrease in the percentage of open water within the ice pack. There is *high confidence* that there are strong regional differences in this annual rate, with some regions increasing in extent/area and some decreasing. There are also contrasting regions around the Antarctic where the ice-free season has lengthened, and others where it has decreased over the satellite period (*high confidence*). {4.2.3}

TS.2.5.4 Glaciers and Ice Sheets

There is *very high confidence* that glaciers world-wide are persistently shrinking as revealed by the time series of measured changes in glacier length, area, volume and mass (Figures TS.1 and TS.3). The few exceptions are regionally and temporally limited. Measurements of glacier change have increased substantially in number since AR4. Most of the new data sets, along with a globally complete glacier inventory, have been derived from satellite remote sensing {4.3.1, 4.3.3}

There is *very high confidence* that, during the last decade, the largest contributions to global glacier ice loss were from glaciers in Alaska, the Canadian Arctic, the periphery of the Greenland ice sheet, the Southern Andes and the Asian mountains. Together these areas account for more than 80% of the total ice loss. Total mass loss from all glaciers in the world, excluding those on the periphery of the ice sheets, was *very likely* 226 [91 to 361] Gt yr^{-1} (sea level equivalent, 0.62 [0.25 to 0.99] mm yr^{-1}) in the period 1971–2009, 275 [140 to 410] Gt yr^{-1} (0.76 [0.39 to 1.13] mm yr^{-1}) in the period 1993–2009 and 301 [166 to 436] Gt yr^{-1} (0.83 [0.46 to 1.20] mm yr^{-1}) between 2005 and 2009[8]. {4.3.3; Tables 4.4, 4.5}

There is *high confidence* that current glacier extents are out of balance with current climatic conditions, indicating that glaciers will continue to shrink in the future even without further temperature increase. {4.3.3}

There is *very high confidence* that the Greenland ice sheet has lost ice during the last two decades. Combinations of satellite and airborne remote sensing together with field data indicate with *high confidence* that the ice loss has occurred in several sectors and that large rates of mass loss have spread to wider regions than reported in AR4 (Figure TS.3). There is *high confidence* that the mass loss of the Greenland ice sheet has accelerated since 1992: the average rate has *very likely* increased from 34 [–6 to 74] Gt yr^{-1} over the period 1992–2001 (sea level equivalent, 0.09 [–0.02 to 0.20] mm yr^{-1}), to 215 [157 to 274] Gt yr^{-1} over the period 2002–2011 (0.59 [0.43 to 0.76] mm yr^{-1}). There is *high confidence* that ice loss from Greenland resulted from increased surface melt and runoff and increased outlet glacier discharge, and these occurred in similar amounts. There is *high confidence* that the area subject to summer melt has increased over the last two decades. {4.4.2, 4.4.3}

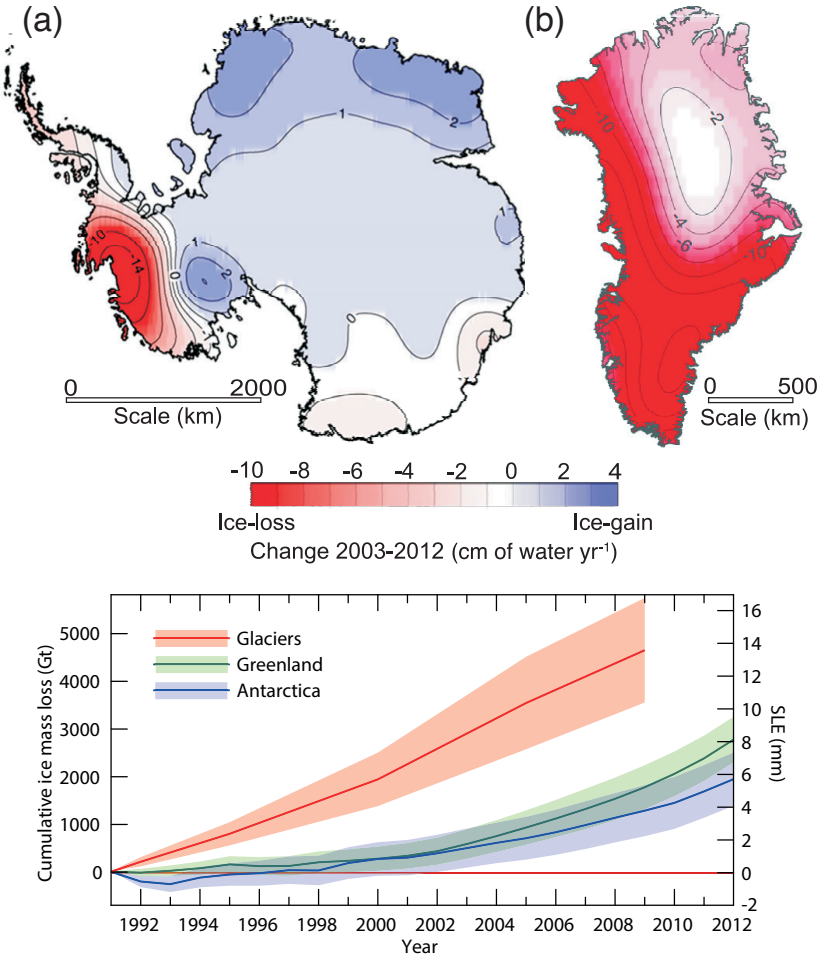

Figure TS.3 | (Upper) Distribution of ice loss determined from Gravity Recovery and Climate Experiment (GRACE) time-variable gravity for (a) Antarctica and (b) Greenland, shown in centimetres of water per year (cm of water yr^{-1}) for the period 2003–2012. (Lower) The assessment of the total loss of ice from glaciers and ice sheets in terms of mass (Gt) and sea level equivalent (mm). The contribution from glaciers excludes those on the periphery of the ice sheets. {4.3.4; Figures 4.12–4.14, 4.16, 4.17, 4.25}

[8] 100 Gt yr^{-1} of ice loss corresponds to about 0.28 mm yr^{-1} of sea level equivalent.

Thematic Focus Elements

TFE.1 | Water Cycle Change

The water cycle describes the continuous movement of water through the climate system in its liquid, solid and vapour forms, and storage in the reservoirs of ocean, cryosphere, land surface and atmosphere. In the atmosphere, water occurs primarily as a gas, water vapour, but it also occurs as ice and liquid water in clouds. The ocean is primarily liquid water, but the ocean is partly covered by ice in polar regions. Terrestrial water in liquid form appears as surface water (lakes, rivers), soil moisture and groundwater. Solid terrestrial water occurs in ice sheets, glaciers, snow and ice on the surface and permafrost. The movement of water in the climate system is essential to life on land, as much of the water that falls on land as precipitation and supplies the soil moisture and river flow has been evaporated from the ocean and transported to land by the atmosphere. Water that falls as snow in winter can provide soil moisture in springtime and river flow in summer and is essential to both natural and human systems. The movement of fresh water between the atmosphere and the ocean can also influence oceanic salinity, which is an important driver of the density and circulation of the ocean. The latent heat contained in water vapour in the atmosphere is critical to driving the circulation of the atmosphere on scales ranging from individual thunderstorms to the global circulation of the atmosphere. {12.4.5; FAQ 3.2, FAQ 12.2}

Observations of Water Cycle Change

Because the saturation vapour pressure of air increases with temperature, it is expected that the amount of water vapour in air will increase with a warming climate. Observations from surface stations, radiosondes, global positioning systems and satellite measurements indicate increases in tropospheric water vapour at large spatial scales (TFE.1, Figure 1). It is *very likely* that tropospheric specific humidity has increased since the 1970s. The magnitude of the observed global change in tropospheric water vapour of about 3.5% in the past 40 years is consistent with the observed temperature change of about 0.5°C during the same period, and the relative humidity has stayed approximately constant. The water vapour change can be attributed to human influence with *medium confidence*. {2.5.4, 10.3.2}

Changes in precipitation are harder to measure with the existing records, both because of the greater difficulty in sampling precipitation and also because it is expected that precipitation will have a smaller fractional change than the water vapour content of air as the climate warms. Some regional precipitation trends appear to be robust (TFE.1, Figure 2), but when virtually all the land area is filled in using a reconstruction method, the resulting time series of global mean land precipitation shows little change since 1900. At present there is *medium confidence* that there has been a significant human influence on global scale changes in precipitation patterns, including increases in Northern Hemisphere (NH) mid-to-high latitudes. Changes in the extremes of precipitation, and other climate extremes related to the water cycle are comprehensively discussed in TFE.9. {2.5.1, 10.3.2}

Although direct trends in precipitation and evaporation are difficult to measure with the available records, the observed oceanic surface salinity, which is strongly dependent on the difference between evaporation and precipitation, shows significant trends (TFE.1, Figure 1). The spatial patterns of the salinity trends since 1950 are very similar to the mean salinity and the mean distribution of evaporation minus precipitation: regions of high salinity where evaporation dominates have become more saline, while regions of low salinity where rainfall dominates have become fresher (TFE.1, Figure 1). This provides indirect evidence that the pattern of evaporation minus precipitation over the oceans has been enhanced since the 1950s (*medium confidence*). The inferred changes in evaporation minus precipitation are consistent with the observed increased water vapour content of the warmer air. It is *very likely* that observed changes in surface and subsurface salinity are due in part to anthropogenic climate forcings. {2.5, 3.3.2–3.3.4, 3.4, 3.9, 10.4.2; FAQ 3.2}

In most regions analysed, it is *likely* that decreasing numbers of snowfall events are occurring where increased winter temperatures have been observed. Both satellite and *in situ* observations show significant reductions in the NH snow cover extent over the past 90 years, with most of the reduction occurring in the 1980s. Snow cover decreased most in June when the average extent decreased *very likely* by 53% (40 to 66%) over the period 1967 to 2012. From 1922 to 2012 only data from March and April are available and show *very likely* a 7% (4.5 to 9.5%) decline. Because of earlier spring snowmelt, the duration of the NH snow season has declined by 5.3 days per decade since the 1972/1973 winter. It is *likely* that there has been an anthropogenic component to these observed reductions in snow cover since the 1970s. {4.5.2, 10.5.1, 10.5.3}

(continued on next page)

TFE.1 (continued)

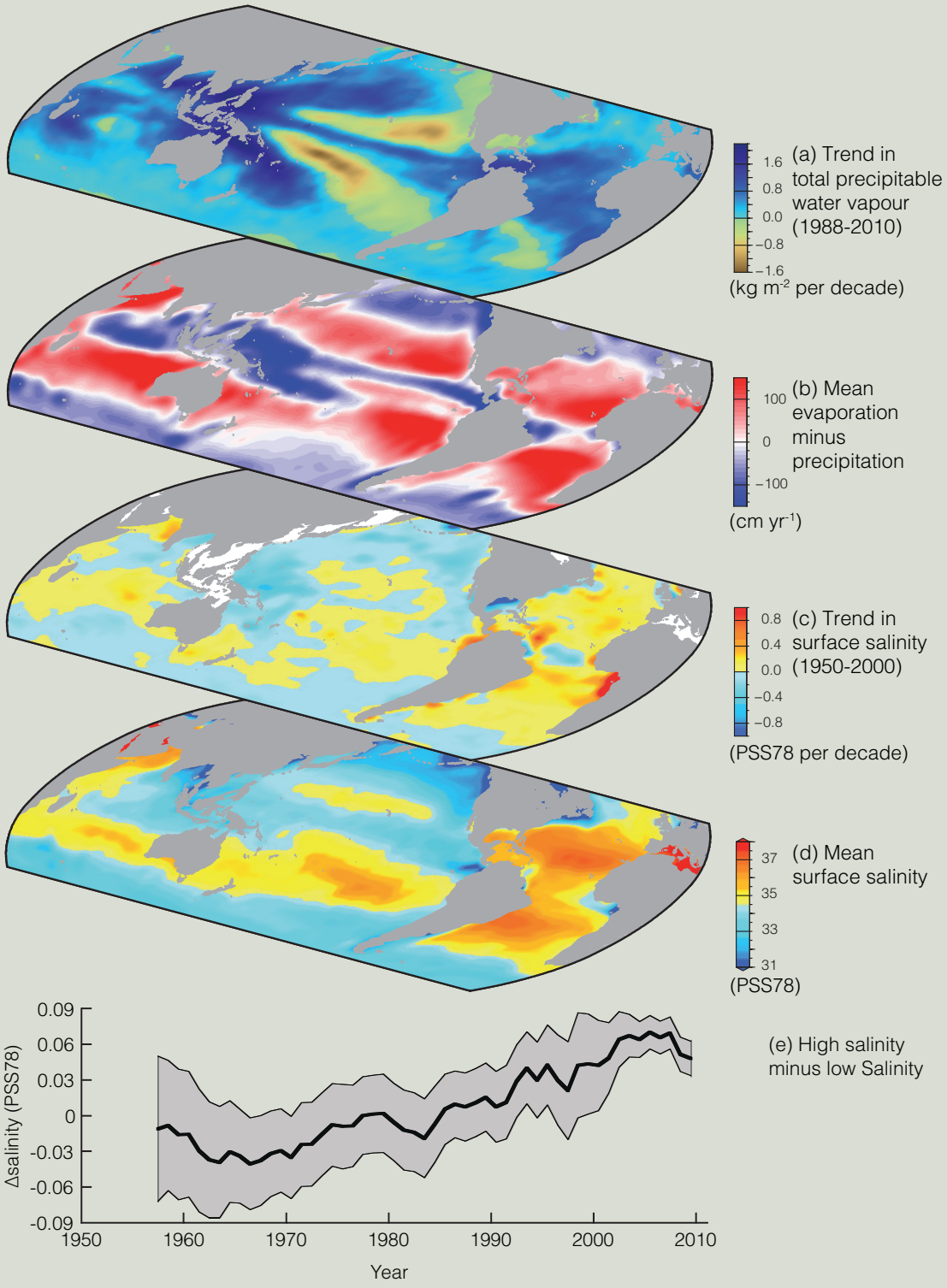

TFE.1, Figure 1 | Changes in sea surface salinity are related to the atmospheric patterns of evaporation minus precipitation ($E - P$) and trends in total precipitable water: (a) Linear trend (1988 to 2010) in total precipitable water (water vapour integrated from the Earth's surface up through the entire atmosphere) (kg m^{-2} per decade) from satellite observations. (b) The 1979–2005 climatological mean net evaporation minus precipitation (cm yr^{-1}) from meteorological reanalysis data. (c) Trend (1950–2000) in surface salinity (Practical Salinity Scale 78 (PSS78) per 50 years). (d) The climatological mean surface salinity (PSS78) (blues <35; yellows-reds >35). (e) Global difference between salinity averaged over regions where the sea surface salinity is greater than the global mean sea surface salinity ("High Salinity") and salinity averaged over regions with values below the global mean ('Low Salinity'). For details of data sources see Figure 3.21 and FAQ 3.2, Figure 1. {3.9}

TFE.1 (continued)

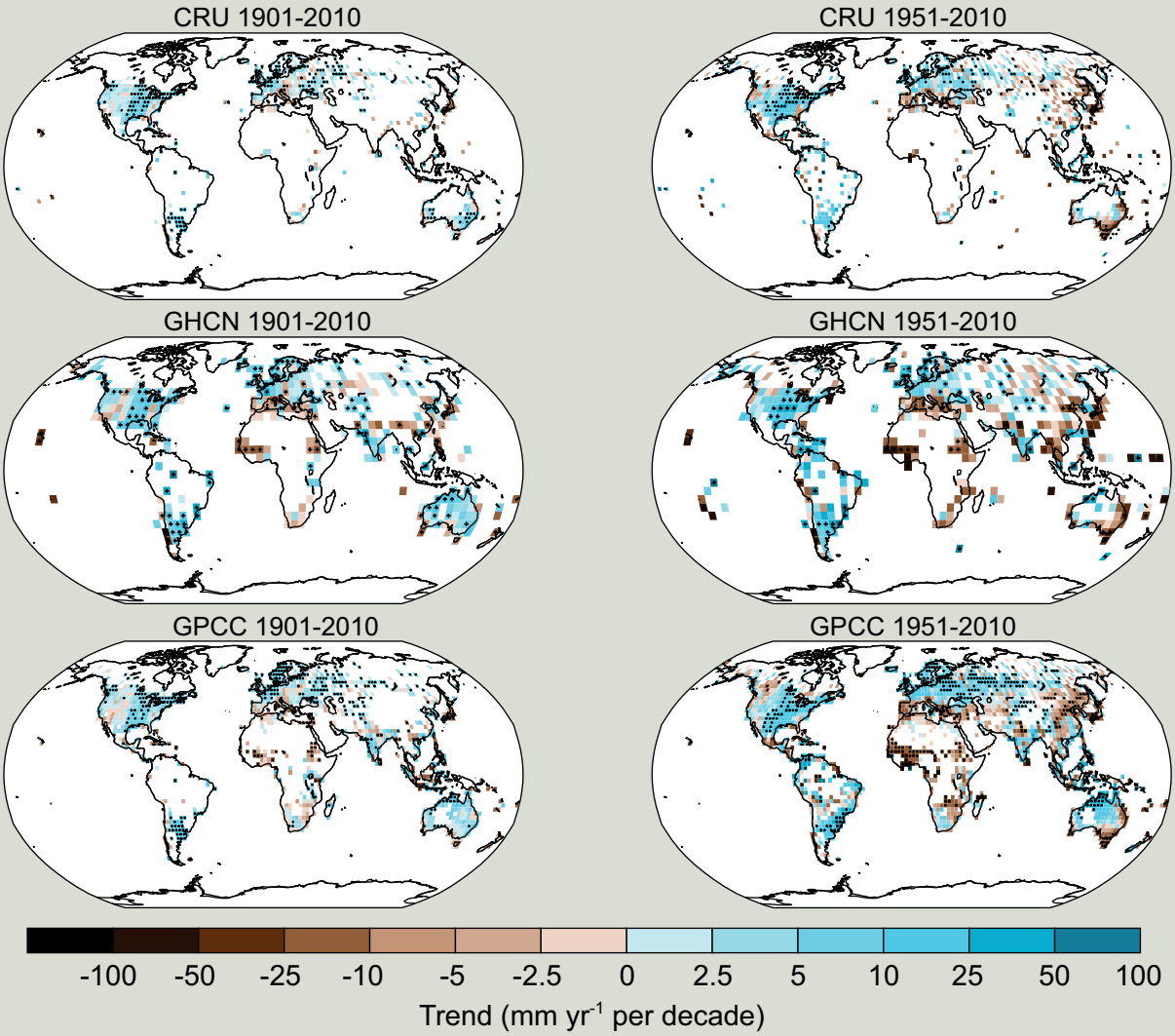

TFE.1, Figure 2 | Maps of observed precipitation change over land from 1901 to 2010 (left-hand panels) and 1951 to 2010 (right-hand panels) from the Climatic Research Unit (CRU), Global Historical Climatology Network (GHCN) and Global Precipitation Climatology Centre (GPCC) data sets. Trends in annual accumulation have been calculated only for those grid boxes with greater than 70% complete records and more than 20% data availability in first and last decile of the period. White areas indicate incomplete or missing data. Black plus signs (+) indicate grid boxes where trends are significant (i.e., a trend of zero lies outside the 90% confidence interval). Further detail regarding the related Figure SPM.2 is given in the TS Supplementary Material. {Figure 2.29; 2.5.1}

The most recent and most comprehensive analyses of river runoff do not support the IPCC Fourth Assessment Report (AR4) conclusion that global runoff has increased during the 20th century. New results also indicate that the AR4 conclusions regarding global increasing trends in droughts since the 1970s are no longer supported. {2.5.2, 2.6.2}

Projections of Future Changes

Changes in the water cycle are projected to occur in a warming climate (TFE.1, Figure 3, see also TS 4.6, TS 5.6, Annex I). Global-scale precipitation is projected to gradually increase in the 21st century. The precipitation increase is projected to be much smaller (about 2% K^{-1}) than the rate of lower tropospheric water vapour increase (about 7% K^{-1}), due to global energetic constraints. Changes of average precipitation in a much warmer world will not be uniform, with some regions experiencing increases, and others with decreases or not much change at all. The high latitude land masses are *likely* to experience greater amounts of precipitation due to the additional water carrying capacity of the warmer troposphere. Many mid-latitude and subtropical arid and semi-arid regions will *likely* experience less precipitation. The largest precipitation changes over northern Eurasia and North America are projected to occur during the winter. {12.4.5, Annex I}

(continued on next page)

TFE.1 (continued)

Regional to global-scale projections of soil moisture and drought remain relatively uncertain compared to other aspects of the water cycle. Nonetheless, drying in the Mediterranean, southwestern USA and southern African regions are consistent with projected changes in the Hadley Circulation, so drying in these regions as global temperatures increase is *likely* for several degrees of warming under the Representative Concentration Pathway RCP8.5. Decreases in runoff are *likely* in southern Europe and the Middle East. Increased runoff is *likely* in high northern latitudes, and consistent with the projected precipitation increases there. {12.4.5}

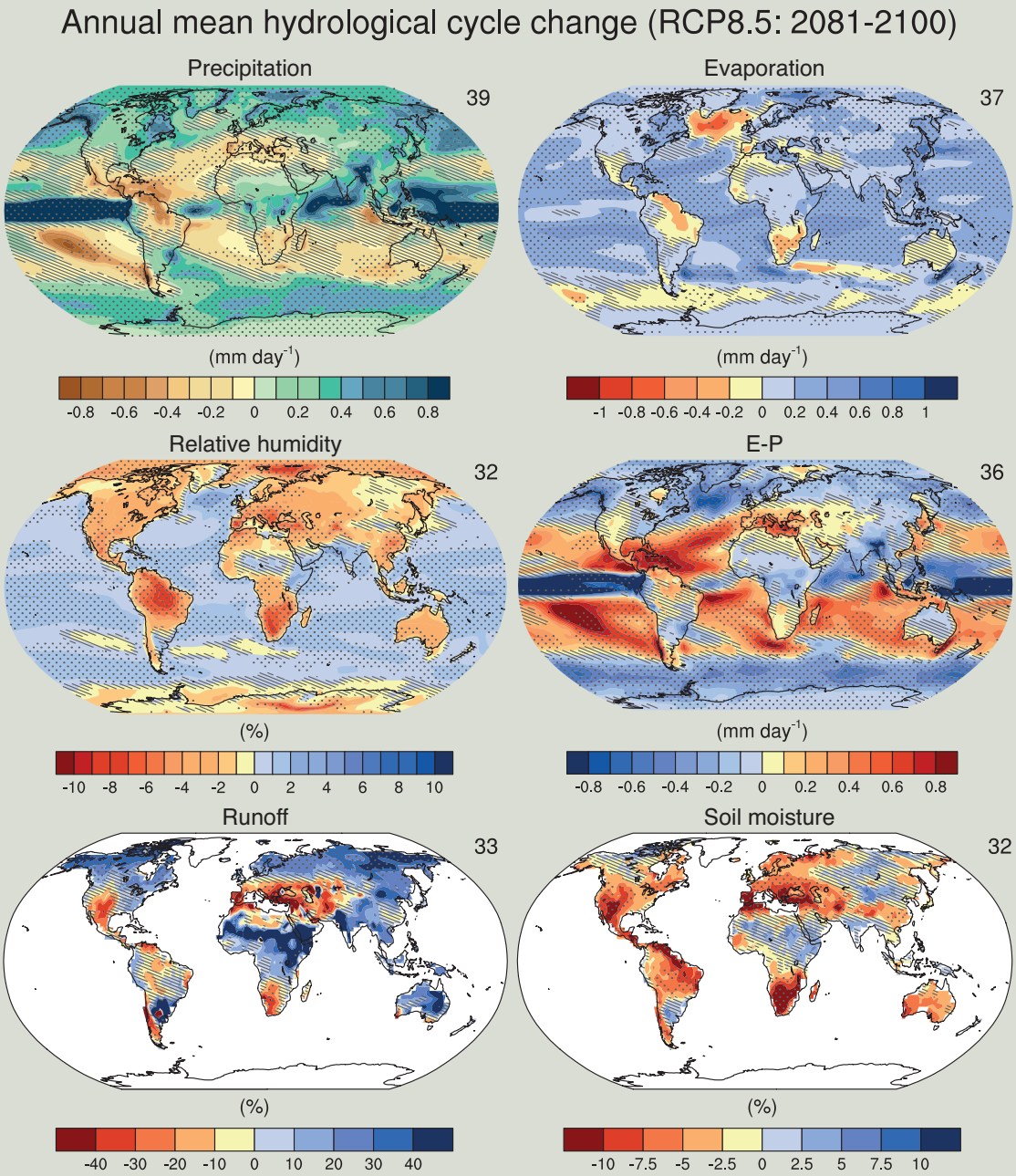

TFE.1, Figure 3 | Annual mean changes in precipitation (*P*), evaporation (*E*), relative humidity, *E* – *P*, runoff and soil moisture for 2081–2100 relative to 1986–2005 under the Representative Concentration Pathway RCP8.5 (see Box TS.6). The number of Coupled Model Intercomparison Project Phase 5 (CMIP5) models to calculate the multi-model mean is indicated in the upper right corner of each panel. Hatching indicates regions where the multi-model mean change is less than one standard deviation of internal variability. Stippling indicates regions where the multi-model mean change is greater than two standard deviations of internal variability and where 90% of models agree on the sign of change (see Box 12.1). {Figures 12.25–12.27}

There is *high confidence* that the Antarctic ice sheet has been losing ice during the last two decades (Figure TS.3). There is *very high confidence* that these losses are mainly from the northern Antarctic Peninsula and the Amundsen Sea sector of West Antarctica and *high confidence* that they result from the acceleration of outlet glaciers. The average rate of ice loss from Antarctica *likely* increased from 30 [–37 to 97] Gt yr^{-1} (sea level equivalent, 0.08 [–0.10 to 0.27] mm yr^{-1}) over the period 1992–2001, to 147 [72 to 221] Gt yr^{-1} over the period 2002–2011 (0.40 [0.20 to 0.61] mm yr^{-1}). {4.4.2, 4.4.3}

There is *high confidence* that in parts of Antarctica floating ice shelves are undergoing substantial changes. There is *medium confidence* that ice shelves are thinning in the Amundsen Sea region of West Antarctica, and *low confidence* that this is due to high ocean heat flux. There is *high confidence* that ice shelves around the Antarctic Peninsula continue a long-term trend of retreat and partial collapse that began decades ago. {4.4.2, 4.4.5}

TS.2.5.5 Snow Cover, Freshwater Ice and Frozen Ground

There is *very high confidence* that snow cover extent has decreased in the NH, especially in spring (Figure TS.1). Satellite records indicate that over the period 1967–2012, snow cover extent *very likely* decreased; the largest change, –53% [–40 to –66%], occurred in June. No month had statistically significant increases. Over the longer period, 1922–2012, data are available only for March and April, but these show *very likely* a 7% [4.5 to 9.5%] decline and a negative correlation (–0.76) with March to April 40°N to 60°N land temperature. In the Southern Hemisphere (SH), evidence is too limited to conclude whether changes have occurred. {4.5.2, 4.5.3}

Permafrost temperatures have increased in most regions around the world since the early 1980s (*high confidence*). These increases were in response to increased air temperature and to changes in the timing and thickness of snow cover (*high confidence*). The temperature increase for colder permafrost was generally greater than for warmer permafrost (*high confidence*). {4.7.2; Table 4.8}

TS.2.6 Changes in Sea Level

The primary contributions to changes in the volume of water in the ocean are the expansion of the ocean water as it warms and the transfer to the ocean of water currently stored on land, particularly from glaciers and ice sheets. Water impoundment in reservoirs and ground water depletion (and its subsequent runoff to the ocean) also affect sea level. Change in sea level relative to the land (relative sea level) can be significantly different from the global mean sea level (GMSL) change because of changes in the distribution of water in the ocean, vertical movement of the land and changes in the Earth's gravitational field. For an overview on the scientific understanding and uncertainties associated with recent (and projected) sea level change see TFE.2. {3.7.3, 13.1}

During warm intervals of the mid Pliocene (3.3 to 3.0 Ma), when there is *medium confidence* that GMSTs were 1.9°C to 3.6°C warmer than for pre-industrial climate and carbon dioxide (CO_2) levels were between 350 and 450 ppm, there is *high confidence* that GMSL was above present, implying reduced volume of polar ice sheets. The best estimates from various methods imply with *high confidence* that sea level has not exceeded +20 m during the warmest periods of the Pliocene, due to deglaciation of the Greenland and West Antarctic ice sheets and areas of the East Antarctic ice sheet. {5.6.1, 13.2}

There is *very high confidence* that maximum GMSL during the last interglacial period (129 to 116 ka) was, for several thousand years, at least 5 m higher than present and *high confidence* that it did not exceed 10 m above present, implying substantial contributions from the Greenland and Antarctic ice sheets. This change in sea level occurred in the context of different orbital forcing and with high-latitude surface temperature, averaged over several thousand years, at least 2°C warmer than present (*high confidence*). Based on ice sheet model simulations consistent with elevation changes derived from a new Greenland ice core, the Greenland ice sheet *very likely* contributed between 1.4 m and 4.3 m sea level equivalent, implying with *medium confidence* a contribution from the Antarctic ice sheet to the GMSL during the Last Interglacial Period. {5.3.4, 5.6.2, 13.2.1}

Proxy and instrumental sea level data indicate a transition in the late 19th to the early 20th century from relatively low mean rates of rise over the previous two millennia to higher rates of rise (*high confidence*) {3.7, 3.7.4, 5.6.3, 13.2}

GMSL has risen by 0.19 [0.17 to 0.21] m, estimated from a linear trend over the period 1901–2010, based on tide gauge records and additionally on satellite data since 1993. It is *very likely* that the mean rate of sea level rise was 1.7 [1.5 to 1.9] mm yr^{-1} between 1901 and 2010. Between 1993 and 2010, the rate was *very likely* higher at 3.2 [2.8 to 3.6] mm yr^{-1}; similarly high rates *likely* occurred between 1920 and 1950. The rate of GMSL rise has *likely* increased since the early 1900s, with estimates ranging from 0.000 [–0.002 to 0.002] to 0.013 [–0.007 to 0.019] mm yr^{-2}. {3.7, 5.6.3, 13.2}

TS.2.7 Changes in Extremes

TS.2.7.1 Atmosphere

Recent analyses of extreme events generally support the AR4 and SREX conclusions (see TFE.9 and in particular TFE.9, Table 1, for a synthesis). It is *very likely* that the number of cold days and nights has decreased and the number of warm days and nights has increased on the global scale between 1951 and 2010. Globally, there is *medium confidence* that the length and frequency of warm spells, including heat waves, has increased since the middle of the 20th century, mostly owing to lack of data or studies in Africa and South America. However, it is *likely* that heat wave frequency has increased over this period in large parts of Europe, Asia and Australia. {2.6.1; Tables 2.12, 2.13}

It is *likely* that since about 1950 the number of heavy precipitation events over land has increased in more regions than it has decreased. Confidence is highest for North America and Europe where there have been *likely* increases in either the frequency or intensity of heavy precipitation with some seasonal and regional variations. It is *very likely* that there have been trends towards heavier precipitation events in central North America. {2.6.2; Table 2.13}

Thematic Focus Elements

TFE.2 | Sea Level Change: Scientific Understanding and Uncertainties

After the Last Glacial Maximum, global mean sea levels (GMSLs) reached close to present-day values several thousand years ago. Since then, it is *virtually certain* that the rate of sea level rise has increased from low rates of sea level change during the late Holocene (order tenths of mm yr^{-1}) to 20th century rates (order mm yr^{-1}, Figure TS1). {3.7, 5.6, 13.2}

Ocean thermal expansion and glacier mass loss are the dominant contributors to GMSL rise during the 20th century (*high confidence*). It is *very likely* that warming of the ocean has contributed 0.8 [0.5 to 1.1] mm yr^{-1} of sea level change during 1971–2010, with the majority of the contribution coming from the upper 700 m. The model mean rate of ocean thermal expansion for 1971–2010 is close to observations. {3.7, 13.3}

Observations, combined with improved methods of analysis, indicate that the global glacier contribution (excluding the peripheral glaciers around Greenland and Antarctica) to sea level was 0.25 to 0.99 mm yr^{-1} sea level equivalent during 1971–2010. *Medium confidence* in global glacier mass balance models used for projections of glacier changes arises from the process-based understanding of glacier surface mass balance, the consistency of observations and models of glacier changes, and the evidence that Atmosphere–Ocean General Circulation Model (AOGCM) climate simulations can provide realitistic climate input. A simulation using observed climate data shows a larger rate of glacier mass loss during the 1930s than the simulations using AOGCM input, possibly a result of an episode of warming in Greenland associated with unforced regional climate variability. {4.3, 13.3}

Observations indicate that the Greenland ice sheet has *very likely* experienced a net loss of mass due to both increased surface melting and runoff, and increased ice discharge over the last two decades (Figure TS.3). Regional climate models indicate that Greenland ice sheet surface mass balance showed no significant trend from the 1960s to the 1980s, but melting and consequent runoff has increased since the early 1990s. This tendency is related to pronounced regional warming, which may be attributed to a combination of anomalous regional variability in recent years and anthropogenic climate change. *High confidence* in projections of future warming in Greenland and increased surface melting is based on the qualitative agreements of models in projecting amplified warming at high northern latitudes for well-understood physical reasons. {4.4, 13.3}

There is *high confidence* that the Antarctic ice sheet is in a state of net mass loss and its contribution to sea level is also *likely* to have increased over the last two decades. Acceleration in ice outflow has been observed since the 1990s, especially in the Amundsen Sea sector of West Antarctica. Interannual variability in accumulation is large and as a result no significant trend is present in accumulation since 1979 in either models or observations. Surface melting is currently negligible in Antarctica. {4.4, 13.3}

Model-based estimates of climate-related changes in water storage on land (as snow cover, surface water, soil moisture and ground water) do not show significant long-term contributions to sea level change for recent decades. However, human-induced changes (reservoir impoundment and groundwater depletion) have each contributed at least several tenths of mm yr^{-1} to sea level change. Reservoir impoundment exceeded groundwater depletion for the majority of the 20th century but the rate of groundwater depletion has increased and now exceeds the rate of impoundment. Their combined net contribution for the 20th century is estimated to be small. {13.3}

The observed GMSL rise for 1993–2010 is consistent with the sum of the observationally estimated contributions (TFE.2, Figure 1e). The closure of the observational budget for recent periods within uncertainties represents a significant advance since the IPCC Fourth Assessment Report in physical understanding of the causes of past GMSL change, and provides an improved basis for critical evaluation of models of these contributions in order to assess their reliability for making projections. {13.3}

The sum of modelled ocean thermal expansion and glacier contributions and the estimated change in land water storage (which is relatively small) accounts for about 65% of the observed GMSL rise for 1901–1990, and 90% for 1971–2010 and 1993–2010 (TFE.2, Figure 1). After inclusion of small long-term contributions from ice sheets and the possible greater mass loss from glaciers during the 1930s due to unforced climate variability, the sum of the modelled contribution is close to the observed rise. The addition of the observed ice sheet contribution since 1993 improves the agreement further between the observed and modelled sea level rise (TFE.2, Figure 1). The evidence now available gives a clearer account than in previous IPCC assessments of 20th century sea level change. {13.3}

(continued on next page)

TFE.2 (continued)

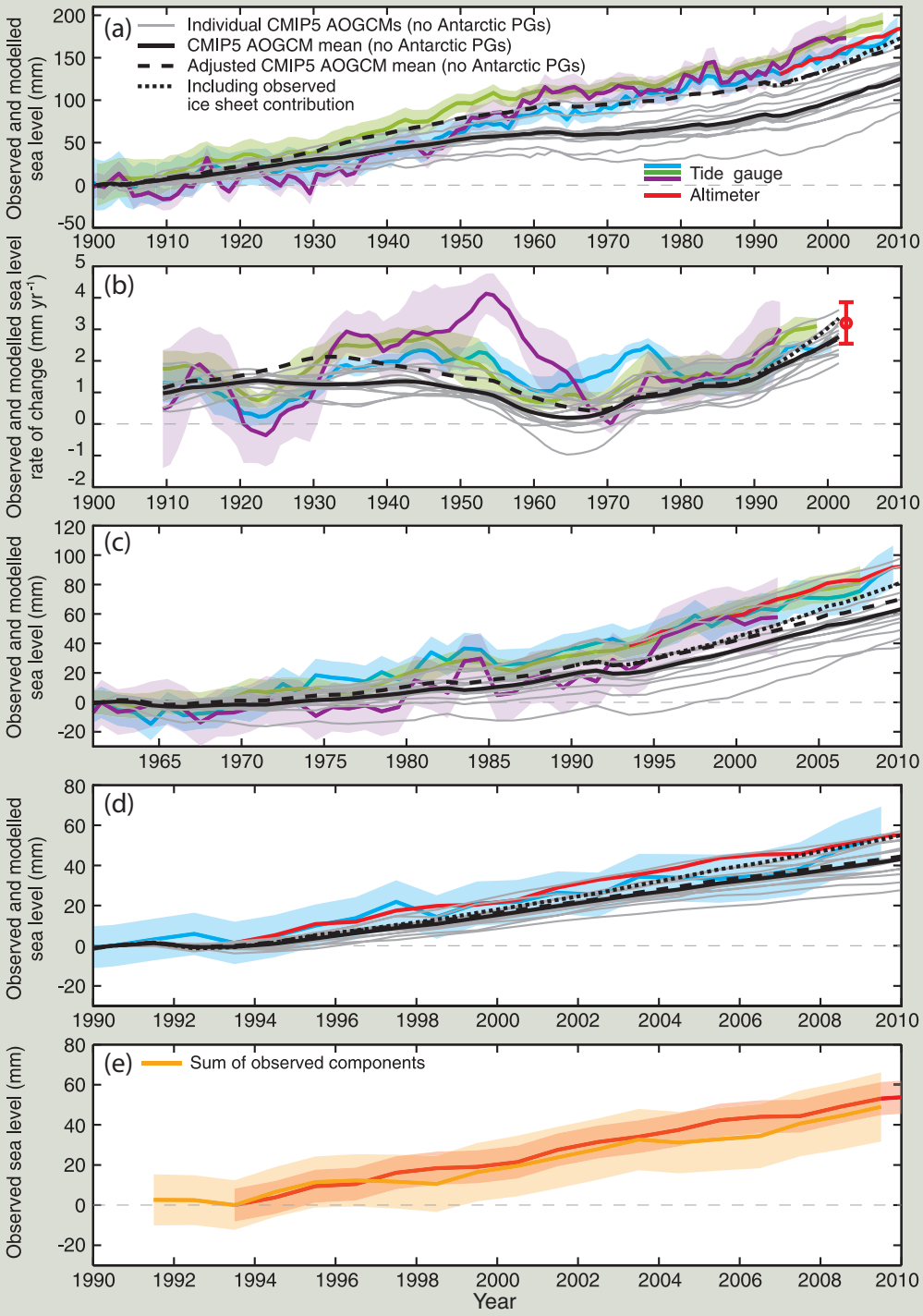

TFE.2, Figure 1 | (a) The observed and modelled sea level for 1900 to 2010. (b) The rates of sea level change for the same period, with the satellite altimeter data shown as a red dot for the rate. (c) The observed and modelled sea level for 1961 to 2010. (d) The observed and modelled sea level for 1990 to 2010. Panel (e) compares the sum of the observed contributions (orange) and the observed sea level from the satellite altimeter data (red). Estimates of GMSL from different sources are given, with the shading indicating the uncertainty estimates (two standard deviations). The satellite altimeter data since 1993 are shown in red. The grey lines in panels (a)-(d) are the sums of the contributions from modelled ocean thermal expansion and glaciers (excluding glaciers peripheral to the Antarctic ice sheet), plus changes in land-water storage (see Figure 13.4). The black line is the mean of the grey lines plus a correction of thermal expansion for the omission of volcanic forcing in the Atmosphere–Ocean General Circulation Model (AOGCM) control experiments (see Section 13.3.1). The dashed black line (adjusted model mean) is the sum of the corrected model mean thermal expansion, the change in land water storage, the glacier estimate using observed (rather than modelled) climate (see Figure 13.4), and an illustrative long-term ice-sheet contribution (of 0.1 mm yr^{-1}). The dotted black line is the adjusted model mean but now including the observed ice-sheet contributions, which begin in 1993. Because the observational ice-sheet estimates include the glaciers peripheral to the Greenland and Antarctic ice sheets (from Section 4.4), the contribution from glaciers to the adjusted model mean excludes the peripheral glaciers (PGs) to avoid double counting. {13.3; Figure 13.7}

TFE.2 (continued)

When calibrated appropriately, recently improved dynamical ice sheet models can reproduce the observed rapid changes in ice sheet outflow for individual glacier systems (e.g., Pine Island Glacier in Antarctica; *medium confidence*). However, models of ice sheet response to global warming and particularly ice sheet–ocean interactions are incomplete and the omission of ice sheet models, especially of dynamics, from the model budget of the past means that they have not been as critically evaluated as other contributions. {13.3, 13.4}

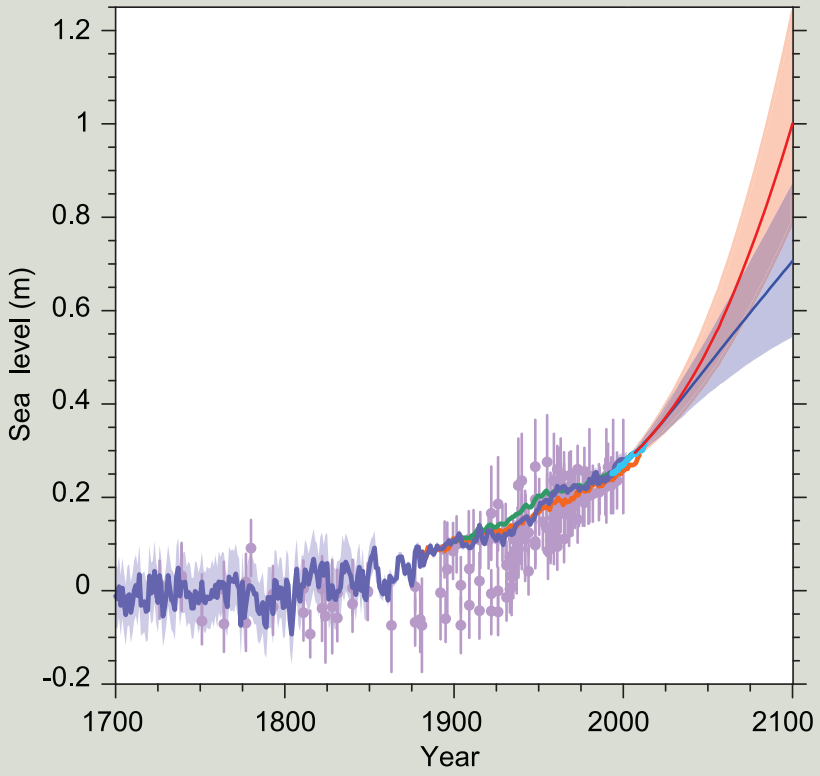

TFE.2, Figure 2 | Compilation of paleo sealevel data (purple), tide gauge data (blue, red and green), altimeter data (light blue) and central estimates and *likely* ranges for projections of global mean sea level rise from the combination of CMIP5 and process-based models for RCP2.6 (blue) and RCP8.5 (red) scenarios, all relative to pre-industrial values. {Figures 13.3, 13.11, 13.27}

GMSL rise for 2081–2100 (relative to 1986–2005) for the Representative Concentration Pathways (RCPs) will *likely* be in the 5 to 95% ranges derived from Coupled Model Intercomparison Project Phase 5 (CMIP5) climate projections in combination with process-based models of other contributions (*medium confidence*), that is, 0.26 to 0.55 m (RCP2.6), 0.32 to 0.63 m (RCP4.5), 0.33 to 0.63 m (RCP6.0), 0.45 to 0.82 (RCP8.5) m (see Table TS.1 and Figure TS.15 for RCP forcing). For RCP8.5 the range at 2100 is 0.52 to 0.98 m. Confidence in the projected *likely* ranges comes from the consistency of process-based models with observations and physical understanding. It is assessed that there is currently insufficient evidence to evaluate the probability of specific levels above the *likely* range. Based on current understanding, only the collapse of marine-based sectors of the Antarctic ice sheet, if initiated, could cause GMSL to rise substantially above the *likely* range during the 21st century. There is a lack of consensus on the probability for such a collapse, and the potential additional contribution to GMSL rise cannot be precisely quantified, but there is *medium confidence* that it would not exceed several tenths of a metre of sea level rise during the 21st century. It is *virtually certain* that GMSL rise will continue beyond 2100. {13.5.1, 13.5.3}

Many semi-empirical models projections of GMSL rise are higher than process-based model projections, but there is no consensus in the scientific community about their reliability and there is thus *low confidence* in their projections. {13.5.2, 13.5.3}

TFE.2, Figure 2 combines the paleo, tide gauge and altimeter observations of sea level rise from 1700 with the projected GMSL change to 2100. {13.5, 13.7, 13.8}

There is *low confidence* in a global-scale observed trend in drought or dryness (lack of rainfall), owing to lack of direct observations, dependencies of inferred trends on the index choice and geographical inconsistencies in the trends. However, this masks important regional changes and, for example, the frequency and intensity of drought have *likely* increased in the Mediterranean and West Africa and *likely* decreased in central North America and northwest Australia since 1950. {2.6.2; Table 2.13}

There is *high confidence* for droughts during the last millennium of greater magnitude and longer duration than those observed since the beginning of the 20th century in many regions. There is *medium confidence* that more megadroughts occurred in monsoon Asia and wetter conditions prevailed in arid Central Asia and the South American monsoon region during the Little Ice Age (1450–1850) compared to the Medieval Climate Anomaly (950–1250). {5.5.4, 5.5.5}

Confidence remains *low* for long-term (centennial) changes in tropical cyclone activity, after accounting for past changes in observing capabilities. However, for the years since the 1970s, it is *virtually certain* that the frequency and intensity of storms in the North Atlantic have increased although the reasons for this increase are debated (see TFE.9). There is *low confidence* of large-scale trends in storminess over the last century and there is still insufficient evidence to determine whether robust trends exist in small-scale severe weather events such as hail or thunderstorms. {2.6.2–2.6.4}

With *high confidence*, floods larger than recorded since the 20th century occurred during the past five centuries in northern and central Europe, the western Mediterranean region and eastern Asia. There is *medium confidence* that in the Near East, India and central North America, modern large floods are comparable or surpass historical floods in magnitude and/or frequency. {5.5.5}

TS.2.7.2 Oceans

It is *likely* that the magnitude of extreme high sea level events has increased since 1970 (see TFE.9, Table 1). Most of the increase in extreme sea level can be explained by the mean sea level rise: changes in extreme high sea levels are reduced to less than 5 mm yr^{-1} at 94% of tide gauges once the rise in mean sea level is accounted for. There is *medium confidence* based on reanalysis forced model hindcasts and ship observations that mean significant wave height has increased since the 1950s over much of the North Atlantic north of 45°N, with typical winter season trends of up to 20 cm per decade. {3.4.5, 3.7.5}

TS.2.8 Changes in Carbon and Other Biogeochemical Cycles

Concentrations of the atmospheric greenhouse gases (GHGs) carbon dioxide (CO_2), methane (CH_4) and nitrous oxide (N_2O) in 2011 exceed the range of concentrations recorded in ice cores during the past 800 kyr. Past changes in atmospheric GHG concentrations are determined with *very high confidence* from polar ice cores. Since AR4 these records have been extended from 650 ka to 800 ka. {5.2.2}

With *very high confidence*, the current rates of CO_2, CH_4 and N_2O rise in atmospheric concentrations and the associated increases in RF are unprecedented with respect to the 'highest resolution' ice core records of the last 22 kyr. There is *medium confidence* that the rate of change of the observed GHG rise is also unprecedented compared with the lower resolution records of the past 800 kyr. {2.2.1, 5.2.2}

In several periods characterized by high atmospheric CO_2 concentrations, there is *medium confidence* that global mean temperature was significantly above pre-industrial level. During the mid-Pliocene (3.3 to 3.0 Ma), atmospheric CO_2 concentration between 350 ppm and 450 ppm (*medium confidence*) occurred when GMST was 1.9°C to 3.6°C warmer (*medium confidence*) than for pre-industrial climate. During the Early Eocene (52 to 48 Ma), atmospheric CO_2 concentration exceeded about 1000 ppm when GMST was 9°C to 14°C higher (*medium confidence*) than for pre-industrial conditions. {5.3.1}

TS.2.8.1 Carbon Dioxide

Between 1750 and 2011, CO_2 emissions from fossil fuel combustion and cement production are estimated from energy and fuel use statistics to have released 375 [345 to 405] PgC[9]. In 2002–2011, average fossil fuel and cement manufacturing emissions were 8.3 [7.6 to 9.0] PgC yr^{-1} (*high confidence*), with an average growth rate of 3.2% yr^{-1} (Figure TS.4). This rate of increase of fossil fuel emissions is higher than during the 1990s (1.0% yr^{-1}). In 2011, fossil fuel emissions were 9.5 [8.7 to 10.3] PgC. {2.2.1, 6.3.1; Table 6.1}

Between 1750 and 2011, land use change (mainly deforestation), derived from land cover data and modelling, is estimated to have released 180 [100 to 260] PgC. Land use change emissions between 2002 and 2011 are dominated by tropical deforestation, and are estimated at 0.9 [0.1 to 1.7] PgC yr^{-1} (*medium confidence*), with possibly a small decrease from the 1990s due to lower reported forest loss during this decade. This estimate includes gross deforestation emissions of around 3 PgC yr^{-1} compensated by around 2 PgC yr^{-1} of forest regrowth in some regions, mainly abandoned agricultural land. {6.3.2; Table 6.2}

Of the 555 [470 to 640] PgC released to the atmosphere from fossil fuel and land use emissions from 1750 to 2011, 240 [230 to 250] PgC accumulated in the atmosphere, as estimated with very high accuracy from the observed increase of atmospheric CO_2 concentration from 278 [273 to 283] ppm[10] in 1750 to 390.5 [390.4 to 390.6] ppm in 2011. The amount of CO_2 in the atmosphere grew by 4.0 [3.8 to 4.2] PgC yr^{-1} in the first decade of the 21st century. The distribution of observed atmospheric CO_2 increases with latitude clearly shows that the increases are driven by anthropogenic emissions that occur primarily in the industrialized countries north of the equator. Based on annual average concentrations, stations in the NH show slightly higher concentrations than stations in the SH. An independent line of evidence

[9] 1 Petagram of carbon = 1 PgC = 10^{15} grams of carbon = 1 Gigatonne of carbon = 1 GtC. This corresponds to 3.667 $GtCO_2$.

[10] ppm (parts per million) or ppb (parts per billion, 1 billion = 1000 million) is the ratio of the number of greenhouse gas molecules to the total number of molecules of dry air. For example, 300 ppm means 300 molecules of a greenhouse gas per million molecules of dry air.

for the anthropogenic origin of the observed atmospheric CO_2 increase comes from the observed consistent decrease in atmospheric oxygen (O_2) content and a decrease in the stable isotopic ratio of CO_2 ($^{13}C/^{12}C$) in the atmosphere (Figure TS.5). {2.2.1, 6.1.3}

The remaining amount of carbon released by fossil fuel and land use emissions has been re-absorbed by the ocean and terrestrial ecosystems. Based on high agreement between independent estimates using different methods and data sets (e.g., oceanic carbon, oxygen and transient tracer data), it is *very likely* that the global ocean inventory of anthropogenic carbon increased from 1994 to 2010. In 2011, it is estimated to be 155 [125 to 185] PgC. The annual global oceanic uptake rates calculated from independent data sets (from changes in the oceanic inventory of anthropogenic carbon, from measurements of the atmospheric oxygen to nitrogen ratio (O_2/N_2) or from CO_2 partial pressure (pCO_2) data) and for different time periods agree with each other within their uncertainties, and *very likely* are in the range of 1.0 to 3.2 PgC yr^{-1}. Regional observations of the storage rate of anthropogenic carbon in the ocean are in broad agreement with the expected rate resulting from the increase in atmospheric CO_2

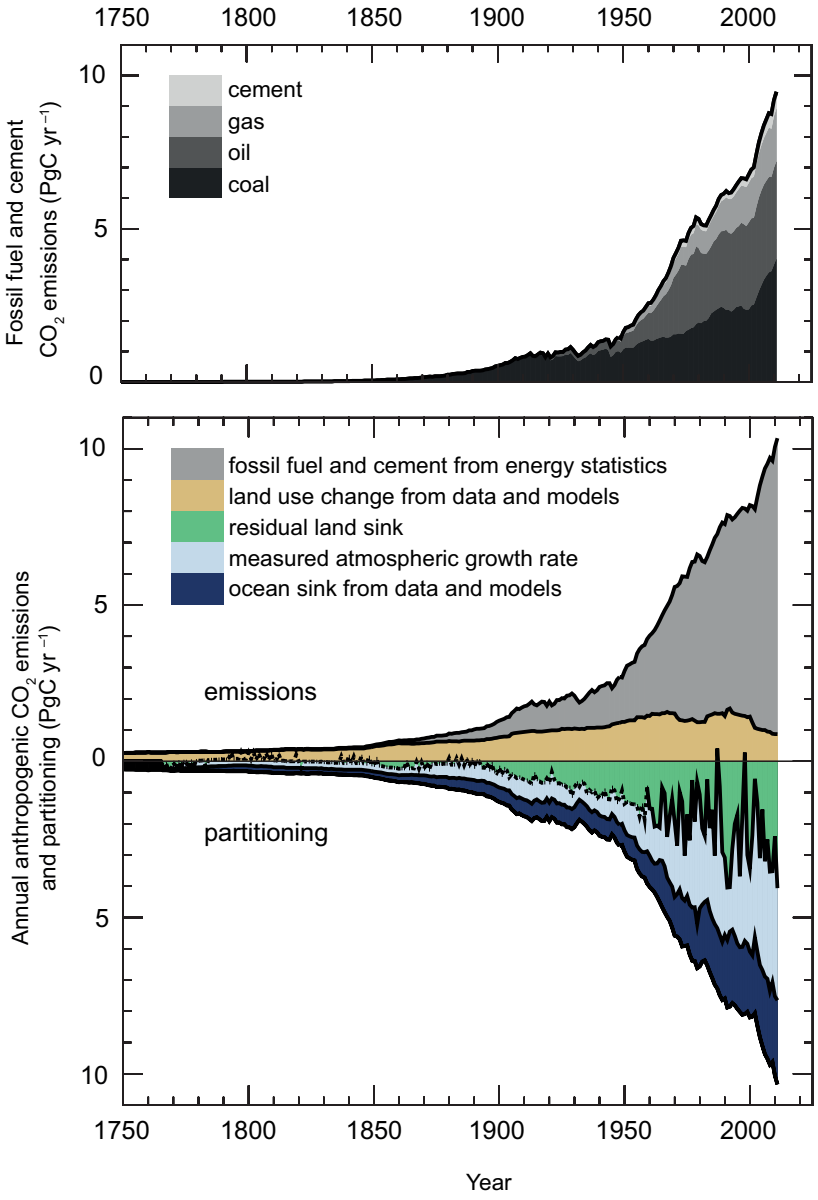

Figure TS.4 | Annual anthropogenic CO_2 emissions and their partitioning among the atmosphere, land and ocean (PgC yr^{-1}) from 1750 to 2011. (Top) Fossil fuel and cement CO_2 emissions by category, estimated by the Carbon Dioxide Information Analysis Center (CDIAC). (Bottom) Fossil fuel and cement CO_2 emissions as above. CO_2 emissions from net land use change, mainly deforestation, are based on land cover change data (see Table 6.2). The atmospheric CO_2 growth rate prior to 1959 is based on a spline fit to ice core observations and a synthesis of atmospheric measurements from 1959. The fit to ice core observations does not capture the large interannual variability in atmospheric CO_2 and is represented with a dashed line. The ocean CO_2 sink is from a combination of models and observations. The residual land sink (term in green in the figure) is computed from the residual of the other terms. The emissions and their partitioning include only the fluxes that have changed since 1750, and not the natural CO_2 fluxes (e.g., atmospheric CO_2 uptake from weathering, outgassing of CO_2 from lakes and rivers and outgassing of CO_2 by the ocean from carbon delivered by rivers; see Figure 6.1) between the atmosphere, land and ocean reservoirs that existed before that time and still exist today. The uncertainties in the various terms are discussed in Chapter 6 and reported in Table 6.1 for decadal mean values. {Figure 6.8}

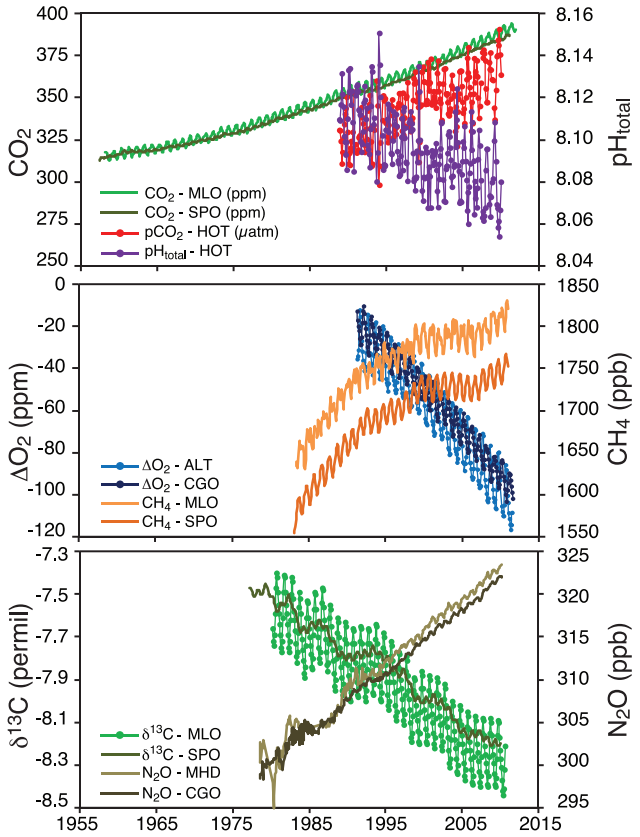

Figure TS.5 | Atmospheric concentration of CO_2, oxygen, $^{13}C/^{12}C$ stable isotope ratio in CO_2, as well as CH_4 and N_2O atmospheric concentrations and oceanic surface observations of CO_2 partial pressure (pCO_2) and pH, recorded at representative time series stations in the Northern and the Southern Hemispheres. MLO: Mauna Loa Observatory, Hawaii; SPO: South Pole; HOT: Hawaii Ocean Time-Series station; MHD: Mace Head, Ireland; CGO: Cape Grim, Tasmania; ALT: Alert, Northwest Territories, Canada. Further detail regarding the related Figure SPM.4 is given in the TS Supplementary Material. {Figures 3.18, 6.3; FAQ 3.3, Figure 1}

concentrations, but with significant spatial and temporal variations. {3.8.1, 6.3}

Natural terrestrial ecosystems (those not affected by land use change) are estimated by difference from changes in other reservoirs to have accumulated 160 [70 to 250] PgC between 1750 and 2011. The gain of carbon by natural terrestrial ecosystems is estimated to take place mainly through the uptake of CO_2 by enhanced photosynthesis at higher CO_2 levels and nitrogen deposition and longer growing seasons in mid and high latitudes. Natural carbon sinks vary regionally owing to physical, biological and chemical processes acting on different time scales. An excess of atmospheric CO_2 absorbed by land ecosystems gets stored as organic matter in diverse carbon pools, from short-lived (leaves, fine roots) to long-lived (stems, soil carbon). {6.3; Table 6.1}

TS.2.8.2 Carbon and Ocean Acidification

Oceanic uptake of anthropogenic CO_2 results in gradual acidification of the ocean. The pH[11] of ocean surface water has decreased by 0.1 since the beginning of the industrial era (*high confidence*), corresponding to a 26% increase in hydrogen ion concentration. The observed pH trends range between –0.0014 and –0.0024 per year in surface waters. In the ocean interior, natural physical and biological processes, as well as uptake of anthropogenic CO_2, can cause changes in pH over decadal and longer time scales. {3.8.2; Box 3.2; Table 3.2; FAQ 3.3}

TS.2.8.3 Methane

The concentration of CH_4 has increased by a factor of 2.5 since pre-industrial times, from 722 [697 to 747] ppb in 1750 to 1803 [1799 to 1807] ppb in 2011 (Figure TS.5). There is *very high confidence* that the atmospheric CH_4 increase during the Industrial Era is caused by anthropogenic activities. The massive increase in the number of ruminants, the emissions from fossil fuel extraction and use, the expansion of rice paddy agriculture and the emissions from landfills and waste are the dominant anthropogenic CH_4 sources. Anthropogenic emissions account for 50 to 65% of total emissions. By including natural geological CH_4 emissions that were not accounted for in previous budgets, the fossil component of the total CH_4 emissions (i.e., anthropogenic emissions related to leaks in the fossil fuel industry and natural geological leaks) is now estimated to amount to about 30% of the total CH_4 emissions (*medium confidence*). {2.2.1, 6.1, 6.3.3}

In recent decades, CH_4 growth in the atmosphere has been variable. CH_4 concentrations were relatively stable for about a decade in the 1990s, but then started growing again starting in 2007. The exact drivers of this renewed growth are still debated. Climate-driven fluctuations of CH_4 emissions from natural wetlands (177 to 284 $\times 10^{12}$ g (CH_4) yr^{-1} for 2000–2009 based on bottom-up estimates) are the main drivers of the global interannual variability of CH_4 emissions (*high confidence*), with a smaller contribution from biomass burning emissions during high fire years {2.2.1, 6.3.3; Table 6.8}.

TS.2.8.4 Nitrous Oxide

Since pre-industrial times, the concentration of N_2O in the atmosphere has increased by a factor of 1.2 (Figure TS.5). Changes in the nitrogen cycle, in addition to interactions with CO_2 sources and sinks, affect emissions of N_2O both on land and from the ocean. {2.2.1, 6.4.6}

TS.2.8.5 Oceanic Oxygen

High agreement among analyses provides *medium confidence* that oxygen concentrations have decreased in the open ocean thermocline in many ocean regions since the 1960s. The general decline is consistent with the expectation that warming-induced stratification leads to a decrease in the supply of oxygen to the thermocline from near surface waters, that warmer waters can hold less oxygen and that changes in wind-driven circulation affect oxygen concentrations. It is *likely* that the tropical oxygen minimum zones have expanded in recent decades. {3.8.3}

[11] pH is a measure of acidity: a decrease in pH value means an increase in acidity, that is, acidification.

TS.3 Drivers of Climate Change

TS.3.1 Introduction

Human activities have changed and continue to change the Earth's surface and atmospheric composition. Some of these changes have a direct or indirect impact on the energy balance of the Earth and are thus drivers of climate change. Radiative forcing (RF) is a measure of the net change in the energy balance of the Earth system in response to some external perturbation (see Box TS.2), with positive RF leading to a warming and negative RF to a cooling. The RF concept is valuable for comparing the influence on GMST of most individual agents affecting the Earth's radiation balance. The quantitative values provided in AR5 are consistent with those in previous IPCC reports, though there have been some important revisions (Figure TS.6). Effective radiative forcing (ERF) is now used to quantify the impact of some forcing agents that involve rapid adjustments of components of the atmosphere and surface that are assumed constant in the RF concept (see Box TS.2). RF and ERF are estimated from the change between 1750 and 2011, referred to as 'Industrial Era', if other time periods are not explicitly stated. Uncertainties are given associated with the best estimates of RF and ERF, with values representing the 5 to 95% (90%) confidence range. {8.1, 7.1}

In addition to the global mean RF or ERF, the spatial distribution and temporal evolution of forcing, as well as climate feedbacks, play a role in determining the eventual impact of various drivers on climate. Land surface changes may also impact the local and regional climate through processes that are not radiative in nature. {8.1, 8.3.5, 8.6}

TS.3.2 Radiative Forcing from Greenhouse Gases

Human activity leads to change in the atmospheric composition either directly (via emissions of gases or particles) or indirectly (via atmospheric chemistry). Anthropogenic emissions have driven the changes in well-mixed greenhouse gas (WMGHG) concentrations during the Industrial Era (see Section TS.2.8 and TFE.7). As historical WMGHG concentrations since the pre-industrial are well known based on direct measurements and ice core records, and WMGHG radiative properties are also well known, the computation of RF due to concentration changes provides tightly constrained values (Figure TS.6). There has not been significant change in our understanding of WMGHG radiative impact, so that the changes in RF estimates relative to AR4 are due essentially to concentration increases. The best estimate for WMGHG ERF is the same as RF, but the uncertainty range is twice as large due to the poorly constrained cloud responses. Owing to high-quality observations, it is certain that increasing atmospheric burdens of most WMGHGs, especially CO_2, resulted in a further increase in their RF from 2005 to 2011. Based on concentration changes, the RF of all WMGHGs in 2011 is 2.83 [2.54 to 3.12] W m^{-2} (*very high confidence*). This is an increase since AR4 of 0.20 [0.18 to 0.22] W m^{-2}, with nearly all of the increase due to the increase in the abundance of CO_2 since 2005. The Industrial Era RF for CO_2 alone is 1.82 [1.63 to 2.01] W m^{-2}. Over the last 15 years, CO_2 has been the dominant contributor to the increase in RF from the WMGHGs, with RF of CO_2 having an average growth rate slightly less than 0.3 W m^{-2} per decade. The uncertainty in the WMGHG RF is due in part to its radiative properties but mostly to the full accounting of atmospheric radiative transfer including clouds. {2.2.1, 5.2, 6.3, 8.3, 8.3.2; Table 6.1}

After a decade of near stability, the recent increase of CH_4 concentration led to an enhanced RF compared to AR4 by 2% to 0.48 [0.43 to 0.53] W m^{-2}. It is *very likely* that the RF from CH_4 is now larger than that of all halocarbons combined. {2.2.1, 8.3.2}

Atmospheric N_2O has increased by 6% since AR4, causing an RF of 0.17 [0.14 to 0.20] W m^{-2}. N_2O concentrations continue to rise while those of dichlorodifluoromethane (CF_2Cl_2, CFC-12), the third largest WMGHG contributor to RF for several decades, are decreasing due to phase-out of emissions of this chemical under the Montreal Protocol. Since

Box TS.2 | Radiative Forcing and Effective Radiative Forcing

RF and ERF are used to quantify the change in the Earth's energy balance that occurs as a result of an externally imposed change. They are expressed in watts per square metre (W m^{-2}). RF is defined in AR5, as in previous IPCC assessments, as the change in net downward flux (shortwave + longwave) at the tropopause after allowing for stratospheric temperatures to readjust to radiative equilibrium, while holding other state variables such as tropospheric temperatures, water vapour and cloud cover fixed at the unperturbed values (see Glossary). {8.1.1}

Although the RF concept has proved very valuable, improved understanding has shown that including rapid adjustments of the Earth's surface and troposphere can provide a better metric for quantifying the climate response. These rapid adjustments occur over a variety of time scales, but are relatively distinct from responses to GMST change. Aerosols in particular impact the atmosphere temperature profile and cloud properties on a time scale much shorter than adjustments of the ocean (even the upper layer) to forcings. The ERF concept defined in AR5 allows rapid adjustments to perturbations, for all variables except for GMST or ocean temperature and sea ice cover. The ERF and RF values are significantly different for the anthropogenic aerosols, owing to their influence on clouds and on snow or ice cover. For other components that drive the Earth's energy balance, such as GHGs, ERF and RF are fairly similar, and RF may have comparable utility given that it requires fewer computational resources to calculate and is not affected by meteorological variability and hence can better isolate small forcings. In cases where RF and ERF differ substantially, ERF has been shown to be a better indicator of the GMST response and is therefore emphasized in AR5. {7.1, 8.1; Box 8.1}

AR4, N_2O has overtaken CFC-12 to become the third largest WMGHG contributor to RF. The RF from halocarbons is very similar to the value in AR4, with a reduced RF from CFCs but increases in many of their replacements. Four of the halocarbons (trichlorofluoromethane ($CFCl_3$, CFC-11), CFC-12, trichlorotrifluoroethane ($CF_2ClCFCl_2$, CFC-113) and chlorodifluoromethane (CHF_2Cl, HCFC-22) account for 85% of the total halocarbon RF. The former three compounds have declining RF over the last 5 years but are more than compensated for by the increased RF from HCFC-22. There is *high confidence* that the growth rate in RF from all WMGHG is weaker over the last decade than in the 1970s and 1980s owing to a slower increase in the non-CO_2 RF. {2.2.1, 8.3.2}

The short-lived GHGs ozone (O_3) and stratospheric water vapour also contribute to anthropogenic forcing. Observations indicate that O_3 *likely* increased at many undisturbed (background) locations through the 1990s. These increases have continued mainly over Asia (though

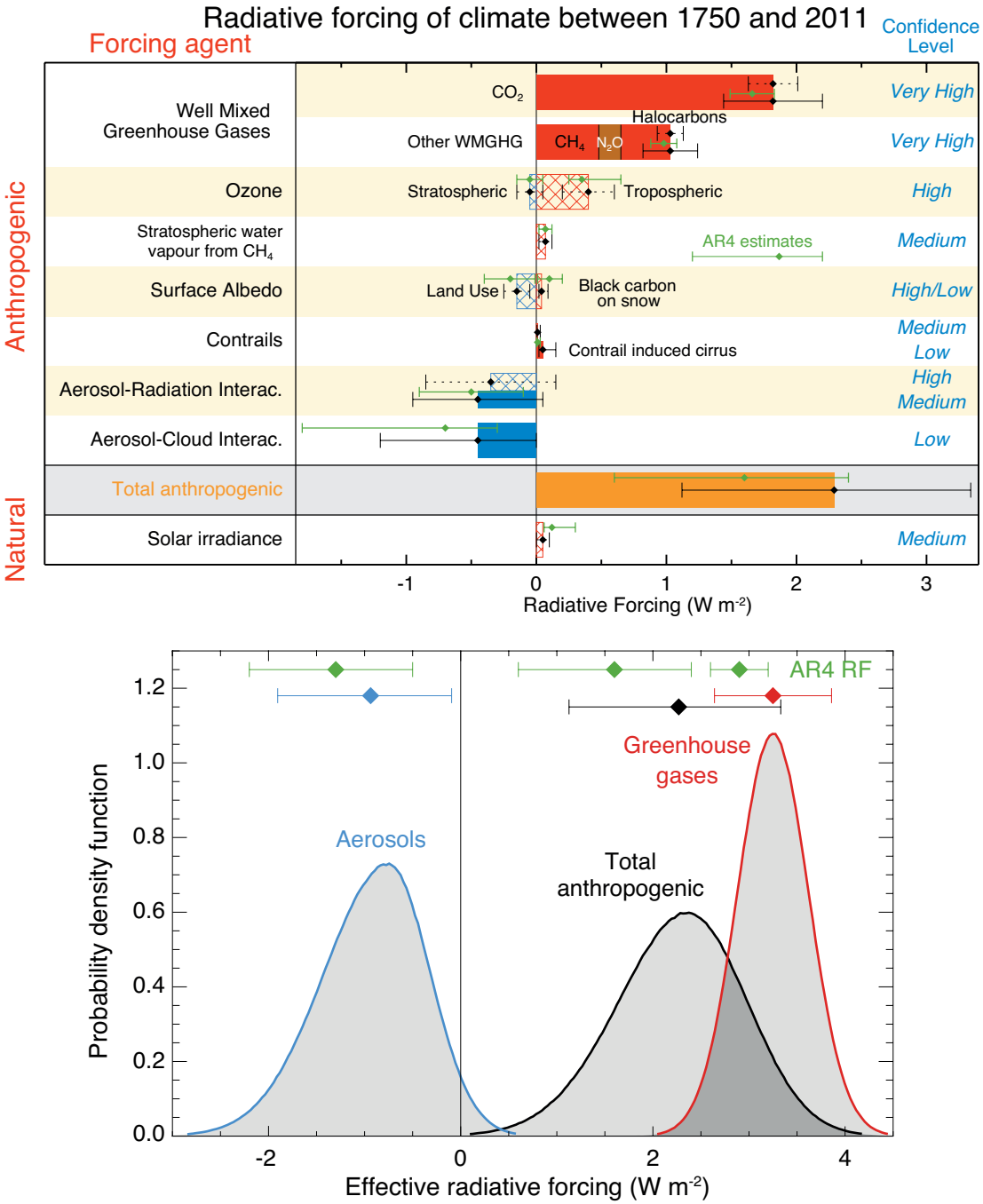

Figure TS.6 | Radiative forcing (RF) and Effective radiative forcing (ERF) of climate change during the Industrial Era. (Top) Forcing by concentration change between 1750 and 2011 with associated uncertainty range (solid bars are ERF, hatched bars are RF, green diamonds and associated uncertainties are for RF assessed in AR4). (Bottom) Probability density functions (PDFs) for the ERF, for the aerosol, greenhouse gas (GHG) and total. The green lines show the AR4 RF 90% confidence intervals and can be compared with the red, blue and black lines which show the AR5 ERF 90% confidence intervals (although RF and ERF differ, especially for aerosols). The ERF from surface albedo changes and combined contrails and contrail-induced cirrus is included in the total anthropogenic forcing, but not shown as a separate PDF. For some forcing mechanisms (ozone, land use, solar) the RF is assumed to be representative of the ERF but an additional uncertainty of 17% is added in quadrature to the RF uncertainty. {Figures 8.15, 8.16}

observations cover a limited area) and flattened over Europe during the last decade. The total RF due to changes in O_3 is 0.35 [0.15 to 0.55] W m^{-2} (*high confidence*), with RF due to tropospheric O_3 of 0.40 [0.20 to 0.60] W m^{-2} (*high confidence*) and due to stratospheric O_3 of –0.05 [–0.15 to +0.05] W m^{-2} (*high confidence*). O_3 is not emitted directly into the atmosphere; instead it is formed by photochemical reactions. In the troposphere these reactions involve precursor compounds that are emitted into the atmosphere from a variety of natural and anthropogenic sources. Tropospheric O_3 RF is largely attributed to increases in emissions of CH_4, carbon monoxide, volatile organics and nitrogen oxides, while stratospheric RF results primarily from O_3 depletion by anthropogenic halocarbons. However, there is now strong evidence for substantial links between the changes in tropospheric and stratospheric O_3 and a total O_3 RF of 0.50 [0.30 to 0.70] W m^{-2} is attributed to tropospheric O_3 precursor emissions and –0.15 [–0.30 to 0.00] W m^{-2} to O_3 depletion by halocarbons. There is strong evidence that tropospheric O_3 also has a detrimental impact on vegetation physiology, and therefore on its CO_2 uptake. This reduced uptake leads to an indirect increase in the atmospheric CO_2 concentration. Thus a fraction of the CO_2 RF should be attributed to ozone or its precursors rather than direct emission of CO_2, but there is a *low confidence* on the quantitative estimates. RF for stratospheric water vapour produced from CH_4 oxidation is 0.07 [0.02 to 0.12] W m^{-2}. Other changes in stratospheric water vapour, and all changes in water vapour in the troposphere, are regarded as a feedback rather than a forcing. {2.2.2, 8.1–8.3; FAQ 8.1}

TS.3.3 Radiative Forcing from Anthropogenic Aerosols

Anthropogenic aerosols are responsible for an RF of climate through multiple processes which can be grouped into two types: aerosol–radiation interactions (ari) and aerosol–cloud interactions (aci). There has been progress since AR4 on observing and modelling climate-relevant aerosol properties (including their size distribution, hygroscopicity, chemical composition, mixing state, optical and cloud nucleation properties) and their atmospheric distribution. Nevertheless, substantial uncertainties remain in assessments of long-term trends of global aerosol optical depth and other global properties of aerosols due to difficulties in measurement and lack of observations of some relevant parameters, high spatial and temporal variability and the relatively short observational records that exist. The anthropogenic RFari is given a best estimate of –0.35 [–0.85 to +0.15] W m^{-2} (*high confidence*) using evidence from aerosol models and some constraints from observations. The RFari is caused by multiple aerosol types (see Section TS3.6). The rapid adjustment to RFari leads to further negative forcing, in particular through cloud adjustments, and is attributable primarily to black carbon. As a consequence, the ERFari is more negative than the RFari (*low confidence*) and given a best estimate of –0.45 [–0.95 to +0.05] W m^{-2}. The assessment for RFari is less negative than reported in AR4 because of a re-evaluation of aerosol absorption. The uncertainty estimate is wider but more robust. {2.2.3, 7.3, 7.5.2}

Improved understanding of aerosol–cloud interactions has led to a reduction in the magnitude of many global aerosol–cloud forcings estimates. The total ERF due to aerosols (ERFari+aci, excluding the effect of absorbing aerosol on snow and ice) is assessed to be –0.9 [–1.9 to –0.1] W m^{-2} (*medium confidence*). This estimate encompasses all rapid adjustments, including changes to the cloud lifetime and aerosol microphysical effects on mixed-phase, ice and convective clouds. This range was obtained by giving equal weight to satellite-based studies and estimates from climate models. It is consistent with multiple lines of evidence suggesting less negative estimates for aerosol–cloud interactions than those discussed in AR4. {7.4, 7.5, 8.5}

The RF from black carbon (BC) on snow and ice is assessed to be 0.04 [0.02 to 0.09] W m^{-2} (*low confidence*). Unlike in the previous IPCC assessment, this estimate includes the effects on sea ice, accounts for more physical processes and incorporates evidence from both models and observations. This RF causes a two to four times larger GMST change per unit forcing than CO_2 primarily because all of the forcing energy is deposited directly into the cryosphere, whose evolution drives a positive albedo feedback on climate. This effect thus can represent a significant forcing mechanism in the Arctic and other snow- or ice-covered regions. {7.3, 7.5.2, 8.3.4, 8.5}

Despite the large uncertainty ranges on aerosol forcing, there is a *high confidence* that aerosols have offset a substantial portion of GHG forcing. Aerosol–cloud interactions can influence the character of individual storms, but evidence for a systematic aerosol effect on storm or precipitation intensity is more limited and ambiguous. {7.4, 7.6, 8.5}

TS.3.4 Radiative Forcing from Land Surface Changes and Contrails

There is robust evidence that anthropogenic land use changes such as deforestation have increased the land surface albedo, which leads to an RF of –0.15 [–0.25 to –0.05] W m^{-2}. There is still a large spread of quantitative estimates owing to different assumptions for the albedo of natural and managed surfaces (e.g., croplands, pastures). In addition, the time evolution of the land use change, and in particular how much was already completed in the reference year 1750, are still debated. Furthermore, land use change causes other modifications that are not radiative but impact the surface temperature, including modifications in the surface roughness, latent heat flux, river runoff and irrigation. These are more uncertain and they are difficult to quantify, but they tend to offset the impact of albedo changes at the global scale. As a consequence, there is low agreement on the sign of the net change in global mean temperature as a result of land use change. Land use change, and in particular deforestation, also has significant impacts on WMGHG concentrations. It contributes to the corresponding RF associated with CO_2 emissions or concentration changes. {8.3.5}

Persistent contrails from aviation contribute a positive RF of 0.01 [0.005 to 0.03] W m^{-2} (*medium confidence*) for year 2011, and the combined contrail and contrail-cirrus ERF from aviation is assessed to be 0.05 [0.02 to 0.15] W m^{-2} (*low confidence*). This forcing can be much larger regionally but there is now *medium confidence* that it does not produce observable regional effects on either the mean or diurnal range of surface temperature. {7.2.7}

TS.3.5 Radiative Forcing from Natural Drivers of Climate Change

Solar and volcanic forcings are the two dominant natural contributors to global climate change during the Industrial Era. Satellite observations

of total solar irradiance (TSI) changes since 1978 show quasi-periodic cyclical variation with a period of roughly 11 years. Longer term forcing is typically estimated by comparison of solar minima (during which variability is least). This gives an RF change of –0.04 [–0.08 to 0.00] W m^{-2} between the most recent (2008) minimum and the 1986 minimum. There is some diversity in the estimated trends of the composites of various satellite data, however. Secular trends of TSI before the start of satellite observations rely on a number of indirect proxies. The best estimate of RF from TSI changes over the industrial era is 0.05 [0.00 to 0.10] W m^{-2} (*medium confidence*), which includes greater RF up to around 1980 and then a small downward trend. This RF estimate is substantially smaller than the AR4 estimate due to the addition of the latest solar cycle and inconsistencies in how solar RF was estimated in earlier IPCC assessments. The recent solar minimum appears to have been unusually low and long-lasting and several projections indicate lower TSI for the forthcoming decades. However, current abilities to project solar irradiance are extremely limited so that there is *very low confidence* concerning future solar forcing. Nonetheless, there is a *high confidence* that 21st century solar forcing will be much smaller than the projected increased forcing due to WMGHGs. {5.2.1, 8.4.1; FAQ 5.1}

Changes in solar activity affect the cosmic ray flux impinging upon the Earth's atmosphere, which has been hypothesized to affect climate through changes in cloudiness. Cosmic rays enhance aerosol nucleation and thus may affect cloud condensation nuclei production in the free troposphere, but the effect is too weak to have any climatic influence during a solar cycle or over the last century (medium evidence, high agreement). No robust association between changes in cosmic rays and cloudiness has been identified. In the event that such an association existed, a mechanism other than cosmic ray–induced nucleation of new aerosol particles would be needed to explain it. {7.3, 7.4.6}

The RF of stratospheric volcanic aerosols is now well understood and there is a large RF for a few years after major volcanic eruptions (Box TS.5, Figure 1). Although volcanic eruptions inject both mineral particles and sulphate aerosol precursors into the atmosphere, it is the latter, because of their small size and long lifetimes, that are responsible for RF important for climate. The emissions of CO_2 from volcanic eruptions are at least 100 times smaller than anthropogenic emissions, and inconsequential for climate on century time scales. Large tropical volcanic eruptions have played an important role in driving annual to decadal scale climate change during the Industrial Era owing to their sometimes very large negative RF. There has not been any major volcanic eruption since Mt Pinatubo in 1991, which caused a 1-year RF of about –3.0 W m^{-2}, but several smaller eruptions have caused an RF averaged over the years 2008–2011 of –0.11 [–0.15 to –0.08] W m^{-2} (*high confidence*), twice as strong in magnitude compared to the 1999–2002 average. The smaller eruptions have led to better understanding of the dependence of RF on the amount of material from high-latitude injections as well as the time of the year when they take place. {5.2.1, 5.3.5, 8.4.2; Annex II}

TS.3.6 Synthesis of Forcings; Spatial and Temporal Evolution

A synthesis of the Industrial Era forcing finds that among the forcing agents, there is a *very high confidence* only for the WMGHG RF. Relative to AR4, the confidence level has been elevated for seven forcing agents owing to improved evidence and understanding. {8.5; Figure 8.14}

The time evolution of the total anthropogenic RF shows a nearly continuous increase from 1750, primarily since about 1860. The total anthropogenic RF increase rate since 1960 has been much greater than during earlier Industrial Era periods, driven primarily by the continuous increase in most WMGHG concentrations. There is still low agreement on the time evolution of the total aerosol ERF, which is the primary factor for the uncertainty in the total anthropogenic forcing. The fractional uncertainty in the total anthropogenic forcing decreases gradually after 1950 owing to the smaller offset of positive WMGHG forcing by negative aerosol forcing. There is robust evidence and high agreement that natural forcing is a small fraction of the WMGHG forcing. Natural forcing changes over the last 15 years have *likely* offset a substantial fraction (at least 30%) of the anthropogenic forcing increase during this period (Box TS.3). Forcing by CO_2 is the largest single contributor to the total forcing during the Industrial Era and from 1980–2011. Compared to the entire Industrial Era, the dominance of CO_2 forcing is larger for the 1980–2011 change with respect to other WMGHGs, and there is *high confidence* that the offset from aerosol forcing to WMGHG forcing during this period was much smaller than over the 1950–1980 period. {8.5.2}

Forcing can also be attributed to emissions rather than to the resulting concentration changes (Figure TS.7). Carbon dioxide is the largest single contributor to historical RF from either the perspective of changes in the atmospheric concentration of CO_2 or the impact of changes in net emissions of CO_2. The relative importance of other forcing agents can vary markedly with the perspective chosen, however. In particular, CH_4 emissions have a much larger forcing (about 1.0 W m^{-2} over the Industrial Era) than CH_4 concentration increases (about 0.5 W m^{-2}) due to several indirect effects through atmospheric chemistry. In addition, carbon monoxide emissions are *virtually certain* to cause a positive forcing, while emissions of reactive nitrogen oxides *likely* cause a net negative forcing but uncertainties are large. Emissions of ozone-depleting halocarbons *very likely* cause a net positive forcing as their direct radiative effect is larger than the impact of the stratospheric ozone depletion that they induce. Emissions of SO_2, organic carbon and ammonia cause a negative forcing, while emissions of black carbon lead to positive forcing via aerosol–radiation interactions. Note that mineral dust forcing may include a natural component or a climate feedback effect. {7.3, 7.5.2, 8.5.1}

Although the WMGHGs show a spatially fairly homogeneous forcing, other agents such as aerosols, ozone and land use changes are highly heterogeneous spatially. RFari showed maximum negative values over eastern North America and Europe during the early 20th century, with large negative values extending to East and Southeast Asia, South America and central Africa by 1980. Since then, however, the magnitude has decreased over eastern North America and Europe due to pollution control, and the peak negative forcing has shifted to South and East Asia primarily as a result of economic growth and the resulting increase in emissions in those areas. Total aerosol ERF shows similar behaviour for locations with maximum negative forcing, but also shows substantial positive forcing over some deserts and the Arctic. In contrast, the global mean whole atmosphere ozone forcing increased throughout

the 20th century, and has peak positive amplitudes around 15°N to 30°N but negative values over Antarctica. Negative land use forcing by albedo changes has been strongest in industrialized and biomass burning regions. The inhomogeneous nature of these forcings can cause them to have a substantially larger influence on the hydrologic cycle than an equivalent global mean homogeneous forcing. {8.3.5, 8.6}

Over the 21st century, anthropogenic RF is projected to increase under the Representative Concentration Pathways (RCPs; see Box TS.6). Simple model estimates of the RF resulting from the RCPs, which include WMGHG emissions spanning a broad range of possible futures, show anthropogenic RF relative to 1750 increasing to 3.0 to 4.8 W m^{-2} in 2050, and 2.7 to 8.4 W m^{-2} at 2100. In the near term, the RCPs are quite similar to one another (and emissions of near-term climate forcers do not span the literature range of possible futures), with RF at 2030 ranging only from 2.9 to 3.3 W m^{-2} (additional 2010 to 2030 RF of 0.7 to 1.1 W m^{-2}), but they show highly diverging values for the second half of the 21st century driven largely by CO_2. Results based on the RCP scenarios suggest only small changes in aerosol ERF between 2000 and 2030, followed by a strong reduction in the aerosols and a substantial weakening of the negative total aerosol ERF. Nitrate aerosols are an exception to this reduction, with a substantially increased negative forcing which is a robust feature among the few available models. The divergence across the RCPs indicates that, although a certain amount of future climate change is already 'in the system' due to the current radiative imbalance caused by historical emissions and the long lifetime of some atmospheric forcing agents, societal choices can still have a very large effect on future RF, and hence on climate change. {8.2, 8.5.3, 12.3; Figures 8.22, 12.4}

TS.3.7 Climate Feedbacks

Feedbacks will also play an important role in determining future climate change. Indeed, climate change may induce modification in the water, carbon and other biogeochemical cycles which may reinforce (positive feedback) or dampen (negative feedback) the expected

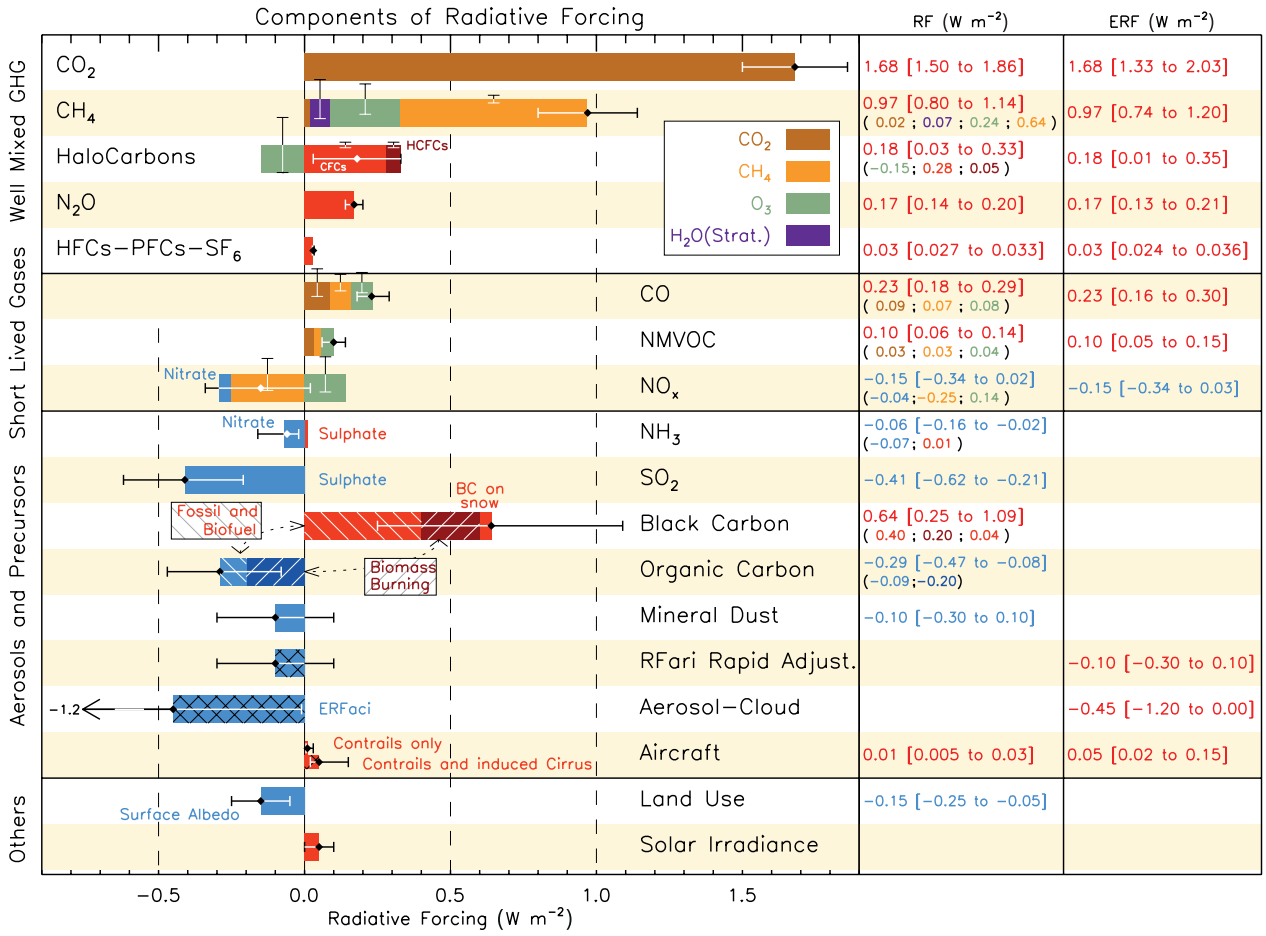

Figure TS.7 | Radiative forcing (RF) of climate change during the Industrial Era shown by emitted components from 1750 to 2011. The horizontal bars indicate the overall uncertainty, while the vertical bars are for the individual components (vertical bar lengths proportional to the relative uncertainty, with a total length equal to the bar width for a ±50% uncertainty). Best estimates for the totals and individual components (from left to right) of the response are given in the right column. Values are RF except for the effective radiative forcing (ERF) due to aerosol–cloud interactions (ERFaci) and rapid adjustment associated with the RF due to aerosol-radiation interaction (RFari Rapid Adjust.). Note that the total RF due to aerosol-radiation interaction (–0.35 Wm^{-2}) is slightly different from the sum of the RF of the individual components (–0.33 Wm^{-2}). The total RF due to aerosol-radiation interaction is the basis for Figure SPM.5. Secondary organic aerosol has not been included since the formation depends on a variety of factors not currently sufficiently quantified. The ERF of contrails includes contrail induced cirrus. Combining ERFaci –0.45 [–1.2 to 0.0] Wm^{-2} and rapid adjustment of ari –0.1 [–0.3 to +0.1] Wm^{-2} results in an integrated component of adjustment due to aerosols of –0.55 [–1.33 to –0.06] Wm^{-2}. CFCs = chlorofluorocarbons, HCFCs = hydrochlorofluorocarbons, HFCs = hydrofluorocarbons, PFCs = perfluorocarbons, NMVOC = Non-Methane Volatile Organic Compounds, BC = black carbon. Further detail regarding the related Figure SPM.5 is given in the TS Supplementary Material. {Figure 8.17}

temperature increase. Snow and ice albedo feedbacks are known to be positive. The combined water vapour and lapse rate feedback is *extremely likely* to be positive and now fairly well quantified, while cloud feedbacks continue to have larger uncertainties (see TFE.6). In addition, the new Coupled Model Intercomparison Project Phase 5 (CMIP5) models consistently estimate a positive carbon-cycle feedback, that is, reduced natural CO_2 sinks in response to future climate change. In particular, carbon-cycle feedbacks in the oceans are positive in the models. Carbon sinks in tropical land ecosystems are less consistent, and may be susceptible to climate change via processes such as drought and fire that are sometimes not yet fully represented. A key update since AR4 is the introduction of nutrient dynamics in some of the CMIP5 land carbon models, in particular the limitations on plant growth imposed by nitrogen availability. The net effect of accounting for the nitrogen cycle is a smaller projected land sink for a given trajectory of anthropogenic CO_2 emissions (see TFE.7). {6.4, Box 6.1, 7.2}

Models and ecosystem warming experiments show high agreement that wetland CH_4 emissions will increase per unit area in a warmer climate, but wetland areal extent may increase or decrease depending on regional changes in temperature and precipitation affecting wetland hydrology, so that there is *low confidence* in quantitative projections of wetland CH_4 emissions. Reservoirs of carbon in hydrates and permafrost are very large, and thus could potentially act as very powerful feedbacks. Although poorly constrained, the 21st century global release of CH_4 from hydrates to the atmosphere is *likely* to be low due to the under-saturated state of the ocean, long ventilation time of the ocean and slow propagation of warming through the seafloor. There is *high confidence* that release of carbon from thawing permafrost provides a positive feedback, but there is *low confidence* in quantitative projections of its strength. {6.4.7}

Aerosol-climate feedbacks occur mainly through changes in the source strength of natural aerosols or changes in the sink efficiency of natural and anthropogenic aerosols; a limited number of modelling studies have assessed the magnitude of this feedback to be small with a *low confidence*. There is *medium confidence* for a weak feedback (of uncertain sign) involving dimethylsulphide, cloud condensation nuclei and cloud albedo due to a weak sensitivity of cloud condensation nuclei population to changes in dimethylsulphide emissions. {7.3.5}

TS.3.8 Emission Metrics

Different metrics can be used to quantify and communicate the relative and absolute contributions to climate change of emissions of different substances, and of emissions from regions/countries or sources/sectors. Up to AR4, the most common metric has been the Global Warming Potential (GWP) that integrates RF out to a particular time horizon. This metric thus accounts for the radiative efficiencies of the various substances, and their lifetimes in the atmosphere, and gives values relative to those for the reference gas CO_2. There is now increasing focus on the Global Temperature change Potential (GTP), which is based on the change in GMST at a chosen point in time, again relative to that caused by the reference gas CO_2, and thus accounts for climate response along with radiative efficiencies and atmospheric lifetimes. Both the GWP and the GTP use a time horizon (Figure TS.8 top), the choice of which is subjective and context dependent. In general, GWPs for near-term climate forcers are higher than GTPs due to the equal time weighting in the integrated forcing used in the GWP. Hence the choice of metric can greatly affect the relative importance of near-term climate forcers and WMGHGs, as can the choice of time horizon. Analysis of the impact of current emissions (1-year pulse of emissions) shows that near-term climate forcers, such as black carbon, sulphur dioxide or CH_4, can have contributions comparable to that of CO_2 for short time horizons (of either the same or opposite sign), but their impacts become progressively less for longer time horizons over which emissions of CO_2 dominate (Figure TS.8 top). {8.7}

A large number of other metrics may be defined down the driver–response–impact chain. No single metric can accurately compare all consequences (i.e., responses in climate parameters over time) of different emissions, and a metric that establishes equivalence with regard to one effect will not give equivalence with regard to other effects. The choice of metric therefore depends strongly on the particular consequence one wants to evaluate. It is important to note that the metrics do not define policies or goals, but facilitate analysis and implementation of multi-component policies to meet particular goals. All choices of metric contain implicit value-related judgements such as type of effect considered and weighting of effects over time. Whereas GWP integrates the effects up to a chosen time horizon (i.e., giving equal weight to all times up to the horizon and zero weight thereafter), the GTP gives the temperature just for one chosen year with no weight on years before or after. {8.7}

The GWP and GTP have limitations and suffer from inconsistencies related to the treatment of indirect effects and feedbacks, for instance, if climate–carbon feedbacks are included for the reference gas CO_2 but not for the non-CO_2 gases. The uncertainty in the GWP increases with time horizon, and for the 100-year GWP of WMGHGs the uncertainty can be as large as ±40%. Several studies also point out that this metric is not well suited for policies with a maximum temperature target. Uncertainties in GTP also increase with time as they arise from the same factors contributing to GWP uncertainties along with additional contributions from it being further down the driver–response–impact chain and including climate response. The GTP metric is better suited to target-based policies, but is again not appropriate for every goal. Updated metric values accounting for changes in knowledge of lifetimes and radiative efficiencies and for climate–carbon feedbacks are now available. {8.7, Table 8.7, Table 8.A.1, Chapter 8 Supplementary Material Table 8.SM.16}

With these emission metrics, the climate impact of past or current emissions attributable to various activities can be assessed. Such activity-based accounting can provide additional policy-relevant information, as these activities are more directly affected by particular societal choices than overall emissions. A single year's worth of emissions (a pulse) is often used to quantify the impact on future climate. From this perspective and with the absolute GTP metric used to illustrate the results, energy and industry have the largest contributions to warming over the next 50 to 100 years (Figure TS.8, bottom). Household fossil and biofuel, biomass burning and on-road transportation are also relatively large contributors to warming over these time scales, while current emissions from sectors that emit large amounts of CH_4 (animal husbandry, waste/landfills and agriculture) are also important over

shorter time horizons (up to about 20 years). Another useful perspective is to examine the effect of sustained current emissions. Because emitted substances are removed according to their residence time, short-lived species remain at nearly constant values while long-lived gases accumulate in this analysis. In both cases, the sectors that have the greatest long-term warming impacts (energy and industry) lead to cooling in the near term (primarily due to SO_2 emissions), and thus emissions from those sectors can lead to opposite global mean temperature responses at short and long time scales. The relative importance of the other sectors depends on the time and perspective chosen. As with RF or ERF, uncertainties in aerosol impacts are large, and in particular attribution of aerosol–cloud interactions to individual components is poorly constrained. {8.7; Chapter 8 Supplementary Material Figures 8.SM.9, 8.SM.10}

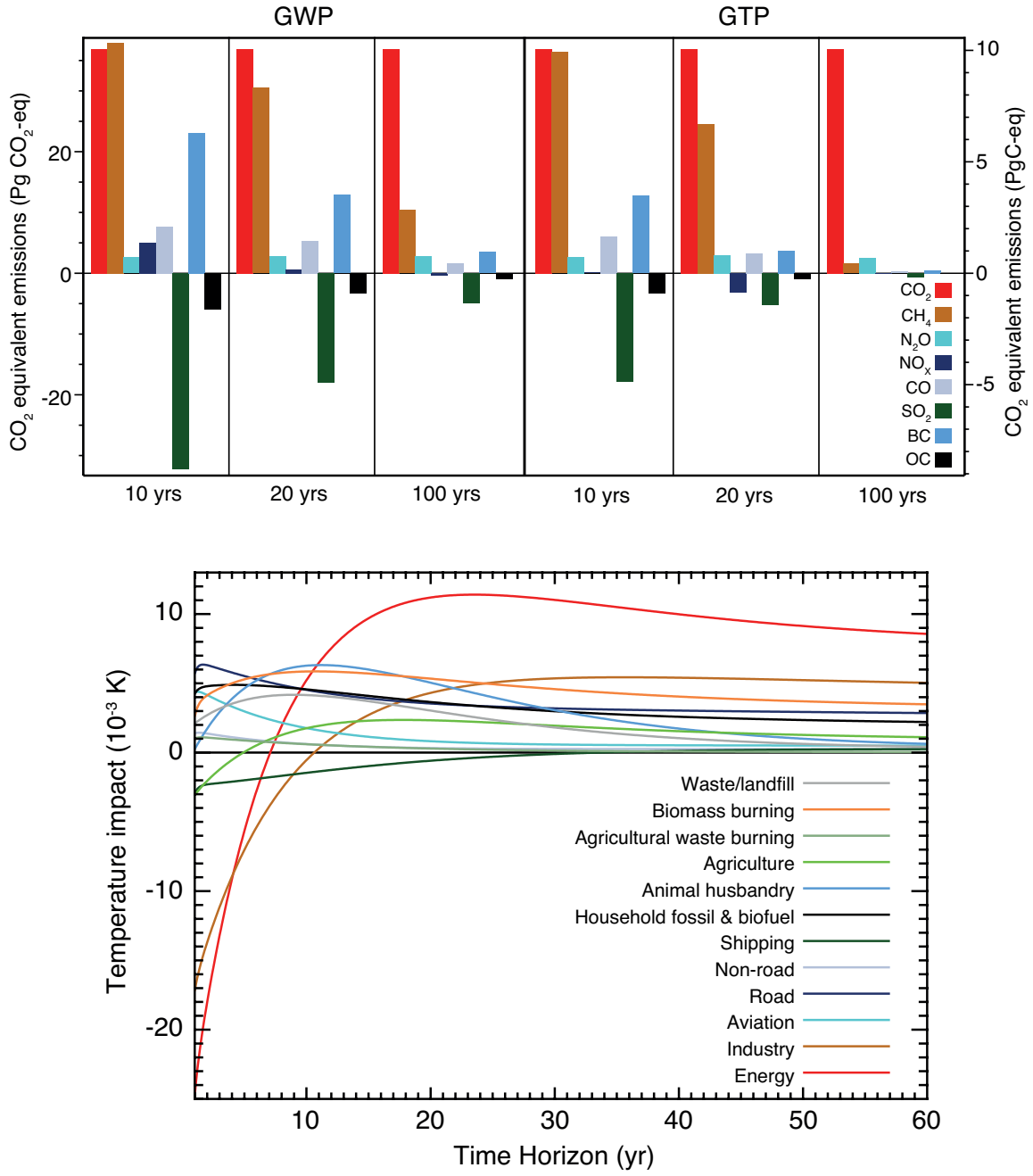

Figure TS.8 | (Upper) Global anthropogenic present-day emissions weighted by the Global Warming Potential (GWP) and the Global Temperature change Potential (GTP) for the chosen time horizons. Year 2008 (single-year pulse) emissions weighted by GWP, which is the global mean radiative forcing (RF) per unit mass emitted integrated over the indicated number of years relative to the forcing from CO_2 emissions, and GTP which estimates the impact on global mean temperature based on the temporal evolution of both RF and climate response per unit mass emitted relative to the impact of CO_2 emissions. The units are 'CO_2 equivalents', which reflects equivalence only in the impact parameter of the chosen metric (integrated RF over the chosen time horizon for GWP; temperature change at the chosen point in time for GTP), given as Pg(CO_2)eq (left axis) and PgCeq (right axis). (Bottom) The Absolute GTP (AGTP) as a function of time multiplied by the present-day emissions of all compounds from the indicated sectors is used to estimate global mean temperature response (AGTP is the same as GTP, except is not normalized by the impact of CO_2 emissions). There is little change in the relative values for the sectors over the 60 to 100-year time horizon. The effects of aerosol–cloud interactions and contrail-induced cirrus are not included in the upper panel. {Figures 8.32, 8.33}

TS.4 Understanding the Climate System and Its Recent Changes

TS.4.1 Introduction

Understanding of the climate system results from combining observations, theoretical studies of feedback processes and model simulations. Compared to AR4, more detailed observations and improved climate models (see Box TS.4) now enable the attribution of detected changes to human influences in more climate system components. The consistency of observed and modelled changes across the climate system, including in regional temperatures, the water cycle, global energy budget, cryosphere and oceans (including ocean acidification), points to global climate change resulting primarily from anthropogenic increases in WMGHG concentrations. {10}

TS.4.2 Surface Temperature

Several advances since the AR4 have allowed a more robust quantification of human influence on surface temperature changes. Observational uncertainty has been explored much more thoroughly than previously and the assessment now considers observations from the first decade of the 21st century and simulations from a new generation of climate models whose ability to simulate historical climate has improved in many respects relative to the previous generation of models considered in AR4. Observed GMST anomalies relative to 1880–1919 in recent years lie well outside the range of GMST anomalies in CMIP5 simulations with natural forcing only, but are consistent with the ensemble of CMIP5 simulations including both anthropogenic and natural forcing (Figure TS.9) even though some individual models overestimate the warming trend, while others underestimate it. Simulations with WMGHG changes only, and no aerosol changes, generally exhibit stronger warming than has been observed (Figure TS.9). Observed temperature trends over the period 1951–2010, which are characterized by warming over most of the globe with the most intense warming over the NH continents, are, at most observed locations, consistent with the temperature trends in CMIP5 simulations including anthropogenic and natural forcings and inconsistent with the temperature trends in CMIP5 simulations including natural forcings only. A number of studies have investigated the effects of the Atlantic Multi-decadal Oscillation (AMO) on GMST. Although some studies find a significant role for the AMO in driving multi-decadal variability in GMST, the AMO exhibited little trend over the period 1951–2010 on which the current assessments are based, and the AMO is assessed with *high confidence* to have made little contribution to the GMST trend between 1951 and 2010 (considerably less than 0.1°C). {2.4, 9.8.1, 10.3; FAQ 9.1}

It is *extremely likely* that human activities caused more than half of the observed increase in global average surface temperature from 1951 to 2010. This assessment is supported by robust evidence from multiple studies using different methods. In particular, the temperature trend attributable to all anthropogenic forcings combined can be more closely constrained in multi-signal detection and attribution analyses. Uncertainties in forcings and in climate models' responses to those forcings, together with difficulty in distinguishing the patterns of temperature response due to WMGHGs and other anthropogenic forcings, prevent as precise a quantification of the temperature changes attributable to

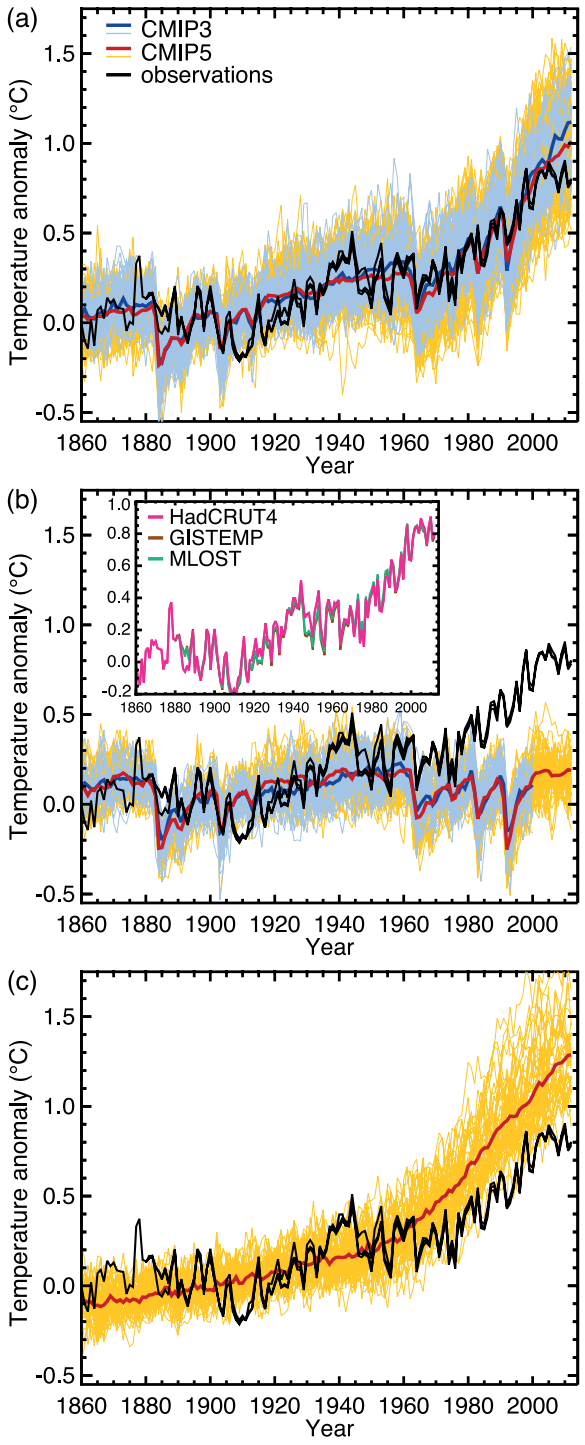

Figure TS.9 | Three observational estimates of global mean surface temperature (black lines) from the Hadley Centre/Climatic Research Unit gridded surface temperature data set 4 (HadCRUT4), Goddard Institute for Space Studies Surface Temperature Analysis (GISTEMP), and Merged Land–Ocean Surface Temperature Analysis (MLOST), compared to model simulations (CMIP3 models— thin blue lines and CMIP5 models—thin yellow lines) with anthropogenic and natural forcings (a), natural forcings only (b) and greenhouse gas forcing only (c). Thick red and blue lines are averages across all available CMIP5 and CMIP3 simulations respectively. All simulated and observed data were masked using the HadCRUT4 coverage (as this data set has the most restricted spatial coverage), and global average anomalies are shown with respect to 1880–1919, where all data are first calculated as anomalies relative to 1961–1990 in each grid box. Inset to (b) shows the three observational data sets distinguished by different colours. {Figure 10.1}

Box TS.3 | Climate Models and the Hiatus in Global Mean Surface Warming of the Past 15 Years

The observed GMST has shown a much smaller increasing linear trend over the past 15 years than over the past 30 to 60 years (Box TS.3, Figure 1a, c). Depending on the observational data set, the GMST trend over 1998–2012 is estimated to be around one third to one half of the trend over 1951–2012. For example, in HadCRUT4 the trend is 0.04°C per decade over 1998–2012, compared to 0.11°C per decade over 1951–2012. The reduction in observed GMST trend is most marked in NH winter. Even with this 'hiatus' in GMST trend, the decade of the 2000s has been the warmest in the instrumental record of GMST. Nevertheless, the occurrence of the hiatus in GMST trend during the past 15 years raises the two related questions of what has caused it and whether climate models are able to reproduce it. {2.4.3, 9.4.1; Box 9.2; Table 2.7}

Fifteen-year-long hiatus periods are common in both the observed and CMIP5 historical GMST time series. However, an analysis of the full suite of CMIP5 historical simulations (augmented for the period 2006–2012 by RCP4.5 simulations) reveals that 111 out of 114 realizations show a GMST trend over 1998–2012 that is higher than the entire HadCRUT4 trend ensemble (Box TS.3, Figure 1a; CMIP5 ensemble mean trend is 0.21°C per decade). This difference between simulated and observed trends could be caused by some combination of (a) internal climate variability, (b) missing or incorrect RF, and (c) model response error. These potential sources of the difference, which are not mutually exclusive, are assessed below, as is the cause of the observed GMST trend hiatus. {2.4.3, 9.3.2, 9.4.1; Box 9.2}

Internal Climate Variability

Hiatus periods of 10 to 15 years can arise as a manifestation of internal decadal climate variability, which sometimes enhances and sometimes counteracts the long-term externally forced trend. Internal variability thus diminishes the relevance of trends over periods as short as 10 to 15 years for long-term climate change. Furthermore, the timing of internal decadal climate variability is not expected to be matched by the CMIP5 historical simulations, owing to the predictability horizon of at most 10 to 20 years (CMIP5 historical simulations are typically started around nominally 1850 from a control run). However, climate models exhibit individual decades of GMST trend hiatus even during a prolonged phase of energy uptake of the climate system, in which case the energy budget would be balanced by increasing subsurface–ocean heat uptake. {2.4.3, 9.3.2, 11.2.2; Boxes 2.2, 9.2}

Owing to sampling limitations, it is uncertain whether an increase in the rate of subsurface–ocean heat uptake occurred during the past 15 years. However, it is *very likely* that the climate system, including the ocean below 700 m depth, has continued to accumulate energy over the period 1998–2010. Consistent with this energy accumulation, GMSL has continued to rise during 1998–2012, at a rate only slightly and insignificantly lower than during 1993–2012. The consistency between observed heat content and sea level changes yields *high confidence* in the assessment of continued ocean energy accumulation, which is in turn consistent with the positive radiative imbalance of the climate system. By contrast, there is limited evidence that the hiatus in GMST trend has been accompanied by a slower rate of increase in ocean heat content over the depth range 0 to 700 m, when comparing the period 2003–2010 against 1971–2010. There is low agreement on this slowdown, as three of five analyses show a slowdown in the rate of increase while the other two show the increase continuing unabated. {3.2.3, 3.2.4, 3.7, 8.5.1, 13.3; Boxes 3.1, 13.1}

During the 15-year period beginning in 1998, the ensemble of HadCRUT4 GMST trends lies below almost all model-simulated trends (Box TS.3, Figure 1a), whereas during the 15-year period ending in 1998, it lies above 93 out of 114 modelled trends (Box TS.3, Figure 1b; HadCRUT4 ensemble mean trend 0.26°C per decade, CMIP5 ensemble mean trend 0.16°C per decade). Over the 62-year period 1951–2012, observed and CMIP5 ensemble mean trend agree to within 0.02°C per decade (Box TS.3, Figure 1c; CMIP5 ensemble mean trend 0.13°C per decade). There is hence *very high confidence* that the CMIP5 models show long-term GMST trends consistent with observations, despite the disagreement over the most recent 15-year period. Due to internal climate variability, in any given 15-year period the observed GMST trend sometimes lies near one end of a model ensemble, an effect that is pronounced in Box TS.3, Figure 1a, b as GMST was influenced by a very strong El Niño event in 1998. {Box 9.2}

Unlike the CMIP5 historical simulations referred to above, some CMIP5 predictions were initialized from the observed climate state during the late 1990s and the early 21st century. There is medium evidence that these initialized predictions show a GMST lower by about 0.05°C to 0.1°C compared to the historical (uninitialized) simulations and maintain this lower GMST during the first few years of the simulation. In some initialized models this lower GMST occurs in part because they correctly simulate a shift, around 2000, from a positive to a negative phase of the Inter-decadal Pacific Oscillation (IPO). However, the improvement of this phasing of the IPO through initialization is not universal across the CMIP5 predictions. Moreover, although part of the GMST reduction through initialization indeed results from initializing at the correct phase of internal variability, another part may result from correcting a model bias that was caused by incorrect past forcing or incorrect model response to past forcing, especially in the ocean. The relative magnitudes of these effects are at present unknown; moreover, the quality of a forecasting system cannot be evaluated from a single prediction (here, a 10-year prediction within

(continued on next page)

Box TS.3 (continued)

the period 1998–2012). Overall, there is *medium confidence* that initialization leads to simulations of GMST during 1998–2012 that are more consistent with the observed trend hiatus than are the uninitialized CMIP5 historical simulations, and that the hiatus is in part a consequence of internal variability that is predictable on the multi-year time scale. {11.1, 11.2.3; Boxes 2.5, 9.2, 11.1, 11.2}

Radiative Forcing

On decadal to interdecadal time scales and under continually increasing ERF, the forced component of the GMST trend responds to the ERF trend relatively rapidly and almost linearly (*medium confidence*). The expected forced-response GMST trend is related to the ERF trend by a factor that has been estimated for the 1% per year CO_2 increases in the CMIP5 ensemble as 2.0 [1.3 to 2.7] W m^{-2} °C^{-1} (90% uncertainty range). Hence, an ERF trend can be approximately converted to a forced-response GMST trend, permitting an assessment of how much of the change in the GMST trends shown in Box TS.3, Figure 1 is due to a change in ERF trend. {Box 9.2}

The AR5 best-estimate ERF trend over 1998–2011 is 0.22 [0.10 to 0.34] W m^{-2} per decade (90% uncertainty range), which is substantially lower than the trend over 1984–1998 (0.32 [0.22 to 0.42] W m^{-2} per decade; note that there was a strong volcanic eruption in 1982) and the trend over 1951–2011 (0.31 [0.19 to 0.40] W m^{-2} per decade; Box TS.3, Figure 1d–f; the end year 2011 is chosen because data availability is more limited than for GMST). The resulting forced-response GMST trend would approximately be 0.12 [0.05 to 0.29] °C per decade, 0.19 [0.09 to 0.39] °C per decade, and 0.18 [0.08 to 0.37] °C per decade for the periods 1998–2011, 1984–1998, and 1951–2011, respectively (the uncertainty ranges assume that the range of the conversion factor to GMST trend and the range of ERF trend itself are independent). The AR5 best-estimate ERF forcing trend difference between 1998–2011 and 1951–2011 thus might explain about one-half (0.05 °C per decade) of the observed GMST trend difference between these periods (0.06 to 0.08 °C per decade, depending on observational data set). {8.5.2}

The reduction in AR5 best-estimate ERF trend over 1998–2011 compared to both 1984–1998 and 1951–2011 is mostly due to decreasing trends in the natural forcings, –0.16 [–0.27 to –0.06] W m^{-2} per decade over 1998–2011 compared to 0.01 [–0.00 to +0.01] W m^{-2} per decade over 1951–2011. Solar forcing went from a relative maximum in 2000 to a relative minimum in 2009, with a peak-to-peak difference of around 0.15 W m^{-2} and a linear trend over 1998–2011 of around –0.10 W m^{-2} per decade. Furthermore, a series of small volcanic eruptions has increased the observed stratospheric aerosol loading after 2000, leading to an additional negative ERF linear-trend contribution of around –0.06 W m^{-2} per decade over 1998–2011 (Box TS.3, Figure 1d, f). By contrast, satellite-derived estimates of tropospheric aerosol optical depth suggests little overall trend in global mean aerosol optical depth over the last 10 years, implying little change in ERF due to aerosol–radiative interaction (*low confidence* because of *low confidence* in aerosol optical depth trend itself). Moreover, because there is only *low confidence* in estimates of ERF due to aerosol–cloud interaction, there is likewise *low confidence* in its trend over the last 15 years. {2.2.3, 8.4.2, 8.5.1, 8.5.2, 10.3.1; Box 10.2; Table 8.5}

For the periods 1984–1998 and 1951–2011, the CMIP5 ensemble mean ERF trend deviates from the AR5 best-estimate ERF trend by only 0.01 W m^{-2} per decade (Box TS.3, Figure 1e, f). After 1998, however, some contributions to a decreasing ERF trend are missing in the CMIP5 models, such as the increasing stratospheric aerosol loading after 2000 and the unusually low solar minimum in 2009. Nonetheless, over 1998–2011 the CMIP5 ensemble mean ERF trend is lower than the AR5 best-estimate ERF trend by 0.03 W m^{-2} per decade (Box TS.3, Figure 1d). Furthermore, global mean aerosol optical depth in the CMIP5 models shows little trend over 1998–2012, similar to the observations. Although the forcing uncertainties are substantial, there are no apparent incorrect or missing global mean forcings in the CMIP5 models over the last 15 years that could explain the model–observations difference during the warming hiatus. {9.4.6}

Model Response Error

The discrepancy between simulated and observed GMST trends during 1998–2012 could be explained in part by a tendency for some CMIP5 models to simulate stronger warming in response to increases in greenhouse-gas concentration than is consistent with observations. Averaged over the ensembles of models assessed in Section 10.3.1, the best-estimate GHG and other anthropogenic scaling factors are less than one (though not significantly so, Figure 10.4), indicating that the model-mean GHG and other anthropogenic responses should be scaled down to best match observations. This finding provides evidence that some CMIP5 models show a larger response to GHGs and other anthropogenic factors (dominated by the effects of aerosols) than the real world (*medium confidence*). As a consequence, it is argued in Chapter 11 that near-term model projections of GMST increase should be scaled down by about 10%. This downward scaling is, however, not sufficient to explain the model mean overestimate of GMST trend over the hiatus period. {10.3.1, 11.3.6}

Another possible source of model error is the poor representation of water vapour in the upper atmosphere. It has been suggested that a reduction in stratospheric water vapour after 2000 caused a reduction in downward longwave radiation and hence a surface-cooling contribution, possibly missed by the models. However, this effect is assessed here to be small, because there was a recovery in stratospheric water vapour after 2005. {2.2.2, 9.4.1; Box 9.2} *(continued on next page)*

Box TS.3 (continued)

In summary, the observed recent warming hiatus, defined as the reduction in GMST trend during 1998–2012 as compared to the trend during 1951–2012, is attributable in roughly equal measure to a cooling contribution from internal variability and a reduced trend in external forcing (expert judgement, *medium confidence*). The forcing trend reduction is due primarily to a negative forcing trend from both volcanic eruptions and the downward phase of the solar cycle. However, there is *low confidence* in quantifying the role of forcing trend in causing the hiatus, because of uncertainty in the magnitude of the volcanic forcing trend and *low confidence* in the aerosol forcing trend. {Box 9.2}

Almost all CMIP5 historical simulations do not reproduce the observed recent warming hiatus. There is *medium confidence* that the GMST trend difference between models and observations during 1998–2012 is to a substantial degree caused by internal variability, with possible contributions from forcing error and some CMIP5 models overestimating the response to increasing GHG forcing. The CMIP5 model trend in ERF shows no apparent bias against the AR5 best estimate over 1998–2012. However, *confidence* in this assessment of CMIP5 ERF trend is *low*, primarily because of the uncertainties in model aerosol forcing and processes, which through spatial heterogeneity might well cause an undetected global mean ERF trend error even in the absence of a trend in the global mean aerosol loading. {Box 9.2}

The causes of both the observed GMST trend hiatus and of the model–observation GMST trend difference during 1998–2012 imply that, barring a major volcanic eruption, most 15-year GMST trends in the near-term future will be larger than during 1998–2012 (*high confidence*; see Section 11.3.6 for a full assessment of near-term projections of GMST). The reasons for this implication are fourfold: first, anthropogenic GHG concentrations are expected to rise further in all RCP scenarios; second, anthropogenic aerosol concentration is expected to decline in all RCP scenarios, and so is the resulting cooling effect; third, the trend in solar forcing is expected to be larger over most near-term 15-year periods than over 1998–2012 (*medium confidence*), because 1998–2012 contained the full downward phase of the solar cycle; and fourth, it is *more likely than not* that internal climate variability in the near term will enhance and not counteract the surface warming expected to arise from the increasing anthropogenic forcing. {Box 9.2}

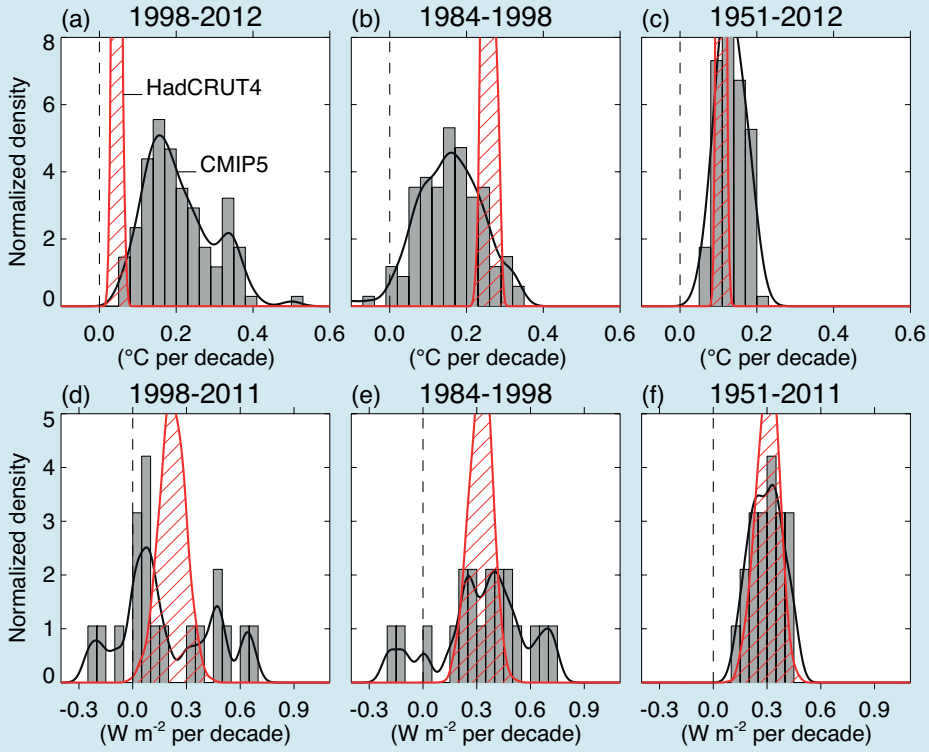

Box TS.3, Figure 1 | (Top) Observed and simulated GMST trends in °C per decade, over the periods 1998–2012 (a), 1984–1998 (b), and 1951–2012 (c). For the observations, 100 realizations of the Hadley Centre/Climatic Research Unit gridded surface temperature data set 4 (HadCRUT4) ensemble are shown (red, hatched). The uncertainty displayed by the ensemble width is that of the statistical construction of the global average only, in contrast to the trend uncertainties quoted in Section 2.4.3, which include an estimate of internal climate variability. Here, by contrast, internal variability is characterized through the width of the model ensemble. For the models, all 114 available CMIP5 historical realizations are shown, extended after 2005 with the RCP4.5 scenario and through 2012 (grey, shaded). (Bottom) Trends in effective radiative forcing (ERF, in W m^{-2} per decade) over the periods 1998–2011 (d), 1984–1998 (e), and 1951–2011 (f). The figure shows AR5 best-estimate ERF trends (red, hatched) and CMIP5 ERF (grey, shaded). Black lines are smoothed versions of the histograms. Each histogram is normalized so that its area sums up to one. {2.4.3, 8.5.2; Box 9.2; Figure 8.18; Box 9.2, Figure 1}

Thematic Focus Elements

TFE.3 | Comparing Projections from Previous IPCC Assessments with Observations

Verification of projections is arguably the most convincing way of establishing the credibility of climate change science. Results of projected changes in carbon dioxide (CO_2), global mean surface temperature (GMST) and global mean sea level (GMSL) from previous IPCC assessment reports are quantitatively compared with the best available observational estimates. The comparison between the four previous reports highlights the evolution in our understanding of how the climate system responds to changes in both natural and anthropogenic forcing and provides an assessment of how the projections compare with observational estimates. TFE.3, Figure 1, for example, shows the projected and observed estimates of: (1) CO_2 changes (top row), (2) GMST anomaly relative to 1961–1990 (middle row) and (3) GMSL relative to 1961–1990 (bottom row). Results from previous assessment reports are in the left-hand column, and for completeness results from current assessment are given in the right-hand column. {2.4, 3.7, 6.3, 11.3, 13.3} *(continued on next page)*

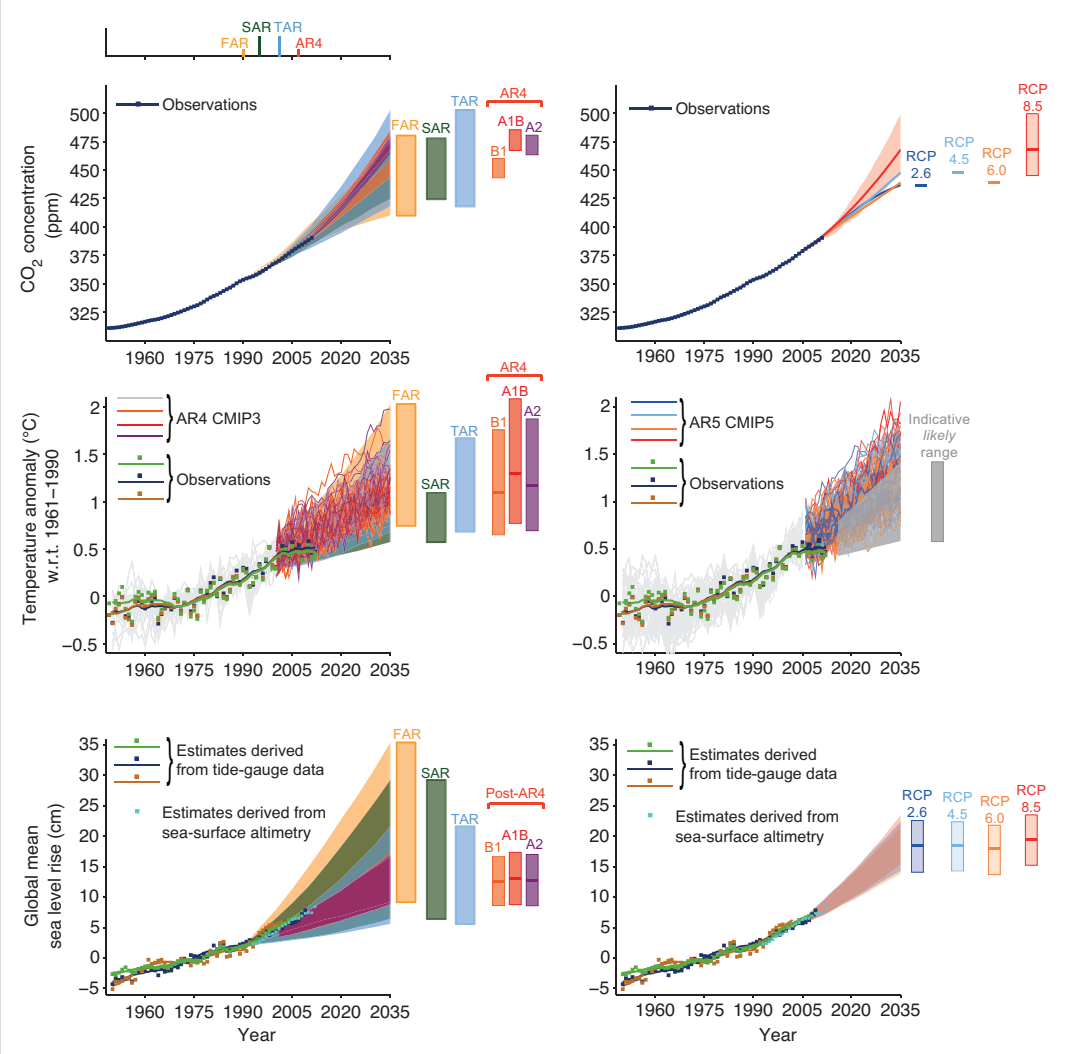

TFE.3, Figure 1 | (Top left) Observed globally and annually averaged CO_2 concentrations in parts per million (ppm) since 1950 compared with projections from the previous IPCC assessments. Observed global annual CO_2 concentrations are shown in dark blue. The shading shows the largest model projected range of global annual CO_2 concentrations from 1950 to 2035 from FAR (First Assessment Report; Figure A.3 in the Summary for Policymakers (SPM) of IPCC 1990), SAR (Second Assessment Report; Figure 5b in the TS of IPCC 1996), TAR (Third Assessment Report; Appendix II of IPCC 2001), and for the IPCC Special Report on Emission Scenarios (SRES) A2, A1B and B1 scenarios presented in the AR4 (Fourth Assessment Report; Figure 10.26). The publication years of the assessment reports are shown. (Top right) Same observed globally averaged CO_2 concentrations and the projections from this report. Only RCP8.5 has a range of values because the emission-driven senarios were carried out only for this RCP. For the other RCPs the best estimate is given. (Middle left) Estimated changes in the observed globally and annually averaged surface temperature anomaly relative to 1961–1990 (in °C) since 1950 compared with the range of projections from the previous IPCC assessments. Values are harmonized

TFE.3 (continued)

to start from the same value at 1990. Observed global annual temperature anomaly, relative to 1961–1990, from three data sets is shown as squares and smoothed time series as solid lines from the Hadley Centre/Climatic Research Unit gridded surface temperature data set 4 (HadCRUT4; bright green), Merged Land–Ocean Surface Temperature Analysis (MLOST; warm mustard) and Goddard Institute for Space Studies Surface Temperature Analysis (GISTEMP; dark blue) data sets. The coloured shading shows the projected range of global annual mean near surface temperature change from 1990 to 2035 for models used in FAR (Figure 6.11), SAR (Figure 19 in the TS of IPCC 1996), TAR (full range of TAR, Figure 9.13(b)). TAR results are based on the simple climate model analyses presented in this assessment and not on the individual full three-dimensional climate model simulations. For the AR4 results are presented as single model runs of the CMIP3 ensemble for the historical period from 1950 to 2000 (light grey lines) and for three SRES scenarios (A2, A1B and B1) from 2001 to 2035. For the three SRES scenarios the bars show the CMIP3 ensemble mean and the *likely* range given by –40 % to +60% of the mean as assessed in Chapter 10 of AR4. (Middle right) Projections of annual mean global mean surface air temperature (GMST) for 1950–2035 (anomalies relative to 1961–1990) under different RCPs from CMIP5 models (light grey and coloured lines, one ensemble member per model), and observational estimates the same as the middle left panel. The grey shaded region shows the indicative *likely* range for annual mean GMST during the period 2016–2035 for all RCPs (see Figure TS.14 for more details). The grey bar shows this same indicative *likely* range for the year 2035. (Bottom left) Estimated changes in the observed global annual mean sea level (GMSL) since 1950. Different estimates of changes in global annual sea level anomalies from tide gauge data (dark blue, warm mustard, dark green) and based on annual averages of altimeter data (light blue) starting in 1993 (the values have been aligned to fit the 1993 value of the tide gauge data). Squares indicate annual mean values, solid lines smoothed values. The shading shows the largest model projected range of global annual sea level rise from 1950 to 2035 for FAR (Figures 9.6 and 9.7), SAR (Figure 21 in TS of IPCC, 1996), TAR (Appendix II of IPCC, 2001) and based on the CMIP3 model results available at the time of AR4 using the SRES A1B scenario. Note that in the AR4 no full range was given for the sea level projections for this period. Therefore, the figure shows results that have been published subsequent to the AR4. The bars at the right hand side of each graph show the full range given for 2035 for each assessment report. (Bottom right) Same observational estimate as bottom left. The bars are the *likely* ranges (*medium confidence*) for global mean sea level rise at 2035 with respect to 1961–1990 following the four RCPs. Appendix 1.A provides details on the data and calculations used to create these figures. See Chapters 1, 11 and 13 for more details. {Figures 1.4, 1.5, 1.10, 11.9, 11.19, 11.25, 13.11}

Carbon Dioxide Changes

From 1950 to 2011 the observed concentrations of atmospheric CO_2 have steadily increased. Considering the period 1990–2011, the observed CO_2 concentration changes lie within the envelope of the scenarios used in the four assessment reports. As the most recent assessment prior to the current, the IPCC Fourth Assessment Report (AR4) (TFE.3.Figure 1; top left) has the narrowest scenario range and the observed concentration follows this range. The results from the IPCC Fifth Assessment Report (AR5) (TFE.3, Figure 1; top right) are consistent with AR4, and during 2002–2011, atmospheric CO_2 concentrations increased at a rate of 1.9 to 2.1 ppm yr^{-1}. {2.2.1, 6.3; Table 6.1}

Global Mean Temperature Anomaly

Relative to the 1961–1990 mean, the GMST anomaly has been positive and larger than 0.25°C since 2001. Observations are generally well within the range of the extent of the earlier IPCC projections (TFE.3, Figure1, middle left) This is also true for the Coupled Model Intercomparison Project Phase 5 (CMIP5) results (TFE.3, Figure 1; middle right) in the sense that the observed record lies within the range of the model projections, but on the lower end of the plume. Mt Pinatubo erupted in 1991 (see FAQ 11.2 for discussion of how volcanoes impact the climate system), leading to a brief period of relative global mean cooling during the early 1990s. The IPCC First, Second and Third Assessment Reports (FAR, SAR and TAR) did not include the effects of volcanic eruptions and thus failed to include the cooling associated with the Pinatubo eruption. AR4 and AR5, however, did include the effects from volcanoes and did simulate successfully the associated cooling. During 1995–2000 the global mean temperature anomaly was quite variable—a significant fraction of this variability was due to the large El Niño in 1997–1998 and the strong back-to-back La Niñas in 1999–2001. The projections associated with these assessment reports do not attempt to capture the actual evolution of these El Niño and La Niña events, but include them as a source of uncertainty due to natural variability as encompassed by, for example, the range given by the individual CMIP3 and CMIP5 simulations and projection (TFE.3, Figure 1). The grey wedge in TFE.3, Figure 1 (middle right) corresponds to the indicative *likely* range for annual temperatures, which is determined from the Representative Concentration Pathways (RCPs) assessed value for the 20-year mean 2016–2035 (see discussion of Figure TS.14 and Section 11.3.6 for details). From 1998 to 2012 the observational estimates have largely been on the low end of the range given by the scenarios alone in previous assessment reports and CMIP3 and CMIP5 projections. {2.4; Box 9.2}

Global Mean Sea Level

Based on both tide gauge and satellite altimetry data, relative to 1961–1990, the GMSL has continued to rise. While the increase is fairly steady, both observational records show short periods of either no change or a slight decrease. The observed estimates lie within the envelope of all the projections except perhaps in the very early 1990s. The sea level rise uncertainty due to scenario-related uncertainty is smallest for the most recent assessments (AR4 and AR5) and observed estimates lie well within this scenario-related uncertainty. It is *virtually certain* that over the 20th century sea level rose. The mean rate of sea level increase was 1.7 mm yr^{-1} with a *very likely* range between 1.5 to 1.9 between 1901 and 2010 and this rate increased to 3.2 with a *likely* range of 2.8 to 3.6 mm yr^{-1} between 1993 and 2010 (see TFE.2). {3.7.2, 3.7.4}

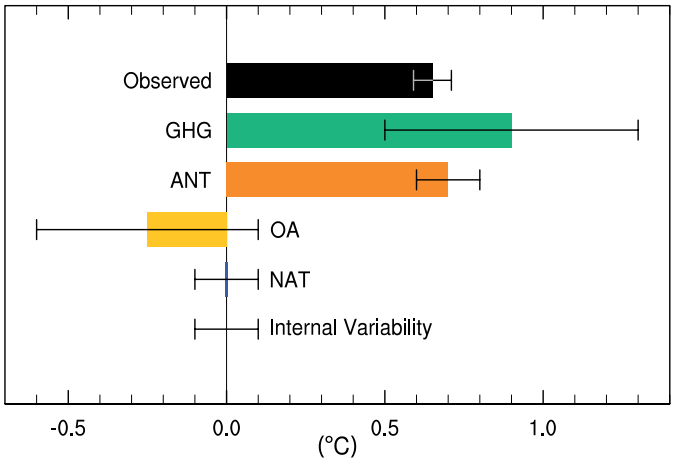

Figure TS.10 | Assessed *likely* ranges (whiskers) and their midpoints (bars) for warming trends over the 1951–2010 period due to well-mixed greenhouse gases (GHG), anthropogenic forcings (ANT) anthropogenic forcings other than well-mixed greenhouse gases (OA), natural forcings (NAT) and internal variability. The trend in the Hadley Centre/Climatic Research Unit gridded surface temperature data set 4 (HadCRUT4) observations is shown in black with its 5 to 95% uncertainty range due only to observational uncertainty in this record. {Figure 10.5}

WMGHGs and other anthropogenic forcings individually. Consistent with AR4, it is assessed that more than half of the observed increase in global average surface temperature from 1951 to 2010 is *very likely* due to the observed anthropogenic increase in WMGHG concentrations. WMGHGs contributed a global mean surface warming *likely* to be between 0.5°C and 1.3°C over the period between 1951 and 2010, with the contributions from other anthropogenic forcings *likely* to be between –0.6°C and 0.1°C and from natural forcings *likely* to be between –0.1°C and 0.1°C. Together these assessed contributions are consistent with the observed warming of approximately 0.6°C over this period (Figure TS.10). {10.3}

Solar forcing is the only known natural forcing acting to warm the climate over the 1951–2010 period but it has increased much less than WMGHG forcing, and the observed pattern of long-term tropospheric warming and stratospheric cooling is not consistent with the expected response to solar irradiance variations. Considering this evidence together with the assessed contribution of natural forcings to observed trends over this period, it is assessed that the contribution from solar forcing to the observed global warming since 1951 is *extremely unlikely* to be larger than that from WMGHGs. Because solar forcing has *very likely* decreased over a period with direct satellite measurements of solar output from 1986 to 2008, there is *high confidence* that changes in total solar irradiance have not contributed to global warming during that period. However, there is *medium confidence* that the 11-year cycle of solar variability influences decadal climate fluctuations in some regions through amplifying mechanisms. {8.4, 10.3; Box 10.2}

Observed warming over the past 60 years is far outside the range of internal climate variability estimated from pre-instrumental data, and it is also far outside the range of internal variability simulated in climate models. Model-based simulations of internal variability are assessed to be adequate to make this assessment. Further, the spatial pattern of observed warming differs from those associated with internal variability. Based on this evidence, the contribution of internal variability to the 1951–2010 GMST trend was assessed to be *likely* between –0.1°C and 0.1°C, and it is *virtually certain* that warming since 1951 cannot be explained by internal variability alone. {9.5, 10.3, 10.7}

The instrumental record shows a pronounced warming during the first half of the 20th century. Consistent with AR4, it is assessed that the early 20th century warming is *very unlikely* to be due to internal variability alone. It remains difficult to quantify the contributions to this early century warming from internal variability, natural forcing and anthropogenic forcing, due to forcing and response uncertainties and incomplete observational coverage. {10.3}

TS.4.3 Atmospheric Temperature

A number of studies since the AR4 have investigated the consistency of simulated and observed trends in free tropospheric temperatures (see section TS.2). Most, though not all, CMIP3 and CMIP5 models overestimate the observed warming trend in the tropical troposphere during the satellite period 1979–2012. Roughly one half to two thirds of this difference from the observed trend is due to an overestimate of the SST trend, which is propagated upward because models attempt to maintain static stability. There is *low confidence* in these assessments, however, owing to the *low confidence* in observed tropical tropospheric trend rates and vertical structure. Outside the tropics, and over the period of the radiosonde record beginning in 1961, the discrepancy between simulated and observed trends is smaller. {2.4.4, 9.4, 10.3}

Analysis of both radiosonde and satellite data sets, combined with CMIP5 and CMIP3 simulations, continues to find that observed tropospheric warming is inconsistent with internal variability and simulations of the response to natural forcings alone. Over the period 1961–2010 CMIP5 models simulate tropospheric warming driven by WMGHG changes, with only a small offsetting cooling due to the combined effects of changes in reflecting and absorbing aerosols and tropospheric ozone. Taking this evidence together with the results of multi-signal detection and attribution analyses, it is *likely* that anthropogenic forcings, dominated by WMGHGs, have contributed to the warming of the troposphere since 1961. Uncertainties in radiosonde and satellite records makes assessment of causes of observed trends in the upper troposphere less confident than an assessment of the overall atmospheric temperature changes. {2.4.4, 9.4, 10.3}

CMIP5 simulations including WMGHGs, ozone and natural forcing changes broadly reproduce the observed evolution of lower stratospheric temperature, with some tendency to underestimate the observed cooling trend over the satellite era (see Section TS.2). New studies of stratospheric temperature, considering the responses to natural forcings, WMGHGs and ozone-depleting substances, demonstrate that it is *very likely* that anthropogenic forcings, dominated by the depletion of the ozone layer due to ozone depleting substances have contributed to the cooling of the lower stratosphere since 1979. CMIP5 models simulate only a very weak cooling of the lower stratosphere in response to historical WMGHG changes, and the influence of WMGHGs on lower stratospheric temperature has not been formally detected. Considering both regions together, it is *very likely* that anthropogenic

Thematic Focus Elements

TFE.4 | The Changing Energy Budget of the Global Climate System

The global energy budget is a fundamental aspect of the Earth's climate system and depends on many phenomena within it. The ocean has stored about 93% of the increase in energy in the climate system over recent decades, resulting in ocean thermal expansion and hence sea level rise. The rate of storage of energy in the Earth system must be equal to the net downward radiative flux at the top of the atmosphere, which is the difference between effective radiative forcing (ERF) due to changes imposed on the system and the radiative response of the system. There are also significant transfers of energy between components of the climate system and from one location to another. The focus here is on the Earth's global energy budget since 1970, when better global observational data coverage is available. {3.7, 9.4, 13.4; Box 3.1}

The ERF of the climate system has been positive as a result of increases in well-mixed (long-lived) greenhouse gas (GHG) concentrations, changes in short-lived GHGs (tropospheric and stratospheric ozone and stratospheric water vapour), and an increase in solar irradiance (TFE.4, Figure 1a). This has been partly compensated by a negative contribution to the ERF of the climate system as a result of changes in tropospheric aerosol, which predominantly reflect sunlight and furthermore enhance the brightness of clouds, although black carbon produces positive forcing. Explosive volcanic eruptions (such as El Chichón in Mexico in 1982 and Mt Pinatubo in the Philippines in 1991)

(continued on next page)

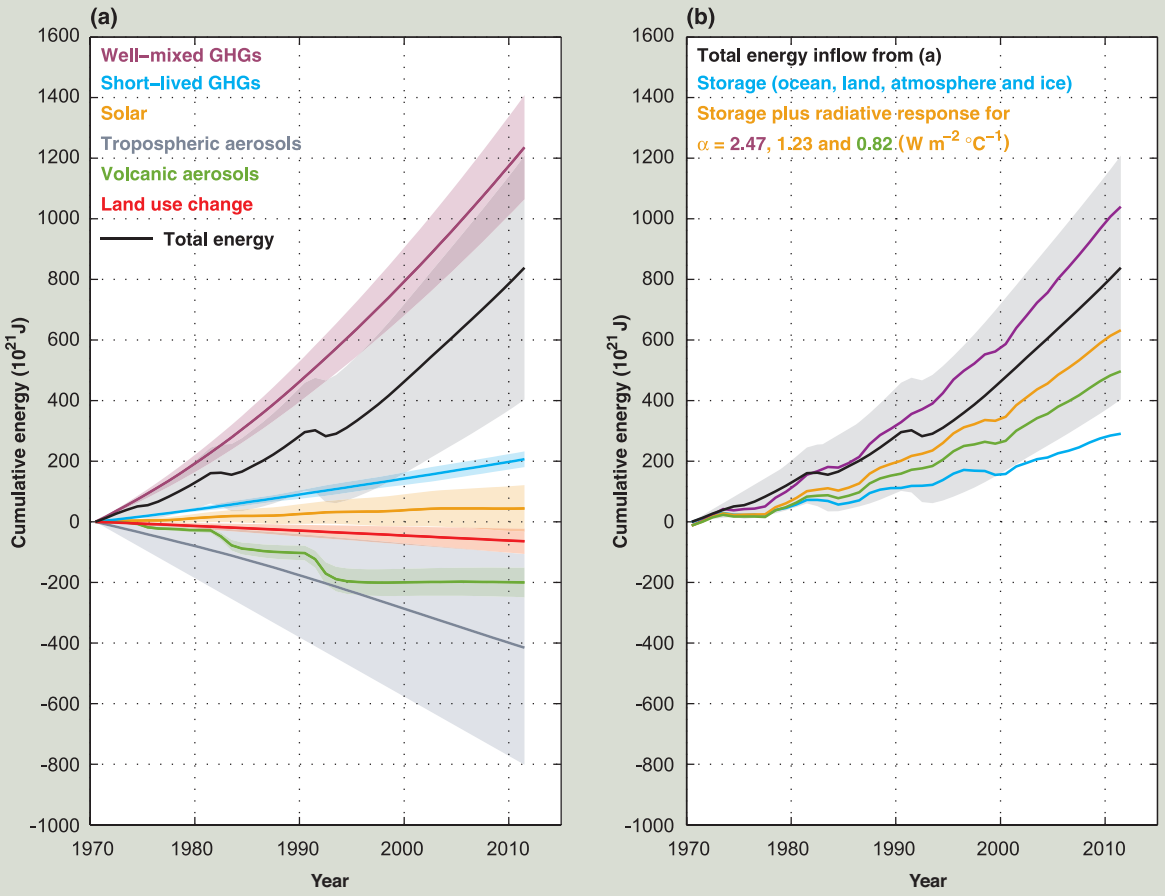

TFE.4, Figure 1 | The Earth's energy budget from 1970 through 2011. (a) The cumulative energy inflow into the Earth system from changes in well-mixed and short-lived greenhouse gases, solar forcing, tropospheric aerosol forcing, volcanic forcing and changes in surface albedo due to land use change (all relative to 1860–1879) are shown by the coloured lines; these contributions are added to give the total energy inflow (black; contributions from black carbon on snow and contrails as well as contrail-induced cirrus are included but not shown separately). (b) The cumulative total energy inflow from (a, black) is balanced by the sum of the energy uptake of the Earth system (blue; energy absorbed in warming the ocean, the atmosphere and the land, as well as in the melting of ice) and an increase in outgoing radiation inferred from changes in the global mean surface temperature. The sum of these two terms is given for a climate feedback parameter α of 2.47, 1.23 and 0.82 W m^{-2} °C^{-1}, corresponding to an equilibrium climate sensitivity of 1.5°C, 3.0°C and 4.5°C, respectively; 1.5°C to 4.5°C is assessed to be the *likely* range of equilibrium climate sensitivity. The energy budget would be closed for a particular value of α if the corresponding line coincided with the total energy inflow. For clarity, all uncertainties (shading) shown are *likely* ranges. {Box 12.2; Box 13.1, Figure 1}

TFE.4 (continued)

can inject sulphur dioxide into the stratosphere, giving rise to stratospheric aerosol, which persists for several years. Stratospheric aerosol reflects some of the incoming solar radiation and thus gives a negative forcing. Changes in surface albedo from land use change have also led to a greater reflection of shortwave radiation back to space and hence a negative forcing. Since 1970, the net ERF of the climate system has increased, and the integrated impact of these forcings is an energy inflow over this period (TFE.4, Figure 1a). {2.3, 8.5; Box 13.1}

As the climate system warms, energy is lost to space through increased outgoing radiation. This radiative response by the system is due predominantly to increased thermal radiation, but it is modified by climate feedbacks such as changes in water vapour, clouds and surface albedo, which affect both outgoing longwave and reflected shortwave radiation. The top of the atmosphere fluxes have been measured by the Earth Radiation Budget Experiment (ERBE) satellites from 1985 to 1999 and the Cloud and the Earth's Radiant Energy System (CERES) satellites from March 2000 to the present. The top of the atmosphere radiative flux measurements are highly precise, allowing identification of changes in the Earth's net energy budget from year to year within the ERBE and CERES missions, but the absolute calibration of the instruments is not sufficiently accurate to allow determination of the absolute top of the atmosphere energy flux or to provide continuity across missions. TFE.4, Figure 1b relates the cumulative total energy change of the Earth system to the change in energy storage and the cumulative outgoing radiation. Calculation of the latter is based on the observed global mean surface temperature multiplied by the climate feedback parameter α, which in turn is related to the equilibrium climate sensitivity. The mid-range value for α, 1.23 W m^{-2} °C^{-1}, corresponds to an ERF for a doubled carbon dioxide (CO_2) concentration of 3.7 [2.96 to 4.44] W m^{-2} combined with an equilibrium climate sensitivity of 3.0°C. The climate feedback parameter α is *likely* to be in the range from 0.82 to 2.47 W m^{-2} °C^{-1} (corresponding to the *likely* range in equilibrium climate sensitivity of 1.5°C to 4.5°C). {9.7.1; Box 12.2}

If ERF were fixed, the climate system would eventually warm sufficiently that the radiative response would balance the ERF, and there would be no further change in energy storage in the climate system. However, the forcing is increasing, and the ocean's large heat capacity means that the climate system is not in radiative equilibrium and its energy content is increasing (TFE.4, Figure 1b). This storage provides strong evidence of a changing climate. The majority of this additional heat is in the upper 700 m of the ocean, but there is also warming in the deep and abyssal ocean. The associated thermal expansion of the ocean has contributed about 40% of the observed sea level rise since 1970. A small amount of additional heat has been used to warm the continents, warm and melt glacial and sea ice and warm the atmosphere. {13.4.2; Boxes 3.1, 13.1}

In addition to these forced variations in the Earth's energy budget, there is also internal variability on decadal time scales. Observations and models indicate that, because of the comparatively small heat capacity of the atmosphere, a decade of steady or even decreasing surface temperature can occur in a warming world. Climate model simulations suggest that these periods are associated with a transfer of heat from the upper to the deeper ocean, of the order 0.1 W m^{-2}, with a near-steady or an increased radiation to space, again of the order 0.1 W m^{-2}. Although these natural fluctuations represent a large amount of heat, they are significantly smaller than the anthropogenic forcing of the Earth's energy budget, particularly on time scales of several decades or longer. {9.4; Boxes 9.2, 13.1}

The available independent estimates of ERF, of observed heat storage, and of surface warming combine to give an energy budget for the Earth that is consistent with the assessed *likely* range of equilibrium climate sensitivity to within estimated uncertainties (*high confidence*). Quantification of the terms in the Earth's energy budget and verification that these terms balance over recent decades provides strong evidence for our understanding of anthropogenic climate change. {Box 13.1}

forcing, particularly WMGHGs and stratospheric ozone depletion, has led to a detectable observed pattern of tropospheric warming and lower stratospheric cooling since 1961. {2.4, 9.4, 10.3}

TS.4.4 Oceans

The observed upper-ocean warming during the late 20th and early 21st centuries and its causes have been assessed more completely since AR4 using updated observations and more simulations (see Section TS.2.2). The long term trends and variability in the observations are most consistent with simulations of the response to both anthropogenic forcing and volcanic forcing. The anthropogenic fingerprint in observed upper-ocean warming, consisting of global mean and basin-scale pattern changes, has also been detected. This result is robust to a number of observational, model and methodological or structural uncertainties. It is *very likely* that anthropogenic forcings have made

a substantial contribution to upper ocean warming (above 700 m) observed since the 1970s. This anthropogenic ocean warming has contributed to global sea level rise over this period through thermal expansion. {3.2.2, 3.2.3, 3.7.2, 10.4.1, 10.4.3; Box 3.1}

Observed surface salinity changes also suggest a change in the global water cycle has occurred (see TFE.1). The long-term trends show that there is a strong positive correlation between the mean climate of the surface salinity and the temporal changes of surface salinity from 1950 to 2000. This correlation shows an enhancement of the climatological salinity pattern—so fresh areas have become fresher and salty areas saltier. The strongest anthropogenic signals are in the tropics (30°S to 30°N) and the Western Pacific. The salinity contrast between the Pacific and Atlantic Oceans has also increased with significant contributions from anthropogenic forcing. {3.3, 10.3.2, 10.4.2; FAQ 3.2}

On a global scale, surface and subsurface salinity changes (1955–2004) over the upper 250 m of the water column do not match changes expected from natural variability but do match the modelled distribution of forced changes (WMGHGs and tropospheric aerosols). Natural external variability taken from the simulations with just the variations in solar and volcanic forcing does not match the observations at all, thus excluding the hypothesis that observed trends can be explained by just solar or volcanic variations. These lines of evidence and our understanding of the physical processes leads to the conclusion that it is *very likely* that anthropogenic forcings have made a discernible contribution to surface and subsurface oceanic salinity changes since the 1960s. {10.4.2; Table 10.1}

Oxygen is an important physical and biological tracer in the ocean. Global analyses of oxygen data from the 1960s to 1990s extend the spatial coverage from local to global scales and have been used in attribution studies with output from a limited range of Earth System Models (ESMs). It is concluded that there is *medium confidence* that the observed global pattern of decrease in dissolved oxygen in the oceans can be attributed in part to human influences. {3.8.3, 10.4.4; Table 10.1}

The observations show distinct trends for ocean acidification (which is observed to be between –0.0014 and –0.0024 pH units per year). There is *high confidence* that the pH of ocean surface seawater decreased by about 0.1 since the beginning of the industrial era as a consequence of the oceanic uptake of anthropogenic CO_2. {3.8.2, 10.4.4; Box 3.2; Table 10.1}

TS.4.5 Cryosphere

The reductions in Arctic sea ice extent and NH snow cover extent and widespread glacier retreat and increased surface melt of Greenland are all evidence of systematic changes in the cryosphere. All of these changes in the cryosphere have been linked to anthropogenic forcings. {4.2.2, 4.4–4.6, 10.5.1, 10.5.3; Table 10.1}

Attribution studies, comparing the seasonal evolution of Arctic sea ice extent from observations from the 1950s with that simulated by coupled model simulations, demonstrate that human influence on the sea ice extent changes can be robustly detected since the early 1990s. The anthropogenic signal is also detectable for individual months from May to December, suggesting that human influence, strongest in late summer, now also extends into colder seasons. From these simulations of sea ice and observed sea ice extent from the instrumental record with high agreement between studies, it is concluded that anthropogenic forcings are *very likely* to have contributed to Arctic sea ice loss since 1979 (Figure TS.12). {10.5.1}

For Antarctic sea ice extent, the shortness of the observed record and differences in simulated and observed variability preclude an assessment of whether or not the observed increase since 1979 is inconsistent with internal variability. Untangling the processes involved with trends and variability in Antarctica and surrounding waters remains complex and several studies are contradictory. In conclusion, there is *low confidence* in the scientific understanding of the observed increase in Antarctic sea ice extent since 1979, due to the large differences between sea ice simulations from CMIP5 models and to the incomplete and competing scientific explanations for the causes of change and *low confidence* in estimates of internal variability (Figure TS.12). {9.4.3, 10.5.1; Table 10.1}

The Greenland ice sheet shows recent major melting episodes in response to record temperatures relative to the 20th century associated with persistent shifts in early summer atmospheric circulation, and these shifts have become more pronounced since 2007. Although many Greenland instrumental records are relatively short (two decades), regional modelling and observations tell a consistent story of the response of Greenland temperatures and ice sheet runoff to shifts in regional atmospheric circulation associated with larger scale flow patterns and global temperature increases. Mass loss and melt is also occurring in Greenland through the intrusion of warm water into the major fjords containing glaciers such as Jacobshaven Glacier. It is *likely* that anthropogenic forcing has contributed to surface melting of the Greenland ice sheet since 1993. {10.5.2; Table 10.1}

Estimates of ice mass in Antarctica since 2000 show that the greatest losses are at the edges. An analysis of observations underneath a floating ice shelf off West Antarctica leads to the conclusion that ocean warming in this region and increased transport of heat by ocean circulation are largely responsible for accelerating melt rates. The observational record of Antarctic mass loss is short and the internal variability of the ice sheet is poorly understood. Due to a low level of scientific understanding there is *low confidence* in attributing the causes of the observed loss of mass from the Antarctic ice sheet since 1993. {3.2, 4.2, 4.4.3, 10.5.2}

The evidence for the retreat of glaciers due to warming and moisture change is now more complete than at the time of AR4. There is *high confidence* in the estimates of observed mass loss and the estimates of natural variations and internal variability from long-term glacier records. Based on these factors and our understanding of glacier response to climatic drivers there is *high confidence* that a substantial part of the mass loss of glaciers is *likely* due to human influence. It is *likely* that there has been an anthropogenic component to observed reductions in NH snow cover since 1970. {4.3.3, 10.5.2, 10.5.3; Table 10.1}

Thematic Focus Elements

TFE.5 | Irreversibility and Abrupt Change

A number of components or phenomena within the climate system have been proposed as potentially exhibiting threshold behaviour. Crossing such thresholds can lead to an abrupt or irreversible transition into a different state of the climate system or some of its components.

Abrupt climate change is defined in this IPCC Fifth Assessment Report (AR5) as a large-scale change in the climate system that takes place over a few decades or less, persists (or is anticipated to persist) for at least a few decades and causes substantial disruptions in human and natural systems. There is information on potential consequences of some abrupt changes, but in general there is *low confidence* and little consensus on the likelihood of such events over the 21st century. Examples of components susceptible to such abrupt change are the strength of the Atlantic Meridional Overturning Circulation (AMOC), clathrate methane release, tropical and boreal forest dieback, disappearance of summer sea ice in the Arctic Ocean, long-term drought and monsoonal circulation. {5.7, 6.4.7, 12.5.5; Table 12.4}

A change is said to be *irreversible* if the recovery time scale from this state due to natural processes is significantly longer than the time it takes for the system to reach this perturbed state. Such behaviour may arise because the time scales for perturbations and recovery processes are different, or because climate change may persist due to the long residence time of a carbon dioxide (CO_2) perturbation in the atmosphere (see TFE.8). Whereas changes in Arctic Ocean summer sea ice extent, long-term droughts and monsoonal circulation are assessed to be reversible within years to decades, tropical or boreal forest dieback may be reversible only within centuries. Changes in clathrate methane and permafrost carbon release, Greenland and Antarctic ice sheet collapse may be irreversible during millennia after the causal perturbation. {5.8, 6.4.7, 12.5.5, 13.4.3, 13.4.4; Table 12.4}

Abrupt Climate Change Linked with AMOC

New transient climate model simulations have confirmed with *high confidence* that strong changes in the strength of the AMOC produce abrupt climate changes at global scale with magnitude and pattern resembling past glacial Dansgaard–Oeschger events and Heinrich stadials. Confidence in the link between changes in North Atlantic climate and low-latitude precipitation has increased since the IPCC Fourth Assessment Report (AR4). From new paleoclimate reconstructions and modelling studies, there is *very high confidence* that a reduced strength of the AMOC and the associated surface cooling in the North Atlantic region caused southward shifts of the Atlantic Intertropical Convergence Zone and affected the American (north and south), African and Asian monsoons. {5.7}

The interglacial mode of the AMOC can recover (*high confidence*) from a short-lived freshwater input into the subpolar North Atlantic. Approximately 8.2 ka, a sudden freshwater release occurred during the final stages of North America ice sheet melting. Paleoclimate observations and model results indicate, with *high confidence*, a marked reduction in the strength of the AMOC followed by a rapid recovery, within approximately 200 years after the perturbation. {5.8.2}

Although many more model simulations have been conducted since AR4 under a wide range of future forcing scenarios, projections of the AMOC behaviour have not changed. It remains *very likely* that the AMOC will weaken over the 21st century relative to 1850-1900 values. Best estimates and ranges for the reduction from the Coupled Model Intercomparison Project Phase 5 (CMIP5) are 11% (1 to 24%) for the Representative Concentration Pathway RCP2.6 and 34% (12 to 54%) for RCP8.5, but there is *low confidence* on the magnitude of weakening. It also remains *very unlikely* that the AMOC will undergo an abrupt transition or collapse in the 21st century for the scenarios considered (*high confidence*) (TFE.5, Figure 1). For an abrupt transition of the AMOC to occur, the sensitivity of the AMOC to forcing would have to be far greater than seen in current models, or would require meltwater flux from the Greenland ice sheet greatly exceeding even the highest of current projections. Although neither possibility can be excluded entirely, it is *unlikely* that the AMOC will collapse beyond the end of the 21st century for the scenarios considered, but a collapse beyond the 21st century for large sustained warming cannot be excluded. There is *low confidence* in assessing the evolution of AMOC beyond the 21st century because of limited number of analyses and equivocal results. {12.4.7, 12.5.5}

Potential Irreversibility of Changes in Permafrost, Methane Clathrates and Forests

In a warming climate, permafrost thawing may induce decomposition of carbon accumulated in frozen soils which could persist for hundreds to thousands of years, leading to an increase of atmospheric CO_2 and/or methane (CH_4)

(continued on next page)

TFE.5 (continued)

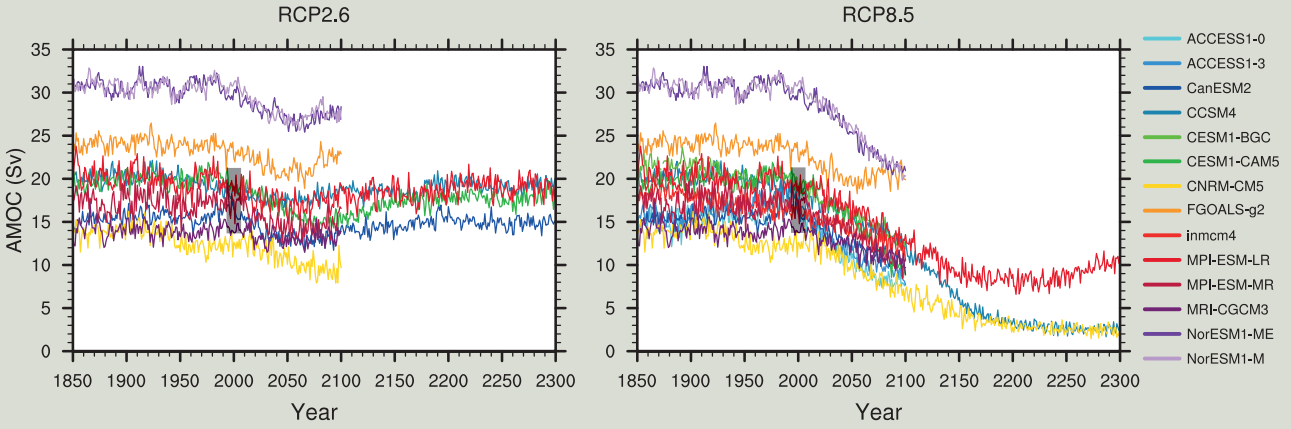

TFE.5, Figure 1 | Atlantic Meridional Overturning Circulation (AMOC) strength at 30°N (Sv) as a function of year, from 1850 to 2300 as simulated by different Atmosphere–Ocean General Circulation Models in response to scenario RCP2.6 (left) and RCP8.5 (right). The vertical black bar shows the range of AMOC strength measured at 26°N, from 2004 to 2011 {Figures 3.11, 12.35}

concentrations. The existing modelling studies of permafrost carbon balance under future warming that take into account at least some of the essential permafrost-related processes do not yield consistent results, beyond the fact that present-day permafrost will become a net emitter of carbon during the 21st century under plausible future warming scenarios (*low confidence*). This also reflects an insufficient understanding of the relevant soil processes during and after permafrost thaw, including processes leading to stabilization of unfrozen soil carbon, and precludes any quantitative assessment of the amplitude of irreversible changes in the climate system potentially related to permafrost degassing and associated feedbacks. {6.4.7, 12.5.5}

Anthropogenic warming will *very likely* lead to enhanced CH_4 emissions from both terrestrial and oceanic clathrates. Deposits of CH_4 clathrates below the sea floor are susceptible to destabilization via ocean warming. However, sea level rise due to changes in ocean mass enhances clathrate stability in the ocean. While difficult to formally assess, initial estimates of the 21st century feedback from CH_4 clathrate destabilization are small but not insignificant. It is *very unlikely* that CH_4 from clathrates will undergo catastrophic release during the 21st century (*high confidence*). On multi-millennial time scales, such CH_4 emissions may provide a positive feedback to anthropogenic warming and may be irreversible, due to the diffference between release and accumulation time scales. {6.4.7, 12.5.5}

The existence of critical climate change driven dieback thresholds in the Amazonian and other tropical rainforests purely driven by climate change remains highly uncertain. The possibility of a critical threshold being crossed in precipitation volume and duration of dry seasons cannot be ruled out. The response of boreal forest to projected climate change is also highly uncertain, and the existence of critical thresholds cannot at present be ruled out. There is *low confidence* in projections of the collapse of large areas of tropical and/or boreal forests. {12.5.5}

Potential Irreversibility of Changes in the Cryosphere

The reversibility of sea ice loss has been directly assessed in sensitivity studies to CO_2 increase and decrease with Atmosphere–Ocean General Circulation Models (AOGCMs) or Earth System Models (ESMs). None of them show evidence of an irreversible change in Arctic sea ice at any point. By contrast, as a result of the strong coupling between surface and deep waters in the Southern Ocean, the Antarctic sea ice in some models integrated with ramp-up and ramp-down atmospheric CO_2 concentration exhibits some hysteresis behaviour. {12.5.5}

At present, both the Greenland and Antarctic ice sheets have a positive surface mass balance (snowfall exceeds melting), although both are losing mass because ice outflow into the sea exceeds the net surface mass balance. A positive feedback operates to reduce ice sheet volume and extent when a decrease of the surface elevation of the ice sheet induces a decreased surface mass balance. This arises generally through increased surface melting, and therefore applies in the 21st century to Greenland, but not to Antarctica, where surface melting is currently very small. Surface melting in Antarctica is projected to become important after several centuries under high well-mixed greenhouse gas radiative forcing scenarios. {4.4, 13.4.4; Boxes 5.2, 13.2}

Abrupt change in ice sheet outflow to the sea may be caused by unstable retreat of the grounding line in regions where the bedrock is below sea level and slopes downwards towards the interior of the ice sheet. This mainly

(continued on next page)

TFE.5 (continued)

applies to West Antarctica, but also to parts of East Antarctica and Greenland. Grounding line retreat can be triggered by ice shelf decay, due to warmer ocean water under ice shelves enhancing submarine ice shelf melt, or melt water ponds on the surface of the ice shelf promoting ice shelf fracture. Because ice sheet growth is a slow process, such changes would be irreversible in the definition adopted here. {4.4.5; Box 13.2}

There is *high confidence* that the volumes of the Greenland and West Antarctic ice sheets were reduced during periods of the past few million years that were globally warmer than present. Ice sheet model simulations and geological data suggest that the West Antarctic ice sheet is very sensitive to subsurface ocean warming and imply with *medium confidence* a West Antarctic ice sheet retreat if atmospheric CO_2 concentration stays within, or above, the range of 350–450 ppm for several millennia. {5.8.1, 13.4.4; Box 13.2}

The available evidence indicates that global warming beyond a threshold would lead to the near-complete loss of the Greenland ice sheet over a millennium or longer, causing a global mean sea level rise of approximately 7 m. Studies with fixed present-day ice sheet topography indicate that the threshold is greater than 2°C but less than 4°C (*medium confidence*) of global mean surface temperature rise above pre-industrial. The one study with a dynamical ice sheet suggests the threshold is greater than about 1°C (*low confidence*) global mean warming with respect to pre-industrial. Considering the present state of scientific uncertainty, a *likely* range cannot be quantified. The complete loss of the Greenland ice sheet is not inevitable because this would take a millennium or more; if temperatures decline before the ice sheet has completely vanished, the ice sheet might regrow. However, some part of the mass loss might be irreversible, depending on the duration and degree of exceedance of the threshold, because the ice sheet may have multiple steady states, due to its interaction with regional climate. {13.4.3, 13.4.4}

TS.4.6 Water Cycle

Since the AR4, new evidence has emerged of a detectable human influence on several aspects of the water cycle. There is *medium confidence* that observed changes in near-surface specific humidity since 1973 contain a detectable anthropogenic component. The anthropogenic water vapour fingerprint simulated by an ensemble of climate models has been detected in lower tropospheric moisture content estimates derived from Special Sensor Microwave/Imager (SSM/I) data covering the period 1988–2006. An anthropogenic contribution to increases in tropospheric specific humidity is found with *medium confidence*. {2.5, 10.3}

Attribution studies of global zonal mean terrestrial precipitation and Arctic precipitation both find a detectable anthropogenic influence. Overall there is *medium confidence* in a significant human influence on global scale changes in precipitation patterns, including increases in NH mid-to-high latitudes. Remaining observational and modelling uncertainties and the large effect of internal variability on observed precipitation preclude a more confident assessment. {2.5, 7.6, 10.3}

Based on the collected evidence for attributable changes (with varying levels of confidence and likelihood) in specific humidity, terrestrial precipitation and ocean surface salinity through its connection to precipitation and evaporation, and from physical understanding of the water cycle, it is *likely* that human influence has affected the global water cycle since 1960. This is a major advance since AR4. {2.4, 2.5, 3.3, 9.4.1, 10.3, 10.4.2; Table 10.1; FAQ 3.2}

TS.4.7 Climate Extremes

Several new attribution studies have found a detectable anthropogenic influence in the observed increased frequency of warm days and nights and decreased frequency of cold days and nights. Since the AR4 and SREX, there is new evidence for detection of human influence on extremely warm daytime temperature and there is new evidence that the influence of anthropogenic forcing may be detected separately from the influence of natural forcing at global scales and in some continental and sub-continental regions. This strengthens the conclusions from both AR4 and SREX, and it is now *very likely* that anthropogenic forcing has contributed to the observed changes in the frequency and intensity of daily temperature extremes on the global scale since the mid-20th century. It is *likely* that human influence has significantly increased the probability of occurrence of heat waves in some locations. See TFE.9 and TFE.9, Table 1 for a summary of the assessment of extreme weather and climate events. {10.6}

Since the AR4, there is some new limited direct evidence for an anthropogenic influence on extreme precipitation, including a formal detection and attribution study and indirect evidence that extreme precipitation would be expected to have increased given the evidence of anthropogenic influence on various aspects of the global hydrological cycle and *high confidence* that the intensity of extreme precipitation events will increase with warming, at a rate well exceeding that of the mean precipitation. In land regions where observational coverage is sufficient for assessment, there is *medium confidence* that anthropogenic forcing has contributed to a global-scale intensification of heavy precipitation over the second half of the 20th century. {7.6, 10.6}

Globally, there is *low confidence* in attribution of changes in tropical cyclone activity to human influence. This is due to insufficient observational evidence, lack of physical understanding of the links between anthropogenic drivers of climate and tropical cyclone activity, and the low level of agreement between studies as to the relative importance of internal variability, and anthropogenic and natural forcings. In the North Atlantic region there is *medium confidence* that a reduction in aerosol forcing over the North Atlantic has contributed at least in part to the observed increase in tropical cyclone activity there since the 1970s. There remains substantial disagreement on the relative importance of internal variability, WMGHG forcing and aerosols for this observed trend. {2.6, 10.6, 14.6}

Although the AR4 concluded that it is *more likely than not* that anthropogenic influence has contributed to an increased risk of drought in the second half of the 20th century, an updated assessment of the observational evidence indicates that the AR4 conclusions regarding global increasing trends in hydrological droughts since the 1970s are no longer supported. Owing to the *low confidence* in observed large-scale trends in dryness combined with difficulties in distinguishing decadal-scale variability in drought from long-term climate change, there is now *low confidence* in the attribution of changes in drought over global land since the mid-20th century to human influence. {2.6, 10.6}

TS.4.8 From Global to Regional

Taking a longer term perspective shows the substantial role played by external forcings in driving climate variability on hemispheric scales in pre-industrial times (Box TS.5). It is *very unlikely* that NH temperature variations from 1400 to 1850 can be explained by internal variability alone. There is *medium confidence* that external forcing contributed to NH temperature variability from 850 to 1400 and that external forcing contributed to European temperature variations over the last 5 centuries. {5.3.3, 5.5.1, 10.7.2, 10.7.5; Table 10.1}

Changes in atmospheric circulation are important for local climate change because they could lead to greater or smaller changes in climate in a particular region than elsewhere. It is *likely* that human influence has altered sea level pressure patterns globally. There is *medium confidence* that stratospheric ozone depletion has contributed to the observed poleward shift of the southern Hadley Cell border during austral summer. It is *likely* that stratospheric ozone depletion has contributed to the positive trend in the SAM seen in austral summer since the mid-20th century which corresponds to sea level pressure reductions over the high latitudes and increase in the subtropics (Figure TS.11). {10.3}

The evidence is stronger that observed changes in the climate system can now be attributed to human activities on global and regional scales in many components (Figure TS.12). Observational uncertainty has been explored much more thoroughly than previously, and fingerprints of human influence have been deduced from a new generation of climate models. There is improved understanding of ocean changes, including salinity changes, that are consistent with large scale intensification of the water cycle predicted by climate models. The changes in near surface temperatures, free atmosphere temperatures, ocean temperatures and NH snow cover and sea ice extent, when taken together, show not just global mean changes, but also distinctive regional patterns consistent with the expected fingerprints of change from anthropogenic forcings and the expected responses from volcanic eruptions (Figure TS.12). {10.3–10.6, 10.9}

Human influence has been detected in nearly all of the major assessed components of the climate system (Figure TS.12). Taken together, the combined evidence increases the overall level of confidence in the attribution of observed climate change, and reduces the uncertainties associated with assessment based on a single climate variable. From this combined evidence it is *virtually certain* that human influence has warmed the global climate system. Anthropogenic influence has been identified in changes in temperature near the surface of the Earth, in the atmosphere and in the oceans, as well as in changes in the cryosphere, the water cycle and some extremes. There is strong evidence that excludes solar forcing, volcanoes and internal variability as the strongest drivers of warming since 1950. {10.9; Table 10.1; FAQ 5.1}

Over every continent except Antarctica, anthropogenic influence has *likely* made a substantial contribution to surface temperature increases since the mid-20th century (Figure TS.12). It is *likely* that there has been a significant anthropogenic contribution to the very substantial warming in Arctic land surface temperatures over the past 50 years. For Antarctica large observational uncertainties result in *low confidence* that anthropogenic influence has contributed to observed warming averaged over available stations. Detection and attribution at regional

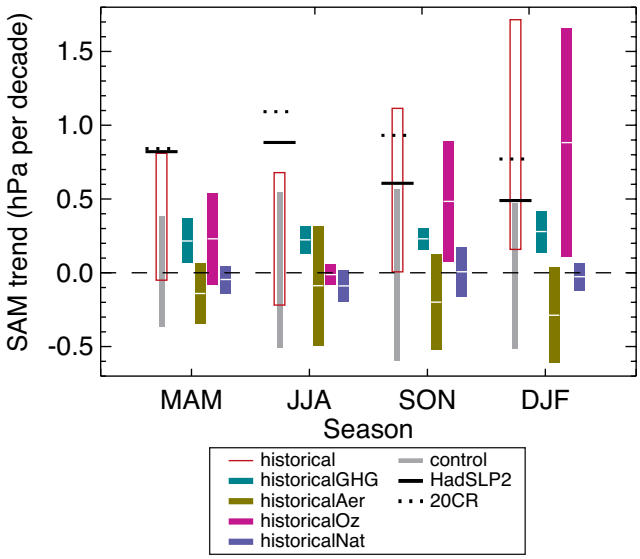

Figure TS.11 | Simulated and observed 1951–2011 trends in the Southern Annular Mode (SAM) index by season. The SAM index is a difference between zonal mean sea level pressure (SLP) at 40°S and 65°S. The SAM index is defined without normalization, so that the magnitudes of simulated and observed trends can be compared. Black lines show observed trends from the Hadley Centre Sea Level Pressure 2r (HadSLP2r) data set (solid), and the 20th Century Reanalysis (dotted). Grey bars show 5th to 95th percentile ranges of control trends, and red boxes show the 5th to 95th percentile range of trends in historical simulations including anthropogenic and natural forcings. Coloured bars show ensemble mean trends and their associated 5 to 95% confidence ranges simulated in response to well-mixed greenhouse gas (light green), aerosol (dark green), ozone (magenta) and natural forcing changes (blue) in CMIP5 individual-forcing simulations. {Figure 10.13b}

scales is complicated by the greater role played by dynamical factors (circulation changes), a greater range of forcings that may be regionally important, and the greater difficulty of modelling relevant processes at regional scales. Nevertheless, human influence has *likely* contributed to temperature increases in many sub-continental regions. {10.3; Box 5.1}

The coherence of observed changes with simulations of anthropogenic and natural forcing in the physical system is remarkable (Figure TS.12), particularly for temperature-related variables. Surface temperature and ocean heat content show emerging anthropogenic and natural signals in both records, and a clear separation from the alternative hypothesis of just natural variations. These signals do not appear just in the global means, but also appear at regional scales on continents and in ocean basins in each of these variables. Sea ice extent emerges clearly from the range of internal variability for the Arctic. At sub-continental scales human influence is *likely* to have substantially increased the probability of occurrence of heat waves in some locations. {Table 10.1}

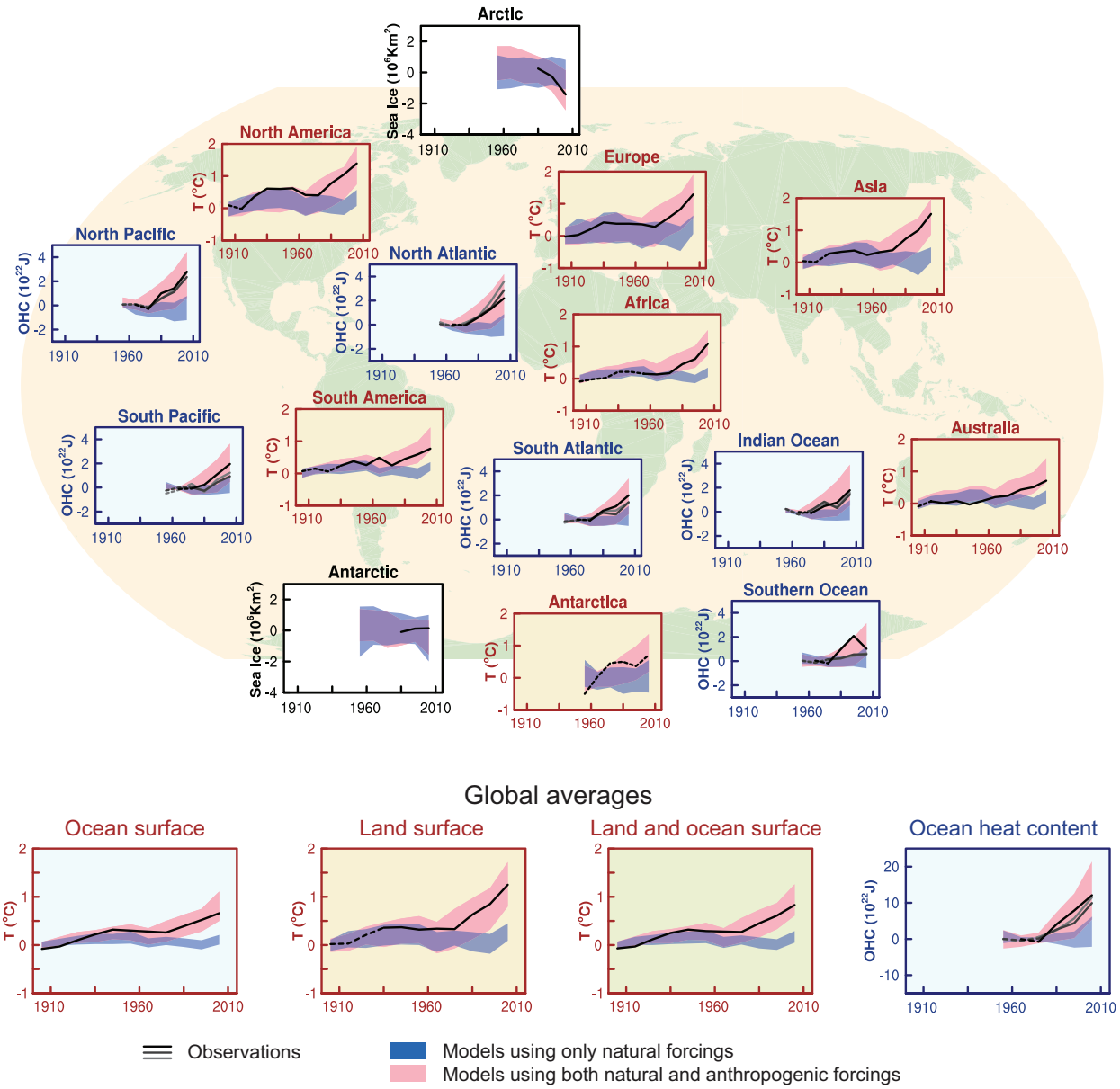

Figure TS.12 | Comparison of observed and simulated change in the climate system, at regional scales (top panels) and global scales (bottom four panels). Brown panels are land surface temperature time series, blue panels are ocean heat content time series and white panels are sea ice time series (decadal averages). Each panel shows observations (black or black and shades of grey), and the 5 to 95% range of the simulated response to natural forcings (blue shading) and natural and anthropogenic forcings (pink shading), together with the corresponding ensemble means (dark blue and dark red respectively). The observed surface temperature is from the Hadley Centre/Climatic Research Unit gridded surface temperature data set 4 (HadCRUT4). Three observed records of ocean heat content (OHC) are shown. Sea ice anomalies (rather than absolute values) are plotted and based on models in Figure 10.16. The observations lines are either solid or dashed and indicate the quality of the observations and estimates. For land and ocean surface temperatures panels and precipitation panels, solid observation lines indicate where spatial coverage of areas being examined is above 50% coverage and dashed observation lines where coverage is below 50%. For example, data coverage of Antarctica never goes above 50% of the land area of the continent. For ocean heat content and sea ice panels the solid observations line is where the coverage of data is good and higher in quality, and the dashed line is where the data coverage is only adequate. This figure is based on Figure 10.21 except presented as decadal averages rather than yearly averages. Further detail regarding the related Figure SPM.6 is given in the TS Supplementary Material. {Figure 10.21}

Box TS.4 | Model Evaluation

Climate models have continued to be improved since the AR4, and many models have been extended into Earth System Models (ESMs) by including the representation of biogeochemical cycles important to climate change. Box TS.4, Figure 1 provides a partial overview of model capabilities as assessed in this report, including improvements or lack thereof relative to models that were assessed in the AR4 or that were available at the time of the AR4. {9.1, 9.8.1; Box 9.1}

The ability of climate models to simulate surface temperature has improved in many, though not all, important aspects relative to the generation of models assessed in the AR4. There continues to be *very high confidence* that models reproduce the observed large-scale time-mean surface temperature patterns (pattern correlation of about 0.99), although systematic errors of several degrees Celsius are found in some regions. There is *high confidence* that on the regional scale (sub-continental and smaller), time-mean surface temperature is better simulated than at the time of the AR4; however, confidence in model capability is lower than for the large scale. Models are able to reproduce the magnitude of the observed global mean or northern-hemisphere-mean temperature variability on interannual to centennial time scales. Models are also able to reproduce the large-scale patterns of temperature during the Last Glacial Maximum indicating an ability to simulate a climate state much different from the present (see also Box TS.5). {9.4.1, 9.6.1}

There is *very high confidence* that models reproduce the general features of the global and annual mean surface temperature changes over the historical period, including the warming in the second half of the 20th century and the cooling immediately following large volcanic eruptions. Most simulations of the historical period do not reproduce the observed reduction in global mean surface warming trend over the last 10 to 15 years (see Box TS.3). There is *medium confidence* that the trend difference between models and observations during 1998–2012 is to a substantial degree caused by internal variability, with possible contributions from forcing inadequacies in models and some models overestimating the response to increasing greenhouse gas forcing. Most, though not all, models overestimate the observed warming trend in the tropical troposphere over the last 30 years, and tend to underestimate the long-term lower-stratospheric cooling trend. {9.4.1; Box 9.2}

The simulation of large-scale patterns of precipitation has improved somewhat since the AR4, although models continue to perform less well for precipitation than for surface temperature. The spatial pattern correlation between modelled and observed annual mean precipitation has increased from 0.77 for models available at the time of the AR4 to 0.82 for current models. At regional scales, precipitation is not simulated as well, and the assessment remains difficult owing to observational uncertainties. {9.4.1, 9.6.1}

Many models are able to reproduce the observed changes in upper-ocean heat content from 1961 to 2005. The time series of the multi-model mean falls within the range of the available observational estimates for most of the period. {9.4.2}

There is robust evidence that the downward trend in Arctic summer sea ice extent is better simulated than at the time of the AR4. About one quarter of the models show a trend as strong as, or stronger, than the trend in observations over the satellite era 1979–2012. Most models simulate a small decreasing trend in Antarctic sea ice extent, albeit with large inter-model spread, in contrast to the small increasing trend in observations. {9.4.3}

There has been substantial progress since the AR4 in the assessment of model simulations of extreme events. Changes in the frequency of extreme warm and cold days and nights over the second half of the 20th century are consistent between models and observations, with the ensemble mean global mean time series generally falling within the range of observational estimates. The majority of models underestimate the sensitivity of extreme precipitation to temperature variability or trends, especially in the tropics. {9.5.4}

In the majority of the models that include an interactive carbon cycle, the simulated global land and ocean carbon sinks over the latter part of the 20th century fall within the range of observational estimates. However, models systematically underestimate the NH land sink implied by atmospheric inversion techniques. {9.4.5}

Regional downscaling methods provide climate information at the smaller scales needed for many climate impact studies. There is *high confidence* that downscaling adds value both in regions with highly variable topography and for various small-scale phenomena. {9.6.4}

The model spread in equilibrium climate sensitivity ranges from 2.1°C to 4.7°C and is very similar to the assessment in the AR4. There is *very high confidence* that the primary factor contributing to the spread in equilibrium climate sensitivity continues to be the cloud feedback. This applies to both the modern climate and the last glacial maximum. There is likewise *very high confidence* that, consistent with observations, models show a strong positive correlation between tropospheric temperature and water vapour on regional to global scales, implying a positive water vapour feedback in both models and observations. {5.3.3, 9.4.1, 9.7} *(continued on next page)*

Box TS.4 (continued)

Climate models are based on physical principles, and they reproduce many important elements of observed climate. Both aspects contribute to our confidence in the models' suitability for their application in detection and attribution studies (see Chapter 10) and for quantitative future predictions and projections (see Chapters 11 to 14). There is increasing evidence that some elements of observed variability or trends are well correlated with inter-model differences in model projections for quantities such as Arctic summer sea ice trends, the snow–albedo feedback, and the carbon loss from tropical land. However, there is still no universal strategy for transferring a model's past performance to a relative weight of this model in a multi-model-ensemble mean of climate projections. {9.8.3}

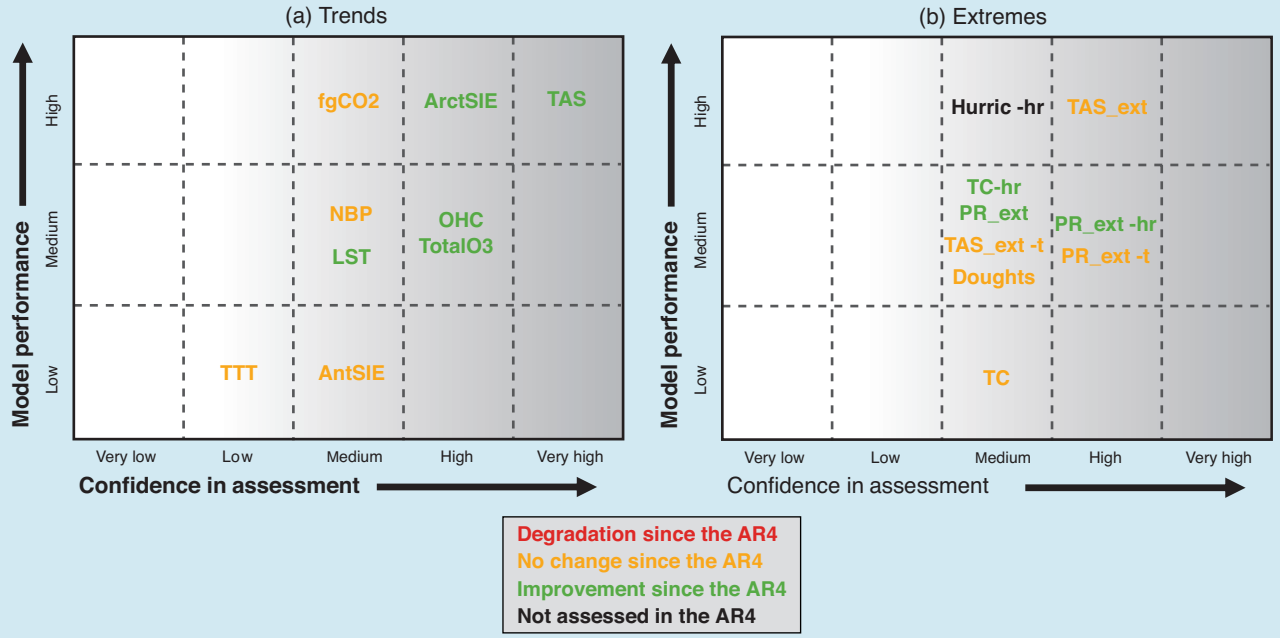

Box TS.4, Figure1 | Summary of how well the current-generation climate models simulate important features of the climate of the 20th century. Confidence in the assessment increases towards the right as suggested by the increasing strength of shading. Model quality increases from bottom to top. The colour coding indicates improvements from the models available at the time of the AR4 to the current assessment. There have been a number of improvements since the AR4, and some some modelled quantities are not better simulated. The major climate quantities are listed in this summary and none shows degradation. The assessment is based mostly on the multi-model mean, not excluding that deviations for individual models could exist. Assessed model quality is simplified for representation in this figure; details of each assessment are found in Chapter 9. {9.8.1; Figure 9.44}

The figure highlights the following key features, with the sections that back up the assessment added in brackets:

(a) Trends in:

AntSIE	Antarctic sea ice extent {9.4.3}
ArctSIE	Arctic sea ice extent {9.4.3}
fgCO2	Global ocean carbon sink {9.4.5}
LST	Lower-stratospheric temperature {9.4.1.}
NBP	Global land carbon sink {9.4.5}
OHC	Global ocean heat content {9.4.2}
TotalO3	Total-column ozone {9.4.1}
TAS	Surface air temperature {9.4.1}
TTT	Tropical tropospheric temperature {9.4.1}

(b) Extremes:

Droughts	Droughts {9.5.4}
Hurric-hr	Year-to-year count of Atlantic hurricanes in high-resolution AGCMs {9.5.4}
PR_ext	Global distribution of precipitation extremes {9.5.4}
PR_ext-hr	Global distribution of precipitation extremes in high-resolution AGCMs {9.5.4}
PR_ext-t	Global trends in precipitation extremes {9.5.4}
TAS_ext	Global distributions of surface air temperature extremes {9.5.4}
TAS_ext-t	Global trends in surface air temperature extremes {9.5.4}
TC	Tropical cyclone tracks and intensity {9.5.4}
TC-hr	Tropical cyclone tracks and intensity in high-resolution AGCMs {9.5.4}

Box TS.5 | Paleoclimate

Reconstructions from paleoclimate archives allow current changes in atmospheric composition, sea level and climate (including extreme events such as droughts and floods), as well as future projections, to be placed in a broader perspective of past climate variability (see Section TS.2). {5.2–5.6, 6.2, 10.7}

Past climate information also documents the behaviour of slow components of the climate system including the carbon cycle, ice sheets and the deep ocean for which instrumental records are short compared to their characteristic time scales of responses to perturbations, thus informing on mechanisms of abrupt and irreversible changes. Together with the knowledge of past external climate forcings, syntheses of paleoclimate data have documented polar amplification, characterized by enhanced temperature changes in the Arctic compared to the global mean, in response to high or low CO_2 concentrations. {5.2.1, 5.2.2, 5.6, 5.7, 5.8, 6.2, 8.4.2, 13.2.1, 13.4; Boxes 5.1, 5.2}

Since AR4, the inclusion of paleoclimate simulations in the PMIP3 (Paleoclimate Modelling Intercomparison Project)/CMIP5 framework has enabled paleoclimate information to be more closely linked with future climate projections. Paleoclimate information for the mid-Holocene (6 ka), the Last Glacial Maximum (approximately 21 ka), and last millennium has been used to test the ability of models to simulate realistically the magnitude and large-scale patterns of past changes. Combining information from paleoclimate simulations and reconstructions enables to quantify the response of the climate system to radiative perturbations, constraints to be placed on the range of equilibrium climate sensitivity, and past patterns of internal climate variability to be documented on inter-annual to multi-centennial scales. {5.3.1–5.3.5, 5.4, 5.5.1, 9.4.1, 9.4.2, 9.5.3, 9.7.2, 10.7.2, 14.1.2}

Box TS.5, Figure 1 illustrates the comparison between the last millennium Paleoclimate Modelling Intercomparison Project Phase 3 (PMIP3)/CMIP5 simulations and reconstructions, together with the associated solar, volcanic and WMGHG RFs. For average annual NH temperatures, the period 1983–2012 was *very likely* the warmest 30-year period of the last 800 years (*high confidence*) and *likely* the warmest 30-year period of the last 1400 years (*medium confidence*). This is supported by comparison of instrumental temperatures with multiple reconstructions from a variety of proxy data and statistical methods, and is consistent with AR4. In response to solar, volcanic and anthropogenic radiative changes, climate models simulate multi-decadal temperature changes in the last 1200 years in the NH that are generally consistent in magnitude and timing with reconstructions, within their uncertainty ranges. Continental-scale temperature reconstructions show, with *high confidence*, multi-decadal periods during the Medieval Climate Anomaly (about 950 to 1250) that were in some regions as warm as the mid-20th century and in others as warm as in the late 20th century. With *high confidence*, these regional warm periods were not as synchronous across regions as the warming since the mid-20th century. Based on the comparison between reconstructions and simulations, there is *high confidence* that not only external orbital, solar and volcanic forcing but also internal variability contributed substantially to the spatial pattern and timing of surface temperature changes between the Medieval Climate Anomaly and the Little Ice Age (about 1450 to 1850). However, there is only *very low confidence* in quantitative estimates of their relative contributions. It is *very unlikely* that NH temperature variations from 1400 to 1850 can be explained by internal variability alone. There is *medium confidence* that external forcing contributed to Northern Hemispheric temperature variability from 850 to 1400 and that external forcing contributed to European temperature variations over the last 5 centuries. {5.3.5, 5.5.1, 10.7.2, 10.7.5; Table 10.1} *(continued on next page)*

Box TS.5 (continued)

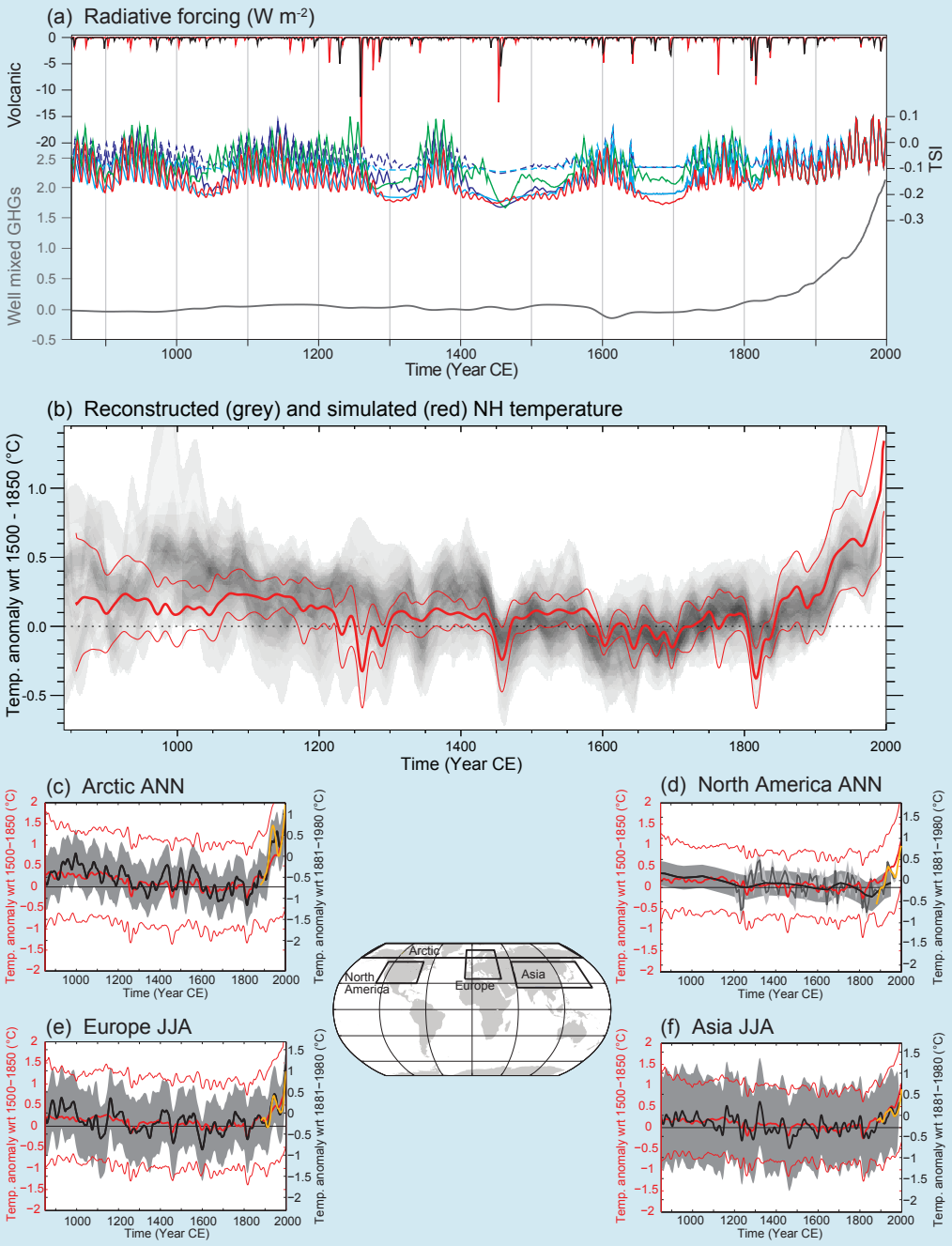

Box TS.5, Figure 1 | Last-millennium simulations and reconstructions. (a) 850–2000 PMIP3/CMIP5 radiative forcing due to volcanic, solar and well-mixed greenhouse gases. Different colours illustrate the two existing data sets for volcanic forcing and four estimates of solar forcing. For solar forcing, solid (dashed) lines stand for reconstruction variants in which background changes in irradiance are (not) considered; (b) 850–2000 PMIP3/CMIP5 simulated (red) and reconstructed (shading) Northern Hemisphere (NH) temperature changes. The thick red line depicts the multi-model mean while the thin red lines show the multi-model 90% range. The overlap of reconstructed temperatures is shown by grey shading; all data are expressed as anomalies from their 1500–1850 mean and smoothed with a 30-year filter. Note that some reconstructions represent a smaller spatial domain than the full NH or a specific season, while annual temperatures for the full NH mean are shown for the simulations. (c), (d), (e) and (f) Arctic and North America annual mean temperature, and Europe and Asia June, July and August (JJA) temperature, from 950 to 2000 from reconstructions (black line), and PMIP3/CMIP5 simulations (thick red, multi-model mean; thin red, 90% multi-model range). All red curves are expressed as anomalies from their 1500–1850 mean and smoothed with a 30-year filter. The shaded envelope depicts the uncertainties from each reconstruction (Arctic: 90% confidence bands, North American: ±2 standard deviation. Asia: ±2 root mean square error. Europe: 95% confidence bands). For comparison with instrumental record, the Climatic Research Unit land station Temperature (CRUTEM4) data set is shown (yellow line). These instrumental data are not necessarily those used in calibration of the reconstrctions, and thus may show greater or lesser correspondence with the reconstructions than the instrumental data actually used for calibration; cutoff timing may also lead to end effects for smoothed data shown. All lines are smoothed by applying a 30-year moving average. Map shows the individual regions for each reconstruction. {5.3.5; Table 5.A.1; Figures 5.1, 5.8, 5.12}

TS.5 Projections of Global and Regional Climate Change

TS.5.1 Introduction

Projections of changes in the climate system are made using a hierarchy of climate models ranging from simple climate models, to models of intermediate complexity, to comprehensive climate models, and Earth System Models (ESMs). These models simulate changes based on a set of scenarios of anthropogenic forcings. A new set of scenarios, the Representative Concentration Pathways (RCPs), was used for the new climate model simulations carried out under the framework of the Coupled Model Intercomparison Project Phase 5 (CMIP5) of the World Climate Research Programme. A large number of comprehensive climate models and ESMs have participated in CMIP5, whose results form the core of the climate system projections.

This section summarizes the assessment of these climate change projections. First, future forcing and scenarios are presented. The following subsections then address various aspects of projections of global and regional climate change, including near-term (up to about mid-century) and long-term (end of the 21st century) projections in the atmosphere, ocean and cryosphere; projections of carbon and other biogeochemical cycles; projections in sea level change; and finally changes to climate phenomena and other aspects of regional climate over the 21st century. Projected changes are given relative to the 1986–2005 average unless indicated otherwise. Projections of climate change on longer term and information on climate stabilization and targets are provided in TFE.8. Methods to counter climate change, termed geoengineering, have been proposed and an overview is provided in Box TS.7. {11.3, 12.3–12.5, 13.5–13.7, 14.1–14.6, Annex I}

TS.5.2 Future Forcing and Scenarios

In this assessment report a series of new RCPs are used that largely replace the IPCC Special Report on Emission Scenarios (SRES) scenarios (see Box TS.6 and Annex II for Climate System Scenario Tables). They produce a range of responses from ongoing warming, to approximately stabilized forcing, to a stringent mitigation scenario (RCP2.6) that stabilizes and then slowly reduces the RF after mid-21st century. In contrast to the AR4, the climate change from the RCP scenarios in the AR5 is framed as a combination of adaptation and mitigation. Mitigation actions starting now in the various RCP scenarios do not produce discernibly different climate change outcomes for the next 30 years or so, whereas long-term climate change after mid-century is appreciably different across the RCPs. {Box 1.1}

Box TS.6 | The New Representative Concentration Pathway Scenarios and Coupled Model Intercomparison Project Phase 5 Models

Future anthropogenic emissions of GHGs, aerosol particles and other forcing agents such as land use change are dependent on socioeconomic factors, and may be affected by global geopolitical agreements to control those emissions to achieve mitigation. AR4 made extensive use of the SRES scenarios that do not include additional climate initiatives, which means that no scenarios were available that explicitly assume implementation of the United Nations Framework Convention on Climate Change (UNFCCC) or the emissions targets of the Kyoto Protocol. However, GHG emissions are directly affected by non-climate change policies designed for a wide range of other purposes. The SRES scenarios were developed using a sequential approach, that is, socioeconomic factors fed into emissions scenarios, which were then used in simple climate models to determine concentrations of GHGs, and other agents required to drive the more complex AOGCMs. In this report, outcomes of climate simulations that use new scenarios (some of which include implied policy actions to achieve mitigation) referred to as RCPs are assessed. These RCPs represent a larger set of mitigation scenarios and were selected to have different targets in terms of radiative forcing at 2100 (about 2.6, 4.5, 6.0 and 8.5 W m^{-2}; Figure TS.15). The scenarios should be considered plausible and illustrative, and do not have probabilities attached to them. {12.3.1; Box 1.1}

The RCPs were developed using Integrated Assessment Models (IAMs) that typically include economic, demographic, energy, and simple climate components. The emission scenarios they produce are then run through a simple model to produce time series of GHG concentrations that can be run in AOGCMs. The emission time series from the RCPs can then be used directly in ESMs that include interactive biogeochemistry (at least a land and ocean carbon cycle). {12.3.1; Box 1.1}

The CMIP5 multi-model experiment (coordinated through the World Climate Research Programme) presents an unprecedented level of information on which to base assessments of climate variability and change. CMIP5 includes new ESMs in addition to AOGCMs, new model experiments and more diagnostic output. CMIP5 is much more comprehensive than the preceding CMIP3 multi-model experiment that was available at the time of the IPCC AR4. CMIP5 has more than twice as many models, many more experiments (that also include experiments to address understanding of the responses in the future climate change scenario runs), and nearly 2×10^{15} bytes of data (as compared to over 30×10^{12} bytes of data in CMIP3). A larger number of forcing agents are treated more completely in the CMIP5 models, with respect to aerosols and land use particularly. Black carbon aerosol is now a commonly included forcing agent. Considering CO_2, both 'concentrations-driven' projections and 'emissions-driven' projections are assessed from CMIP5. These allow quantification of the physical response uncertainties as well as climate–carbon cycle interactions. {1.5.2}

(continued on next page)

Box TS.6 (continued)

The assessment of the mean values and ranges of global mean temperature changes in AR4 would not have been substantially different if the CMIP5 models had been used in that report. The differences in global temperature projections can largely be attributed to the different scenarios. The global mean temperature response simulated by CMIP3 and CMIP5 models is very similar, both in the mean and the model range, transiently and in equilibrium. The range of temperature change across all scenarios is wider because the RCPs include a strong mitigation scenario (RCP2.6) that had no equivalent among the SRES scenarios used in CMIP3. For each scenario, the 5 to 95% range of the CMIP5 projections is obtained by approximating the CMIP5 distributions by a normal distribution with same mean and standard deviation and assessed as being *likely* for projections of global temperature change for the end of the 21st century. Probabilistic projections with simpler models calibrated to span the range of equilibrium climate sensitivity assessed by the AR4 provide uncertainty ranges that are consistent with those from CMIP5. In AR4 the uncertainties in global temperature projections were found to be approximately constant when expressed as a fraction of the model mean warming (constant fractional uncertainty). For the higher RCPs, the uncertainty is now estimated to be smaller than with the AR4 method for long-term climate change, because the carbon cycle–climate feedbacks are not relevant for the concentration-driven RCP projections (in contrast, the assessed projection uncertainties of global temperature in AR4 did account of carbon cycle–climate feedbacks, even though these were not part of the CMIP3 models). When forced with RCP8.5, CO_2 emissions, as opposed to the RCP8.5 CO_2 concentrations, CMIP5 ESMs with interactive carbon cycle simulate, on average, a 50 (–140 to +210) ppm (CMIP5 model spread) larger atmospheric CO_2 concentration and 0.2°C larger global surface temperature increase by 2100. For the low RCPs the fractional uncertainty is larger because internal variability and non-CO_2 forcings make a larger relative contribution to the total uncertainty. {12.4.1, 12.4.8, 12.4.9} *(continued on next page)*

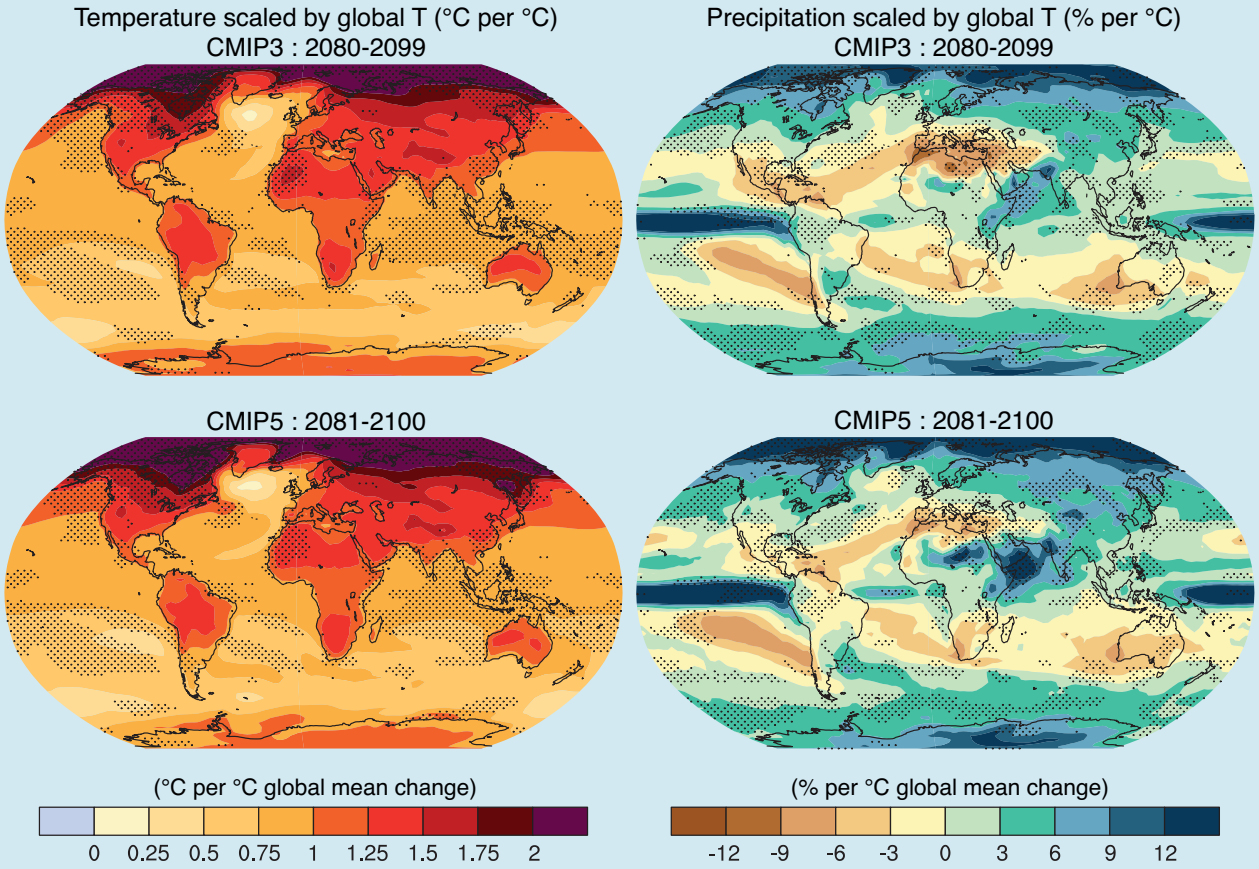

Box TS.6, Figure 1 | Patterns of temperature (left column) and percent precipitation change (right column) for the CMIP3 models average (first row) and CMIP5 models average (second row), scaled by the corresponding global average temperature changes. The patterns are computed in both cases by taking the difference between the averages over the last 20 years of the 21st century experiments (2080–2099 for CMIP3 and 2081–2100 for CMIP5) and the last 20 years of the historic experiments (1980–1999 for CMIP3, 1986–2005 for CMIP5) and rescaling each difference by the corresponding change in global average temperature. This is done first for each individual model, then the results are averaged across models. Stippling indicates a measure of significance of the difference between the two corresponding patterns obtained by a bootstrap exercise. Two subsets of the pooled set of CMIP3 and CMIP5 ensemble members of the same size as the original ensembles, but without distinguishing CMIP3 from CMIP5 members, were randomly sampled 500 times. For each random sample the corresponding patterns and their difference are computed, then the true difference is compared, grid-point by grid-point, to the distribution of the bootstrapped differences, and only grid-points at which the value of the difference falls in the tails of the bootstrapped distribution (less than the 2.5th percentiles or the 97.5th percentiles) are stippled. {Figure 12.41}

Box TS.6 (continued)

There is overall consistency between the projections of temperature and precipitation based on CMIP3 and CMIP5, both for large-scale patterns and magnitudes of change (Box TS.6, Figure 1). Model agreement and confidence in projections depends on the variable and on spatial and temporal averaging, with better agreement for larger scales. Confidence is higher for temperature than for those quantities related to the water cycle or atmospheric circulation. Improved methods to quantify and display model robustness have been developed to indicate where lack of agreement across models on local trends is a result of internal variability, rather than models actually disagreeing on their forced response. Understanding of the sources and means of characterizing uncertainties in long-term large scale projections of climate change has not changed significantly since AR4, but new experiments and studies have continued to work towards a more complete and rigorous characterization. {9.7.3, 12.2, 12.4.1, 12.4.4, 12.4.5, 12.4.9; Box 12.1}

The well-established stability of geographical patterns of temperature and precipitation change during a transient experiment remains valid in the CMIP5 models (Box TS.6, Figure 1). Patterns are similar over time and across scenarios and to first order can be scaled by the global mean temperature change. There remain limitations to the validity of this technique when it is applied to strong mitigation scenarios, to scenarios where localized forcings (e.g., aerosols) are significant and vary in time and for variables other than average seasonal mean temperature and precipitation. {12.4.2}

The range in anthropogenic aerosol emissions across all scenarios has a larger impact on near-term climate projections than the corresponding range in long-lived GHGs, particularly on regional scales and for hydrological cycle variables. The RCP scenarios do not span the range of future aerosol emissions found in the SRES and alternative scenarios (Box TS.6). {11.3.1, 11.3.6}

If rapid reductions in sulphate aerosol are undertaken for improving air quality or as part of decreasing fossil-fuel CO_2 emissions, then there is *medium confidence* that this could lead to rapid near-term warming. There is evidence that accompanying controls on CH_4 emissions would offset some of this sulphate-induced warming, although the cooling from CH_4 mitigation will emerge more slowly than the warming from sulphate mitigation due to the different time scales over which atmospheric concentrations of these substances decrease in response to decreases in emissions. Although removal of black carbon aerosol could also counter warming associated with sulphate removal, uncertainties are too large to constrain the net sign of the global temperature response to black carbon emission reductions, which depends on reduction of co-emitted (reflective) aerosols and on aerosol indirect effects. {11.3.6}

Including uncertainties in projecting the chemically reactive GHGs CH_4 and N_2O from RCP emissions gives a range in abundance pathways that is *likely* 30% larger than the range in RCP concentrations used to force the CMIP5 climate models. Including uncertainties in emission estimates from agricultural, forest and land use sources, in atmospheric lifetimes, and in chemical feedbacks, results in a much wider range of abundances for N_2O, CH_4 and HFCs and their RF. In the case of CH_4, by year 2100 the *likely* range of RCP8.5 CH_4 abundance extends 520 ppb above the single-valued RCP8.5 CH_4 abundance, and RCP2.6 CH_4 extends 230 ppb below RCP2.6 CH_4. {11.3.5}

There is *very low confidence* in projections of natural forcing. Major volcanic eruptions cause a negative RF up to several watts per square metre, with a typical lifetime of one year, but the possible occurrence and timing of future eruptions is unknown. Except for the 11-year solar cycle, changes in the total solar irradiance are uncertain. Except where explicitly indicated, future volcanic eruptions and changes in total solar irradiance additional to a repeating 11-year solar cycle are not included in the projections of near- and long-term climate assessed. {8, 11.3.6}

TS.5.3 Quantification of Climate System Response

Estimates of the equilibrium climate sensitivity (ECS) based on observed climate change, climate models and feedback analysis, as well as paleoclimate evidence indicate that ECS is positive, *likely* in the range 1.5°C to 4.5°C with *high confidence*, *extremely unlikely* less than 1°C (*high confidence*) and *very unlikely* greater than 6°C (*medium confidence*). Earth system sensitivity over millennia time scales including long-term feedbacks not typically included in models could be significantly higher than ECS (see TFE.6 for further details). {5.3.1, 10.8; Box 12.2}

With *high confidence* the transient climate response (TCR) is positive, *likely* in the range 1°C to 2.5°C and *extremely unlikely* greater than 3°C, based on observed climate change and climate models (see TFE.6 for further details). {10.8; Box 12.2}

The ratio of GMST change to total cumulative anthropogenic carbon emissions is relatively constant and independent of the scenario, but is model dependent, as it is a function of the model cumulative airborne fraction of carbon and the transient climate response. For any given temperature target, higher emissions in earlier decades therefore imply lower emissions by about the same amount later on. The transient climate response to cumulative carbon emission (TCRE) is *likely* between 0.8°C to 2.5°C per 1000 PgC (*high confidence*), for cumulative carbon emissions less than about 2000 PgC until the time at which temperatures peak (see TFE.8 for further details). {10.8, 12.5.4; Box 12.2}

Thematic Focus Elements

TFE.6 | Climate Sensitivity and Feedbacks

The description of climate change as a response to a forcing that is amplified by feedbacks goes back many decades. The concepts of radiative forcing (RF) and climate feedbacks continue to be refined, and limitations are now better understood; for instance, feedbacks may be much faster than the surface warming, feedbacks depend on the type of forcing agent (e.g., greenhouse gas (GHG) vs. solar forcing), or may have intrinsic time scales (associated mainly with vegetation change and ice sheets) of several centuries to millennia. The analysis of physical feedbacks in models and from observations remains a powerful framework that provides constraints on transient future warming for different scenarios, on climate sensitivity and, combined with estimates of carbon cycle feedbacks (see TFE.5), determines the GHG emissions that are compatible with climate stabilization or targets (see TFE.8). {7.1, 9.7.2, 12.5.3; Box 12.2}

The water vapour/lapse rate, albedo and cloud feedbacks are the principal determinants of equilibrium climate sensitivity. All of these feedbacks are assessed to be positive, but with different levels of likelihood assigned ranging from *likely* to *extremely likely*. Therefore, there is *high confidence* that the net feedback is positive and the black body response of the climate to a forcing will therefore be amplified. Cloud feedbacks continue to be the largest uncertainty. The net feedback from water vapour and lapse rate changes together is *extremely likely* positive and approximately doubles the black body response. The mean value and spread of these two processes in climate models are essentially unchanged from the IPCC Fourth Assessment Report (AR4), but are now supported by stronger observational evidence and better process understanding of what determines relative humidity distributions. Clouds respond to climate forcing mechanisms in multiple ways and individual cloud feedbacks can be positive or negative. Key issues include the representation of both deep and shallow cumulus convection, microphysical processes in ice clouds and partial cloudiness that results from small-scale variations of cloud-producing and cloud-dissipating processes. New approaches to diagnosing cloud feedback in General Circulation Models (GCMs) have clarified robust cloud responses, while continuing to implicate low cloud cover as the most important source of intermodel spread in simulated cloud feedbacks. The net radiative feedback due to all cloud types is *likely* positive. This conclusion is reached by considering a plausible range for unknown contributions by processes yet to be accounted for, in addition to those occurring in current climate models. Observations alone do not currently provide a robust, direct constraint, but multiple lines of evidence now indicate positive feedback contributions from changes in both the height of high clouds and the horizontal distribution of clouds. The additional feedback from low cloud amount is also positive in most climate models, but that result is not well understood, nor effectively constrained by observations, so *confidence* in it is *low*. {7.2.4–7.2.6, 9.7.2}

The representation of aerosol–cloud processes in climate models continues to be a challenge. Aerosol and cloud variability at scales significantly smaller than those resolved in climate models, and the subtle responses of clouds to aerosol at those scales, mean that, for the foreseeable future, climate models will continue to rely on parameterizations of aerosol–cloud interactions or other methods that represent subgrid variability. This implies large uncertainties for estimates of the forcings associated with aerosol–cloud interactions. {7.4, 7.5.3, 7.5.4}

Equilibrium climate sensitivity (ECS) and transient climate response (TCR) are useful metrics summarising the global climate system's temperature response to an externally imposed RF. ECS is defined as the equilibrium change in annual mean global mean surface temperature (GMST) following a doubling of the atmospheric carbon dioxide (CO_2) concentration, while TCR is defined as the annual mean GMST change at the time of CO_2 doubling following a linear increase in CO_2 forcing over a period of 70 years (see Glossary). Both metrics have a broader application than these definitions imply: ECS determines the eventual warming in response to stabilisation of atmospheric composition on multi-century time scales, while TCR determines the warming expected at a given time following any steady increase in forcing over a 50- to 100-year time scale. {Box 12.2; 12.5.3}

ECS and TCR can be estimated from various lines of evidence (TFE.6, Figures 1 and 2). The estimates can be based on the values of ECS and TCR diagnosed from climate models, or they can be constrained by analysis of feedbacks in climate models, patterns of mean climate and variability in models compared to observations, temperature fluctuations as reconstructed from paleoclimate archives, observed and modelled short term perturbations of the energy balance like those caused by volcanic eruptions, and the observed surface and ocean temperature trends since pre-industrial. For many applications, the limitations of the forcing-feedback analysis framework and the dependence of feedbacks on time scales and the climate state must be kept in mind. {5.3.1, 5.3.3, 9.7.1–9.7.3, 10.8.1, 10.8.2, 12.5.3; Box 5.2; Table 9.5} *(continued on next page)*

TFE.6 (continued)

Newer studies of constraints on ECS are based on the observed warming since pre-industrial, analysed using simple and intermediate complexity models, improved statistical methods and several different and newer data sets. Together with paleoclimate constraints but without considering the CMIP based evidence these studies show ECS is *likely* between 1.5°C to 4.5°C (*medium confidence*) and *extremely unlikely* less than 1.0°C. {5.3.1, 5.3.3, 10.8.2; Boxes 5.2, 12.2}

Estimates based on Atmosphere–Ocean General Circulation Models (AOGCMs) and feedback analysis indicate a range of 2°C to 4.5°C, with the Coupled Model Intercomparison Project Phase 5 (CMIP5) model mean at 3.2°C, similar to CMIP3. High climate sensitivities are found in some perturbed parameter ensembles models, but recent comparisons of perturbed-physics ensembles against the observed climate find that models with ECS values in the range 3°C to 4°C show the smallest errors for many fields. Relationships between climatological quantities and climate sensitivity are often found within a specific perturbed parameter ensemble model but in many cases the relationship is not robust across perturbed parameter ensembles models from different models or in CMIP3 and CMIP5. The assessed literature suggests that the range of climate sensitivities and transient responses covered by CMIP3 and CMIP5 cannot be narrowed significantly by constraining the models with observations of the mean climate and variability. Studies based on perturbed parameter ensembles models and CMIP3 support the conclusion that a credible representation of the mean climate and variability is very difficult to achieve with ECSs below 2°C. {9.2.2, 9.7.3; Box 12.2}

New estimates of ECS based on reconstructions and simulations of the Last Glacial Maximum (21 ka to 19 ka) show that values below 1°C as well as above 6°C are *very unlikely*. In some models climate sensitivity differs between warm and cold climates because of differences in the representation of cloud feedbacks. Estimates of an Earth system sensitivity including slow feedbacks (e.g., ice sheets or vegetation) are even more difficult to relate to climate sensitivity of the current climate state. The main limitations of ECS estimates from paleoclimate states are uncertainties in proxy data, spatial coverage of the data, uncertainties in some forcings, and structural limitations in models used in model–data comparisons. {5.3, 10.8.2, 12.5.3}

Bayesian methods to constrain ECS or TCR are sensitive to the assumed prior distributions. They can in principle yield narrower estimates by combining constraints from the observed warming trend, volcanic eruptions, model climatology and paleoclimate, and that has been done in some studies, but there is no consensus on how this should be done robustly. This approach is sensitive to the assumptions regarding the independence of the various lines of evidence, the possibility of shared biases in models or feedback estimates and the assumption that each individual line of evidence is unbiased. The combination of different estimates in this assessment is based on expert judgement. {10.8.2; Box 12.2}

Based on the combined evidence from observed climate change including the observed 20th century warming, climate models, feedback analysis and paleoclimate, as discussed above, ECS is *likely* in the range 1.5°C to 4.5°C with *high confidence*. ECS is positive, *extremely unlikely*

(continued on next page)

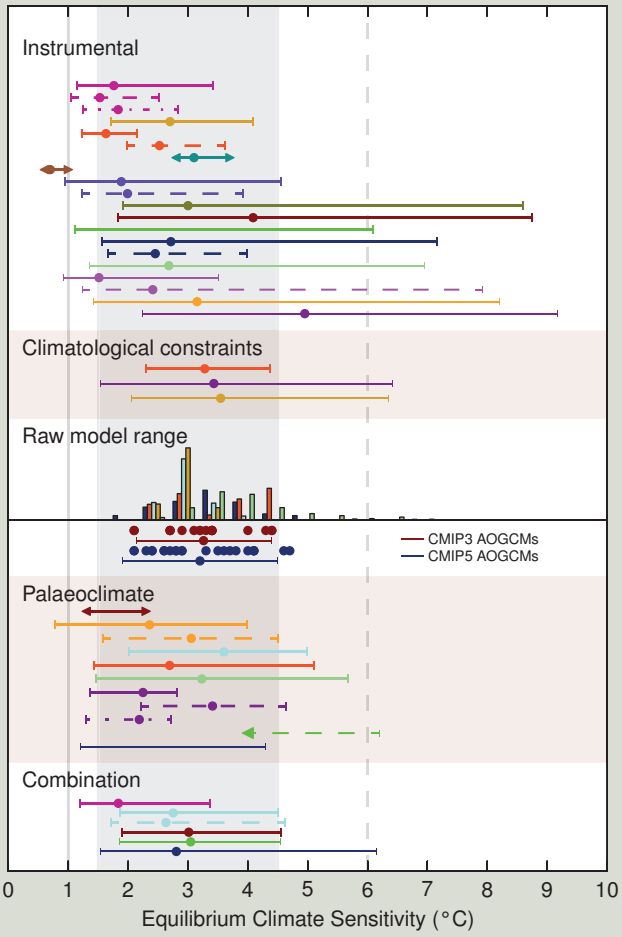

TFE.6, Figure 1 | Probability density functions, distributions and ranges for equilibrium climate sensitivity, based on Figure 10.20b plus climatological constraints shown in IPCC AR4 (Box AR4 10.2 Figure 1), and results from CMIP5 (Table 9.5). The grey shaded range marks the *likely* 1.5°C to 4.5°C range, grey solid line the *extremely unlikely* less than 1°C, the grey dashed line the *very unlikely* greater than 6°C. See Figure 10.20b and Chapter 10 Supplementary Material for full caption and details. {Box 12.2, Figure 1}

TFE.6 (continued)

less than 1°C (*high confidence*), and *very unlikely* greater than 6°C (*medium confidence*). The tails of the ECS distribution are now better understood. Multiple lines of evidence provide *high confidence* that an ECS value less than 1°C is *extremely unlikely*. The upper limit of the *likely* range is unchanged compared to AR4. The lower limit of the *likely* range of 1.5°C is less than the lower limit of 2°C in AR4. This change reflects the evidence from new studies of observed temperature change, using the extended records in atmosphere and ocean. These studies suggest a best fit to the observed surface and ocean warming for ECS values in the lower part of the *likely* range. Note that these studies are not purely observational, because they require an estimate of the response to RF from models. In addition, the uncertainty in ocean heat uptake remains substantial. Accounting for short-term variability in simple models remains challenging, and it is important not to give undue weight to any short time period which might be strongly affected by internal variability. On the other hand, AOGCMs with observed climatology with ECS values in the upper part of the 1.5 to 4.5°C range show very good agreement with observed climatology, but the simulation of key feedbacks like clouds remains challenging in those models. The estimates from the observed warming, paleoclimate, and from climate models are consistent within their uncertainties, each is supported by many studies and multiple data sets, and in combination they provide *high confidence* for the assessed *likely* range. Even though this assessed range is similar to previous reports, confidence today is much higher as a result of high quality and longer observational records with a clearer anthropogenic signal, better process understanding, more and better understood evidence from paleoclimate reconstructions, and better climate models with higher resolution that capture many more processes more realistically. All these lines of evidence individually support the assessed *likely* range of 1.5°C to 4.5°C. {3.2, 9.7.3, 10.8; Boxes 9.2, 13.1}

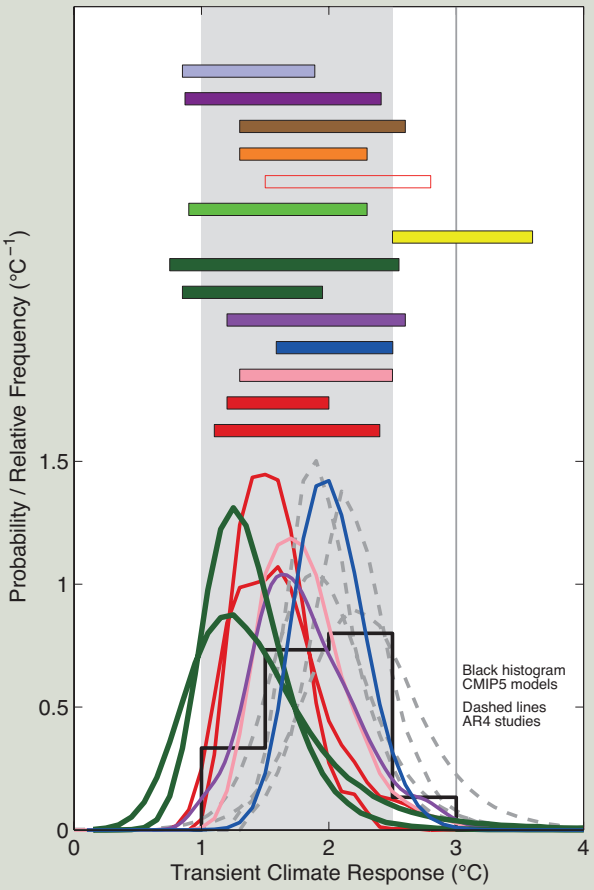

TFE.6, Figure 2 | Probability density functions, distributions and ranges (5 to 95%) for the transient climate response from different studies, based on Figure 10.20a, and results from CMIP5 (black histogram, Table 9.5). The grey shaded range marks the *likely* 1°C to 2.5°C range, the grey solid line marks the *extremely unlikely* greater than 3°C. See Figure 10.20a and Chapter 10 Supplementary Material for full caption and details. {Box 12.2, Figure 2}

On time scales of many centuries and longer, additional feedbacks with their own intrinsic time scales (e.g., vegetation, ice sheets) may become important but are not usually modelled in AOGCMs. The resulting equilibrium temperature response to a doubling of CO_2 on millennial time scales or Earth system sensitivity is less well constrained but *likely* to be larger than ECS, implying that lower atmospheric CO_2 concentrations are compatible with limiting warming to below a given temperature level. These slow feedbacks are less likely to be proportional to global mean temperature change, implying that Earth system sensitivity changes over time. Estimates of Earth system sensitivity are also difficult to relate to climate sensitivity of the current climate state. {5.3.3, 10.8.2, 12.5.3}

For scenarios of increasing RF, TCR is a more informative indicator of future climate change than ECS. This assessment concludes with *high confidence* that the TCR is *likely* in the range 1°C to 2.5°C, close to the estimated 5 to 95% range of CMIP5 (1.2°C to 2.4°C), is positive and *extremely unlikely* greater than 3°C. As with the ECS, this is an expert-assessed range, supported by several different and partly independent lines of evidence, each based on multiple studies, models and data sets. TCR is estimated from the observed global changes in surface temperature, ocean heat uptake and RF including detection/attribution studies identifying the response patterns to increasing GHG concentrations, and the results of CMIP3 and CMIP5. Estimating TCR suffers from fewer difficulties in terms of state- or time-dependent feedbacks, and is less affected by uncertainty as to how much energy is taken up by the

(continued on next page)

TFE.6 (continued)

ocean. Unlike ECS, the ranges of TCR estimated from the observed warming and from AOGCMs agree well, increasing our confidence in the assessment of uncertainties in projections over the 21st century.

The assessed ranges of ECS and TCR are largely consistent with the observed warming, the estimated forcing and the projected future warming. In contrast to AR4, no best estimate for ECS is given because of a lack of agreement on the best estimate across lines of evidence and studies and an improved understanding of the uncertainties in estimates based on the observed warming. Climate models with ECS values in the upper part of the *likely* range show very good agreement with observed climatology, whereas estimates derived from observed climate change tend to best fit the observed surface and ocean warming for ECS values in the lower part of the *likely* range. In estimates based on the observed warming the most likely value is sensitive to observational and model uncertainties, internal climate variability and to assumptions about the prior distribution of ECS. In addition, "best estimate" and "most likely value" are defined in various ways in different studies. {9.7.1, 10.8.1, 12.5.3; Table 9.5}

TS.5.4 Near-term Climate Change

Near-term decadal climate prediction provides information not available from existing seasonal to interannual (months to a year or two) predictions or from long-term (mid 21st century and beyond) climate change projections. Prediction efforts on seasonal to interannual time scales require accurate estimates of the initial climate state with less focus extended to changes in external forcing[12], whereas long-term climate projections rely more heavily on estimations of external forcing with little reliance on the initial state of internal variability. Estimates of near-term climate depend on the committed warming (caused by the inertia of the oceans as they respond to historical external forcing) the time evolution of internally generated climate variability, and the future path of external forcing. Near-term predictions out to about a decade (Figure TS.13) depend more heavily on an accurate depiction of the internally generated climate variability. {11.1, 12, 14}

Further near-term warming from past emissions is unavoidable owing to thermal inertia of the oceans. This warming will be increased by ongoing emissions of GHGs over the near term, and the climate observed in the near term will also be strongly influenced by the internally generated variability of the climate system. Previous IPCC Assessments only described climate-change projections wherein the externally forced component of future climate was included but no attempt was made to initialize the internally generated climate variability. Decadal climate predictions, on the other hand, are intended to predict both the externally forced component of future climate change, and the internally generated component. Near-term predictions do not provide detailed information of the evolution of weather. Instead they can provide estimated changes in the time evolution of the statistics of near-term climate. {11.1, 11.2.2; Box 11.1; FAQ 11.1}

Retrospective prediction experiments have been used to assess forecast quality. There is *high confidence* that the retrospective prediction experiments for forecast periods of up to 10 years exhibit positive skill when verified against observations over large regions of the planet and of the global mean. Observation-based initialization of the forecasts contributes to the skill of predictions of annual mean temperature for the first couple of years and to the skill of predictions of the GMST and the temperature over the North Atlantic, regions of the South Pacific and the tropical Indian Ocean up to 10 years (*high confidence*) partly due to a correction of the forced response. Probabilistic temperature predictions are statistically reliable (see Section 11.2.3 for definition of reliability) owing to the correct representation of global trends, but still unreliable at the regional scale when probabilities are computed from the multi-model ensemble. Predictions initialized over 2000–2005 improve estimates of the recent global mean temperature hiatus. Predictions of precipitation over continental areas with large forced trends also exhibit positive skill. {11.2.2, 11.2.3; Box 9.2}

TS.5.4.1 Projected Near-term Changes in Climate

Projections of near-term climate show small sensitivity to GHG scenarios compared to model spread, but substantial sensitivity to uncertainties in aerosol emissions, especially on regional scales and for hydrological cycle variables. In some regions, the local and regional responses in precipitation and in mean and extreme temperature to land use change will be larger than those due to large-scale GHGs and aerosol forcing. These scenarios presume that there are no major volcanic eruptions and that anthropogenic aerosol emissions are rapidly reduced during the near term. {11.3.1, 11.3.2, 11.3.6}

TS.5.4.2 Projected Near-term Changes in Temperature

In the absence of major volcanic eruptions—which would cause significant but temporary cooling—and, assuming no significant future long-term changes in solar irradiance, it is *likely* that the GMST anomaly for the period 2016–2035, relative to the reference period of 1986–2005 will be in the range 0.3°C to 0.7°C (*medium confidence*). This is based on multiple lines of evidence. This range is consistent

[12] Seasonal-to-interannual predictions typically include the impact of external forcing.

with the range obtained by using CMIP5 5 to 95% model trends for 2012–2035. It is also consistent with the CMIP5 5 to 95% range for all four RCP scenarios of 0.36°C to 0.79°C, using the 2006–2012 reference period, after the upper and lower bounds are reduced by 10% to take into account the evidence that some models may be too sensitive to anthropogenic forcing (see Table TS.1 and Figure TS.14). {11.3.6}

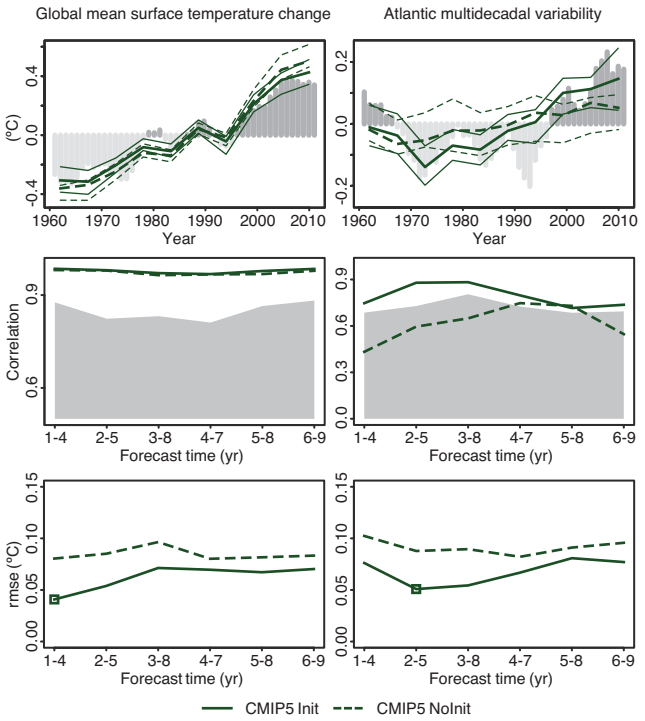

Figure TS.13 | Decadal prediction forecast quality of several climate indices. (Top row) Time series of the 2- to 5-year average ensemble mean initialized hindcast anomalies and the corresponding non-initialized experiments for three climate indices: global mean surface temperature (GMST, left) and the Atlantic Multi-decadal Variability (AMV, right). The observational time series, Goddard Institute of Space Studies Goddard Institute for Space Studies Surface Temperature Analysis (GISTEMP) global mean temperature and Extended Reconstructed Sea Surface Tempearture (ERSST) for the AMV, are represented with dark grey (positive anomalies) and light grey (negative anomalies) vertical bars, where a 4-year running mean has been applied for consistency with the time averaging of the predictions. Predicted time series are shown for the CMIP5 Init (solid) and NoInit (dotted) simulations with hindcasts started every 5 years over the period 1960–2005. The lower and upper quartile of the multi-model ensemble are plotted using thin lines. The AMV index was computed as the sea surface temperature (SST) anomalies averaged over the region Equator to 60ºN and 80ºW to 0ºW minus the SST anomalies averaged over 60ºS to 60ºN. Note that the vertical axes are different for each time series. (Middle row) Correlation of the ensemble mean prediction with the observational reference along the forecast time for 4-year averages of the three sets of CMIP5 hindcasts for Init (solid) and NoInit (dashed). The one-sided 95% confidence level with a *t* distribution is represented in grey. The effective sample size has been computed taking into account the autocorrelation of the observational time series. A two-sided *t* test (where the effective sample size has been computed taking into account the autocorrelation of the observational time series) has been used to test the differences between the correlation of the initialized and non-initialized experiments, but no differences were found statistically significant with a confidence equal or higher than 90%. (Bottom row) Root mean square error (RMSE) of the ensemble mean prediction along the forecast time for 4-year averages of the CMIP5 hindcasts for Init (solid) and NoInit (dashed). A two-sided *F* test (where the effective sample size has been computed taking into account the autocorrelation of the observational time series) has been used to test the ratio between the RMSE of the Init and NoInit, and those forecast times with differences statistically significant with a confidence equal or higher than 90% are indicated with an open square. {Figure 11.3}

Higher concentrations of GHGs and lower amounts of sulphate aerosol lead to greater warming. In the near-term, differences in global mean surface air temperature across RCP scenarios for a single climate model are typically smaller than across climate models for a single RCP scenario. In 2030, the CMIP5 ensemble median values for global mean temperature differ by at most 0.2°C between the RCP scenarios, whereas the model spread (defined as the 17 to 83% range) for each RCP is around 0.4°C. The inter-scenario spread increases in time and by 2050 is comparable to the model spread. Regionally, the largest differences in surface air temperature between RCP scenarios are found in the Arctic. {11.3.2. 11.3.6}

The projected warming of global mean temperatures implies *high confidence* that new levels of warming relative to 1850-1900 mean climate will be crossed, particularly under higher GHG emissions scenarios. Relative to a reference period of 1850–1900, under RCP4.5 or RCP6.0, it is *more likely than not* that the mean GMST for the period 2016–2035 will be more than 1°C above the mean for 1850–1900, and *very unlikely* that it will be more than 1.5°C above the 1850–1900 mean (*medium confidence*). {11.3.6}

A future volcanic eruption similar in size to the 1991 eruption of Mt Pinatubo would cause a rapid drop in global mean surface air temperature of about 0.5°C in the following year, with recovery over the next few years. Larger eruptions, or several eruptions occurring close together in time, would lead to larger and more persistent effects. {11.3.6}

Possible future changes in solar irradiance could influence the rate at which GMST increases, but there is *high confidence* that this influence will be small in comparison to the influence of increasing concentrations of GHGs in the atmosphere. {11.3.6}

The spatial patterns of near-term warming projected by the CMIP5 models following the RCP scenarios (Figure TS.15) are broadly consistent with the AR4. It is *very likely* that anthropogenic warming of surface air temperature over the next few decades will proceed more rapidly over land areas than over oceans, and it is *very likely* that the anthropogenic warming over the Arctic in winter will be greater than the global mean warming, consistent with the AR4. Relative to background levels of internally generated variability there is *high confidence* that the anthropogenic warming relative to the reference period is expected to be larger in the tropics and subtropics than in mid-latitudes. {11.3.2}

It is *likely* that in the next decades the frequency of warm days and warm nights will increase in most land regions, while the frequency of cold days and cold nights will decrease. Models also project increases in the duration, intensity and spatial extent of heat waves and warm spells for the near term. These changes may proceed at a different rate than the mean warming. For example, several studies project that European high-percentile summer temperatures are projected to warm faster than mean temperatures (see also TFE.9). {11.3.2}

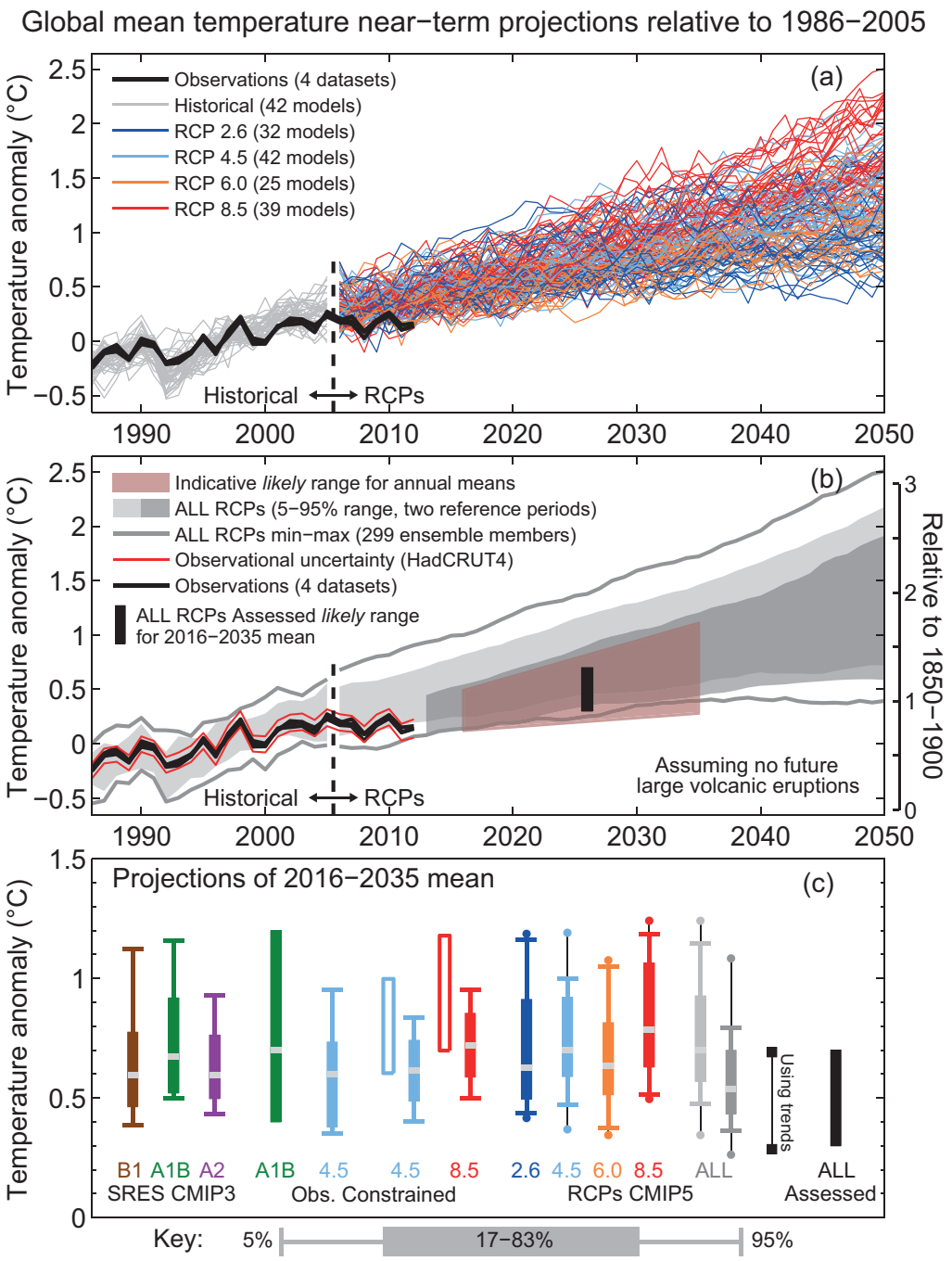

Figure TS.14 | Synthesis of near-term projections of global mean surface air temperature (GMST). (a) Projections of annual mean GMST 1986–2050 (anomalies relative to 1986–2005) under all RCPs from CMIP5 models (grey and coloured lines, one ensemble member per model), with four observational estimates (Hadley Centre/Climatic Research Unit gridded surface temperature data set 4 (HadCRUT4), European Centre for Medium Range Weather Forecasts (ECMWF) interim re-analysis of the global atmosphere and surface conditions (ERA-Interim), Goddard Institute for Space Studies Surface Temperature Analysis (GISTEMP), National Oceanic and Atmospheric Administration (NOAA)) for the period 1986–2012 (black lines). (b) As (a) but showing the 5 to 95% range of annual mean CMIP5 projections (using one ensemble member per model) for all RCPs using a reference period of 1986–2005 (light grey shade) and all RCPs using a reference period of 2006–2012, together with the observed anomaly for (2006–2012) minus (1986–2005) of 0.16°C (dark grey shade). The percentiles for 2006 onwards have been smoothed with a 5-year running mean for clarity. The maximum and minimum values from CMIP5 using all ensemble members and the 1986–2005 reference period are shown by the grey lines (also smoothed). Black lines show annual mean observational estimates. The red shaded region shows the indicative *likely* range for annual mean GMST during the period 2016–2035 based on the 'ALL RCPs Assessed' *likely* range for the 20-year mean GMST anomaly for 2016–2035, which is shown as a black bar in both (b) and (c) (see text for details). The temperature scale relative to 1850-1900 mean climate on the right-hand side assumes a warming of GMST prior to 1986–2005 of 0.61°C estimated from HadCRUT4. (c) A synthesis of projections for the mean GMST anomaly for 2016–2035 relative to 1986–2005. The box and whiskers represent the 66% and 90% ranges. Shown are: unconstrained SRES CMIP3 and RCP CMIP5 projections; observationally constrained projections for the SRES A1B and, the RCP4.5 and 8.5 scenarios; unconstrained projections for all four RCP scenarios using two reference periods as in (b) (light grey and dark grey shades), consistent with (b); 90% range estimated using CMIP5 trends for the period 2012–2035 and the observed GMST anomaly for 2012; an overall *likely* (>66%) assessed range for all RCP scenarios. The dots for the CMIP5 estimates show the maximum and minimum values using all ensemble members. The medians (or maximum likelihood estimate; green filled bar) are indicated by a grey band. (Adapted from Figure 11.25.) See Section 11.3.6 for details. {Figure 11.25}

TS.5.4.3 Projected Near-term Changes in the Water Cycle

Zonal mean precipitation will *very likely* increase in high and some of the mid latitudes, and will *more likely than not* decrease in the subtropics. At more regional scales precipitation changes may be dominated by a combination of natural internal variability, volcanic forcing and anthropogenic aerosol effects. {11.3.2}

Over the next few decades increases in near-surface specific humidity are *very likely*. It is *likely* that there will be increases in evaporation in many regions. There is *low confidence* in projected changes in soil moisture and surface runoff. {11.3.2}

In the near term, it is *likely* that the frequency and intensity of heavy precipitation events will increase over land. These changes are primarily driven by increases in atmospheric water vapour content, but also affected by changes in atmospheric circulation. The impact of anthropogenic forcing at regional scales is less obvious, as regional-scale changes are strongly affected by natural variability and also depend on the course of future aerosol emissions, volcanic forcing and land use changes (see also TFE.9). {11.3.2}

TS.5.4.4 Projected Near-term Changes in Atmospheric Circulation

Internally generated climate variability and multiple RF agents (e.g., volcanoes, GHGs, ozone and anthropogenic aerosols) will all contribute to near-term changes in the atmospheric circulation. For example, it is *likely* that the annual mean Hadley Circulation and the SH mid-latitude westerlies will shift poleward, while it is *likely* that the projected recovery of stratospheric ozone and increases in GHG concentrations will have counteracting impacts on the width of the Hadley Circulation and the meridional position of the SH storm track. Therefore it is *unlikely* that they will continue to expand poleward as rapidly as in recent decades. {11.3.2}

There is *low confidence* in near-term projections of the position and strength of NH storm tracks. Natural variations are larger than the projected impact of GHGs in the near term. {11.3.2}

There is *low confidence* in basin-scale projections of changes in intensity and frequency of tropical cyclones in all basins to the mid-21st century. This *low confidence* reflects the small number of studies exploring near-term tropical cyclone activity, the differences across published projections of tropical cyclone activity, and the large role for natural variability. There is *low confidence* in near-term projections for increased tropical cyclone intensity in the Atlantic; this projection is in part due to projected reductions in aerosol loading. {11.3.2}

TS.5.4.5 Projected Near-term Changes in the Ocean

It is *very likely* that globally averaged surface and vertically averaged ocean temperatures will increase in the near-term. In the absence of multiple major volcanic eruptions, it is *very likely* that globally averaged surface and depth-averaged temperatures averaged for 2016–2035 will be warmer than those averaged over 1986–2005. {11.3.3}

It is *likely* that salinity will increase in the tropical and (especially) subtropical Atlantic, and decrease in the western tropical Pacific over the next few decades. Overall, it is *likely* that there will be some decline in the Atlantic Meridional Overturning Circulation by 2050 (*medium confidence*). However, the rate and magnitude of weakening is very uncertain and decades when this circulation increases are also to be expected. {11.3.3}

TS.5.4.6 Projected Near-term Changes in the Cryosphere

A nearly ice-free Arctic Ocean (sea ice extent less than 10^6 km^2 for at least five consecutive years) in September is *likely* before mid-century under RCP8.5 (*medium confidence*). This assessment is based on a subset of models that most closely reproduce the climatological mean state and 1979 to 2012 trend of Arctic sea ice cover. It is *very likely* that there will be further shrinking and thinning of Arctic sea ice cover, and decreases of northern high-latitude spring time snow cover and near surface permafrost as GMST rises (Figures TS.17 and TS.18). There is *low confidence* in projected near-term decreases in the Antarctic sea ice extent and volume. {11.3.4}

TS.5.4.7 Possibility of Near-term Abrupt Changes in Climate

There are various mechanisms that could lead to changes in global or regional climate that are abrupt by comparison with rates experienced in recent decades. The likelihood of such changes is generally lower for the near term than for the long term. For this reason the relevant mechanisms are primarily assessed in the TS.5 sections on long-term changes and in TFE.5. {11.3.4}

TS.5.4.8 Projected Near-term Changes in Air Quality

The range in projections of air quality (O_3 and $PM_{2.5}$ in surface air) is driven primarily by emissions (including CH_4), rather than by physical climate change (*medium confidence*). The response of air quality to climate-driven changes is more uncertain than the response to emission-driven changes (*high confidence*). Globally, warming decreases background surface O_3 (*high confidence*). High CH_4 levels (such as RCP8.5 and SRES A2) can offset this decrease, raising 2100 background surface O_3 on average by about 8 ppb (25% of current levels) relative to scenarios with small CH_4 changes (such as RCP4.5 and RCP6.0) (*high confidence*). On a continental scale, projected air pollution levels are lower under the new RCP scenarios than under the SRES scenarios because the SRES did not incorporate air quality legislation (*high confidence*). {11.3.5, 11.3.5.2; Figures 11.22 and 11.23ab, AII.4.2, AII.7.1–AII.7.4}

Observational and modelling evidence indicates that, all else being equal, locally higher surface temperatures in polluted regions will trigger regional feedbacks in chemistry and local emissions that will increase peak levels of O_3 and $PM_{2.5}$ (*medium confidence*). Local emissions combined with background levels and with meteorological conditions conducive to the formation and accumulation of pollution are known to produce extreme pollution episodes on local and regional scales. There is *low confidence* in projecting changes in meteorological blocking associated with these extreme episodes. For $PM_{2.5}$, climate change may alter natural aerosol sources (wildfires, wind-lofted

dust, biogenic precursors) as well as precipitation scavenging, but no confidence level is attached to the overall impact of climate change on $PM_{2.5}$ distributions. {11.3.5, 11.3.5.2; Box 14.2}

TS.5.5 Long-term Climate Change

TS.5.5.1 Projected Long-term Changes in Global Temperature

Global mean temperatures will continue to rise over the 21st century under all of the RCPs. From around the mid-21st century, the rate of global warming begins to be more strongly dependent on the scenario (Figure TS.15). {12.4.1}

Under the assumptions of the concentration-driven RCPs, GMSTs for 2081–2100, relative to 1986–2005 will *likely* be in the 5 to 95% range of the CMIP5 models; 0.3°C to 1.7°C (RCP2.6), 1.1 to 2.6°C (RCP4.5), 1.4°C to 3.1°C (RCP6.0), 2.6°C to 4.8°C (RCP8.5) (see Table TS.1). With *high confidence*, the 5 to 95% range of CMIP5 is assessed as *likely* rather than *very likely* based on the assessment of TCR (see TFE.6). The 5 to 95% range of CMIP5 for global mean temperature change is also assessed as *likely* for mid-21st century, but only with *medium confidence*. With respect to 1850–1900 mean conditions, global temperatures averaged in the period 2081–2100 are projected to *likely* exceed 1.5°C above 1850–1900 values for RCP4.5, RCP6.0 and RCP8.5 (*high confidence*) and are *likely* to exceed 2°C above 1850–1900 values for RCP6.0 and RCP8.5 (*high confidence*). Temperature change above 2°C relative to 1850–1900 under RCP2.6 is *unlikely* (*medium confidence*). Warming above 4°C by 2081–2100 is *unlikely* in all RCPs (*high confidence*) except for RCP8.5, where it is *about as likely as not* (*medium confidence*). {12.4.1; Tables 12.2, 12.3}

TS.5.5.2 Projected Long-term Changes in Regional Temperature

There is *very high confidence* that globally averaged changes over land will exceed changes over the ocean at the end of the 21st century by a factor that is *likely* in the range 1.4 to 1.7. In the absence of a strong reduction in the Atlantic Meridional Overturning, the Arctic region is projected to warm most (*very high confidence*) (Figure TS.15). As

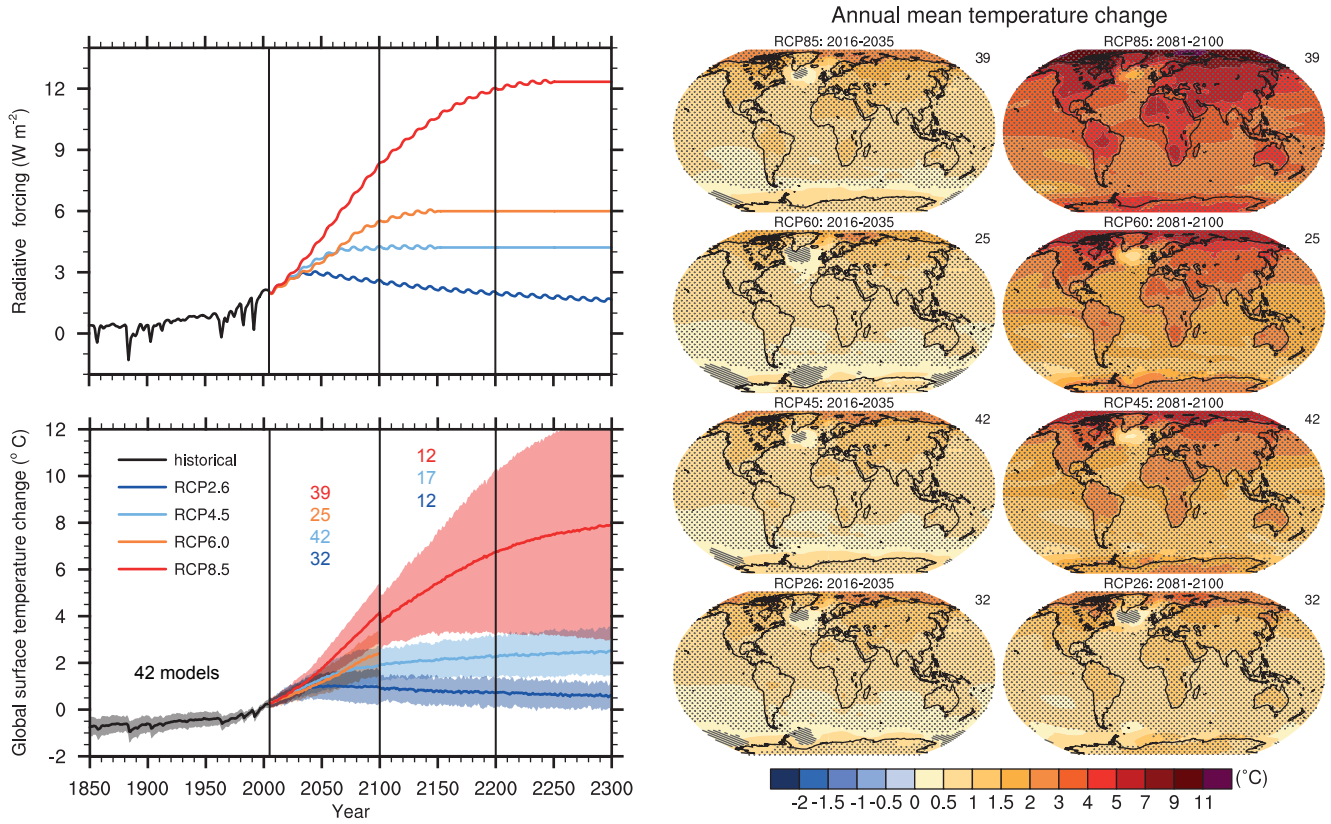

Figure TS.15 | (Top left) Total global mean radiative forcing for the four RCP scenarios based on the Model for the Assessment of Greenhouse-gas Induced Climate Change (MAGICC) energy balance model. Note that the actual forcing simulated by the CMIP5 models differs slightly between models. (Bottom left) Time series of global annual mean surface air temperature anomalies (relative to 1986–2005) from CMIP5 concentration-driven experiments. Projections are shown for each RCP for the multi-model mean (solid lines) and ±1.64 standard deviation (5 to 95%) across the distribution of individual models (shading), based on annual means. The 1.64 standard deviation range based on the 20 yr averages 2081–2100, relative to 1986–2005, are interpreted as *likely* changes for the end of the 21st century. Discontinuities at 2100 are due to different numbers of models performing the extension runs beyond the 21st century and have no physical meaning. Numbers in the same colours as the lines indicate the number of different models contributing to the different time periods. Maps: Multi-model ensemble average of annual mean surface air temperature change (compared to 1986–2005 base period) for 2016–2035 and 2081–2100, for RCP2.6, 4.5, 6.0 and 8.5. Hatching indicates regions where the multi-model mean signal is less than one standard deviation of internal variability. Stippling indicates regions where the multi-model mean signal is greater than two standard deviations of internal variability and where 90% of the models agree on the sign of change. The number of CMIP5 models used is indicated in the upper right corner of each panel. Further detail regarding the related Figures SPM.7a and SPM.8.a is given in the TS Supplementary Material. {Box 12.1; Figures 12.4, 12.5, 12.11; Annex I}

Table TS.1 | Projected change in global mean surface air temperature and global mean sea level rise for the mid- and late 21st century relative to the reference period of 1986–2005. {12.4.1; Tables 12.2,13.5}

		2046–2065		2081–2100	
	Scenario	**Mean**	***Likely* range[c]**	**Mean**	***Likely* range[c]**
Global Mean Surface Temperature Change (°C)[a]	RCP2.6	1.0	0.4 to 1.6	1.0	0.3 to 1.7
	RCP4.5	1.4	0.9 to 2.0	1.8	1.1 to 2.6
	RCP6.0	1.3	0.8 to 1.8	2.2	1.4 to 3.1
	RCP8.5	2.0	1.4 to 2.6	3.7	2.6 to 4.8
	Scenario	**Mean**	***Likely* range[d]**	**Mean**	***Likely* range[d]**
Global Mean Sea Level Rise (m)[b]	RCP2.6	0.24	0.17 to 0.32	0.40	0.26 to 0.55
	RCP4.5	0.26	0.19 to 0.33	0.47	0.32 to 0.63
	RCP6.0	0.25	0.18 to 0.32	0.48	0.33 to 0.63
	RCP8.5	0.30	0.22 to 0.38	0.63	0.45 to 0.82

Notes:

[a] Based on the CMIP5 ensemble; anomalies calculated with respect to 1986–2005. Using HadCRUT4 and its uncertainty estimate (5–95% confidence interval), the observed warming to the reference period 1986–2005 is 0.61 [0.55 to 0.67] °C from 1850–1900, and 0.11 [0.09 to 0.13] °C from 1980–1999, the reference period for projections used in AR4. *Likely* ranges have not been assessed here with respect to earlier reference periods because methods are not generally available in the literature for combining the uncertainties in models and observations. Adding projected and observed changes does not account for potential effects of model biases compared to observations, and for natural internal variability during the observational reference period. {2.4; 11.2; Tables 12.2 and 12.3}

[b] Based on 21 CMIP5 models; anomalies calculated with respect to 1986–2005. Where CMIP5 results were not available for a particular AOGCM and scenario, they were estimated as explained in Chapter 13, Table 13.5. The contributions from ice sheet rapid dynamical change and anthropogenic land water storage are treated as having uniform probability distributions, and as largely independent of scenario. This treatment does not imply that the contributions concerned will not depend on the scenario followed, only that the current state of knowledge does not permit a quantitative assessment of the dependence. Based on current understanding, only the collapse of marine-based sectors of the Antarctic ice sheet, if initiated, could cause global mean sea level to rise substantially above the *likely* range during the 21st century. There is *medium confidence* that this additional contribution would not exceed several tenths of a metre of sea level rise during the 21st century.

[c] Calculated from projections as 5–95% model ranges. These ranges are then assessed to be *likely* ranges after accounting for additional uncertainties or different levels of confidence in models. For projections of global mean surface temperature change in 2046–2065 *confidence* is *medium*, because the relative importance of natural internal variability, and uncertainty in non-greenhouse gas forcing and response, are larger than for 2081–2100. The *likely* ranges for 2046–2065 do not take into account the possible influence of factors that lead to the assessed range for near-term (2016–2035) global mean surface temperature change that is lower than the 5–95% model range, because the influence of these factors on longer term projections has not been quantified due to insufficient scientific understanding. {11.3}

[d] Calculated from projections as 5–95% model ranges. These ranges are then assessed to be *likely* ranges after accounting for additional uncertainties or different levels of confidence in models. For projections of global mean sea level rise *confidence* is *medium* for both time horizons.

GMST rises, the pattern of atmospheric zonal mean temperatures show warming throughout the troposphere and cooling in the stratosphere, consistent with previous assessments. The consistency is especially clear in the tropical upper troposphere and the northern high latitudes. {12.4.3; Box 5.1}

It is *virtually certain* that, in most places, there will be more hot and fewer cold temperature extremes as global mean temperatures increase. These changes are expected for events defined as extremes on both daily and seasonal time scales. Increases in the frequency, duration and magnitude of hot extremes along with heat stress are expected; however, occasional cold winter extremes will continue to occur. Twenty-year return values of low-temperature events are projected to increase at a rate greater than winter mean temperatures in most regions, with the largest changes in the return values of low temperatures at high latitudes. Twenty-year return values for high-temperature events are projected to increase at a rate similar to or greater than the rate of increase of summer mean temperatures in most regions. Under RCP8.5 it is *likely* that, in most land regions, a current 20-year high-temperature event will occur more frequently by the end of the 21st century (at least doubling its frequency, but in many regions becoming an annual or 2-year event) and a current 20-year low-temperature event will become exceedingly rare (See also TFE.9). {12.4.3}

Models simulate a decrease in cloud amount in the future over most of the tropics and mid-latitudes, due mostly to reductions in low clouds. Changes in marine boundary layer clouds are most uncertain. Increases in cloud fraction and cloud optical depth and therefore cloud reflection are simulated in high latitudes, poleward of 50°. {12.4.3}

TS.5.5.3 Projected Long-term Changes in Atmospheric Circulation

Mean sea level pressure is projected to decrease in high latitudes and increase in the mid-latitudes as global temperatures rise. In the tropics, the Hadley and Walker Circulations are *likely* to slow down. Poleward shifts in the mid-latitude jets of about 1 to 2 degrees latitude are *likely* at the end of the 21st century under RCP8.5 in both hemispheres (*medium confidence*), with weaker shifts in the NH. In austral summer, the additional influence of stratospheric ozone recovery in the SH opposes changes due to GHGs there, though the net response varies strongly across models and scenarios. Substantial uncertainty and thus *low confidence* remains in projecting changes in NH storm tracks, especially for the North Atlantic basin. The Hadley Cell is *likely* to widen, which translates to broader tropical regions and a poleward encroachment of subtropical dry zones. In the stratosphere, the Brewer–Dobson circulation is *likely* to strengthen. {12.4.4}

TS.5.5.4 Projected Long-term Changes in the Water Cycle

On the planetary scale, relative humidity is projected to remain roughly constant, but specific humidity to increase in a warming climate. The projected differential warming of land and ocean promotes changes in atmospheric moistening that lead to small decreases in near-surface relative humidity over most land areas with the notable exception of parts of tropical Africa (*medium confidence*) (see TFE.1, Figure 1). {12.4.5}

It is *virtually certain* that, in the long term, global precipitation will increase with increased GMST. Global mean precipitation will increase at a rate per °C smaller than that of atmospheric water vapour. It will *likely* increase by 1 to 3% $°C^{-1}$ for scenarios other than RCP2.6. For RCP2.6 the range of sensitivities in the CMIP5 models is 0.5 to 4% $°C^{-1}$ at the end of the 21st century. {7.6.2, 7.6.3, 12.4.1}

Changes in average precipitation in a warmer world will exhibit substantial spatial variation under RCP8.5. Some regions will experience increases, other regions will experience decreases and yet others will not experience significant changes at all (see Figure TS.16). There is *high confidence* that the contrast of annual mean precipitation between dry and wet regions and that the contrast between wet and dry seasons will increase over most of the globe as temperatures increase. The general pattern of change indicates that high latitudes are *very likely* to experience greater amounts of precipitation due to the increased specific humidity of the warmer troposphere as well as increased transport of water vapour from the tropics by the end of this century under the RCP8.5 scenario. Many mid-latitude and subtropical arid and semi-arid regions will *likely* experience less precipitation and many moist mid-latitude regions will *likely* experience more precipitation by the end of this century under the RCP8.5 scenario. Maps of precipitation change for the four RCP scenarios are shown in Figure TS.16. {12.4.2, 12.4.5}

Globally, for short-duration precipitation events, a shift to more intense individual storms and fewer weak storms is *likely* as temperatures increase. Over most of the mid-latitude land masses and over wet tropical regions, extreme precipitation events will *very likely* be more intense and more frequent in a warmer world. The global average sensitivity of the 20-year return value of the annual maximum daily precipitation ranges from 4% $°C^{-1}$ of local temperature increase (average of CMIP3 models) to 5.3% $°C^{-1}$ of local temperature increase (average of CMIP5 models), but regionally there are wide variations. {12.4.2, 12.4.5}

Annual surface evaporation is projected to increase as global temperatures rise over most of the ocean and is projected to change over land following a similar pattern as precipitation. Decreases in annual runoff are *likely* in parts of southern Europe, the Middle East and southern Africa by the end of this century under the RCP8.5 scenario. Increases in annual runoff are *likely* in the high northern latitudes corresponding to large increases in winter and spring precipitation by the end of the 21st century under the RCP8.5 scenario. Regional to global-scale projected decreases in soil moisture and increased risk of agricultural drought are *likely* in presently dry regions and are projected with *medium confidence* by the end of this century under the RCP8.5 scenario. Prominent

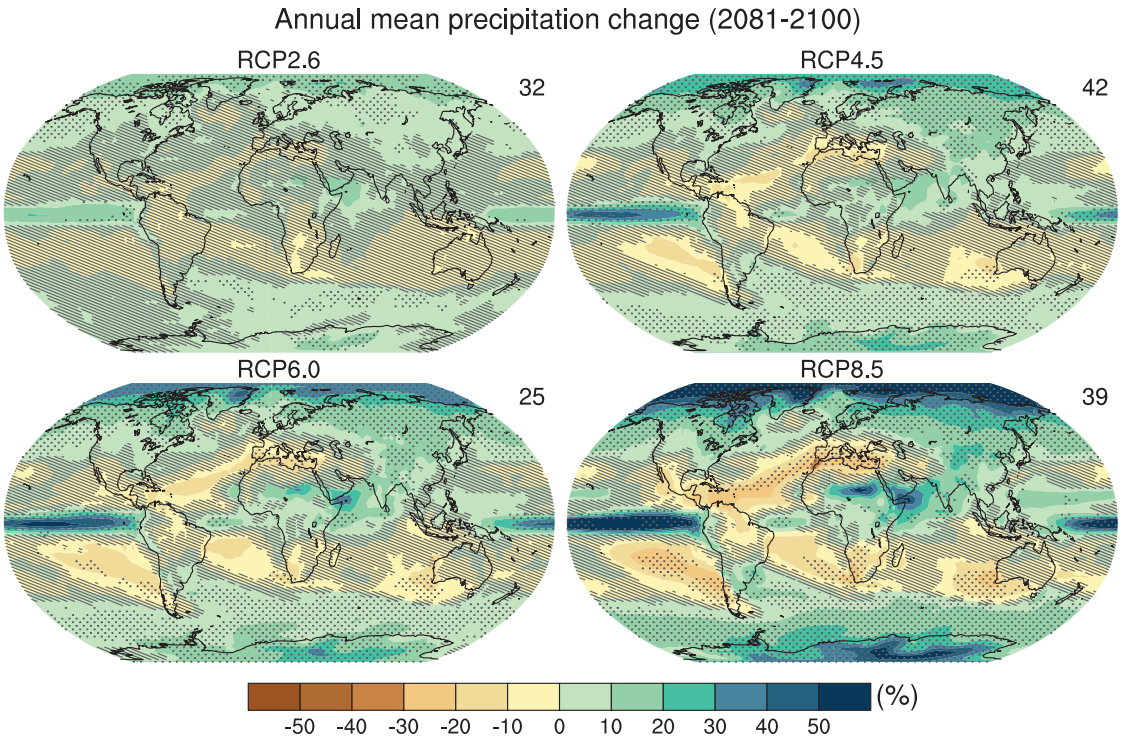

Figure TS.16 | Maps of multi-model results for the scenarios RCP2.6, RCP4.5, RCP6.0 and RCP8.5 in 2081–2100 of average percent change in mean precipitation. Changes are shown relative to 1986–2005. The number of CMIP5 models to calculate the multi-model mean is indicated in the upper right corner of each panel. Hatching indicates regions where the multi- model mean signal is less than 1 standard deviation of internal variability. Stippling indicates regions where the multi- model mean signal is greater than 2 standard deviations of internal variability and where 90% of models agree on the sign of change (see Box 12.1). Further detail regarding the related Figure SPM.8b is given in the TS Supplementary Material. {Figure 12.22; Annex I}

areas of projected decreases in evaporation include southern Africa and northwestern Africa along the Mediterranean. Soil moisture drying in the Mediterranean and southern African regions is consistent with projected changes in Hadley Circulation and increased surface temperatures, so surface drying in these regions as global temperatures increase is *likely* with *high confidence* by the end of this century under the RCP8.5 scenario. In regions where surface moistening is projected, changes are generally smaller than natural variability on the 20-year time scale. A summary of the projected changes in the water cycle from the CMIP5 models is shown in TFE.1, Figure 1. {12.4.5; Box 12.1}

TS.5.5.5 Projected Long-term Changes in the Cryosphere

It is *very likely* that the Arctic sea ice cover will continue shrinking and thinning year-round in the course of the 21st century as GMST rises. At the same time, in the Antarctic, a decrease in sea ice extent and volume is expected, but with *low confidence*. The CMIP5 multi-model projections give average reductions in Arctic sea ice extent for 2081–2100 compared to 1986–2005 ranging from 8% for RCP2.6 to 34% for RCP8.5 in February and from 43% for RCP2.6 to 94% for RCP8.5 in September (*medium confidence*) (Figure TS.17). A nearly ice-free Arctic Ocean (sea ice extent less than 10^6 km^2 for at least five consecutive years) in September before mid-century is *likely* under RCP8.5 (*medium confidence*), based on an assessment of a subset of models that most closely reproduce the climatological mean state and 1979–2012 trend of the Arctic sea ice cover. Some climate projections exhibit 5- to 10-year periods of sharp summer Arctic sea ice decline—even steeper than observed over the last decade—and it is *likely* that such instances of rapid ice loss will occur in the future. There is little evidence in global climate models of a tipping point (or critical threshold) in the transition from a perennially ice-covered to a seasonally ice-free Arctic Ocean beyond which further sea ice loss is unstoppable and irreversible. In the Antarctic, the CMIP5 multi-model mean projects a decrease in sea ice extent that ranges from 16% for RCP2.6 to 67% for RCP8.5 in February and from 8% for RCP2.6 to 30% for RCP8.5 in September for 2081–2100 compared to 1986–2005. There is, however, *low confidence* in those projections because of the wide inter-model spread and the inability of almost all of the available models to reproduce the overall increase of the Antarctic sea ice areal coverage observed during the satellite era. {12.4.6, 12.5.5}

It is *very likely* that NH snow cover will reduce as global temperatures rise over the coming century. A retreat of permafrost extent with rising global temperatures is *virtually certain*. Snow cover changes result from precipitation and ablation changes, which are sometimes opposite. Projections of the NH spring snow covered area by the end of the 21st century vary between a decrease of 7 [3 to 10] % (RCP2.6) and 25 [18 to 32] % (RCP8.5) (Figure TS.18), but *confidence* is those numbers is only *medium* because snow processes in global climate models are strongly simplified. The projected changes in permafrost are a response not only to warming, but also to changes in snow cover, which exerts a control on the underlying soil. By the end of the 21st century, diagnosed near-surface permafrost area is projected to decrease by between 37% (RCP2.6) to 81% (RCP8.5) (*medium confidence*). {12.4.6}

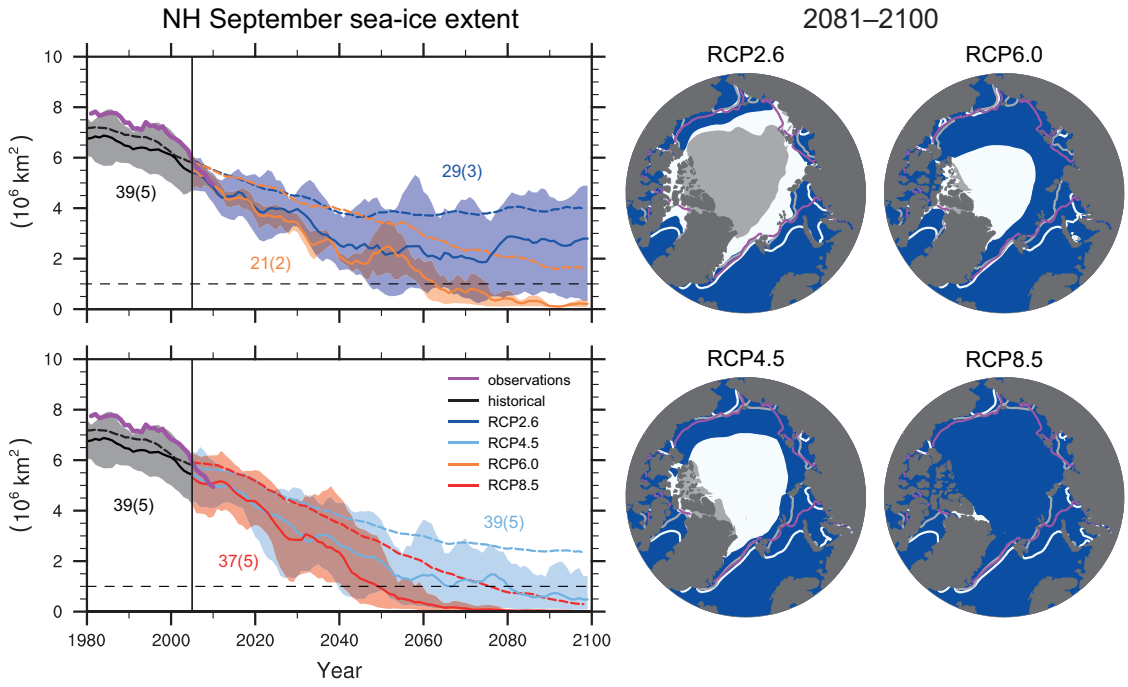

Figure TS.17 | Northern Hemisphere (NH) sea ice extent in September over the late 20th century and the whole 21st century for the scenarios RCP2.6, RCP4.5, RCP6.0 and RCP8.5 in the CMIP5 models, and corresponding maps of multi-model results in 2081–2100 of NH September sea ice extent. In the time series, the number of CMIP5 models to calculate the multi-model mean is indicated (subset in brackets). Time series are given as 5-year running means. The projected mean sea ice extent of a subset of models that most closely reproduce the climatological mean state and 1979–2012 trend of the Arctic sea ice is given (solid lines), with the minimum to maximum range of the subset indicated with shading. Black (grey shading) is the modelled historical evolution using historical reconstructed forcings. The CMIP5 multi-model mean is indicated with dashed lines. In the maps, the CMIP5 multi-model mean is given in white and the results for the subset in grey. Filled areas mark the averages over the 2081–2100 period, lines mark the sea ice extent averaged over the 1986–2005 period. The observed sea ice extent is given in pink as a time series and averaged over 1986–2005 as a pink line in the map. Further detail regarding the related Figures SPM.7b and SPM.8c is given in the TS Supplementary Material. {Figures 12.18, 12.29, 12.31}

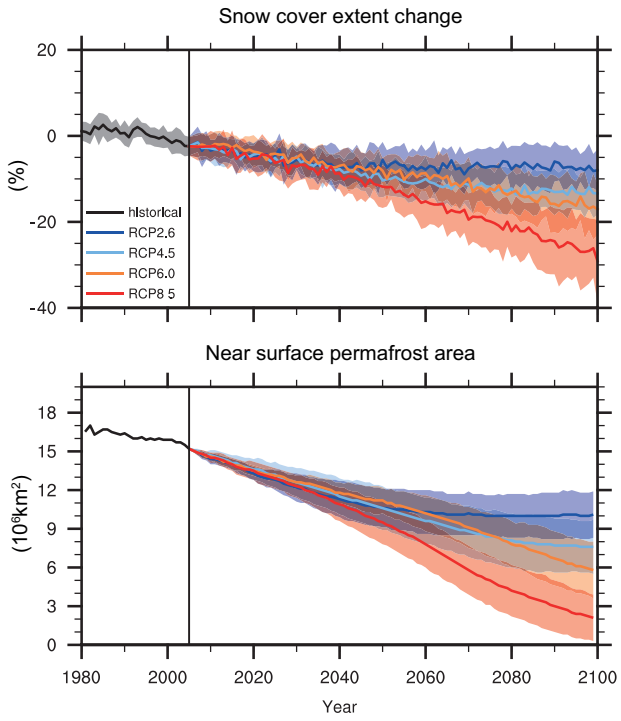

Figure TS.18 | (Top) Northern Hemisphere (NH) spring (March to April average) relative snow-covered area (RSCA) in CMIP5, obtained by dividing the simulated 5-year box smoothed spring snow-covered area (SCA) by the simulated average spring SCA of 1986–2005 reference period. (Bottom) NH diagnosed near-surface permafrost area in CMIP5, using 20-year average monthly surface air temperatures and snow depths. Lines indicate the multi model average, shading indicates the inter-model spread (one standard deviation). {Figures 12.32, 12.33}

TS.5.5.6 Projected Long-term Changes in the Ocean

Over the course of the 21st century, the global ocean will warm in all RCP scenarios. The strongest ocean warming is projected for the surface in subtropical and tropical regions. At greater depth the warming is projected to be most pronounced in the Southern Ocean. Best estimates of ocean warming in the top one hundred metres are about 0.6°C (RCP2.6) to 2.0°C (RCP8.5), and 0.3°C (RCP2.6) to 0.6°C (RCP8.5) at a depth of about 1 km by the end of the 21st century. For RCP4.5 by the end of the 21st century, half of the energy taken up by the ocean is in the uppermost 700 m, and 85% is in the uppermost 2000 m. Due to the long time scales of this heat transfer from the surface to depth, ocean warming will continue for centuries, even if GHG emissions are decreased or concentrations kept constant, and will result in a continued contribution to sea level rise (see Section TS5.7). {12.4.3, 12.4.7}

TS.5.6 Long-term Projections of Carbon and Other Biogeochemical Cycles

Projections of the global carbon cycle to 2100 using the CMIP5 ESMs represent a wider range of complex interactions between the carbon cycle and the physical climate system. {6}

With *very high confidence*, ocean carbon uptake of anthropogenic CO_2 will continue under all four RCPs through to 2100, with higher uptake in higher concentration pathways. The future evolution of the land carbon uptake is much more uncertain. A majority of CMIP5 ESMs project a continued net carbon uptake by land ecosystems through 2100. Yet, a minority of models simulate a net CO_2 source to the atmosphere by 2100 due to the combined effect of climate change and land use change. In view of the large spread of model results and incomplete process representation, there is *low confidence* on the magnitude of modelled future land carbon changes. {6.4.3}

There is *high confidence* that climate change will partially offset increases in global land and ocean carbon sinks caused by rising atmospheric CO_2. Yet, there are regional differences among CMIP5 ESMs in the response of ocean and land CO_2 fluxes to climate. There is high agreement between models that tropical ecosystems will store less carbon in a warmer climate. There is medium agreement between the CMIP5 ESMs that at high latitudes warming will increase land carbon storage, although none of these models accounts for decomposition of carbon in permafrost which may offset increased land carbon storage. There is *high confidence* that reductions in permafrost extent due to warming will cause thawing of some currently frozen carbon. However, there is *low confidence* on the magnitude of carbon losses through CO_2 and CH_4 emissions to the atmosphere with a range from 50 to 250 PgC between 2000 and 2100 for RCP8.5. {6.4.2, 6.4.3}

The loss of carbon from frozen soils constitutes a positive radiative feedback that is missing in current coupled ESM projections. There is high agreement between CMIP5 ESMs that ocean warming and circulation changes will reduce the rate of ocean carbon uptake in the Southern Ocean and North Atlantic, but that carbon uptake will nevertheless persist in those regions. {6.4.2}

It is *very likely*, based on new experimental results and modelling, that nutrient shortage will limit the effect of rising atmospheric CO_2 on future land carbon sinks for the four RCP scenarios. There is *high confidence* that low nitrogen availability will limit carbon storage on land even when considering anthropogenic nitrogen deposition. The role of phosphorus limitation is more uncertain. {6.4.6}

For the ESMs simulations driven by CO_2 concentrations, representation of the land and ocean carbon cycle allows quantification of the fossil fuel emissions compatible with the RCP scenarios. Between 2012 and 2100, ESM results imply cumulative compatible fossil fuel emissions of 270 [140 to 410] PgC for RCP2.6, 780 [595 to 1005] PgC for RCP4.5, 1060 [840 to 1250] PgC for RCP6.0 and 1685 [1415 to 1910] PgC for RCP8.5 (values quoted to nearest 5 PgC, range ±1 standard deviation derived from CMIP5 model results) (Figure TS.19). For RCP2.6, the models project an average 50% (range 14 to 96%) emission reduction by 2050 relative to 1990 levels. By the end of the 21st century, about half of the models infer emissions slightly above zero, while the other half infer a net removal of CO_2 from the atmosphere (see also Box TS.7). {6.4.3; Table 6.12}

When forced with RCP8.5 CO_2 emissions, as opposed to the RCP8.5 CO_2 concentrations, CMIP5 ESMs with interactive carbon cycles simulate, on average, a 50 (–140 to +210) ppm larger atmospheric CO_2 concentration and a 0.2 (–0.4 to +0.9) °C larger global surface temperature increase by 2100 (CMIP5 model spread). {12.4.8}

It is *virtually certain* that the increased storage of carbon by the ocean will increase acidification in the future, continuing the observed trends of the past decades. Ocean acidification in the surface ocean will follow atmospheric CO_2 and it will also increase in the deep ocean as CO_2 continues to penetrate the abyss. The CMIP5 models consistently project worldwide increased ocean acidification to 2100 under all RCPs. The corresponding decrease in surface ocean pH by the end of 21st century is 0.065 (0.06 to 0.07) for RCP2.6, 0.145 (0.14 to 0.15) for RCP4.5, 0.203 (0.20 to 0.21) for RCP6.0 and 0.31 (0.30 to 0.32) for RCP8.5 (CMIP5 model spread) (Figure TS.20). Surface waters are projected to become seasonally corrosive to aragonite in parts of the Arctic and in some coastal upwelling systems within a decade, and

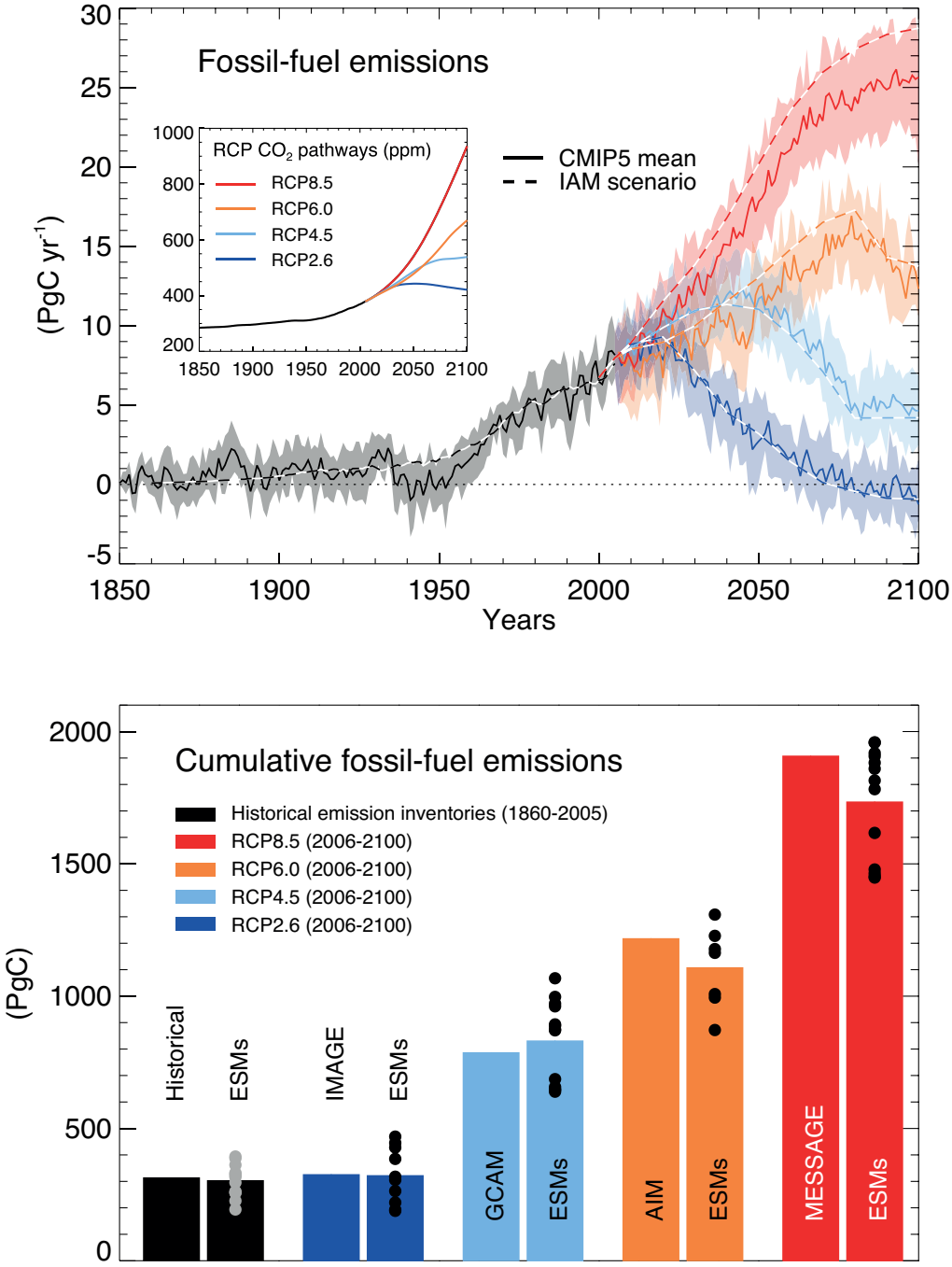

Figure TS.19 | Compatible fossil fuel emissions simulated by the CMIP5 models for the four RCP scenarios. (Top) Time series of annual emission (PgC yr^{-1}). Dashed lines represent the historical estimates and RCP emissions calculated by the Integrated Assessment Models (IAMs) used to define the RCP scenarios, solid lines and plumes show results from CMIP5 Earth System Models (ESMs, model mean, with one standard deviation shaded). (Bottom) Cumulative emissions for the historical period (1860–2005) and 21st century (defined in CMIP5 as 2006–2100) for historical estimates and RCP scenarios. Left bars are cumulative emissions from the IAMs, right bars are the CMIP5 ESMs multi-model mean estimate and dots denote individual ESM results. From the CMIP5 ESMs results, total carbon in the land-atmosphere–ocean system can be tracked and changes in this total must equal fossil fuel emissions to the system. Hence the compatible emissions are given by cumulative emissions = $\Delta C_A + \Delta C_L + \Delta C_O$, while emission rate = d/dt [$C_A + C_L + C_O$], where C_A, C_L, C_O are carbon stored in atmosphere, land and ocean respectively. Other sources and sinks of CO_2 such as from volcanism, sedimentation or rock weathering, which are very small on centennial time scales are not considered here. {Box 6.4; Figure 6.25}

in parts of the Southern Ocean within one to three decades in most scenarios. Aragonite, a less stable form of calcium carbonate, undersaturation becomes widespread in these regions at atmospheric CO_2 levels of 500 to 600 ppm. {6.4.4}

It is *very likely* that the dissolved oxygen content of the ocean will decrease by a few percent during the 21st century in response to surface warming. CMIP5 models suggest that this decrease in dissolved oxygen will predominantly occur in the subsurface mid-latitude oceans, caused by enhanced stratification, reduced ventilation and warming. However, there is no consensus on the future development of the volume of hypoxic and suboxic waters in the open ocean because of large uncertainties in potential biogeochemical effects and in the evolution of tropical ocean dynamics. {6.4.5}

With *very high confidence*, the carbon cycle in the ocean and on land will continue to respond to climate change and atmospheric CO_2 increases that arise during the 21st century (see TFE.7 and TFE 8). {6.4}

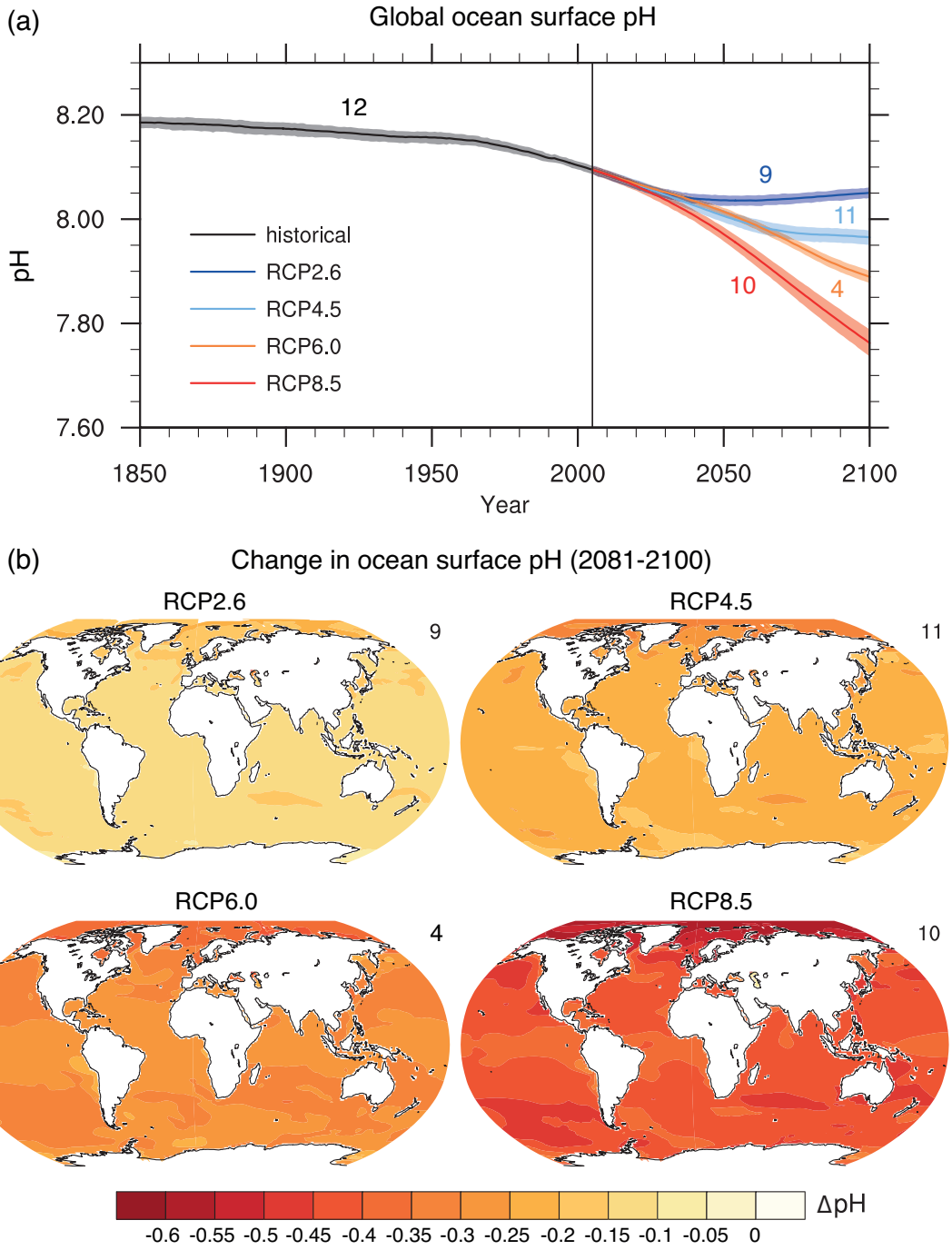

Figure TS.20 | (a) Time series (model averages and minimum to maximum ranges) and (b) maps of multi-model surface ocean pH for the scenarios RCP2.6, RCP4.5, RCP6.0 and RCP8.5 in 2081–2100. The maps in (b) show change in global ocean surface pH in 2081–2100 relative to 1986–2005. The number of CMIP5 models to calculate the multi-model mean is indicated in the upper right corner of each panel. Further detail regarding the related Figures SPM.7c and SPM.8.d is given in the TS Supplementary Material. {Figure 6.28}

Thematic Focus Elements

TFE.7 | Carbon Cycle Perturbation and Uncertainties

The natural carbon cycle has been perturbed since the beginning of the Industrial Revolution (about 1750) by the anthropogenic release of carbon dioxide (CO_2) to the atmosphere, virtually all from fossil fuel combustion and land use change, with a small contribution from cement production. Fossil fuel burning is a process related to energy production. Fossil fuel carbon comes from geological deposits of coal, oil and gas that were buried in the Earth crust for millions of years. Land use change CO_2 emissions are related to the conversion of natural ecosystems into managed ecosystems for food, feed and timber production with CO_2 being emitted from the burning of plant material or from the decomposition of dead plants and soil organic carbon. For instance when a forest is cleared, the plant material may be released to the atmosphere quickly through burning or over many years as the dead biomass and soil carbon decay on their own. {6.1, 6.3; Table 6.1}

The human caused excess of CO_2 in the atmosphere is partly removed from the atmosphere by carbon sinks in land ecosystems and in the ocean, currently leaving less than half of the CO_2 emissions in the atmosphere. Natural carbon sinks are due to physical, biological and chemical processes acting on different time scales. An excess of atmospheric CO_2 supports photosynthetic CO_2 fixation by plants that is stored as plant biomass or in the soil. The residence times of stored carbon on land depends on the compartments (plant/soil) and composition of the organic carbon, with time horizons varying from days to centuries. The increased storage in terrestrial ecosystems not affected by land use change is *likely* to be caused by enhanced photosynthesis at higher CO_2 levels and nitrogen deposition, and changes in climate favoring carbon sinks such as longer growing seasons in mid-to-high latitudes. {6.3, 6.3.1}

The uptake of anthropogenic CO_2 by the ocean is primarily a response to increasing CO_2 in the atmosphere. Excess atmospheric CO_2 absorbed by the surface ocean or transported to the ocean through aquatic systems (e.g., rivers, groundwaters) gets buried in coastal sediments or transported to deep waters where it is stored for decades to centuries. The deep ocean carbon can dissolve ocean carbonate sediments to store excess CO_2 on time scales of centuries to millennia. Within a 1 kyr, the remaining atmospheric fraction of the CO_2 emissions will be between 15 and 40%, depending on the amount of carbon released (TFE.7, Figure 1). On geological time scales of 10 kyr or longer, additional CO_2 is removed very slowly from the atmosphere by rock weathering, pulling the remaining atmospheric CO_2 fraction down to 10 to 25% after 10 kyr. {Box 6.1}

The carbon cycle response to future climate and CO_2 changes can be viewed as two strong and opposing feedbacks. The concentration–carbon feedback determines changes in storage due to elevated CO_2, and the climate–carbon feedback determines changes in carbon storage due to changes in climate. There is *high confidence* that increased atmospheric CO_2 will lead to increased land and ocean carbon uptake but by an uncertain amount. Models agree on the positive sign of land and ocean response to rising CO_2 but show only medium and low agreement for the magnitude of ocean and land carbon uptake respectively (TFE.7, Figure 2). Future climate change will decrease land and ocean carbon uptake compared to the case with constant climate (*medium confidence*). This is further supported by paleoclimate observations and modelling indicating that there is a positive feedback between climate and the carbon cycle on century to millennial time scales. Models agree on the sign, globally negative, of land and ocean response to climate change but show low agreement on the magnitude of this response, especially for the land (TFE.7, Figure 2). A key update since the IPCC Fourth Assessment Report (AR4) is the introduction of nutrient dynamics in some land carbon models, in particular the limitations on plant growth imposed by nitrogen availability. There is *high confidence* that, at the global scale, relative to the Coupled Model Intercomparison Project Phase 5 (CMIP5) carbon-only Earth System

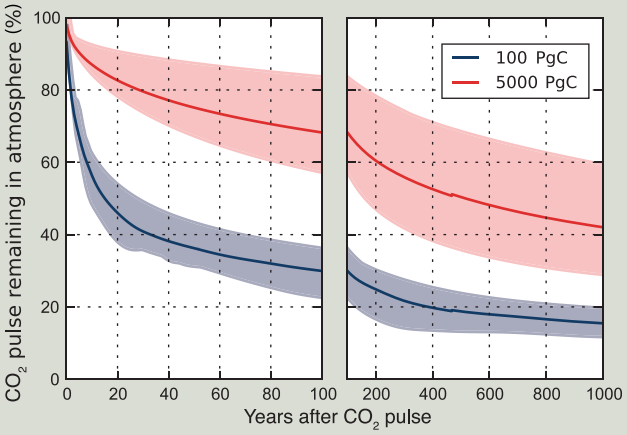

TFE.7, Figure 1 | Percentage of initial atmospheric CO_2 perturbation remaining in the atmosphere in response to an idealized instantaneous CO_2 emission pulse in year 0 as calculated by a range of coupled climate–carbon cycle models. Multi-model mean (line) and the uncertainty interval (maximum model range, shading) simulated during 100 years (left) and 1 kyr (right) following the instantaneous emission pulse of 100 PgC (blue) and 5,000 PgC (red). {Box 6.1, Figure 1}

(continued on next page)

TFE.7 (continued)

Models (ESMs), CMIP5 ESMs including a land nitrogen cycle will reduce the strength of both the concentration–carbon feedback and the climate–carbon feedback of land ecosystems (TFE.7, Figure 2). Inclusion of nitrogen-cycle processes increases the spread across the CMIP5 ensemble. The CMIP5 spread in ocean sensitivity to CO_2 and climate appears reduced compared to AR4 (TFE.7, Figure 2). {6.2.3, 6.4.2}

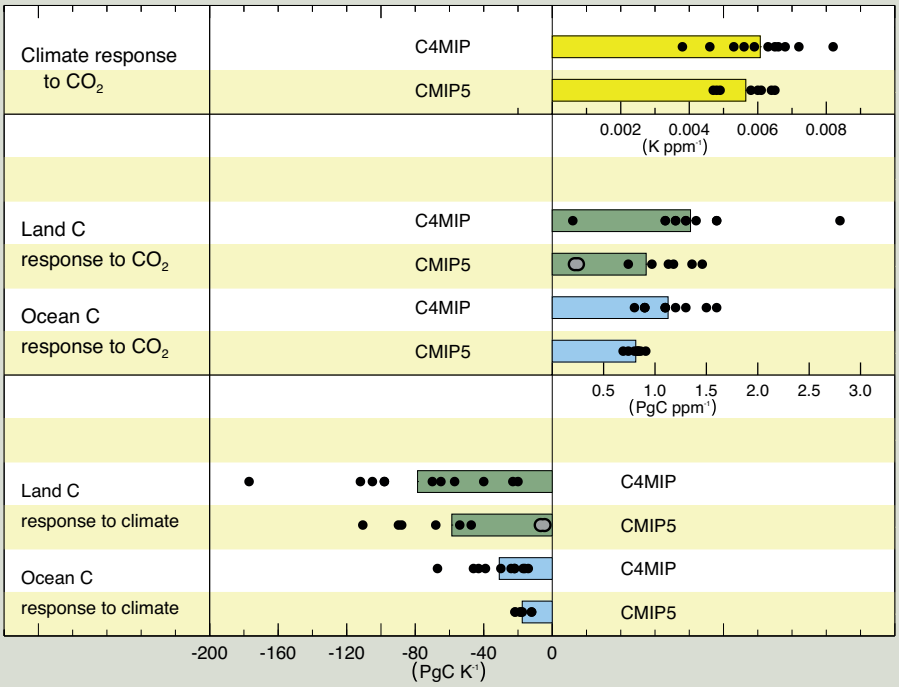

TFE.7, Figure 2 | Comparison of carbon cycle feedback metrics between the ensemble of seven General Circulation Models (GCMs) and four Earth System Models of Intermediate Complexity (EMICs) at the time of AR4 (Coupled Carbon Cycle Climate Model Intercomparison Project (C^4MIP)) under the SRES A2 scenario and the eight CMIP5 models under the 140-year 1% CO_2 increase per year scenario. Black dots represent a single model simulation and coloured bars the mean of the multi-model results, grey dots are used for models with a coupled terrestrial nitrogen cycle. The comparison with C^4MIP models is for context, but these metrics are known to be variable across different scenarios and rates of change (see Section 6.4.2). The SRES A2 scenario is closer in rate of change to a 0.5% CO_2 increase per year scenario and as such it should be expected that the CMIP5 climate–carbon sensitivity terms are comparable, but the concentration–carbon sensitivity terms are *likely* to be around 20% smaller for CMIP5 than for C^4MIP due to lags in the ability of the land and ocean to respond to higher rates of CO_2 increase. This dependence on scenario reduces confidence in any quantitative statements of how CMIP5 carbon cycle feedbacks differ from C^4MIP. {Figure 6.21}

With *very high confidence*, ocean carbon uptake of anthropogenic CO_2 emissions will continue under all four Representative Concentration Pathways (RCPs) through to 2100, with higher uptake corresponding to higher concentration pathways. The future evolution of the land carbon uptake is much more uncertain, with a majority of models projecting a continued net carbon uptake under all RCPs, but with some models simulating a net loss of carbon by the land due to the combined effect of climate change and land use change. In view of the large spread of model results and incomplete process representation, there is *low confidence* on the magnitude of modelled future land carbon changes. {6.4.3; Figure 6.24}

Biogeochemical cycles and feedbacks other than the carbon cycle play an important role in the future of the climate system, although the carbon cycle represents the strongest of these. Changes in the nitrogen cycle, in addition to interactions with CO_2 sources and sinks, affect emissions of nitrous oxide (N_2O) both on land and from the ocean. The human-caused creation of reactive nitrogen has increased steadily over the last two decades and is dominated by the production of ammonia for fertilizer and industry, with important contributions from legume cultivation and combustion of fossil fuels. {6.3}

Many processes, however, are not yet represented in coupled climate-biogeochemistry models (e.g., other processes involving other biogenic elements such as phosphorus, silicon and iron) so their magnitudes have to be estimated in offline or simpler models, which make their quantitative assessment difficult. It is *likely* that there will be nonlinear interactions between many of these processes, but these are not yet well quantified. Therefore any assessment of the future feedbacks between climate and biogeochemical cycles still contains large uncertainty. {6.4}

Box TS.7 | Climate Geoengineering Methods

Geoengineering is defined as the deliberate large-scale intervention in the Earth system to counter undesirable impacts of climate change on the planet. Carbon Dioxide Reduction (CDR) aims to slow or perhaps reverse projected increases in the future atmospheric CO_2 concentrations, accelerating the natural removal of atmospheric CO_2 and increasing the storage of carbon in land, ocean and geological reservoirs. Solar Radiation Management (SRM) aims to counter the warming associated with increasing GHG concentrations by reducing the amount of sunlight absorbed by the climate system. A related technique seeks to deliberately decrease the greenhouse effect in the climate system by altering high-level cloudiness. {6.5, 7.7; FAQ 7.3}

CDR methods could provide mitigation of climate change if CO_2 can be reduced, but there are uncertainties, side effects and risks, and implementation would depend on technological maturity along with economic, political and ethical considerations. CDR would *likely* need to be deployed at large-scale and over at least one century to be able to significantly reduce CO_2 concentrations. There are biogeochemical, and currently technical limitations that make it difficult to provide quantitative estimates of the potential for CDR. It is *virtually certain* that CO_2 removals from the atmosphere by CDR would be partially offset by outgassing of CO_2 previously stored in ocean and terrestrial carbon reservoirs. Some of the climatic and environmental side effects of CDR methods are associated with altered surface albedo from afforestation, ocean de-oxygenation from ocean fertilization, and enhanced N_2O emissions. Land-based CDR methods would probably face competing demands for land. The level of *confidence* on the effectiveness of CDR methods and their side effects on carbon and other biogeochemical cycles is *low*. {6.5; Box 6.2; FAQ 7.3}

SRM remains unimplemented and untested but, if realizable, could offset a global temperature rise and some of its effects. There is *medium confidence* that SRM through stratospheric aerosol injection is scalable to counter the RF and some of the climate effects expected from a twofold increase in CO_2 concentration. There is no consensus on whether a similarly large RF could be achieved from cloud brightening SRM due to insufficient understanding of aerosol–cloud interactions. It does not appear that land albedo change SRM could produce a large RF. Limited literature on other SRM methods precludes their assessment. {7.7.2, 7.7.3}

Numerous side effects, risks and shortcomings from SRM have been identified. SRM would produce an inexact compensation for the RF by GHGs. Several lines of evidence indicate that SRM would produce a small but significant decrease in global precipitation (with larger differences on regional scales) if the global surface temperature were maintained. Another side effect that is relatively well characterized is the likelihood of modest polar stratospheric ozone depletion associated with stratospheric aerosol SRM. There could also be other as yet unanticipated consequences. {7.6.3, 7.7.3, 7.7.4}

As long as GHG concentrations continued to increase, the SRM would require commensurate increase, exacerbating side effects. In addition, scaling SRM to substantial levels would carry the risk that if the SRM were terminated for any reason, there is *high confidence* that surface temperatures would increase rapidly (within a decade or two) to values consistent with the GHG forcing, which would stress systems sensitive to the rate of climate change. Finally, SRM would not compensate for ocean acidification from increasing CO_2. {7.7.3, 7.7.4}

TS.5.7 Long-term Projections of Sea Level Change

TS.5.7.1 Projections of Global Mean Sea Level Change for the 21st Century

GMSL rise for 2081–2100 (relative to 1986–2005) for the RCPs will *likely* be in the 5 to 95% ranges derived from CMIP5 climate projections in combination with process-based models of glacier and ice sheet surface mass balance, with possible ice sheet dynamical changes assessed from the published literature. These *likely* ranges are 0.26 to 0.55 m (RCP2.6), 0.32 to 0.63 m (RCP4.5), 0.33 to 0.63 m (RCP6.0) and 0.45 to 0.82 m (RCP8.5) (*medium confidence*) (Table TS.1, Figure TS.21). For RCP8.5 the range at 2100 is 0.52 to 0.98 m. The central projections for GMSL rise in all scenarios lie within a range of 0.05 m until the middle of the century, when they begin to diverge; by the late 21st century, they have a spread of 0.25 m. Although RCP4.5 and RCP6.0 are very similar at the end of the century, RCP4.5 has a greater rate of rise earlier in the century than RCP6.0. GMSL rise depends on the pathway of CO_2 emissions, not only on the cumulative total; reducing emissions earlier rather than later, for the same cumulative total, leads to a larger mitigation of sea level rise. {12.4.1, 13.4.1, 13.5.1; Table 13.5}

Confidence in the projected *likely* ranges comes from the consistency of process-based models with observations and physical understanding. The basis for higher projections has been considered and it has been concluded that there is currently insufficient evidence to evaluate the probability of specific levels above the *likely* range. Based on current understanding, only the collapse of marine-based sectors of the Antarctic ice sheet, if initiated, could cause GMSL to rise substantially above the *likely* range during the 21st century. There is a lack of consensus on the probability for such a collapse, and the potential additional contribution to GMSL rise cannot be precisely quantified,

but there is *medium confidence* that it would not exceed several tenths of a metre of sea level rise during the 21st century. {13.5.1, 13.5.3}

Under all the RCP scenarios, the time-mean rate of GMSL rise during the 21st century is *very likely* to exceed the rate observed during 1971–2010. In the projections, the rate of rise initially increases. In RCP2.6 it becomes roughly constant (central projection about 4.5 mm yr^{-1}) before the middle of the century, and subsequently declines slightly. The rate of rise becomes roughly constant in RCP4.5 and RCP6.0 by the end of the 21st century, whereas acceleration continues throughout the century in RCP8.5 (reaching 11 [8 to 16] mm yr^{-1} during 2081–2100). {13.5.1; Table 13.5}

In all RCP scenarios, thermal expansion is the largest contribution, accounting for about 30 to 55% of the total. Glaciers are the next largest, accounting for 15-35%. By 2100, 15 to 55% of the present glacier volume is projected to be eliminated under RCP2.6, and 35 to 85% under RCP8.5 (*medium confidence*). The increase in surface melting in Greenland is projected to exceed the increase in accumulation, and there is *high confidence* that the surface mass balance changes on the Greenland ice sheet will make a positive contribution to sea level rise over the 21st century. On the Antarctic ice sheet, surface melting is projected to remain small, while there is *medium confidence* that snowfall will increase (Figure TS.21). {13.3.3, 13.4.3, 13.4.4, 13.5.1; Table 13.5}

There is *medium confidence* in the ability to model future rapid changes in ice sheet dynamics on decadal time scales. At the time of the AR4, scientific understanding was not sufficient to allow an assessment of the possibility of such changes. Since the publication of the AR4, there has been substantial progress in understanding the relevant processes as well as in developing new ice sheet models that are capable of simulating them. However, the published literature as yet provides only a partially sufficient basis for making projections related to particular scenarios. In our projections of GMSL rise by 2081–2100, the *likely* range from rapid changes in ice outflow is 0.03 to 0.20 m from the two ice sheets combined, and its inclusion is the most important reason why the projections are greater than those given in the AR4. {13.1.5, 13.5.1, 13.5.3}

Semi-empirical models are designed to reproduce the observed sea level record over their period of calibration, but do not attribute sea level rise to its individual physical components. For RCPs, some semi-empirical models project a range that overlaps the process-based *likely* range while others project a median and 95-percentile that are about twice as large as the process-based models. In nearly every case, the semi-empirical model 95th percentile is higher than the process-based *likely* range. For 2081–2100 (relative to 1986–2005) under RCP4.5, semi-empirical models give median projections in the range 0.56 to 0.97 m, and their 95th percentiles extend to about 1.2 m. This difference implies either that there is some contribution which is presently

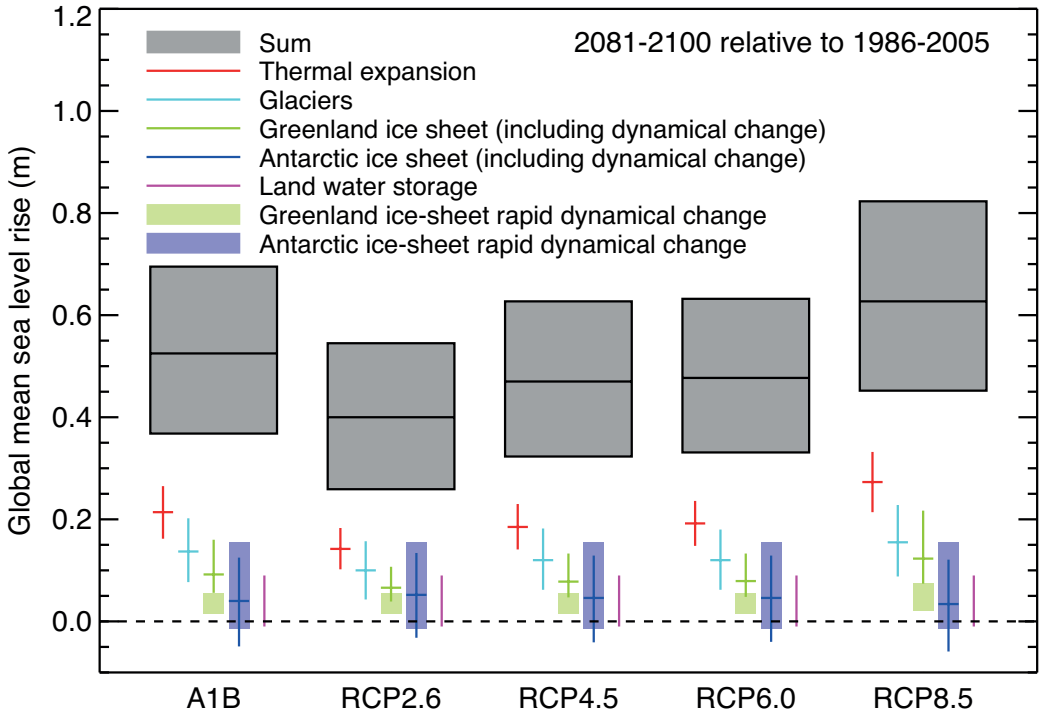

Figure TS.21 | Projections from process-based models with *likely* ranges and median values for global mean sea level (GMSL) rise and its contributions in 2081–2100 relative to 1986–2005 for the four RCP scenarios and scenario SRES A1B used in the AR4. The contributions from ice sheets include the contributions from ice sheet rapid dynamical change, which are also shown separately. The contributions from ice sheet rapid dynamics and anthropogenic land water storage are treated as having uniform probability distributions, and as independent of scenario (except that a higher rate of change is used for Greenland ice sheet outflow under RCP8.5). This treatment does not imply that the contributions concerned will not depend on the scenario followed, only that the current state of knowledge does not permit a quantitative assessment of the dependence. See discussion in Sections 13.5.1 and 13.5.3 and Supplementary Material for methods. Based on current understanding, only the collapse of the marine-based sectors of the Antarctic ice sheet, if initiated, could cause GMSL to rise substantially above the *likely* range during the 21st century. This potential additional contribution cannot be precisely quantified but there is *medium confidence* that it would not exceed several tenths of a metre during the 21st century. {Figure 13.10}

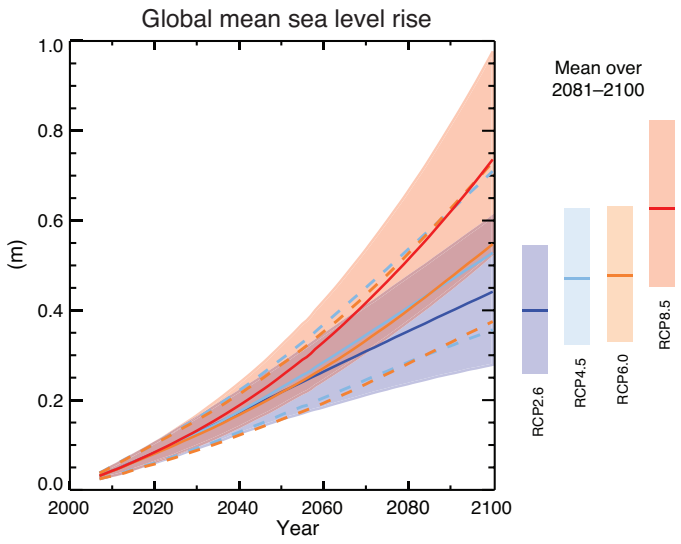

Figure TS.22 | Projections from process-based models of global mean sea level (GMSL) rise relative to 1986–2005 for the four RCP scenarios. The solid lines show the median projections, the dashed lines show the *likely* ranges for RCP4.5 and RCP6.0, and the shading the *likely* ranges for RCP2.6 and RCP8.5. The time means for 2081–2100 are shown as coloured vertical bars. See Sections 13.5.1 and 13.5.3 and Supplementary Material for methods. Based on current understanding, only the collapse of the marine-based sectors of the Antarctic ice sheet, if initiated, could cause GMSL to rise substantially above the *likely* range during the 21st century. This potential additional contribution cannot be precisely quantified but there is *medium confidence* that it would not exceed several tenths of a metre during the 21st century. Further detail regarding the related Figure SPM.9 is given in the TS Supplementary Material. {Table 13.5; Figures 13.10, 13.11}

unidentified or underestimated by process-based models, or that the projections of semi-empirical models are overestimates. Making projections with a semi-empirical model assumes that sea level change in the future will have the same relationship as it has had in the past to RF or global mean temperature change. This may not hold if potentially nonlinear physical processes do not scale in the future in ways which can be calibrated from the past. There is no consensus in the scientific community about the reliability of semi-empirical model projections, and *confidence* in them is assessed to be *low*. {13.5.2, 13.5.3}

TS.5.7.2 Projections of Global Mean Sea Level Change Beyond 2100

It is *virtually certain* that GMSL rise will continue beyond 2100. The few available model results that go beyond 2100 indicate global mean sea level rise above the pre-industrial level (defined here as an equilibrium 280 ppm atmospheric CO_2 concentration) by 2300 to be less than 1 m for a RF that corresponds to CO_2 concentrations that peak and decline and remain below 500 ppm, as in the scenario RCP2.6. For a RF that corresponds to a CO_2 concentration that is above 700 ppm but below 1500 ppm, as in the scenario RCP8.5, the projected rise is 1 m to more than 3 m (*medium confidence*). {13.5.4}

Sea level rise due to ocean thermal expansion will continue for centuries to millennia. The amount of ocean thermal expansion increases with global warming (models give a range of 0.2 to 0.6 m $°C^{-1}$). The glacier contribution decreases over time as their volume (currently about 0.43 m sea level equivalent) decreases. In Antarctica, beyond 2100 and with higher GHG scenarios, the increase in surface melting could exceed the increase in accumulation. {13.5.2, 13.5.4}

The available evidence indicates that global warming greater than a certain threshold would lead to the near-complete loss of the Greenland ice sheet over a millennium or more, causing a GMSL rise of about 7 m. Studies with fixed present-day ice sheet topography indicate the threshold is greater than 2°C but less than 4°C of GMST rise with respect to pre-industrial (*medium confidence*). The one study with a dynamical ice sheet suggests the threshold is greater than about 1°C (*low confidence*) global mean warming with respect to pre-industrial. Considering the present state of scientific uncertainty, a *likely* range cannot be quantified. The complete loss of the ice sheet is not inevitable because this would take a millennium or more; if temperatures decline before the ice sheet is eliminated, the ice sheet might regrow. However, some part of the mass loss might be irreversible, depending on the duration and degree of exceedance of the threshold, because the ice sheet may have multiple steady states, due to its interaction with its regional climate. {13.4.3, 13.5.4}

Currently available information indicates that the dynamical contribution of the ice sheets will continue beyond 2100, but *confidence* in projections is *low*. In Greenland, ice outflow induced from interaction with the ocean is self-limiting as the ice sheet margin retreats inland from the coast. By contrast, the bedrock topography of Antarctica is such that there may be enhanced rates of mass loss as the ice retreats. About 3.3 m of equivalent global sea level of the West Antarctic ice sheet is grounded on areas with downward sloping bedrock, which may be subject to potential ice loss via the marine ice sheet instability. Abrupt and irreversible ice loss from a potential instability of marine-based sectors of the Antarctic Ice Sheet in response to climate forcing is possible, but current evidence and understanding is insufficient to make a quantitative assessment. Due to relatively weak snowfall on Antarctica and the slow ice motion in its interior, it can be expected that the West Antarctic ice sheet would take at least several thousand years to regrow if it was eliminated by dynamic ice discharge. Consequently any significant ice loss from West Antarctic that occurs within the next century will be irreversible on a multi-centennial to millennial time scale. {5.8, 13.4.3, 13.4.4, 13.5.4}

TS.5.7.3 Projections of Regional Sea Level Change

Regional sea level will change due to dynamical ocean circulation changes, changes in the heat content of the ocean, mass redistribution in the entire Earth system and changes in atmospheric pressure. Ocean dynamical change results from changes in wind and buoyancy forcing (heat and freshwater), associated changes in the circulation, and redistribution of heat and freshwater. Over time scales longer than a few days, regional sea level also adjusts nearly isostatically to regional changes in sea level atmospheric pressure relative to its mean over the ocean. Ice sheet mass loss (both contemporary and past), glacier mass loss and changes in terrestrial hydrology cause water mass redistribution among the cryosphere, the land and the oceans, giving rise to distinctive regional changes in the solid Earth, Earth rotation and the gravity field. In some coastal locations, changes in the hydrological cycle, ground subsidence associated with anthropogenic activity,

tectonic processes and coastal processes can dominate the relative sea level change, that is, the change in sea surface height relative to the land. {13.1.3, 13.6.2, 13.6.3, 13.6.4}

By the end of the 21st century, sea level change will have a strong regional pattern, which will dominate over variability, with many regions *likely* experiencing substantial deviations from the global mean change (Figure TS.23). It is *very likely* that over about 95% of the ocean will experience regional relative sea level rise, while most regions experiencing a sea level fall are located near current and former glaciers and ice sheets. Local sea level changes deviate more than 10% and 25% from the global mean projection for as much as 30% and 9% of the ocean area, respectively, indicating that spatial variations can be large. Regional changes in sea level reach values of up to 30% above the global mean value in the Southern Ocean and around North America, between 10% and 20% in equatorial regions, and up to 50% below the global mean in the Arctic region and some regions near Antarctica. About 70% of the coastlines worldwide are projected to experience a relative sea level change within 20% of the GMSL change. Over decadal periods, the rates of regional relative sea level change as a result of climate variability can differ from the global average rate by more than 100%. {13.6.5}

TS.5.7.4 Projections of Change in Sea Level Extremes and Waves During the 21st Century

It is *very likely* that there will be a significant increase in the occurrence of future sea level extremes by the end of the 21st century, with a *likely* increase in the early 21st century (see TFE.9, Table 1). This increase will primarily be the result of an increase in mean sea level (*high confidence*), with extreme return periods decreasing by at least an order of magnitude in some regions by the end of the 21st century. There is *low confidence* in region-specific projections of storminess and associated storm surges. {13.7.2}

It is *likely* (*medium confidence*) that annual mean significant wave heights will increase in the Southern Ocean as a result of enhanced wind speeds. Southern Ocean–generated swells are *likely* to affect heights, periods and directions of waves in adjacent basins. It is *very likely* that wave heights and the duration of the wave season will increase in the Arctic Ocean as a result of reduced sea ice extent. In general, there is *low confidence* in region-specific projections due to the *low confidence* in tropical and extratropical storm projections, and to the challenge of down-scaling future wind states from coarse resolution climate models. {13.7.3}

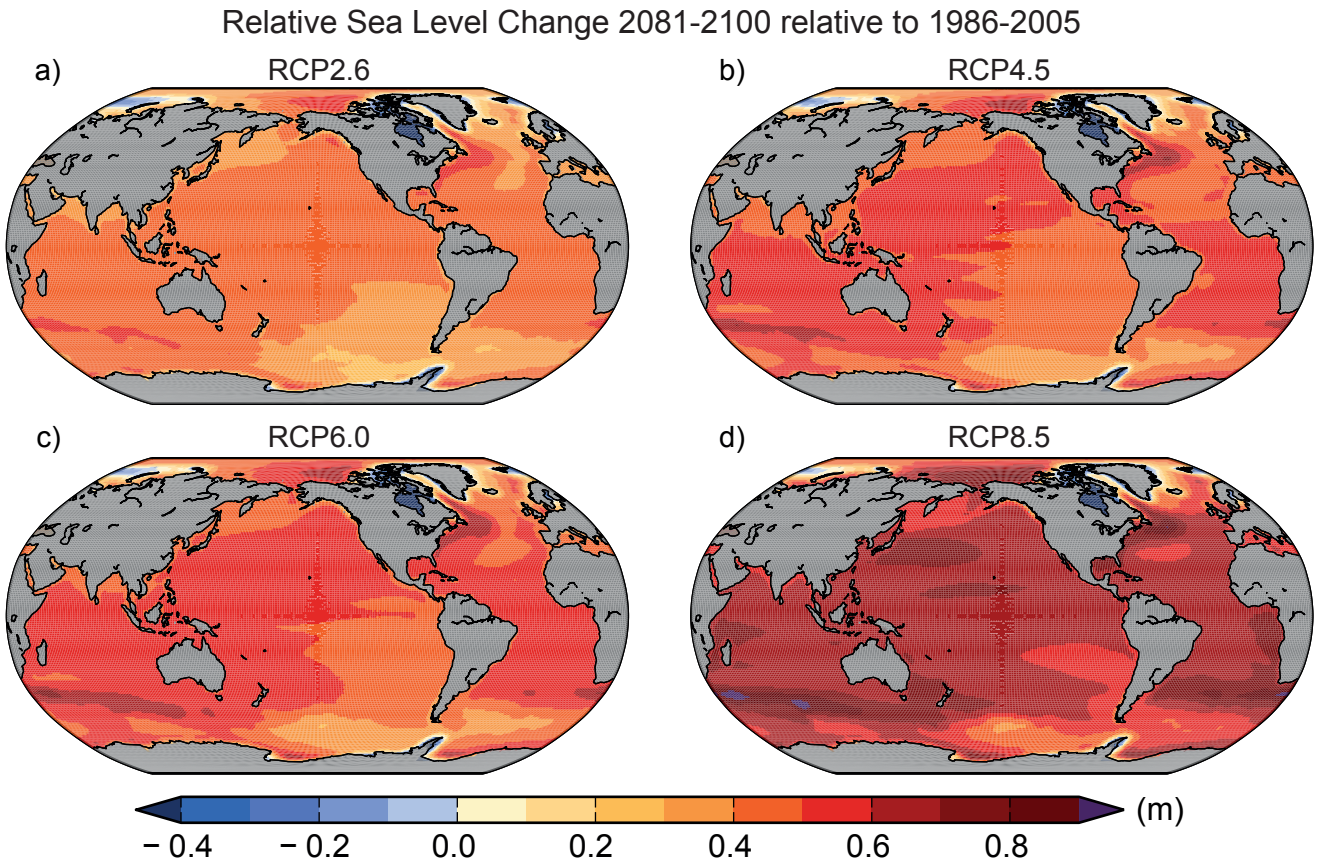

Figure TS.23 | Ensemble mean net regional relative sea level change (metres) evaluated from 21 CMIP5 models for the RCP scenarios (a) 2.6, (b) 4.5, (c) 6.0 and (d) 8.5 between 1986–2005 and 2081–2100. Each map includes effects of atmospheric loading, plus land-ice, glacial isostatic adjustment (GIA) and terrestrial water sources. {Figure 13.20}

Thematic Focus Elements

TFE.8 | Climate Targets and Stabilization

The concept of stabilization is strongly linked to the ultimate objective of the United Nations Framework Convention on Climate Change (UNFCCC), which is 'to achieve […] stabilization of greenhouse gas concentrations in the atmosphere at a level that would prevent dangerous anthropogenic interference with the climate system'. Recent policy discussions focused on limits to a global temperature increase, rather than to greenhouse gas (GHG) concentrations, as climate targets in the context of the UNFCCC objectives. The most widely discussed is that of 2°C, that is, to limit global temperature increase relative to pre-industrial times to below 2°C, but targets other than 2°C have been proposed (e.g., returning warming to well below 1.5°C global warming relative to pre-industrial, or returning below an atmospheric carbon dioxide (CO_2) concentration of 350 ppm). Climate targets generally mean avoiding a warming beyond a predefined threshold. Climate impacts, however, are geographically diverse and sector specific, and no objective threshold defines when dangerous interference is reached. Some changes may be delayed or irreversible, and some impacts could be beneficial. It is thus not possible to define a single critical objective threshold without value judgements and without assumptions on how to aggregate current and future costs and benefits. This TFE does not advocate or defend any threshold or objective, nor does it judge the economic or political feasibility of such goals, but assesses, based on the current understanding of climate and carbon cycle feedbacks, the climate projections following the Representative Concentration Pathways (RCPs) in the context of climate targets, and the implications of different long-term temperature stabilization objectives on allowed carbon emissions. Further below it is highlighted that temperature stabilization does not necessarily imply stabilization of the entire Earth system. {12.5.4}

Temperature targets imply an upper limit on the total radiative forcing (RF). Differences in RF between the four RCP scenarios are relatively small up to 2030, but become very large by the end of the 21st century and dominated by CO_2 forcing. Consequently, in the near term, global mean surface temperatures (GMSTs) are projected to continue to rise at a similar rate for the four RCP scenarios. Around the mid-21st century, the rate of global warming begins to be more strongly dependent on the scenario. By the end of the 21st century, global mean temperatures will be warmer than present day under all the RCPs, global temperature change being largest (>0.3°C per decade) in the highest RCP8.5 and significantly lower in RCP2.6, particularly after about 2050 when global surface temperature response stabilizes (and declines thereafter) (see Figure TS.15). {11.3.1, 12.3.3, 12.4.1}

In the near term (2016–2035), global mean surface warming is *more likely than not* to exceed 1°C and *very unlikely* to be more than 1.5°C relative to the average from year 1850 to 1900 (assuming 0.61°C warming from 1850-1900 to 1986–2005) (*medium confidence*). By the end of the 21st century (2081–2100), global mean surface warming, relative to 1850-1900, is *likely* to exceed 1.5°C for RCP4.5, RCP6.0 and RCP8.5 (*high confidence*) and is *likely* to exceed 2°C for RCP6.0 and RCP8.5 (*high confidence*). It is *more likely than not* to exceed 2°C for RCP4.5 (*medium confidence*). Global mean surface warming above 2°C under RCP2.6 is *unlikely* (*medium confidence*). Global mean surface warming above 4°C by 2081–2100 is *unlikely* in all RCPs (*high confidence*) except for RCP8.5 where it is *about as likely as not* (*medium confidence*). {11.3.6, 12.4.1; Table 12.3}

Continuing GHG emissions beyond 2100 as in the RCP8.5 extension induces a total RF above 12 W m^{-2} by 2300, with global warming reaching 7.8 [3.0 to 12.6] °C for 2281–2300 relative to 1986–2005. Under the RCP4.5 extension, where radiative forcing is kept constant (around 4.5 W m^{-2}) beyond 2100, global warming reaches 2.5 [1.5 to 3.5] °C. Global warming reaches 0.6 [0.0 to 1.2] °C under the RCP2.6 extension where sustained negative emissions lead to a further decrease in RF, reaching values below present-day RF by 2300. See also Box TS.7. {12.3.1, 12.4.1, 12.5.1}

The total amount of anthropogenic CO_2 released in the atmosphere since pre-industrial (often termed cumulative carbon emission, although it applies only to CO_2 emissions) is a good indicator of the atmospheric CO_2 concentration and hence of the global warming response. The ratio of GMST change to total cumulative anthropogenic CO_2 emissions is relatively constant over time and independent of the scenario. This near-linear relationship between total CO_2 emissions and global temperature change makes it possible to define a new quantity, the transient climate response to cumulative carbon emission (TCRE), as the transient GMST change for a given amount of cumulated anthropogenic CO_2 emissions, usually 1000 PgC (TFE.8, Figure 1). TCRE is model dependent, as it is a function of the cumulative CO_2 airborne fraction and the transient climate response, both quantities varying significantly across models. Taking into account the available information from multiple lines of evidence (observations, models and process understanding), the near linear relationship between cumulative CO_2 emissions and peak global mean temperature is

(continued on next page)

TFE.8 (continued)

well established in the literature and robust for cumulative total CO_2 emissions up to about 2000 PgC. It is consistent with the relationship inferred from past cumulative CO_2 emissions and observed warming, is supported by process understanding of the carbon cycle and global energy balance, and emerges as a robust result from the entire hierarchy of models. Expert judgment based on the available evidence suggests that TCRE is *likely* between 0.8°C and 2.5°C per 1000 PgC, for cumulative emissions less than about 2000 PgC until the time at which temperature peaks (TFE.8, Figure 1a). {6.4.3, 12.5.4; Box 12.2}

CO_2-induced warming is projected to remain approximately constant for many centuries following a complete cessation of emissions. A large fraction of climate change is thus irreversible on a human time scale, except if net anthropogenic CO_2 emissions were strongly negative over a sustained period. Based on the assessment of TCRE (assuming a normal distribution with a ±1 standard deviation range of 0.8 to 2.5°C per 1000 PgC), limiting the warming caused by anthropogenic CO_2 emissions alone (i.e., ignoring other radiative forcings) to less than 2°C since the period 1861–1880 with a probability of >33%, >50% and >66%, total CO_2 emissions from all anthropogenic sources would need to be below a cumulative budget of about 1570 PgC, 1210 PgC and 1000 PgC since 1870, respectively. An amount of 515 [445 to 585] PgC was emitted between 1870 and 2011 (TFE.8, Figure 1a,b). Higher emissions in earlier decades therefore imply lower or even negative emissions later on. Accounting for non-CO_2 forcings contributing to peak warming implies lower cumulated CO_2 emissions. Non-CO_2 forcing constituents are important, requiring either assumptions on how CO_2 emission reductions are linked to changes in other forcings, or separate emission budgets and climate modelling for short-lived and long-lived gases. So far, not many studies have considered non-CO_2 forcings. Those that do consider them found significant effects, in particular warming of several tenths of a degree for abrupt reductions in emissions of short-lived species, like aerosols. Accounting for an unanticipated release of GHGs from permafrost or methane hydrates, not included in studies assessed here, would also reduce the anthropogenic CO_2 emissions compatible with a given temperature target. Requiring a higher likelihood of temperatures remaining below a given temperature target would further reduce the compatible emissions (TFE.8, Figure 1c). When accounting for the non-CO_2 forcings as in the RCP scenarios, compatible carbon emissions since 1870 are reduced to about 900 PgC, 820 PgC and 790 PgC to limit warming to less than 2°C since the period 1861–1880 with a probability of >33%, >50%, and >66%, respectively. These estimates were derived by computing the fraction of the Coupled Model Intercomparison Project Phase 5 (CMIP5) Earth System Models (ESMs) and Earth System Models of Intermediate Complexity (EMICs) that stay below 2°C for given cumulative emissions following RCP8.5, as shown in TFE.8 Fig. 1c. The non-CO_2 forcing in RCP8.5 is higher than in RCP2.6. Because all likelihood statements in calibrated IPCC language are open intervals, the estimates provided are thus both conservative and consistent choices valid for non-CO_2 forcings across all RCP scenarios. There is no RCP scenario which limits warming to 2°C with probabilities of >33% or >50%, and which could be used to directly infer compatible cumulative emissions. For a probability of >66% RCP2.6 can be used as a comparison. Combining the average back-calculated fossil fuel carbon emissions for RCP2.6 between 2012 and 2100 (270 PgC) with the average historical estimate of 515 PgC gives a total of 785 PgC, i.e., 790 PgC when rounded to 10 PgC. As the 785 PgC estimate excludes an explicit assessment of future land-use change emissions, the 790 PgC value also remains a conservative estimate consistent with the overall likelihood assessment. The ranges of emissions for these three likelihoods based on the RCP scenarios are rather narrow, as they are based on a single scenario and on the limited sample of models available (TFE.8 Fig. 1c). In contrast to TCRE they do not include observational constraints or account for sources of uncertainty not sampled by the models. The concept of a fixed cumulative CO_2 budget holds not just for 2°C, but for any temperature level explored with models so far (up to about 5°C, see Figures 12.44 to 12.46). Higher temperature targets would allow larger cumulative budgets, while lower temperature target would require lower cumulative budgets (TFE.8, Figure 1). {6.3.1, 12.5.2, 12.5.4}

The climate system has multiple time scales, ranging from annual to multi-millennial, associated with different thermal and carbon reservoirs. These long time scales induce a commitment warming 'already in the pipe-line'. Stabilization of the forcing would not lead to an instantaneous stabilization of the warming. For the RCP scenarios and their extensions to 2300, the fraction of realized warming, at that time when RF stabilizes, would be about 75 to 85% of the equilibrium warming. For a 1% yr^{-1} CO_2 increase to 2 × CO_2 or 4 × CO_2 and constant forcing thereafter, the fraction of realized warming would be much smaller, about 40 to 70% at the time when the forcing is kept constant. Owing to the long time scales in the deep ocean, full equilibrium is reached only after hundreds to thousands of years. {12.5.4}

(continued on next page)

TFE.8 (continued)

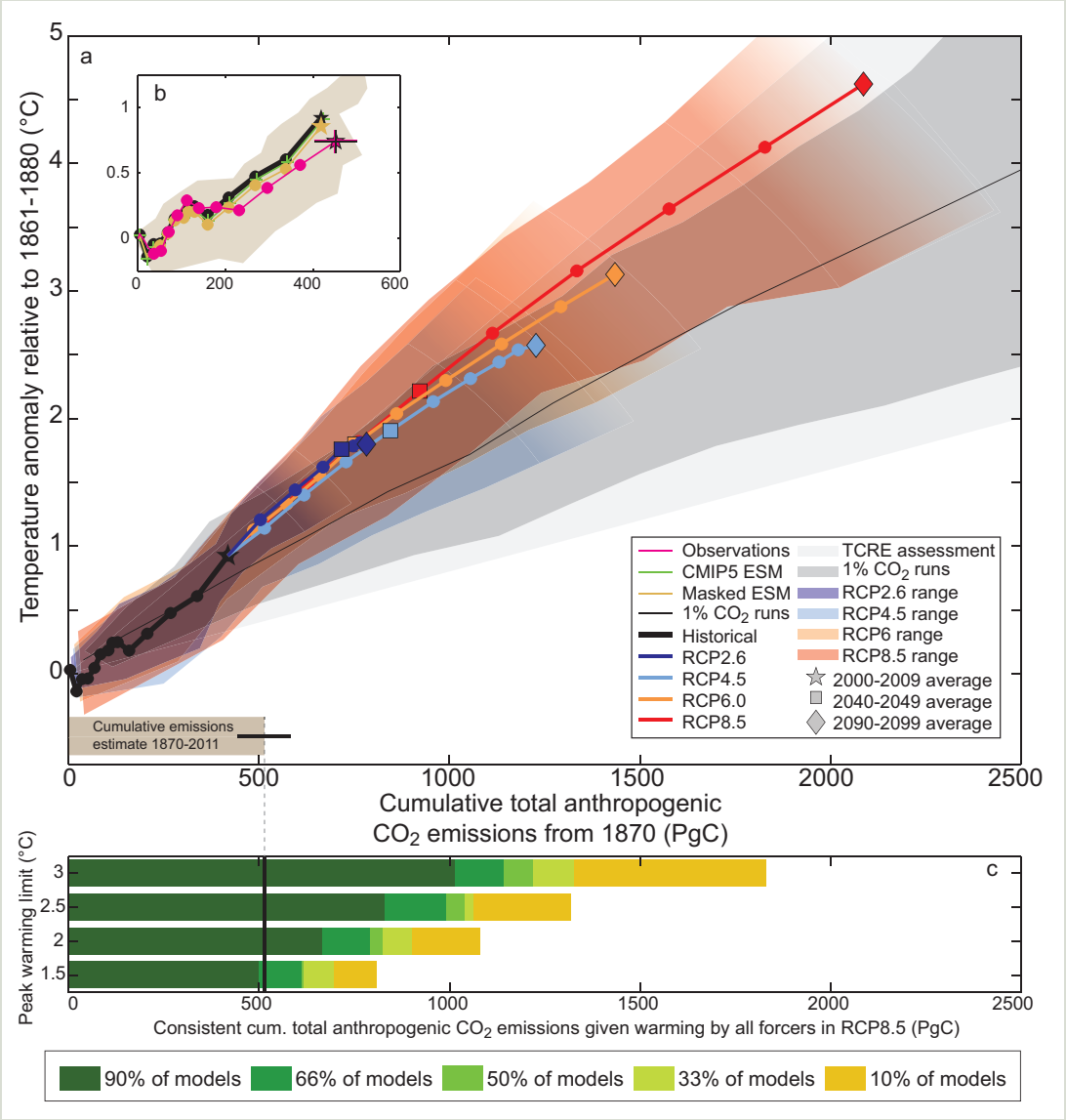

TFE.8, Figure 1 | Global mean temperature increase since 1861–1880 as a function of cumulative total global CO_2 emissions from various lines of evidence. (a) Decadal average results are shown over all CMIP5 Earth System Model of Intermediate Complexity (EMICs) and Earth System Models (ESMs) for each RCP respectively, with coloured lines (multi-model average), decadal markers (dots) and with three decades (2000–2009, 2040–2049 and 2090–2099) highlighted with a star, square and diamond, respectively. The historical time period up to decade 2000–2009 is taken from the CMIP5 historical runs prolonged by RCP8.5 for 2006–2010 and is indicated with a black thick line and black symbols. Coloured ranges illustrate the model spread (90% range) over all CMIP5 ESMs and EMICs and do not represent a formal uncertainty assessment. Ranges are filled as long as data of all models is available and until peak temperature. They are faded out for illustrative purposes afterward. CMIP5 simulations with 1% yr^{-1} CO_2 increase only are illustrated by the dark grey area (range definition similar to RCPs above) and the black thin line (multi-model average). The light grey cone represents this Report's assessment of the transient climate response to emissions (TCRE) from CO_2 only. Estimated cumulative historical CO_2 emissions from 1870 to 2011 with associated uncertainties are illustrated by the grey bar at the bottom of (a). (b) Comparison of historical model results with observations. The magenta line and uncertainty ranges are based on observed emissions from Carbon Dioxide Information Analysis Center (CDIAC) extended by values of the Global Carbon project until 2010 and observed temperature estimates of the Hadley Centre/Climatic Research Unit gridded surface temperature data set 4 (HadCRUT4). The uncertainties in the last decade of observations are based on the assessment in this report. The black thick line is identical to the one in (a). The thin green line with crosses is as the black line but for ESMs only. The yellow-brown line and range show these ESM results until 2010, when corrected for HadCRUT4's incomplete geographical coverage over time. All values are given relative to the 1861–1880 base period. All time-series are derived from decadal averages to illustrate the long-term trends. Note that observations are in addition subject to internal climate variability, adding an uncertainty of about 0.1°C. (c) Cumulative CO_2 emissions over the entire industrial era, consistent with four illustrative peak global temperature limits (1.5°C, 2°C, 2.5°C and 3°C, respectively) when taking into account warming by all forcers. Horizontal bars indicate consistent cumulative emission budgets as a function of the fraction of models (CMIP5 ESMs and EMICs) that at least hold warming below a given temperature limit. Note that the fraction of models cannot be interpreted as a probability. The budgets are derived from the RCP8.5 runs, with relative high non-CO_2 forcing over the 21st century. If non-CO_2 are significantly reduced, the CO_2 emissions compatible with a specific temperature limit might be slightly higher, but only to a very limited degree, as illustrated by the other coloured lines in (a), which assume significantly lower non-CO_2 forcing. Further detail regarding the related Figure SPM.10 is given in the TS Supplementary Material. {Figure 12.45}

TFE.8 (continued)

The commitment to past emissions is a persistent warming for hundreds of years, continuing at about the level of warming that has been realized when emissions were ceased. The persistence of this CO_2-induced warming after emission have ceased results from a compensation between the delayed commitment warming described above and the slow reduction in atmospheric CO_2 resulting from ocean and land carbon uptake. This persistence of warming also results from the nonlinear dependence of RF on atmospheric CO_2, that is, the relative decrease in forcing being smaller than the relative decrease in CO_2 concentration. For high climate sensitivities, and in particular if sulphate aerosol emissions are eliminated at the same time as GHG emissions, the commitment from past emission can be strongly positive, and is a superposition of a fast response to reduced aerosols emissions and a slow response to reduced CO_2. {12.5.4}

Stabilization of global temperature does not imply stabilization for all aspects of the climate system. Processes related to vegetation change, changes in the ice sheets, deep ocean warming and associated sea level rise and potential feedbacks linking, for example, ocean and the ice sheets have their own intrinsic long time scales. Ocean acidification will *very likely* continue in the future as long as the oceans will continue to take up atmospheric CO_2. Committed land ecosystem carbon cycle changes will manifest themselves further beyond the end of the 21st century. It is *virtually certain* that global mean sea level rise will continue beyond 2100, with sea level rise due to thermal expansion to continue for centuries to millennia. Global mean sea level rise depends on the pathway of CO_2 emissions, not only on the cumulative total; reducing emissions earlier rather than later, for the same cumulative total, leads to a larger mitigation of sea level rise. {6.4.4, 12.5.4, 13.5.4}

TS.5.8 Climate Phenomena and Regional Climate Change

This section assesses projected changes over the 21st century in large-scale climate phenomena that affect regional climate (Table TS.2). Some of these phenomena are defined by climatology (e.g., monsoons), and some by interannual variability (e.g., El Niño), the latter affecting climate extremes such as floods, droughts and heat waves. Changes in statistics of weather phenomena such as tropical cyclones and extratropical storms are also summarized here. {14.8}

TS.5.8.1 Monsoon Systems

Global measures of monsoon by the area and summer precipitation are *likely* to increase in the 21st century, while the monsoon circulation weakens. Monsoon onset dates are *likely* to become earlier or not to change much while monsoon withdrawal dates are *likely* to delay, resulting in a lengthening of the monsoon season in many regions (Figure TS.24). The increase in seasonal mean precipitation is pronounced in the East and South Asian summer monsoons while the change in other monsoon regions is subject to larger uncertainties. {14.2.1}

There is *medium confidence* that monsoon-related interannual rainfall variability will increase in the future. Future increase in precipitation extremes related to the monsoon is *very likely* in South America, Africa, East Asia, South Asia, Southeast Asia and Australia. {14.2.1, 14.8.5, 14.8.7, 14.8.9, 14.8.11–14.8.13}

There is *medium confidence* that overall precipitation associated with the Asian-Australian monsoon will increase but with a north–south asymmetry: Indian monsoon rainfall is projected to increase, while projected changes in the Australian summer monsoon rainfall are small. There is *medium confidence* in that the Indian summer monsoon circulation weakens, but this is compensated by increased atmospheric moisture content, leading to more rainfall. For the East Asian summer monsoon, both monsoon circulation and rainfall are projected to increase. {14.2.2, 14.8.9, 14.8.11, 14.8.13}

There is *low confidence* in projections of the North American and South American monsoon precipitation changes, but *medium confidence* that the North American monsoon will arrive and persist later in the annual cycle, and *high confidence* in expansion of South American Monsoon area. {14.2.3, 14.8.3–14.8.5}

There is *low confidence* in projections of a small delay in the West African rainy season, with an intensification of late-season rains. The limited skills of model simulations for the region suggest *low confidence* in the projections. {14.2.4, 14.8.7}

TS.5.8.2 Tropical Phenomena

Precipitation change varies in space, increasing in some regions and decreasing in some others. The spatial distribution of tropical rainfall changes is *likely* shaped by the current climatology and ocean warming pattern. The first effect is to increase rainfall near the currently rainy regions, and the second effect increases rainfall where the ocean warming exceeds the tropical mean. There is *medium confidence* that tropical rainfall projections are more reliable for the seasonal than annual mean changes. {7.6.2, 12.4.5, 14.3.1}

There is *medium confidence* in future increase in seasonal mean precipitation on the equatorial flank of the Intertropical Convergence Zone and a decrease in precipitation in the subtropics including parts

Table TS.2 | Overview of projected regional changes and their relation to major climate phenomena. A phenomenon is considered relevant when there is both sufficient confidence that it has an influence on the given region, and when there is sufficient confidence that the phenomenon will change, particularly under the RCP4.5 or higher end scenarios. See Section 14.8 and Tables 14.2 and 14.3 for full assessment of the confidence in these changes, and their relevance for regional climate. {14.8; Tables 14.2, 14.3}

Regions	Projected Major Changes in Relation to Phenomena
Arctic {14.8.2}	Wintertime changes in temperature and precipitation resulting from the small projected increase in North Atlantic Oscillation (NAO); enhanced warming and sea ice melting; significant increase in precipitation by mid-century due mostly to enhanced precipitation in extratropical cyclones.
North America {14.8.3}	Monsoon precipitation will shift later in the annual cycle; increased precipitation in extratropical cyclones will lead to large increases in wintertime precipitation over the northern third of the continent; extreme precipitation increases in tropical cyclones making landfall along the western coast of USA and Mexico, the Gulf Mexico, and the eastern coast of USA and Canada.
Central America and Caribbean {14.8.4}	Projected reduction in mean precipitation and increase in extreme precipitation; more extreme precipitation in tropical cyclones making landfall along the eastern and western coasts.
South America {14.8.5}	A southward displaced South Atlantic Convergence Zone increases precipitation in the southeast; positive trend in the Southern Annular Mode displaces the extratropical storm track southward, decreasing precipitation in central Chile and increasing it at the southern tip of South America.
Europe and Mediterranean {14.8.6}	Enhanced extremes of storm-related precipitation and decreased frequency of storm-related precipitation over the eastern Mediterranean.
Africa {14.8.7}	Enhanced summer monsoon precipitation in West Africa; increased short rain in East Africa due to the pattern of Indian Ocean warming; increased rainfall extremes of landfall cyclones on the east coast (including Madagascar).
Central and North Asia {14.8.8}	Enhanced summer precipitation; enhanced winter warming over North Asia.
East Asia {14.8.9}	Enhanced summer monsoon precipitation; increased rainfall extremes of landfall typhoons on the coast; reduction in the midwinter suppression of extratropical cyclones.
West Asia {14.8.10}	Increased rainfall extremes of landfall cyclones on the Arabian Peninsula; decreased precipitation in northwest Asia due to a northward shift of extratropical storm tracks.
South Asia {14.8.11}	Enhanced summer monsoon precipitation; increased rainfall extremes of landfall cyclones on the coasts of the Bay of Bengal and Arabian Sea.
Southeast Asia {14.8.12}	Reduced precipitation in Indonesia during July to October due to the pattern of Indian Ocean warming; increased rainfall extremes of landfall cyclones on the coasts of the South China Sea, Gulf of Thailand and Andaman Sea.
Australia and New Zealand {14.8.13}	Summer monsoon precipitation may increase over northern Australia; more frequent episodes of the zonal South Pacific Convergence Zone may reduce precipitation in northeastern Australia; increased warming and reduced precipitation in New Zealand and southern Australia due to projected positive trend in the Southern Annular Mode; increased extreme precipitation associated with tropical and extratropical storms
Pacific Islands {14.8.14}	Tropical convergence zone changes affect rainfall and its extremes; more extreme precipitation associated with tropical cyclones
Antarctica {14.8.15}	Increased warming over Antarctic Peninsula and West Antarctic related to the positive trend in the Southern Annular Mode; increased precipitation in coastal areas due to a poleward shift of storm track.

of North and Central Americas, the Caribbean, South America, Africa and West Asia. There is *medium confidence* that the interannual occurrence of zonally oriented South Pacific Convergence Zone events will increase, leading possibly to more frequent droughts in the southwest Pacific. There is *medium confidence* that the South Atlantic Convergence Zone will shift southwards, leading to a precipitation increase over southeastern South America and a reduction immediately north of the convergence zone. {14.3.1, 14.8.3–14.8.5, 14.8.7, 14.8.11, 14.8.14}

The tropical Indian Ocean is *likely* to feature a zonal pattern with reduced warming and decreased rainfall in the east (including Indonesia), and enhanced warming and increased rainfall in the west (including East Africa). The Indian Ocean dipole mode of interannual variability is *very likely* to remain active, affecting climate extremes in East Africa, Indonesia and Australia. {14.3.3, 14.8.7, 14.8.12}

There is *low confidence* in the projections for the tropical Atlantic—both for the mean and interannual modes, because of large errors in model simulations in the region. Future projections in Atlantic hurricanes and tropical South American and West African precipitation are therefore of *low confidence*. {14.3.4, 14.6.1, 14.8.5,14.8.7}

It is currently not possible to assess how the Madden–Julian Oscillation will change owing to the poor skill in model simulations of this intraseasonal phenomenon and the sensitivity to ocean warming patterns. Future projections of regional climate extremes in West Asia, Southeast Asia and Australia are therefore of *low confidence*. {9.5.2, 14.3.4, 14.8.10, 14.8.12, 14.8.13}

TS.5.8.3 El Niño-Southern Oscillation

There is *high confidence* that the El Niño-Southern Oscillation (ENSO) will remain the dominant mode of natural climate variability in the 21st century with global influences in the 21st century, and that regional rainfall variability it induces *likely* intensifies. Natural variations of the amplitude and spatial pattern of ENSO are so large that *confidence* in any projected change for the 21st century remains *low*. The projected change in El Niño amplitude is small for both RCP4.5 and RCP8.5 compared to the spread of the change among models (Figure TS.25). Over the North Pacific and North America, patterns of temperature and precipitation anomalies related to El Niño and La Niña (teleconnections) are *likely* to move eastwards in the future (*medium confidence*), while *confidence* is *low* in changes in climate impacts on other regions including Central and South Americas, the Caribbean, Africa, most of Asia, Australia and most Pacific Islands. In a warmer climate, the increase in atmospheric moisture intensifies temporal variability

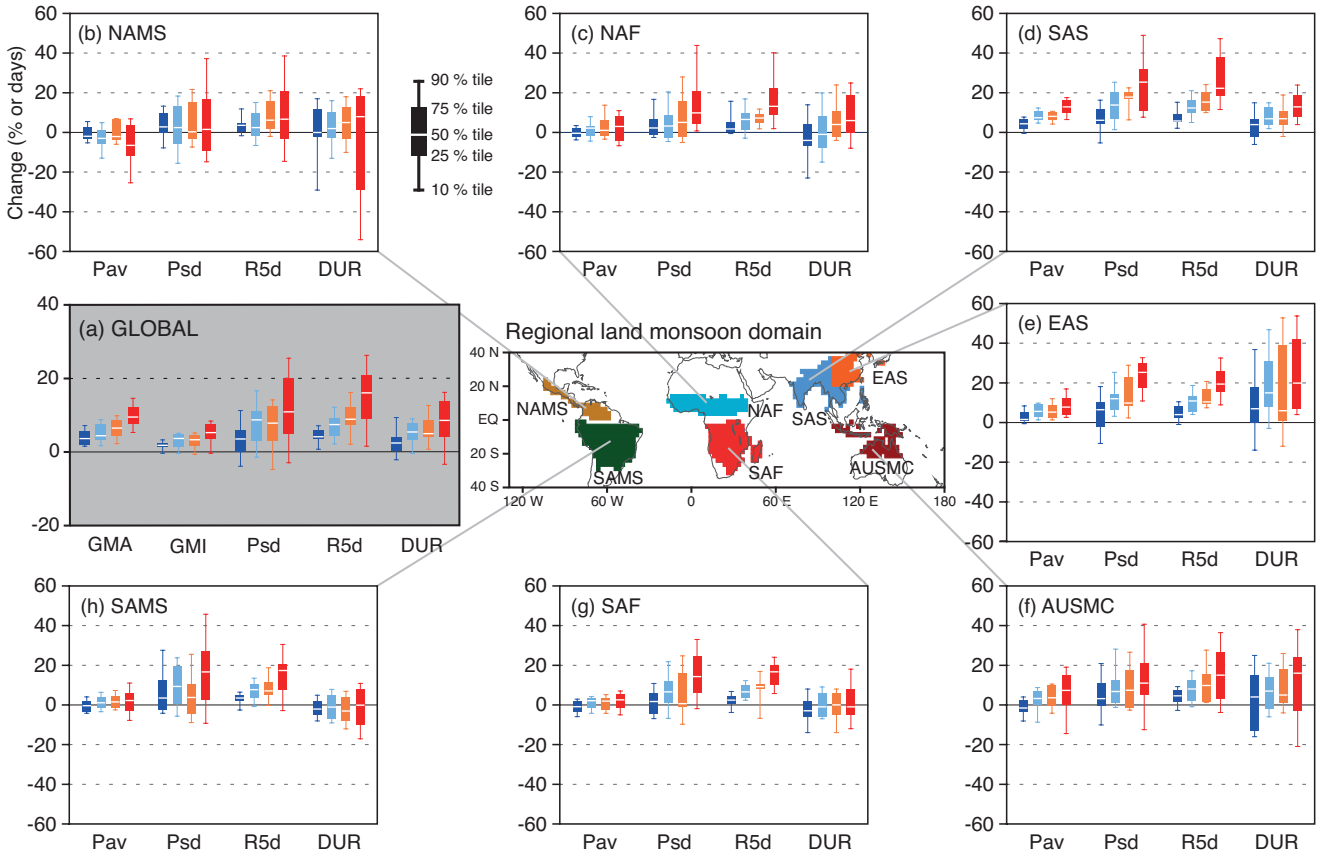

Figure TS.24 | Future change in monsoon statistics between the present-day (1986–2005) and the future (2080–2099) based on CMIP5 ensemble from RCP2.6 (dark blue; 18 models), RCP4.5 (blue; 24), RCP6.0 (yellow; 14), and RCP8.5 (red; 26) simulations. (a) GLOBAL: Global monsoon area (GMA), global monsoon intensity (GMI), standard deviation of inter-annual variability in seasonal precipitation (Psd), seasonal maximum 5-day precipitation total (R5d) and monsoon season duration (DUR). Regional land monsoon domains determined by 24 multi-model mean precipitation in the present-day. (b)–(h) Future change in regional land monsoon statistics: seasonal average precipitation (Pav), Psd, R5d, and DUR in (b) North America (NAMS), (c) North Africa (NAF), (d) South Asia (SAS), (e) East Asia (EAS), (f) Australia-Maritime continent (AUSMC), (g) South Africa (SAF) and (h) South America (SAMS). Units are % except for DUR (days). Box-and-whisker plots show the 10th, 25th, 50th, 75th and 90th percentiles. All the indices are calculated for the summer season (May to September for the Northern, and November to March for the Southern Hemisphere) over each model's monsoon domains. {Figures 14.3, 14.4, 14.6, 14.7}

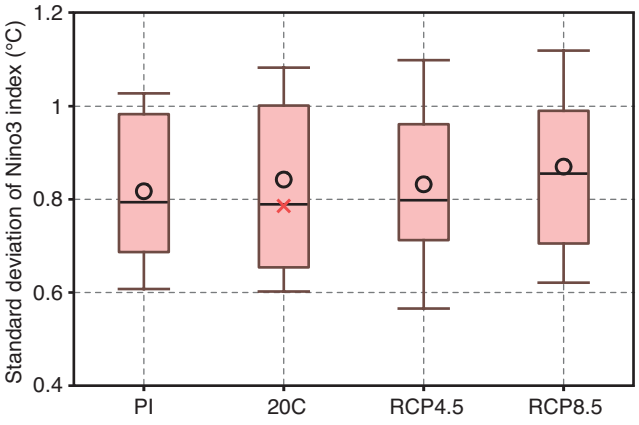

Figure TS.25 | Standard deviation in CMIP5 multi-model ensembles of sea surface temperature variability over the eastern equatorial Pacific Ocean (Nino3 region: 5°S to 5°N, 150°W to 90°W), a measure of El Niño amplitude, for the pre-industrial (PI) control and 20th century (20C) simulations, and 21st century projections using RCP4.5 and RCP8.5. Open circles indicate multi-model ensemble means, and the red cross symbol is the observed standard deviation for the 20th century. Box-and-whisker plots show the 16th, 25th, 50th, 75th and 84th percentiles. {Figure 14.14}

of precipitation even if atmospheric circulation variability remains the same. This applies to ENSO-induced precipitation variability but the possibility of changes in ENSO teleconnections complicates this general conclusion, making it somewhat regional-dependent. {12.4.5, 14.4, 14.8.3–14.8.5, 14.8.7, 14.8.9, 14.8.11–14.8.14}

TS.5.8.4 Cyclones

Projections for the 21st century indicate that it is *likely* that the global frequency of tropical cyclones will either decrease or remain essentially unchanged, concurrent with a *likely* increase in both global mean tropical cyclone maximum wind speed and rain rates (Figure TS.26). The influence of future climate change on tropical cyclones is *likely* to vary by region, but there is *low confidence* in region-specific projections. The frequency of the most intense storms will *more likely than not* increase in some basins. More extreme precipitation near the centers of tropical cyclones making landfall is projected in North and Central America, East Africa, West, East, South and Southeast Asia as well as in Australia and many Pacific islands (*medium confidence*). {14.6.1, 14.8.3, 14.8.4, 14.8.7, 14.8.9–14.8.14}

The global number of extratropical cyclones is *unlikely* to decrease by more than a few percent and future changes in storms are *likely* to be small compared to natural interannual variability and substantial variations between models. A small poleward shift is *likely* in the SH storm track but the magnitude of this change is model dependent. It is *unlikely* that the response of the North Atlantic storm track in climate projections is a simple poleward shift. There is *medium confidence* in a projected poleward shift in the North Pacific storm track. There is *low confidence* in the impact of storm track changes on regional climate at the surface. More precipitation in extratropical cyclones leads to a winter precipitation increase in Arctic, Northern Europe, North America and the mid-to-high-latitude SH. {11.3.2, 12.4.4, 14.6.2, 14.8.2, 14.8.3, 14.8.5, 14.8.6, 14.8.13, 14.8.15}

TS.5.8.5 Annular and Dipolar Modes of Variability

Future boreal wintertime North Atlantic Oscillation (NAO is *very likely* to exhibit large natural variations as observed in the past. The NAO is *likely* to become slightly more positive (on average), with some, but not very well documented implications for winter conditions in the Arctic, North America and Eurasia. The austral summer/autumn positive trend in Southern Annular Mode (SAM) is *likely* to weaken considerably as stratospheric ozone recovers through the mid-21st century with some, but not very well documented, implications for South America, Africa, Australia, New Zealand and Antarctica. {11.3.2, 14.5.2,14.8.5, 14.8.7, 14.8.13, 14.8.15}

TS.5.8.6 Additional Phenomena

It is *unlikely* that the Atlantic Multi-decadal Oscillation (AMO will change its behaviour as the mean climate changes. However, natural fluctuations in the AMO over the coming few decades are *likely* to influence regional climates at least as strongly as will human-induced changes with implications for Atlantic major hurricane frequency, the West African monsoon and North American and European summer conditions. {14.2.4, 14.5.1, 14.6.1, 14.7.6, 14.8.2, 14.8.3, 14.8.6, 14.8.8}

There is *medium confidence* that the frequency of NH and SH blocking will not increase, while the trends in blocking intensity and persistence remain uncertain. {Box 14.2}

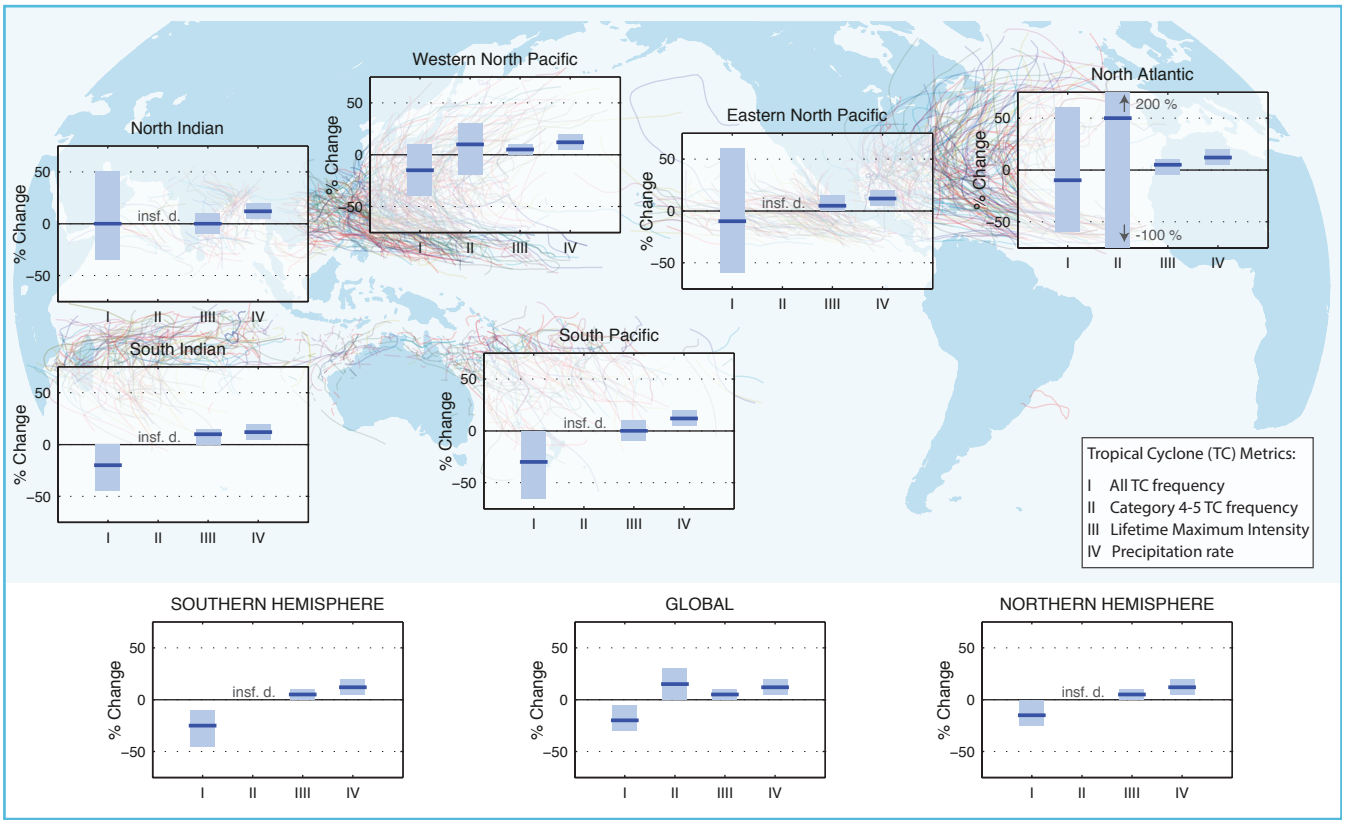

Figure TS.26 | Projected changes in tropical cyclone statistics. All values represent expected percent change in the average over period 2081–2100 relative to 2000–2019, under an A1B-like scenario, based on expert judgement after subjective normalization of the model projections. Four metrics were considered: the percent change in I) the total annual frequency of tropical storms, II) the annual frequency of Category 4 and 5 storms, III) the mean Lifetime Maximum Intensity (LMI; the maximum intensity achieved during a storm's lifetime) and IV) the precipitation rate within 200 km of storm center at the time of LMI. For each metric plotted, the solid blue line is the best guess of the expected percent change, and the coloured bar provides the 67% (*likely*) confidence interval for this value (note that this interval ranges across –100% to +200% for the annual frequency of Category 4 and 5 storms in the North Atlantic). Where a metric is not plotted, there are insufficient data (denoted X) available to complete an assessment. A randomly drawn (and coloured) selection of historical storm tracks are underlaid to identify regions of tropical cyclone activity. See Section 14.6.1 for details. {14.6.1}

Thematic Focus Elements

TFE.9 | Climate Extremes

Assessing changes in climate extremes poses unique challenges, not just because of the intrinsically rare nature of these events, but because they invariably happen in conjunction with disruptive conditions. They are strongly influenced by both small- and large-scale weather patterns, modes of variability, thermodynamic processes, land–atmosphere feedbacks and antecedent conditions. Much progress has been made since the IPCC Fourth Assessment Report (AR4) including the comprehensive assessment of extremes undertaken by the IPCC Special Report on Managing the Risk of Extreme Events and Disasters to Advance Climate Change Adaptation (SREX) but also because of the amount of observational evidence available, improvements in our understanding and the ability of models to simulate extremes. {1.3.3, 2.6, 7.6, 9.5.4}

For some climate extremes such as droughts, floods and heat waves, several factors need to be combined to produce an extreme event. Analyses of rarer extremes such as 1-in-20- to 1-in-100-year events using Extreme Value Theory are making their way into a growing body of literature. Other recent advances concern the notion of 'fraction of attributable risk' that aims to link a particular extreme event to specific causal relationships. {1.3.3, 2.6.1, 2.6.2, 10.6.2, 12.4.3; Box 2.4}

TFE.9, Table 1 indicates the changes that have been observed in a range of weather and climate extremes over the last 50 years, the assessment of the human contribution to those changes, and how those extremes are expected to change in the future. The table also compares the current assessment with that of the AR4 and the SREX where applicable. {2.6, 3.7, 10.6, 11.3, 12.4, 14.6}

Temperature Extremes, Heat Waves and Warm Spells

It is *very likely* that both maximum and minimum temperature extremes have warmed over most land areas since the mid-20th century. These changes are well simulated by current climate models, and it is *very likely* that anthropogenic forcing has affected the frequency of these extremes and *virtually certain* that further changes will occur. This supports AR4 and SREX conclusions although with greater confidence in the anthropogenic forcing component. {2.6.1, 9.5.4, 10.6.1, 12.4.3}

For land areas with sufficient data there has been an overall increase in the number of warm days and nights. Similar decreases are seen in the number of cold days and nights. It is *very likely* that increases in unusually warm days and nights and/or reductions in unusually cold days and nights including frosts have occurred over this period across most continents. Warm spells or heat waves containing consecutive extremely hot days or nights are often associated with quasi-stationary anticyclonic circulation anomalies and are also affected by pre-existing soil conditions and the persistence of soil moisture anomalies that can amplify or dampen heat waves particularly in moisture-limited regions. Most global land areas, with a few exceptions, have experienced more heat waves since the middle of the 20th century. Several studies suggest that increases in mean temperature account for most of the changes in heat wave frequency, however, heat wave intensity/amplitude is highly sensitive to changes in temperature variability and the shape of the temperature distribution and heat wave definition also plays a role. Although in some regions instrumental periods prior to the 1950s had more heat waves (e.g., USA), for other regions such as Europe, an increase in heat wave frequency in the period since the 1950s stands out in long historical temperature series. {2.6, 2.6.1, 5.5.1; Box 2.4; Tables 2.12, 2.13; FAQ 2.2}

The observed features of temperature extremes and heat waves are well simulated by climate models and are similar to the spread among observationally based estimates in most regions. Regional downscaling now offers credible information on the spatial scales required for assessing extremes and improvements in the simulation of the El Niño-Southern Oscillation from Coupled Model Intercomparison Project Phase 3 (CMIP3) to Phase 5 (CMIP5) and other large-scale phenomena is crucial. However simulated changes in frequency and intensity of extreme events is limited by observed data availability and quality issues and by the ability of models to reliably simulate certain feedbacks and mean changes in key features of circulation such as blocking. {2.6, 2.7, 9.4, 9.5.3, 9.5.4, 9.6, 9.6.1, 10.3, 10.6, 14.4; Box 14.2}

Since AR4, the understanding of mechanisms and feedbacks leading to changes in extremes has improved. There continues to be strengthening evidence for a human influence on the observed frequency of extreme temperatures and heat waves in some regions. Near-term (decadal) projections suggest *likely* increases in temperature extremes but with little distinguishable separation between emissions scenarios (TFE.9, Figure 1). Changes may proceed at

(continued on next page)

TFE.9, Table 1 | Extreme weather and climate events: Global-scale assessment of recent observed changes, human contribution to the changes and projected further changes for the early (2016–2035) and late (2081–2100) 21st century. Bold indicates where the AR5 (black) provides a revised* global-scale assessment from the Special Report on Managing the Risk of Extreme Events and Disasters to Advance Climate Change Adaptation (SREX, blue) or AR4 (red). Projections for early 21st century were not provided in previous assessment reports. Projections in the AR5 are relative to the reference period of 1986–2005, and use the new RCP scenarios unless otherwise specified. See the Glossary for definitions of extreme weather and climate events.

Phenomenon and direction of trend	Assessment that changes occurred (typically since 1950 unless otherwise indicated)	Assessment of a human contribution to observed changes	Likelihood of further changes	
			Early 21st century	Late 21st century
Warmer and/or fewer cold days and nights over most land areas	*Very likely* {2.6} *Very likely* *Very likely*	***Very likely*** {10.6} *Likely* *Likely*	*Likely* {11.3}	*Virtually certain* {12.4} *Virtually certain* *Virtually certain*
Warmer and/or more frequent hot days and nights over most land areas	*Very likely* {2.6} *Very likely* *Very likely*	***Very likely*** {10.6} *Likely* *Likely* (nights only)	*Likely* {11.3}	*Virtually certain* {12.4} *Virtually certain* *Virtually certain*
Warm spells/heat waves. Frequency and/or duration increases over most land areas	***Medium confidence*** on a global scale *Likely* in large parts of Europe, Asia and Australia {2.6} *Medium confidence* in many (but not all) regions *Likely*	***Likely***[a] {10.6} Not formally assessed *More likely than not*	Not formally assessed[b] {11.3}	*Very likely* {12.4} *Very likely* *Very likely*
Heavy precipitation events. Increase in the frequency, intensity, and/or amount of heavy precipitation	*Likely* more land areas with increases than decreases[c] {2.6} *Likely* more land areas with increases than decreases *Likely* over most land areas	***Medium confidence*** {7.6, 10.6} *Medium confidence* *More likely than not*	*Likely* over many land areas {11.3}	***Very likely*** over most of the mid-latitude land masses and over wet tropical regions {12.4} *Likely* over many areas *Very likely* over most land areas
Increases in intensity and/or duration of drought	***Low confidence*** on a global scale *Likely* changes in some regions[d] {2.6} *Medium confidence* in some regions *Likely* in many regions, since 1970[e]	***Low confidence*** {10.6} *Medium confidence*[f] *More likely than not*	*Low confidence*[g] {11.3}	***Likely*** *(medium confidence)* on a regional to global scale[h] {12.4} *Medium confidence* in some regions *Likely*[e]
Increases in intense tropical cyclone activity	***Low confidence*** in long term (centennial) changes *Virtually certain* in North Atlantic since 1970 {2.6} *Low confidence* *Likely* in some regions, since 1970	***Low confidence***[i] {10.6} *Low confidence* *More likely than not*	*Low confidence* {11.3}	***More likely than not*** in the Western North Pacific and North Atlantic[j] {14.6} *More likely than not* in some basins *Likely*
Increased incidence and/or magnitude of extreme high sea level	*Likely* (since 1970) {3.7} *Likely* (late 20th century) *Likely*	***Likely***[k] {3.7} *Likely*[k] *More likely than not*[k]	*Likely*[l] {13.7}	***Very likely***[l] {13.7} *Very likely*[m] *Likely*

* The direct comparison of assessment findings between reports is difficult. For some climate variables, different aspects have been assessed, and the revised guidance note on uncertainties has been used for the SREX and AR5. The availability of new information, improved scientific understanding, continued analyses of data and models, and specific differences in methodologies applied in the assessed studies, all contribute to revised assessment findings.

Notes:

[a] Attribution is based on available case studies. It is *likely* that human influence has more than doubled the probability of occurrence of some observed heat waves in some locations.

[b] Models project near-term increases in the duration, intensity and spatial extent of heat waves and warm spells.

[c] In most continents, *confidence* in trends is not higher than *medium* except in North America and Europe where there have been *likely* increases in either the frequency or intensity of heavy precipitation with some seasonal and/or regional variation. It is *very likely* that there have been increases in central North America.

[d] The frequency and intensity of drought has *likely* increased in the Mediterranean and West Africa and *likely* decreased in central North America and north-west Australia.

[e] AR4 assessed the area affected by drought.

[f] SREX assessed *medium confidence* that anthropogenic influence had contributed to some changes in the drought patterns observed in the second half of the 20th century, based on its attributed impact on precipitation and temperature changes. SREX assessed *low confidence* in the attribution of changes in droughts at the level of single regions.

[g] There is *low confidence* in projected changes in soil moisture.

[h] Regional to global-scale projected decreases in soil moisture and increased agricultural drought are *likely* (*medium confidence*) in presently dry regions by the end of this century under the RCP8.5 scenario. Soil moisture drying in the Mediterranean, Southwest USA and southern African regions is consistent with projected changes in Hadley circulation and increased surface temperatures, so there is *high confidence* in *likely* surface drying in these regions by the end of this century under the RCP8.5 scenario.

[i] There is *medium confidence* that a reduction in aerosol forcing over the North Atlantic has contributed at least in part to the observed increase in tropical cyclone activity since the 1970s in this region.

[j] Based on expert judgment and assessment of projections which use an SRES A1B (or similar) scenario.

[k] Attribution is based on the close relationship between observed changes in extreme and mean sea level.

[l] There is *high confidence* that this increase in extreme high sea level will primarily be the result of an increase in mean sea level. There is *low confidence* in region-specific projections of storminess and associated storm surges.

[m] SREX assessed it to be *very likely* that mean sea level rise will contribute to future upward trends in extreme coastal high water levels.

TFE.9 (continued)

a different rate than the mean warming however, with several studies showing that projected European high-percentile summer temperatures will warm faster than mean temperatures. Future changes associated with the warming of temperature extremes in the long-term are *virtually certain* and scale with the strength of emissions scenario, that is, greater anthropogenic emissions correspond to greater warming of extremes (TFE.9, Figure 1). For high-emissions scenarios, it is *likely* that, in most land regions, a current 1-in-20-year maximum temperature event

(continued on next page)

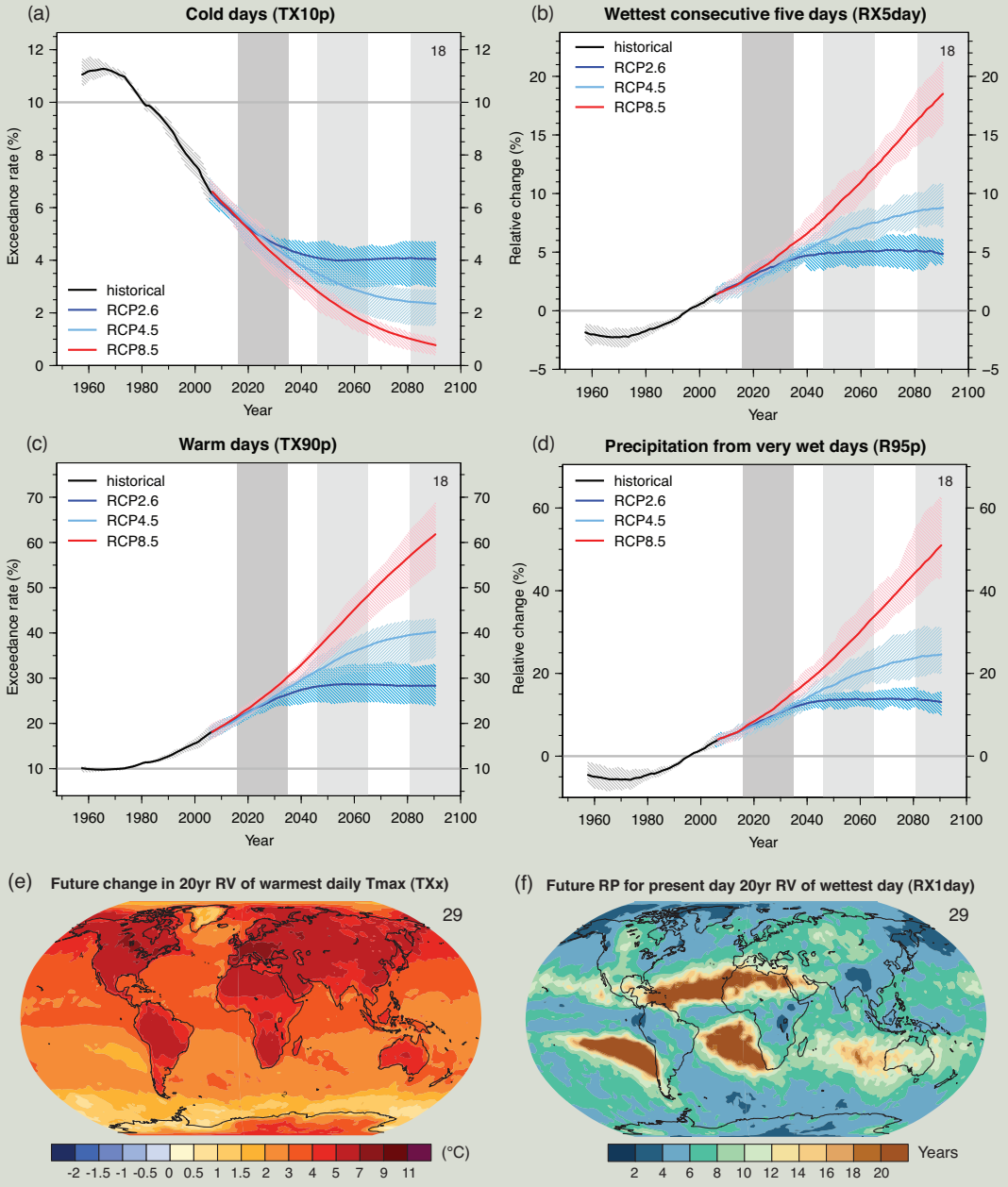

TFE.9, Figure 1 | Global projections of the occurrence of (a) cold days (TX10p)- percentage of days annually with daily maximum surface air temperature (Tmax) below the 10th percentile of Tmax for 1961 to 1990, (b) wettest consecutive 5 days (RX5day) —percentage change relative to 1986–2005 in annual maximum consecutive 5-day precipitation totals, (c) warm days (TX90p)—percentage of days annually with daily maximum surface air temperature (Tmax) exceeding the 90th percentile of Tmax for 1961 to 1990 and (d) very wet day precipitation (R95p)—percentage change relative to 1986–2005 of annual precipitation from days >95th percentile. Results are shown from CMIP5 for the RCP2.6, RCP4.5 and RCP8.5 scenarios. Solid lines indicate the ensemble median and shading indicates the interquartile spread between individual projections (25th and 75th percentiles). Maps show (e) the change from 1986–2005 to 2081–2100 in 20-year return values (RV) of daily maximum temperatures, TXx, and (f) the 2081–2100 return period (RP) for rare daily precipitation values, RX1day, that have a 20-year return period during 1986–2005. Both maps are based on the CMIP5 RCP8.5 scenario. The number of models used to calculate the multi-model mean is indicated in each panel. See Box 2.4, Table 1 for index definitions. {Figures 11.17, 12.14, 12.26, 12.27}

TFE.9 (continued)

will at least double in frequency but in many regions will become an annual or a 1-in-2-year event by the end of the 21st century. The magnitude of both high and low temperature extremes is expected to increase at least at the same rate as the mean, but with 20-year return values for low temperature events projected to increase at a rate greater than winter mean temperatures in most regions. {10.6.1, 11.3.2, 12.4.3}

Precipitation Extremes

It is *likely* that the number of heavy precipitation events over land has increased in more regions than it has decreased in since the mid-20th century, and there is *medium confidence* that anthropogenic forcing has contributed to this increase. {2.6.2, 10.6.1}

There has been substantial progress between CMIP3 and CMIP5 in the ability of models to simulate more realistic precipitation extremes. However, evidence suggests that the majority of models underestimate the sensitivity of extreme precipitation to temperature variability or trends especially in the tropics, which implies that models may underestimate the projected increase in extreme precipitation in the future. While progress has been made in understanding the processes that drive extreme precipitation, challenges remain in quantifying cloud and convective effects in models for example. The complexity of land surface and atmospheric processes limits confidence in regional projections of precipitation change, especially over land, although there is a component of a 'wet-get-wetter' and 'dry-get-drier' response over oceans at the large scale. Even so, there is *high confidence* that, as the climate warms, extreme precipitation rates (e.g., on daily time scales) will increase faster than the time average. Changes in local extremes on daily and sub-daily time scales are expected to increase by roughly 5 to 10% per °C of warming (*medium confidence*). {7.6, 9.5.4}

For the near and long term, CMIP5 projections confirm a clear tendency for increases in heavy precipitation events in the global mean seen in the AR4, but there are substantial variations across regions (TFE.9, Figure 1). Over most of the mid-latitude land masses and over wet tropical regions, extreme precipitation will *very likely* be more intense and more frequent in a warmer world. {11.3.2, 12.4.5}

Floods and Droughts

There continues to be a lack of evidence and thus *low confidence* regarding the sign of trend in the magnitude and/or frequency of floods on a global scale over the instrumental record. There is *high confidence* that past floods larger than those recorded since 1900 have occurred during the past five centuries in northern and central Europe, western Mediterranean region, and eastern Asia. There is *medium confidence* that modern large floods are comparable to or surpass historical floods in magnitude and/or frequency in the Near East, India and central North America. {2.6.2, 5.5.5}

Compelling arguments both for and against significant increases in the land area affected by drought and/or dryness since the mid-20th century have resulted in a *low confidence* assessment of observed and attributable large-scale trends. This is due primarily to a lack and quality of direct observations, dependencies of inferred trends on the index choice, geographical inconsistencies in the trends and difficulties in distinguishing decadal scale variability from long term trends. On millennial time scales, there is *high confidence* that proxy information provides evidence of droughts of greater magnitude and longer duration than observed during the 20th century in many regions. There is *medium confidence* that more megadroughts occurred in monsoon Asia and wetter conditions prevailed in arid Central Asia and the South American monsoon region during the Little Ice Age (1450 to 1850) compared to the Medieval Climate Anomaly (950 to 1250). {2.6.2, 5.5.4, 5.5.5, 10.6.1}

Under the Representative Concentration Pathway RCP8.5, projections by the end of the century indicate an increased risk of drought is *likely* (*medium confidence*) in presently dry regions linked to regional to global-scale projected decreases in soil moisture. Soil moisture drying is most prominent in the Mediterranean, Southwest USA, and southern Africa, consistent with projected changes in the Hadley Circulation and increased surface temperatures, and surface drying in these regions is *likely* (*high confidence*) by the end of the century under RCP8.5. {12.4.5}

Extreme Sea Level

It is *likely* that the magnitude of extreme high sea level events has increased since 1970 and that most of this rise can be explained by increases in mean sea level. When mean sea level changes is taken into account, changes in extreme high sea levels are reduced to less than 5 mm y^{r-1} at 94% of tide gauges. In the future it is *very likely* that there will be a significant increase in the occurrence of sea level extremes and similarly to past observations, this increase will primarily be the result of an increase in mean sea level. {3.7.5, 13.7.2}

(continued on next page)

TFE.9 (continued)

Tropical and Extratropical Cyclones

There is *low confidence* in long-term (centennial) changes in tropical cyclone activity, after accounting for past changes in observing capabilities. However over the satellite era, increases in the frequency and intensity of the strongest storms in the North Atlantic are robust (*very high confidence*). However, the cause of this increase is debated and there is *low confidence* in attribution of changes in tropical cyclone activity to human influence owing to insufficient observational evidence, lack of physical understanding of the links between anthropogenic drivers of climate and tropical cyclone activity and the low level of agreement between studies as to the relative importance of internal variability, and anthropogenic and natural forcings. {2.6.3, 10.6.1, 14.6.1}

Some high-resolution atmospheric models have realistically simulated tracks and counts of tropical cyclones and models generally are able to capture the general characteristics of storm tracks and extratropical cyclones with evidence of improvement since the AR4. Storm track biases in the North Atlantic have improved slightly, but models still produce a storm track that is too zonal and underestimate cyclone intensity. {9.4.1, 9.5.4}

While projections indicate that it is *likely* that the global frequency of tropical cyclones will either decrease or remain essentially unchanged, concurrent with a *likely* increase in both global mean tropical cyclone maximum wind speed and rainfall rates, there is lower confidence in region-specific projections of frequency and intensity. However, due to improvements in model resolution and downscaling techniques, it is *more likely than not* that the frequency of the most intense storms will increase substantially in some basins under projected 21st century warming (see Figure TS.26). {11.3.2, 14.6.1}

Research subsequent to the AR4 and SREX continues to support a *likely* poleward shift of storm tracks since the 1950s. However over the last century there is *low confidence* of a clear trend in storminess due to inconsistencies between studies or lack of long-term data in some parts of the world (particularly in the Southern Hemisphere (SH)). {2.6.4, 2.7.6}

Despite systematic biases in simulating storm tracks, most models and studies are in agreement that the global number of extratropical cyclones is *unlikely* to decrease by more than a few per cent. A small poleward shift is *likely* in the SH storm track. It is *more likely than not* (*medium confidence*) for a projected poleward shift in the North Pacific storm track but it is *unlikely* that the response of the North Atlantic storm track is a simple poleward shift. There is *low confidence* in the magnitude of regional storm track changes, and the impact of such changes on regional surface climate. {14.6.2}

TS.6 Key Uncertainties

This final section of the Technical Summary provides readers with a short overview of key uncertainties in the understanding of the climate system and the ability to project changes in response to anthropogenic influences. The overview is not comprehensive and does not describe in detail the basis for these findings. These are found in the main body of this Technical Summary and in the underlying chapters to which each bullet points in the curly brackets.

TS.6.1 Key Uncertainties in Observation of Changes in the Climate System

- There is only *medium* to *low confidence* in the rate of change of tropospheric warming and its vertical structure. Estimates of tropospheric warming rates encompass surface temperature warming rate estimates. There is *low confidence* in the rate and vertical structure of the stratospheric cooling. {2.4.4}

- *Confidence* in global precipitation change over land is *low* prior to 1951 and *medium* afterwards because of data incompleteness. {2.5.1}

- Substantial ambiguity and therefore *low confidence* remains in the observations of global-scale cloud variability and trends. {2.5.6}

- There is *low confidence* in an observed global-scale trend in drought or dryness (lack of rainfall), due to lack of direct observations, methodological uncertainties and choice and geographical inconsistencies in the trends. {2.6.2}

- There is *low confidence* that any reported long-term (centennial) changes in tropical cyclone characteristics are robust, after accounting for past changes in observing capabilities. {2.6.3}

- Robust conclusions on long-term changes in large-scale atmospheric circulation are presently not possible because of large variability on interannual to decadal time scales and remaining differences between data sets. {2.7}

- Different global estimates of sub-surface ocean temperatures have variations at different times and for different periods, suggesting that sub-decadal variability in the temperature and upper heat content (0 to to 700 m) is still poorly characterized in the historical record. {3.2}

- Below ocean depths of 700 m the sampling in space and time is too sparse to produce annual global ocean temperature and heat content estimates prior to 2005. {3.2.4}

- Observational coverage of the ocean deeper than 2000 m is still limited and hampers more robust estimates of changes in global ocean heat content and carbon content. This also limits the quantification of the contribution of deep ocean warming to sea level rise. {3.2, 3.7, 3.8; Box 3.1}

- The number of continuous observational time series measuring the strength of climate relevant ocean circulation features (e.g., the meridional overturning circulation) is limited and the existing time series are still too short to assess decadal and longer trends. {3.6}.

- In Antarctica, available data are inadequate to assess the status of change of many characteristics of sea ice (e.g., thickness and volume). {4.2.3}

- On a global scale the mass loss from melting at calving fronts and iceberg calving are not yet comprehensively assessed. The largest uncertainty in estimated mass loss from glaciers comes from the Antarctic, and the observational record of ice–ocean interactions around both ice sheets remains poor. {4.3.3, 4.4}

TS.6.2 Key Uncertainties in Drivers of Climate Change

- Uncertainties in aerosol–cloud interactions and the associated radiative forcing remain large. As a result, uncertainties in aerosol forcing remain the dominant contributor to the overall uncertainty in net anthropogenic forcing, despite a better understanding of some of the relevant atmospheric processes and the availability of global satellite monitoring. {2.2, 7.3–7.5, 8.5}

- The cloud feedback is *likely* positive but its quantification remains difficult. {7.2}

- Paleoclimate reconstructions and Earth System Models indicate that there is a positive feedback between climate and the carbon cycle, but *confidence* remains *low* in the strength of this feedback, particularly for the land. {6.4}

TS.6.3 Key Uncertainties in Understanding the Climate System and Its Recent Changes

- The simulation of clouds in AOGCMs has shown modest improvement since AR4; however, it remains challenging. {7.2, 9.2.1, 9.4.1, 9.7.2}

- Observational uncertainties for climate variables other than temperature, uncertainties in forcings such as aerosols, and limits in process understanding continue to hamper attribution of changes in many aspects of the climate system. {10.1, 10.3, 10.7}

- Changes in the water cycle remain less reliably modelled in both their changes and their internal variability, limiting confidence in attribution assessments. Observational uncertainties and the large effect of internal variability on observed precipitation also precludes a more confident assessment of the causes of precipitation changes. {2.5.1, 2.5.4, 10.3.2}

- Modelling uncertainties related to model resolution and incorporation of relevant processes become more important at regional scales, and the effects of internal variability become more significant. Therefore, challenges persist in attributing observed change to external forcing at regional scales. {2.4.1, 10.3.1}

- The ability to simulate changes in frequency and intensity of extreme events is limited by the ability of models to reliably simulate mean changes in key features. {10.6.1}

- In some aspects of the climate system, including changes in drought, changes in tropical cyclone activity, Antarctic warming, Antarctic sea ice extent, and Antarctic mass balance, *confidence* in attribution to human influence remains *low* due to modelling uncertainties and low agreement between scientific studies. {10.3.1, 10.5.2, 10.6.1}

TS.6.4 Key Uncertainties in Projections of Global and Regional Climate Change

- Based on model results there is limited confidence in the predictability of yearly to decadal averages of temperature both for the global average and for some geographical regions. Multi-model results for precipitation indicate a generally low predictability. Short-term climate projection is also limited by the uncertainty in projections of natural forcing. {11.1, 11.2, 11.3.1, 11.3.6; Box 11.1}

- There is *medium confidence* in near-term projections of a northward shift of NH storm track and westerlies. {11.3.2}

- There is generally *low confidence* in basin-scale projections of significant trends in tropical cyclone frequency and intensity in the 21st century. {11.3.2, 14.6.1}

- Projected changes in soil moisture and surface run off are not robust in many regions. {11.3.2, 12.4.5}

- Several components or phenomena in the climate system could potentially exhibit abrupt or nonlinear changes, but for many phenomena there is *low confidence* and little consensus on the likelihood of such events over the 21st century. {12.5.5}

- There is *low confidence* on magnitude of carbon losses through CO_2 or CH_4 emissions to the atmosphere from thawing permafrost. There is *low confidence* in projected future CH_4 emissions from natural sources due to changes in wetlands and gas hydrate release from the sea floor. {6.4.3, 6.4.7}

- There is *medium confidence* in the projected contributions to sea level rise by models of ice sheet dynamics for the 21st century, and *low confidence* in their projections beyond 2100. {13.3.3}

- There is *low confidence* in semi-empirical model projections of global mean sea level rise, and no consensus in the scientific community about their reliability. {13.5.2, 13.5.3}

- There is *low confidence* in projections of many aspects of climate phenomena that influence regional climate change, including changes in amplitude and spatial pattern of modes of climate variability. {9.5.3, 14.2–14.7}

TSSM

Technical Summary
Supplementary Material

Coordinating Lead Authors:
Thomas F. Stocker (Switzerland), Qin Dahe (China), Gian-Kasper Plattner (Switzerland)

Lead Authors:
Lisa V. Alexander (Australia), Simon K. Allen (Switzerland/New Zealand), Nathaniel L. Bindoff (Australia), François-Marie Bréon (France), John A. Church (Australia), Ulrich Cubasch (Germany), Seita Emori (Japan), Piers Forster (UK), Pierre Friedlingstein (UK/Belgium), Nathan Gillett (Canada), Jonathan M. Gregory (UK), Dennis L. Hartmann (USA), Eystein Jansen (Norway), Ben Kirtman (USA), Reto Knutti (Switzerland), Krishna Kumar Kanikicharla (India), Peter Lemke (Germany), Jochem Marotzke (Germany), Valérie Masson-Delmotte (France), Gerald A. Meehl (USA), Igor I. Mokhov (Russian Federation), Shilong Piao (China), Venkatachalam Ramaswamy (USA), David Randall (USA), Monika Rhein (Germany), Maisa Rojas (Chile), Christopher Sabine (USA), Drew Shindell (USA), Lynne D. Talley (USA), David G. Vaughan (UK), Shang-Ping Xie (USA)

Contributing Authors:
Myles R. Allen (UK), Olivier Boucher (France), Don Chambers (USA), Jens Hesselbjerg Christensen (Denmark), Philippe Ciais (France), Peter U. Clark (USA), Matthew Collins (UK), Josefino C. Comiso (USA), Viviane Vasconcellos de Menezes (Australia/Brazil), Richard A. Feely (USA), Thierry Fichefet (Belgium), Gregory Flato (Canada), Jesús Fidel González Rouco (Spain), Ed Hawkins (UK), Paul J. Hezel (Belgium/USA), Gregory C. Johnson (USA), Simon A. Josey (UK), Georg Kaser (Austria/Italy), Albert M.G. Klein Tank (Netherlands), Janina Körper (Germany), Gunnar Myhre (Norway), Timothy Osborn (UK), Scott B. Power (Australia), Stephen R. Rintoul (Australia), Joeri Rogelj (Switzerland/Belgium), Matilde Rusticucci (Argentina), Michael Schulz (Germany), Jan Sedláček (Switzerland), Peter A. Stott (UK), Rowan Sutton (UK), Peter W. Thorne (USA/Norway/UK), Donald Wuebbles (USA)

Review Editors:
Sylvie Joussaume (France), Joyce Penner (USA), Fredolin Tangang (Malaysia)

This supplementary material should be cited as:
Stocker, T.F., D. Qin, G.-K. Plattner, L.V. Alexander, S.K. Allen, N.L. Bindoff, F.-M. Bréon, J.A. Church, U. Cubasch, S. Emori, P. Forster, P. Friedlingstein, N. Gillett, J.M. Gregory, D.L. Hartmann, E. Jansen, B. Kirtman, R. Knutti, K. Krishna Kumar, P. Lemke, J. Marotzke, V. Masson-Delmotte, G.A. Meehl, I.I. Mokhov, S. Piao, V. Ramaswamy, D. Randall, M. Rhein, M. Rojas, C. Sabine, D. Shindell, L.D. Talley, D.G. Vaughan and S.-P. Xie, 2013: Technical Summary Supplementary Material. In: *Climate Change 2013: The Physical Science Basis. Contribution of Working Group I to the Fifth Assessment Report of the Intergovernmental Panel on Climate Change* [Stocker, T.F., D. Qin, G.-K. Plattner, M. Tignor, S.K. Allen, J. Boschung, A. Nauels, Y. Xia, V. Bex and P.M. Midgley (eds.)]. Available from www.climatechange2013.org and www.ipcc.ch.

Table of Contents

TS.SM.1 Notes and Technical Details on Observed Global Surface Temperature Figures in the Summary for Policymakers – Figure SPM.1

Data and programming code (IDL) used to create Summary for Policymakers and Technical Summary figures originating from Sections 2.4 and 2.5 of Chapter 2 can be obtained from the IPCC WGI AR5 website www.climatechange2013.org.

TS.SM.1.1 Annual and Decadal Global Surface Temperature Anomalies – Figure SPM.1a

Global Mean Surface Temperature (GMST) anomalies as provided by the dataset producers are given normalized relative to a 1961–1990 climatology from the latest version (as at 15 March 2013) of three combined Land-Surface Air Temperature (LSAT) and Sea Surface Temperature (SST) datasets. These combined datasets and the corresponding colours used in Figure SPM.1a are:

HadCRUT4 (version 4.1.1.0) – black
NASA GISS – blue
NCDC MLOST (version 3.5.2) – orange.

An overview of methodological diversity between these three temperature datasets is provided in Table 2.SM.6 of the Supplementary Material to Chapter 2, and full comprehensive details on the construction process for these datasets are provided in the references cited in this table. For time-series of LSAT only, and SST only, the reader is referred to Figure TS.1.

For the decadal anomalies, 90% confidence intervals are shown for the HadCRUT4 dataset (based on Morice et al., 2012).

TS.SM.1.2 Maps of Observed Changes in Surface Temperature – Figure SPM.1b

Maps of observed changes in surface temperature are based on trends calculated from the 3 datasets listed above for the period 1901–2012. See the Supplementary Material of Chapter 2 for a detailed description of the methodology used for trend and uncertainty calculations (Section 2.SM.3.3). Trends have been calculated only for those grid boxes with greater than 70% complete records and more than 20% data availability in the first and last 10% of the time period. White areas indicate incomplete or missing data. Black plus signs (+) indicate grid boxes where trends are significant at the 2-tailed 10% significance level (i.e., a trend of zero lies outside the 90% confidence interval).

The Technical Summary provides maps for all 3 datasets (Figure TS.2), while the Summary for Policymakers provides a map based on NCDC MLOST only (Figure SPM.1b).

TS.SM.2 Notes and Technical Details on Observed Change in Precipitation Over Land Figures in the Summary for Policymakers – Figure SPM.2

Data and programming code (IDL) used to create Summary for Policymakers and Technical Summary figures originating from Sections 2.4 and 2.5 of Chapter 2 can be obtained from the IPCC WGI AR5 website www.climatechange2013.org.

TS.SM.2.1 Map of Observed Changes in Precipitation Over Land – Figure SPM.2

Maps of observed changes in annual precipitation over land show trends calculated from 3 datasets:

CRU TS 3.10.01 (updated from Mitchell and Jones, 2005)
GHCN V2 (updated through 2011; Vose et al., 1992)
GPCC V6 (Becker et al., 2013)

Trends in annual precipitation are expressed per decade, and are calculated for the time periods 1901–2010 and 1951–2010. See the Supplementary Material of Chapter 2 for a detailed description of the methodology used for trend and uncertainty calculations (Section 2.SM.3.3). Trends have been calculated only for those grid boxes with greater than 70% complete records and more than 20% data availability in first and last 10% of the time period. White areas indicate incomplete or missing data. Black plus signs (+) indicate grid boxes where trends are significant at the 2-tailed 10% significance level (i.e., a trend of zero lies outside the 90% confidence interval).

The Technical Summary provides maps for all 3 datasets (TS TFE.1, Figure 2), while the Summary for Policymakers provides a map based on GPCC only (Figure SPM.2).

TS.SM.3 Notes and Technical Details on Observed Indicators of a Changing Global Climate Figures for the Summary for Policymakers – Figure SPM.3

This material documents the provenance of the data and plotting procedures that were used to create Figure SPM.3 in the IPCC WGI Fifth Assessment Report. This figure is closely derived from Figure TS.1 and FAQ 2.1, Figure 2 (see Chapter 2 Supplementary Material Section 2.SM.5), but includes fewer observed indicators. In addition, Figure SPM.3 includes an estimate of uncertainty for those datasets where this is available and has been assessed, illustrated with shading. Figure SPM.3 includes datasets and parameters assessed in Chapters 3 (ocean heat content, sea level), and 4 (snow cover, sea ice).

TS.SM.3.1 Northern Hemisphere Spring Snow Cover – Figure SPM.3a

TS.SM.3.1.1 Datasets

Green: Northern Hemisphere annual March-April average snow-cover extent based on an updated series from Brown and Robinson (2011), 1922–2012.

Shaded uncertainty estimate indicated by the 95% confidence interval.

TS.SM.3.1.2 Plotting Techniques

Annual values are plotted.

TS.SM.3.2 Arctic Summer Sea Ice Extent – Figure SPM.3b

All datasets provide Arctic annual July-August-September average sea ice extent.

Green: Updated from Walsh and Chapman (2001). Annual values are from 1900–1978.

Blue: Hadley Centre Sea Ice and Sea Surface Temperature dataset (HadISST1.2) (Rayner et al., 2003). Annual values are from 1900–1939 and 1953–2012. Values are excluded for the period 1940–1952 because the available data showed no change. It was a period when *in situ* data were very sparse and the gaps were filled in for completeness with climatology. For this assessment, this was not considered sufficiently robust and therefore the data during the period were excluded from the time series.

Red: Bootstrap algorithm (SBA) applied to data from the Scanning Multichannel Microwave Radiometer (SMMR) (updated from Comiso and Nishio, 2008). Annual values are from 1979–2012.

Black: NASA Team algorithm (NT1) applied to data from the Special Sensor Microwave/Imager (SSM/I) (Cavalieri et al., 1984) – updated in Cavalieri and Parkinson (2012) and Parkinson and Cavalieri (2012). Annual values are from 1979–2011.

Yellow: Bootstrap algorithm (ABA) applied to data from the Advanced Microwave Scanning Radiometer - Earth Observing System (AMSR-E) (updated from Comiso and Nishio, 2008). Annual values are from 2002–2011.

Orange: Revised NASA Team algorithm (NT2) applied to data from the Advanced Microwave Scanning Radiometer - Earth Observing System (AMSR-E) (updated from Markus and Cavalieri, 2000). Annual values are from 2002–2011.

Uncertainty estimates for each data point in the plots have been calculated based on the interannual variability of the ice extents. The systematic errors are not considered because they are generally unknown and are expected to be approximately constant from one year to another and would not change the results of trend analyses significantly. The interannual variability of the extent and actual area of the sea ice cover during the satellite era (since 1979) can be quantified accurately because of global coverage at good temporal resolution and the high contrast in the signature of ice free and ice covered oceans. The uncertainty (shaded range) that is shown is 1 standard deviation of the more than 30 years of satellite data, assuming a Gaussian distribution. The standard deviation is calculated after the data have been linearly detrended.

For the pre-satellite data (pre 1979), the true interannual variability is not known because available data are sparse and limited to only a few locations. Based on the expected quality of the Walsh and Chapman (2001) data and because of the lack of a better procedure, we use 1.75 standard deviations for the period 1880 to 1952 when data were sparse and 1.5 standard deviation for the period 1953 to 1978 when significantly more data were available. For the HadISST1.2 data set, which includes both pre- and post-satellite data (Rayner et al., 2003), we use 1 standard deviation for the entire period since 1900, calculated after the data has been linearly detrended.

TS.SM.3.2.2 Plotting Techniques

Annual values are plotted.

TS.SM.3.3 Global Average Upper Ocean Heat Content – Figure SPM.3c

TS.SM.3.3.1 Datasets

All datasets provide global annual upper-ocean (0 to 700 m depth) heat content anomalies.

Blue: Updated from Palmer et al. (2007). Annual values are from 1950–2011.

Green: Updated from Domingues et al. (2008). Annual values, smoothed with a 3-year running mean, are from 1950–2011.

Yellow: Updated from Ishii and Kimoto (2009). Annual values are from 1950–2011.

Orange: Updated from Smith and Murphy (2007). Annual values are from 1950–2010.

Black: Updated from Levitus et al. (2012). Annual values are from 1955–2011.

Uncertainty estimates are as reported in the cited publications. These are one standard error of the mean, except for Levitus et al. (2012) which provide one standard deviation. No uncertainty estimate is available for Smith and Murphy (2007).

TS.SM.3.3.2 Plotting Techniques

The published ocean heat content anomaly datasets are relative to different climatological reference periods. Therefore, the datasets have been aligned in Figure SPM.3c for the period 2006–2010, five years that are well measured by Argo, and then plotted relative to the result-

ing mean of all curves for 1970, a time when the increasing availability of annual data from XBTs causes the uncertainty estimates to reduce considerably. Specifically the alignment procedure for Figure SPM.3c involved the following steps:

Obtain all five upper ocean heat content anomaly time series.
1. Recognize that all the time-series values are annual values, centered on the middle of calendar years.
2. Find the average value of each time series for the years 2006–2010.
3. Subtract the average 2006–2010 value for each time series from that specific time-series.
4. Find the value of each time series for the year 1970.
5. Average these five values from the year 1970.
6. Subtract this 1970 average value from all of the time-series.

TS.SM.3.4 Global Average Sea Level – Figure SPM.3d

TS.SM.3.4.1 Datasets

Black: Church and White (2011) tide gauge reconstruction. Annual values are from 1900–2009.

Yellow: Jevrejeva et al. (2008) tide gauge reconstruction. Annual values are from 1900–2002.

Green: Ray and Douglas (2011) tide gauge reconstruction. Annual values are from 1900–2007.

Red: Nerem et al. (2010) satellite altimetry. A 1-year moving average boxcar filter has been applied to give annual values from 1993–2009.

Shaded uncertainty estimates are one standard error as reported in the cited publications. The one standard error on the 1-year averaged altimetry data (Nerem et al., 2010) is estimated at ±1 mm, and thus considerably smaller than for all other datasets.

TS.SM.3.4.2 Plotting Techniques

The published Global Mean Sea Level (GMSL) datasets use arbitrary and different reference periods where they start from zero. Furthermore, the altimetry data begins only in 1993. Therefore, the datasets have been aligned in Figure SPM.3d to a common reference period of time using the following steps:

1. The longest running record (Church and White, 2011) is taken as the reference to which all other datasets are aligned.
2. GMSL from Church and White (2011) is calculated relative to the average for the period 1900–1905, and the resulting value for the year 1993 (127 mm) is identified.
3. All other records are then adjusted to give the same value of 127 mm in 1993 (i.e., for each dataset the offset required to give 127 mm in 1993 is applied to all annual values in that dataset).

TS.SM.4 Notes and Technical Details on Observed Changes in the Global Carbon Cycle Figures in the Summary for Policymakers – Figure SPM.4

TS.SM.4.1 Atmospheric Concentrations of Carbon Dioxide – Figure SPM.4a

The top panel of Figure TS.5, and panel (a) of Figure SPM.4 show time series of atmospheric concentrations of carbon dioxide (CO_2). CO_2 concentrations are expressed as a mole fraction in dry air, micromol/mol, abbreviated as ppm. Time series are shown for the Mauna Loa Observatory (red in Figure SPM.4a), and South Pole (black in Figure SPM.4a). Data were accessed from the following sources (active at the time of publication):

1. Mauna Loa Observatory
   ftp://ftp.cmdl.noaa.gov/ccg/co2/trends/co2_mm_mlo.txt.

Monthly averages are plotted from March 1958 to August 2012. For further details on the measurements see Keeling et al. (1976a) and Thoning et al. (1989).

2. South Pole
   http://scrippsco2.ucsd.edu/data/flask_co2_and_isotopic/monthly_co2/monthly_spo.csv

Monthly averages are plotted from June 1957 to February 2012. For further details on the measurements see Keeling et al. (1976b; 2001).

TS.SM.4.2 Ocean Surface Carbon Dioxide and *In Situ* pH – Figure SPM.4b

The top panel of Figure TS.5, and panel (b) of Figure SPM.4 show time series of observed partial pressure of dissolved CO_2 (pCO_2 given in µatm) at the ocean surface, together with time series of ocean surface *in situ* pH (total scale). All ocean time series are plotted as 12-month running means (6 months before to 6 months after the sample date) for each 6-month period centered on 1 January and 2 July of each year. Data for both pCO_2 and *in situ* pH were measured at the following stations and obtained from the following sources (active at the time of publication):

1. Hawaii Ocean Time-Series program (HOT) from the station ALOHA (updated from, Dore et al., 2009)
   http://hahana.soest.hawaii.edu/hot/products/HOT_surface_CO2.txt

Shown as light green and light blue time series in Figure SPM.4b, for *in situ* pH and pCO_2 respectably. Data were plotted for the period 1988–2011.

Further technical details regarding the data are available from the readme file: http://hahana.soest.hawaii.edu/hot/products/HOT_surface_CO2_readme.pdf.

2. Bermuda Atlantic Time-Series Study (BATS): http://bats.bios.edu/bats_form_bottle.html

Shown as green and blue time series in Figure SPM.4b, for *in situ* pH and pCO_2, respectively, but not shown in Figure TS.5. Data were plotted for the period 1991 – 2011.

Measured dissolved inorganic carbon (DIC) and total alkalinity (TA) at *in situ* temperature were used to calculate pH on the total scale as well as pCO_2 in µatm.

Further technical details are described in Bates (2007).

3. European Station for Time series in the Ocean (ESTOC; see González-Dávila and Santana-Casiano, 2009): http://cdiac.ornl.gov/ftp/oceans/ESTOC_data

Shown as dark green and dark blue time series in Figure SPM.4b, for *in situ* pH and pCO_2, respectively, but not shown in Figure TS.5. Data were plotted for the period 1996–2009.

Further technical details regarding the data are available from González-Dávila (2010).

Note that the data for Figure SPM.4 (and Figure TS.5) provided at the external sources cited above may be subject to revision based on recalibration, and other quality control procedures conducted over time by the data providers.

TS.SM.5 Notes and Technical Details on Radiative Forcing Estimates Figure in the Summary for Policy Makers – Figure SPM.5

This material documents the underlying traceability for values that were used to create Figure SPM.5 in the IPCC WG1 Fifth Assessment Report. This figure is closely related to Figures TS.6 and TS.7 and Chapter 8, Figures 8.14 to 8.18. The reader is therefore referred to the Supplementary Material of Chapter 8 for detailed information on methods and sources used to estimate forcing values.

Figure SPM.5 (and Figure TS.7) plots Radiative Forcing (RF) estimates in 2011 relative to 1750 and aggregated uncertainties for the main drivers of climate change. This figure is different from similar figures shown in previous IPCC report SPMs (though an analogous figure was shown in Chapter 2 of AR4) as it evaluates the RF based on the emissions rather than the concentration changes. An emitted compound changes the atmospheric concentration of the same substance but may also impact that of other atmospheric constituents through chemistry processes.

Values are global average RF, partitioned according to the emitted compounds or processes that result in a combination of drivers. In calculations of RF for well-mixed greenhouse gases and aerosols in this report, physical variables, except for the ocean and sea ice, are allowed to respond to perturbations with rapid adjustments. The resulting forcing is called Effective Radiative Forcing (ERF) in the underlying report. For all drivers other than well-mixed greenhouse gases and aerosols, rapid adjustments are less well characterized and assumed to be small, and thus the traditional RF is used.

The 'level of confidence' given in Figure SPM.5 is based on Table 8.5.

For the main emitted compounds of CO_2, CH_4, Halocarbons, N_2O, CO, NMVOC and NO_x, the underlying values, their sources, and uncertainties can be found in the Chapter 8 Supplementary Material, Tables 8.SM.6 and 8.SM.7.

The value of –0.27 W m^{-2} for aerosols and precursors shown in Figure SPM.5 results from –0.35 W m^{-2} from RFari (Table 8.6) with the addition of 0.04 W m^{-2} from BC-on-snow and the subtraction of the small nitrate contribution from NO_x of –0.04 W m^{-2} (Table 8.SM.6).

The value of –0.55 W m^{-2} for cloud adjustments due to aerosols given in Figure SPM.5 results from the combination of ERFaci –0.45 [–1.2 to 0.0] W m^{-2} and rapid adjustment of ari –0.1 [–0.3 to +0.1] W m^{-2} as reported in Figure TS.7. Detailed information can be found in Chapter 8 and the Chapter 8 Supplementary Material, Table 8.SM.6.

The values for albedo changes due to land use and changes in solar irradiance come from Table 8.6 of Chapter 8.

Total anthropogenic RF relative to 1750 is based on values given in Table 8.6 (for 2011) and Figure 8.18 (values for 1950 and 1980 given in the caption).

TS.SM.6 Notes and Technical Details on Comparison of Observed and Simulated Climate Change Figures for the Summary for Policymakers – Figure SPM.6

Figure SPM.6 and the related Figure TS.12 are reduced versions of Figure 10.21 in Chapter 10. The reader is therefore referred to the detailed description of the main components of Figure 10.21 for datasets and methods used (see the Chapter 10 Supplementary Material, Section 10.SM.1). Here, mainly the differences of Figure SPM.6 and TS.12 from Figure 10.21 are listed.

Figures SPM.6 and TS.12 show time series of decadal average, plotted on a common axis and at the centre of each decade. The decadal averages are taken from the annual time series that Figure 10.21 is based on. Figure TS.12 features the multi-model mean as dark blue and dark red line, while Figure SPM.6 only features the 5–95% confidence interval. Note that the precipitation plot from Figure 10.21 are not included in the Technical Summary and SPM versions of this figure.

TS.SM.6.1 Continental Temperatures

The same model simulations and observational data sets are used as for Figure 10.21. Continental land areas are based on the IPCC Special Report on Managing the Risks of Extreme Events and Disasters to Advance Climate Change Adaptation (SREX) defined regions (IPCC, 2012) shown pictorially in the bottom right most panel of Figure 10.7. Temperature anomalies in Figure SPM.6 are with respect to 1880–1919 (except for Antarctica where anomalies are relative to 1950–2010).

TS.SM.6.2 Ocean Heat Content

The same model simulations and observational data sets are used as for Figure 10.21.

TS.SM.6.3 Sea Ice

The same model simulations and observational data sets are used as for Figure 10.21.

TS.SM.6.4 Data Quality

For land and ocean surface temperatures panels, solid lines indicate where data spatial coverage of areas being examined is above 50% coverage and dashed lines where coverage is below 50%. For example, data coverage of Antarctica never goes above 50% of the land area of the continent. For ocean heat content and sea-ice panels, the solid line is where the coverage of data is good and higher in quality, and the dashed line is where the data coverage is only adequate, based respectively on the spatial coverage and instrument type and on the presence of satellite measurements.

TS.SM.7 Notes and Technical Details on CMIP5 Simulated Time Series Figures in the Summary for Policymakers – Figure SPM.7

This material documents the provenance of the data and plotting procedures that were used to create Figure SPM.7, based on Climate Model Intercomparison Project Phase 5 (CMIP5) model results as of March, 2013. This figure is closely derived from Figures 12.5 and TS.15 (global average surface temperature), 12.28 and TS.17 (sea ice), 6.28 and TS.20a (ocean surface pH), but includes fewer model scenarios. The reader is referred to the Technical Summary and the Chapters 12 and 6 where all RCP scenarios are given for the respective quantity.

TS.SM.7.1 Global Average Surface Temperature Change (Figure SPM.7a) and Global Ocean Surface pH (Figure SPM.7c)

Step 1 – Analyzed simulations

The simulations considered are annual or monthly mean fields from different model simulations carried out as part of the CMIP5 project (when applicable the variable name as given in the CMIP5 archive is indicated in square brackets). The time series between 1850 and 2005 originate from the historical simulations. The two time series of the future projections are from RCP2.6 and RCP8.5. The box plots showing the change at the end of the century additionally use RCP4.5 end RCP6.0. Table TS.SM.1 lists the models and ensemble simulations used for panels (a) and panel (c). Only one ensemble simulation per model is used. All models are weighted equally except for sea ice (panel (b)) where a subset of models is considered.

Step 2a – Interpolation

For panel (a), the monthly temperature fields [tas] are re-gridded to a 2.5° × 2.5° grid using bilinear interpolation. No special treatment is used at the land-sea border.

For panel (c), the monthly temperature [tos] and salinity [sos] fields are first averaged to yield annual means. Then, annual-mean temperature, salinity, dissolved inorganic carbon [dissic] and alkalinity [talk] fields are re-gridded to a 1° × 1° using bilinear interpolation. For the model MIROC-ESM-CHEM the upper-most layers of the 3-dimensional fields of monthly sea water potential temperature [thetao] and monthly sea water salinity [so] are used.

Step 2b – Derivation of pH

For each model, surface pH was computed from simulated DIC, alkalinity, temperature, and salinity. Before computation each simulated input field was corrected for its decadal mean bias relative to modern observations, using the approach of Orr et al. (2005) and Orr (2011). That is, pH was computed after first removing from each model field, the average difference between the model mean during 1989–1998

Table TS.SM.1 | Models and ensembles used for panels (a) and (c).

Model	Ensemble Member	Historical	RCP2.6	RCP4.5	RCP6.0	RCP8.5
ACCESS1.0	r1i1p1	(a)		(a)		(a)
ACCESS1.3	r1i1p1	(a)		(a)		(a)
BCC-CSM1.1	r1i1p1	(a)	(a)	(a)	(a)	(a)
BCC-CSM1.1(m)	r1i1p1	(a)	(a)	(a)	(a)	
BNU-ESM	r1i1p1	(a)	(a)	(a)		(a)
CanESM2	r1i1p1	(a) (c)	(a) (c)	(a) (c)		(a) (c)
CCSM4	r1i1p1	(a)	(a)	(a)	(a)	(a)
CESM1(BGC)	r1i1p1	(a)		(a)		(a)
CESM1(CAM5)	r1i1p1	(a)	(a)	(a)	(a)	(a)
CMCC-CM	r1i1p1	(a)		(a)		(a)
CMCC-CMS	r1i1p1	(a)		(a)		(a)
CNRM-CM5	r1i1p1	(a)		(a)		(a)
CSIRO-Mk3.6.0	r1i1p1	(a)	(a)	(a)	(a)	(a)
EC-EARTH	r8i1p1	(a)	(a)	(a)		(a)

(continued on next page)

Table TS.SM.1 (continued)

Model	Ensemble Member	Historical	RCP2.6	RCP4.5	RCP6.0	RCP8.5
FGOALS-g2	r1i1p1	(a)	(a)	(a)		(a)
FIO-ESM	r1i1p1	(a)	(a)	(a)	(a)	(a)
GFDL-CM3	r1i1p1	(a)	(a)	(a)	(a)	(a)
GFDL-ESM2G	r1i1p1	(a) (c)	(a) (c)	(a) (c)	(a) (c)	(a) (c)
GFDL-ESM2M	r1i1p1	(a) (c)	(a) (c)	(a) (c)	(a) (c)	(a) (c)
GISS-E2-H	r1i1p1	(a)	(a)	(a)	(a)	(a)
GISS-E2-H	r1i1p2	(a)	(a)	(a)	(a)	(a)
GISS-E2-H	r1i1p3	(a)	(a)	(a)	(a)	(a)
GISS-E2-H-CC	r1i1p1	(a)		(a)		
GISS-E2-R	r1i1p1	(a)	(a)	(a)	(a)	(a)
GISS-E2-R	r1i1p2	(a)	(a)	(a)	(a)	(a)
GISS-E2-R	r1i1p3	(a)	(a)	(a)	(a)	(a)
GISS-E2-R-CC	r1i1p1	(a)		(a)		
HadGEM2-AO	r1i1p1	(a)	(a)	(a)	(a)	(a)
HadGEM2-CC	r1i1p1	(a) (c)		(a) (c)		(a)
HadGEM2-ES	r2i1p1	(a)	(a)	(a)	(a)	(a)
INM-CM4	r1i1p1	(a)		(a)		(a)
IPSL-CM5A-LR	r1i1p1	(a) (c)	(a) (c)	(a) (c)	(a) (c)	(a) (c)
IPSL-CM5A-MR	r1i1p1	(a) (c)	(a) (c)	(a) (c)	(a)	(a) (c)
IPSL-CM5B-LR	r1i1p1	(a) (c)		(a)		(a) (c)
MIROC5	r1i1p1	(a)	(a)	(a)	(a)	(a)
MIROC-ESM	r1i1p1	(a) (c)	(a) (c)	(a) (c)	(a)	(a) (c)
MIROC-ESM-CHEM	r1i1p1	(a) (c)	(a) (c)	(a) (c)	(a) (c)	(a) (c)
MPI-ESM-LR	r1i1p1	(a) (c)	(a) (c)	(a) (c)		(a) (c)
MPI-ESM-MR	r1i1p1	(a) (c)	(a) (c)	(a) (c)		(a) (c)
MRI-CGCM3	r1i1p1	(a)	(a)	(a)	(a)	(a)
NorESM1-M	r1i1p1	(a)	(a)	(a)	(a)	(a)
NorESM1-ME	r1i1p1	(a) (c)	(a)	(a) (c)	(a)	(a)

and the observational reference. For observed fields, the GLODAP gridded data product (Key et al., 2004) for DIC and alkalinity along with the 2009 World Ocean Atlas climatology for temperature, salinity, and concentrations of phosphate and silica (Locarnini et al., 2010; Antonov et al., 2010; Garcia et al., 2010) were used. Changes to the concentrations of phosphate and silica were assumed to be zero, because not all models provided those variables. pH was computed using routines based on the standard OCMIP carbonate chemistry adapted for earlier studies (Orr, 2011) to compute all carbonate system variables and use recommended constants from the Guide to Best Practices for Ocean CO_2 Measurements (Dickson et al., 2007).

Step 3 – Global and annual mean

The monthly (temperature) or annual (pH) surface fields are averaged (weighted by the cosine of the latitude) to obtain the global mean values. The monthly global mean temperature values are averaged to annual means.

Step 4 – Reference period

The average from 1986 to 2005 of the annual means for each model is computed and is subtracted from the respective model time series to obtain the corresponding temperature anomalies.

Step 5 – Mean and standard deviation

The mean and standard deviation over all the models is calculated. For the time period after 2006 all the possible models that are listed in Table TS.SM.1 are used. If a model provided several RCPs based on the same historical simulation, that historical simulation is counted only once.

Step 6 – Uncertainty estimates

First, for each model the average from 2081 to 2100 is computed from the above mentioned time series. Then, in a second step, the multi-model average and standard deviation over all model averages are calculated. The *likely* ranges on the right of the figure show the mean plus/minus 1.64 times the standard deviation across the model averages. The shading on the time series indicates the mean value plus/minus 1.64 times the standard deviation across the models for each year.

Step 7 – Graphical display

To close the multi-model mean time series at the year 2005 when the historical simulation ends and the RCP begins, the value at year 2005 is assigned to belong to both the historical time series and also to the corresponding RCP.

TS.SM.7.2 Northern Hemisphere September Sea Ice Extent – Figure SPM.7b

Step 1 – Analyzed simulations

Table TS.SM.2 provides the model and RIP ensemble member included from each RCP to create the multi-model mean time series of the NH September sea ice extent [sic] shown in Figure SPM.7b. In most cases, the first ensemble member (r1i1p1) was used. A selection algorithm produces a subset of models that most closely match observations, and is detailed below. The corresponding historical ensemble member is catenated with the respective RCP scenario ensemble member to create a continuous time series from 1850–2100.

Step 2 – Time series of NH September sea ice extent

Using the sea ice concentration field, a mask of the sea ice concentration >15% for each month of data for the Northern Hemisphere was created. For each month, the sea ice extent is the sum of the area of the ocean [areacello] times the ocean fraction [sftof] times the mask of sic >15% at each grid point. The time series are computed on the original model grids, which is usually the ocean grid. In some cases,

Table TS.SM.2 | Models and ensemble members used.

Model	Ensemble Member	RCP2.6	Historical/RCP4.5	RCP6.0	RCP8.5
ACCESS1.0	r1i1p1		x		x
ACCESS1.3	r1i1p1		x		x
BCC-CSM1.1	r1i1p1	x	x	x	x
BCC-CSM1.1(m)	r1i1p1	x	x	x	x
BNU-ESM	r1i1p1	x	x		x
CanESM2	r1i1p1	x	x		x
CCSM4	r1i1p1	x	x	x	x
CESM1(BGC)	r1i1p1		x		x
CESM1(CAM5)	r1i1p1	x	x	x	x
CESM1(WACCM)	r2i1p1	x	x		x
CMCC-CM	r1i1p1		x		x
CMCC-CMS	r1i1p1		x		x
CNRM-CM5	r1i1p1	x	x		x
CSIRO-Mk3.6.0	r1i1p1	x	x	x	x
EC-EARTH	r1i1p1		x		x
	r8i1p1	x			
FGOALS-g2	r1i1p1	x	x		x
FIO-ESM	r1i1p1	x	x	x	x
GFDL-CM3	r1i1p1	x	x	x	x
GFDL-ESM2G	r1i1p1	x	x	x	x
GFDL-ESM2M	r1i1p1	x	x	x	x
GISS-E2-H	r1i1p1	x	x	x	x
GISS-E2-H-CC	r1i1p1		x		
GISS-E2-R	r1i1p1	x	x	x	x
GISS-E2-R-CC	r1i1p1		x		
HadGEM2-AO	r1i1p1	x	x	x	x
HadGEM2-CC	r1i1p1		x		x
HadGEM2-ES	r2i1p1	x	x	x	x
INM-CM4	r1i1p1		x		x
IPSL-CM5A-LR	r1i1p1	x	x	x	x
IPSL-CM5A-MR	r1i1p1	x	x	x	x
IPSL-CM5B-LR	r1i1p1		x		x
MIROC5	r1i1p1	x	x	x	x
MIROC-ESM	r1i1p1	x	x	x	x
MIROC-ESM-CHEM	r1i1p1	x	x	x	x
MPI-ESM-LR	r1i1p1	x	x		x
MPI-ESM-MR	r1i1p1	x	x		x
MRI-CGCM3	r1i1p1	x	x	x	x
NorESM1-M	r1i1p1	x	x	x	x
NorESM1-ME	r1i1p1	x	x	x	x

sea ice concentration is on the atmospheric grid. In cases where the grid area was not available for regular grids, a regular lat-lon grid was constructed based on the grid dimensions following

areacello=((dlat*2π/360)*R_earth) .* ((dlon*2 π/360).*(R_earth*-cos(LAT))),

with R_earth being the radius of Earth (6,371,000 m), dlat and dlon being the differentials in lat/lon in each dimension, and LAT being the latitude in radians.

If the ocean fraction was unavailable, it was assumed that the ocean fraction was 1 where the sea ice concentration was greater than 0%.

Step 3 – Create multi-model mean time series
The multi-model mean time series of sea ice extent is computed across all model members in Table TS.SM.2. A five-year running mean is applied to this time series. This is plotted as the dotted line in the figure. Some time series start later than 1850 or end earlier than 2100, and these are treated as missing values for those years.

Step 4 – Select models that most closely match observations
The selection process is done in a series of steps which compare the models to observed/reanalyzed data. This selection process is based on the underlying assessment of Chapter 12 and referenced therein. The method proposed by Massonnet et al. (2012) is applied here to the full set of models that provided sea ice output fields to the CMIP5 database. For the model selection, all available ensemble members are used for all of the models that provide simulations for Historical and RCP4.5. These ensemble members are listed in Table TS.SM.3.

Four diagnostics from the models are compared to the same quantities in observations or reanalyses. The diagnostics are: (a) September Arctic sea ice extent (1986–2005), (b) Annual mean Arctic sea ice volume (1986–2005), (c) Amplitude of the seasonal cycle of Arctic sea ice extent (1986–2005), and (d) Trend in September Arctic sea ice extent (1979–2012). Computation of each diagnostic is described and then the method for comparison is described below.

Step 4a – Computation of diagnostic quantities
(a) Sea ice extent is computed for each model ensemble member as outlined above to get the total area where sea ice concentration is >15%. For each ensemble member, an average September sea ice extent is then computed for the years 1986–2005. Observations for sea ice extent use the monthly mean sea ice extents from Comiso and Nishio (2008, updated 2012). The observations were computed in the same way as in the models (i.e., these are the monthly mean extents computed from the observed monthly mean sea ice concentration).

(b) Sea ice volume is computed as the sum of the sea ice thickness field [sit] times the ocean area [areacello] times the ocean fraction [sftof], since the sea ice thickness is given as thickness averaged over the entire ocean grid cell. Caveats for the grids are the same as discussed in Step 2 above. The time series of monthly sea ice volume for each ensemble member is then annually averaged for the period 1986–2005. The bias-adjusted PIOMAS (Pan-Arctic Ice-Ocean Modelling and Assimilation System) reanalysis data (Schweiger et al., 2011) is used to provide estimates for sea ice volume for comparison to the models.

(c) The amplitude of the seasonal cycle of Arctic sea ice extent is computed for each model from a climatology of monthly sea ice extent for 1986–2005. The amplitude is the difference between the maximum (March) and minimum (September) sea ice extent for each model ensemble member. Amplitude of seasonal cycle for observations are computed in the same way from Comiso and Nishio (2008, updated 2012).

(d) The linear trend in September sea ice extent is computed for the period 1979–2012. Again observations are taken from Comiso and Nishio (2008, updated 2012).

Step 4b – Estimation of natural variability for model ensembles
For models with multiple ensemble members, a standard deviation is computed for each of the diagnostics for each ensemble member. Then the mean of all the standard deviations is computed, and using this value, a ±2 standard deviation interval is constructed around the ensemble mean or single realization of each diagnostic for each model.

Step 4c – Model selection - Comparison of modeled diagnostics to observed/reanalyzed diagnostic
For each of the observed/reanalyzed diagnostics, a ±–20% interval is constructed around the mean value for the given period. A model is retained in the selection if, for each diagnostic, either the ±2 standard deviation around the model ensemble mean diagnostic overlaps the ±20% interval around the observed/reanalysed value of the diagnostic OR at least one ensemble member from that model gives a value for the diagnostic that falls within ±20% of the observed/reanalysed data. A model is selected only if all four diagnostic values meet this criterion.

Results of the selection
The model diagnostics are calculated using RCP4.5 which has the largest number of models. Five models are selected by this process: ACCESS1.0, ACCESS1.3, GFDL-CM3, IPSL-CM5A-MR, MPI-ESM-MR, and all five models have simulations for both RCP8.5 and RCP4.5. For RCP2.6 only three of this subset have simulations (GFDL-CM3, IPSL-CM5A-MR, MPI-ESM-MR), and for RCP6.0, only two models have simulations (GFDL-CM3, IPSL-CM5A-MR).

Step 5 – Time series of sea ice extent for the selected models
The multi-model mean time series of September sea ice extent is calculated for the selected models. The solid line shows the multi-model mean smoothed with a five-year running mean, and the shading represents the minimum and maximum range of the selected model time series, also smoothed by the same five year running mean.

The shaded bars on the right are the multi-model mean and the mean of the maximum and minimum range for the selected models for the period 2081–2100.

Table TS.SM.3 | Models and ensembles used for model selection, RCP4.5.

Model	Ensemble Member RCP4.5
ACCESS1.0	r1i1p1
ACCESS1.3	r1i1p1
BCC-CSM1.1	r1i1p1
BCC-CSM1.1(m)	r1i1p1
BNU-ESM	r1i1p1
CanESM2	r1i1p1 r2i1p1 r3i1p1 r4i1p1 r5i1p1
CCSM4	r1i1p1 r2i1p1 r3i1p1 r4i1p1 r5i1p1 r6i1p1
CESM1(BGC)	r1i1p1
CESM1(CAM5)	r1i1p1 r2i1p1 r3i1p1
CESM1(WACCM)	r2i1p1
CMCC-CM	r1i1p1
CMCC-CMS	r1i1p1
CNRM-CM5	r1i1p1
CSIRO-Mk3.6.0	r1i1p1 r2i1p1 r3i1p1 r4i1p1 r5i1p1 r6i1p1 r7i1p1 r8i1p1 r9i1p1 10i1p1
EC-EARTH	r1i1p1 r2i1p1 r3i1p1 r6i1p1 r7i1p1 r8i1p1 r9i1p1 10i1p1 11i1p1 12i1p1 13i1p1 14i1p1
FGOALS-g2	r1i1p1
FIO-ESM	r1i1p1 r2i1p1 r3i1p1
GFDL-CM3	r1i1p1 r3i1p1 r5i1p1
GFDL-ESM2G	r1i1p1
GFDL-ESM2M	r1i1p1
GISS-E2-H	r1i1p1 r2i1p1 r3i1p1 r4i1p1 r5i1p1
GISS-E2-H-CC	r1i1p1
GISS-E2-R	r1i1p1 r2i1p1 r3i1p1 r4i1p1 r5i1p1 r6i1p1
GISS-E2-R-CC	r1i1p1
HadGEM2-AO	r1i1p1
HadGEM2-CC	r1i1p1
HadGEM2-ES	r2i1p1 r3i1p1 r4i1p1
INM-CM4	r1i1p1
IPSL-CM5A-LR	r1i1p1 r2i1p1 r3i1p1 r4i1p1
IPSL-CM5A-MR	r1i1p1
IPSL-CM5B-LR	r1i1p1
MIROC5	r1i1p1 r2i1p1 r3i1p1
MIROC-ESM	r1i1p1
MIROC-ESM-CHEM	r1i1p1
MPI-ESM-LR	r1i1p1 r2i1p1 r3i1p1
MPI-ESM-MR	r1i1p1 r2i1p1 r3i1p1
MRI-CGCM3	r1i1p1
NorESM1-M	r1i1p1
NorESM1-ME	r1i1p1

TS.SM.8 Notes and Technical Details on Maps Showing CMIP5 Results in the Summary for Policymakers – Figure SPM.8

This material documents the provenance of the data and plotting procedures that were used to create Figure SPM.8, based on CMIP5 model results as of March, 2013. This figure is closely derived from Figures 12.11 and TS.15 (global average surface temperature), TS.16 (precipitation), 12.29 and TS.17 (sea ice), 6.28 and TS.20b (ocean surface pH), but includes fewer model scenarios. The reader is referred to the Technical Summary or the Chapters 12 and 6 where all RCP scenarios are given for the respective quantity.

TS.SM.8.1 Change in Average Surface Temperature (Figure SPM.8a) and Change in Average Precipitation (Figure SPM.8b)

Step 1 – Analyzed simulations

The simulations considered are monthly mean fields of surface temperature [tas] and precipitation [pr] from different model simulations carried out as part of the CMIP5 project (when applicable the variable name as given in the CMIP5 archive is indicated in square brackets). Table TS.SM.4 lists the models and ensemble members used for these panels. Only one ensemble member per model is used.

Step 2 – Interpolation

In a first step the monthly fields are re-gridded to a 2.5° × 2.5° grid using bilinear interpolation. No special treatment is used at the land-sea border.

Step 3 – Annual average and period

The monthly mean values are averaged to annual means. Then in a second step the time mean is computed over the 20-year period of interest.

Table TS.SM.4 | Models and ensemble members used.

Model	Ensemble Member	RCP2.6	Historical/RCP4.5	RCP6.0	RCP8.5
ACCESS1.0	r1i1p1		x		x
ACCESS1.3	r1i1p1		x		x
BCC-CSM1.1	r1i1p1	x	x	x	x
BCC-CSM1.1(m)	r1i1p1	x	x	x	
BNU-ESM	r1i1p1	x	x		x
CanESM2	r1i1p1	x	x		x
CCSM4	r1i1p1	x	x	x	x
CESM1(BGC)	r1i1p1		x		x
CESM1(CAM5)	r1i1p1	x	x	x	x
CMCC-CM	r1i1p1		x		x
CMCC-CMS	r1i1p1		x		x
CNRM-CM5	r1i1p1		x		x
CSIRO-Mk3.6.0	r1i1p1	x	x	x	x
EC-EARTH	r8i1p1	x	x		x
FGOALS-g2	r1i1p1	x	x		x
FIO-ESM	r1i1p1	x	x	x	x
GFDL-CM3	r1i1p1	x	x	x	x
GFDL-ESM2G	r1i1p1	x	x	x	x
GFDL-ESM2M	r1i1p1		x	x	x
GISS-E2-H	r1i1p1	x	x	x	x
GISS-E2-H	r1i1p2	x	x	x	x
GISS-E2-H	r1i1p3	x	x	x	x
GISS-E2-H-CC	r1i1p1		x		
GISS-E2-R	r1i1p1	x	x	x	x
GISS-E2-R	r1i1p2	x	x	x	x
GISS-E2-R	r1i1p3	x	x	x	x
GISS-E2-R-CC	r1i1p1		x		
HadGEM2-AO	r1i1p1	x	x	x	x
HadGEM2-CC	r1i1p1		x		x
HadGEM2-ES	r2i1p1	x	x	x	x
INM-CM4	r1i1p1		x		x
IPSL-CM5A-LR	r1i1p1	x	x	x	x
IPSL-CM5A-MR	r1i1p1	x	x	x	x
IPSL-CM5B-LR	r1i1p1		x		x
MIROC5	r1i1p1	x	x	x	x
MIROC-ESM	r1i1p1	x	x	x	x
MIROC-ESM-CHEM	r1i1p1	x	x	x	x
MPI-ESM-LR	r1i1p1	x	x		x
MPI-ESM-MR	r1i1p1	x	x		x
MRI-CGCM3	r1i1p1	x	x	x	x
NorESM1-M	r1i1p1	x	x	x	x
NorESM1-ME	r1i1p1	x	x	x	x

Step 4 – Time average and anomalies
The average from 1986 to 2005 of the annual means for each model is computed as the reference value and the annual mean from 2081 to 2100 are computed as the future period for the two RCPs. For each model the reference value is then subtracted from the future period value.

Step 5 – Calculation of the significance

Step 5a – Natural variability
To compute the natural variability all the models that provide more than 500 years of pre-industrial control simulation [piControl] are used. A list of these models is given in Table TS.SM.5. For each model the first 100 years are discarded to minimize problems with model initialization. Re-gridding and calculation of annual means is done as described in steps 2 and 3. The control runs are divided into 20-year non-overlapping periods. If the available data are not a multiple of 20-year the remaining years after the last 20-year period are not used in the calculation.

Averages over the 20-year periods are computed for every grid point. A quadratic trend is subtracted from this time series of 20-year averaged periods to remove potential model drift at each grid point. Finally for each model the standard deviation is computed over the different 20-year periods and for each grid point.

To obtain the final value of the natural variability the median of the standard deviations of the different models is multiplied with the square root of 2 (the natural variability characterizes the typical difference between two 20-year periods, rather than the difference of one period from the long-term mean, the former being larger than the latter by the square root of two).

Step 5b – Testing for significance
For each model the projected change is taken relative to its reference period and then the multi-model average at every grid point is computed. In a second step, at each grid point the number of models with positive and negative change are counted.

If more than 90% of the models agree on the sign of the change and the multi-model mean change is larger than 2 times the natural variability (as defined above) this grid point is said to be significant and robust across models.

Step 5c – Check for non-significance
Again, for each model the projected change is taken relative to the reference period and then the multi-model average at every grid point is computed.

If the multi-model mean change at one grid point is less than the natural variability (as defined above) the value is said to be non-significant.

Step 6 – Graphical display
For each model the projected change is taken relative to the reference period and then the multi-model average at every grid point is computed. The locations that are significant and robust (as described in step 5b) are marked by small black dots and the locations that are non-significant (as described in step 5c) are marked by hatching.

For panel b, all calculations are performed as absolute changes. To show the relative changes, the multi-model mean precipitation change is divided by the multi-model mean of the reference period.

Table TS.SM.5 | Models and ensemble members from the piControl experiments used for the calculation of the natural variability.

Model	Ensemble Member
ACCESS1.0	r1i1p1
ACCESS1.3	r1i1p1
BCC-CSM1.1	r1i1p1
BNU-ESM	r1i1p1
CanESM2	r1i1p1
CCSM4	r1i1p1
CESM1(BGC)	r1i1p1
CMCC-CMS	r1i1p1
CNRM-CM5	r1i1p1
CSIRO-Mk3-6-0	r1i1p1
FGOALS-g2	r1i1p1
FIO-ESM	r1i1p1
GFDL-CM3	r1i1p1
GFDL-ESM2G	r1i1p1
GFDL-ESM2M	r1i1p1
GISS-E2-H	r1i1p2
GISS-E2-H	r1i1p3
GISS-E2-R	r1i1p2
GISS-E2-R	r1i1p3
INM-CM4	r1i1p1
IPSL-CM5A-LR	r1i1p1
MIROC5	r1i1p1
MIROC-ESM	r1i1p1
MPI-ESM-LR	r1i1p1
MPI-ESM-MR	r1i1p1
MPI-ESM-P	r1i1p1
MRI-CGCM3	r1i1p1
NorESM1-M	r1i1p1

TS.SM.8.2 Northern Hemisphere September Sea Ice Extent (Figure SPM.8c)

Step 1 – Analyzed simulations and subset of models
The simulations analyzed here are the same as those listed for Figure SPM.7b. The subset of models are the same that are selected for Figure SPM.7b outlined in the following Step 4. Only one ensemble member from each model is used to create these figures.

Step 2 – Computation of mean sea ice concentration
For each model ensemble member, the mean sea ice concentration [sic] is calculated for the two periods, 1986–2005 and 2081–2100, on the native model grid (see also recipe for Figure SPM.7b).

Step 3 – Regrid sea ice concentration to common grid
SOSIE (http://sosie.sourceforge.net/) is used to regrid the mean sea ice concentration to a common 1° × 1° grid, applying the bilinear

interpolation scheme (SOSIE: cmethod = 'bilin'). Further, the regridded sea ice concentrations are 'drowned' across the land-sea boundary to eliminate low-biased interpolated values in the area of land-sea transition (SOSIE: ldrown = T). With this approach, interpolation artifacts can occur throughout the Canadian Archipelago, since each model represents this area quite differently. Comparison of individual models on their native grid allows to identify and mask such areas. Note that, for these reasons the interpolated sea ice concentrations shall not be used for quantitative interpretation, but only for visualization purposes. For visualization the MATLAB land-ocean mask is overlaid.

Step 4 – Calculate multi-model mean sea ice concentration
For each RCP, RCP2.6 and RCP8.5, and each period, 1986–2005 and 2081–2100, the mean sea ice concentration is calculated in each grid cell on the common grid. The same is done for the subset of models for each period. For RCP2.6 this subset is GFDL-CM3, IPSL-CM5A-MR, MPI-ESM-MR. For RCP8.5 this subset is ACCESS1.0, ACCESS1.3, GFDL-CM3, IPSL-CM5A-MR, MPI-ESM-MR.

Step 5 – Contour the multi-model mean sea ice concentration of 15%
The multi-model mean sea ice concentration is contoured at 15% according to the following:

1986–2005: multi-model mean all models: white line
1986–2005: subset models: light blue line
2081–2100: multi-model mean all models: white filled patch
2081–2100: subset models: light blue filled patch

Note for RCP8.5 there is no sea ice concentration >15% for the subset of models.

The decision was taken to contour the 15% contour of mean sea ice concentration to make this figure consistent with Figure 12.29, which shows a contour plot of the multi-model mean sea ice concentrations. It is also possible to make binary fields of sea ice concentration >15%, take the mean of those binary fields (for both 20 year averages and then in multi-model averages), and contour the 50% contour of the mean binary field as the mean sea ice extent. This option was not chosen here.

TS.SM.8.3 Change in Ocean Surface pH (Figure SPM.8d)

Step 1 – Analyzed simulations
The simulations considered are annual or monthly mean fields from different model simulations carried out as part of the CMIP5 project (when applicable the variable name as given in the CMIP5 archive is indicated in square brackets). Table TS.SM.6 lists the models and ensemble members used for these panels. Only one ensemble member per model is used.

Step 2a – Interpolation
In a first step, the monthly temperature [tos] and salinity [sos] fields are first averaged to yield annual means. For the model MIROC-ESM-CHEM the upper-most layer of the 3-dimensional fields of monthly sea water potential temperature [thetao] and monthly sea water salinity [so] are used. Then, annual-mean temperature, salinity, dissolved inorganic carbon [dissic] and alkalinity [talk] fields are re-gridded to a 1° × 1° using bilinear interpolation.

Step 2b – Derivation of pH
For each model, surface pH was computed from simulated DIC, alkalinity, temperature, and salinity. Before computation each simulated input field was corrected for its decadal mean bias relative to modern observations, using the approach used in Orr et al. (2005) and Orr (2011). That is, pH was computed after first removing from each model field, the average difference between the model mean during 1989–1998 and the observational reference. For observed fields, we used the GLODAP gridded data product (Key et al., 2004) for DIC and alkalinity along with the 2009 World Ocean Atlas climatology for temperature, salinity, and concentrations of phosphate and silica (Locarnini et al., 2010; Antonov et al., 2010; Garcia et al., 2010). Changes to the concentrations of phosphate and silica were assumed to be zero, because all models did not provide those variables. pH was computed using routines based on the standard OCMIP carbonate chemistry adapted for earlier studies (Orr, 2011) to compute all carbonate system variables and use recommended constants from the Guide to Best Practices for Ocean CO_2 Measurements (Dickson et al., 2007).

Step 3 – Average of 20-year period
The time mean is computed over the 20-year period of interest.

Table TS.SM.6 | Models and ensemble members used.

Model	Ensemble Member	Historical	RCP2.6	RCP4.5	RCP6.0	RCP8.5
CanESM2	r1i1p1	d	d	d		d
GFDL-ESM2G	r1i1p1	d	d	d	d	d
GFDL-ESM2M	r1i1p1	d	d	d	d	d
HadGEM2-CC	r1i1p1	d		d		d
IPSL-CM5A-LR	r1i1p1	d	d	d	d	d
IPSL-CM5A-MR	r1i1p1	d	d	d		d
IPSL-CM5B-LR	r1i1p1	d		d		d
MIROC-ESM	r1i1p1	d	d	d	d	d
MIROC-ESM-CHEM	r1i1p1	d	d	d	d	d
MPI-ESM-LR	r1i1p1	d	d	d		d
MPI-ESM-MR	r1i1p1	d	d	d		d
NorESM1-ME	r1i1p1	d		d		

Step 4 – Time average and anomalies
The average from 1986 to 2005 of the annual means for each model is computed as the reference value and the annual mean from 2081 to 2100 is computed as the future period for the two RCPs. For each model the reference value is then subtracted.

Step 5 – Graphical display
For each model the projected change is taken relative to the reference period and the multi-model mean at every grid point is computed.

TS.SM.9 Notes and Technical Details on the Sea Level Projection Figure for the Summary for Policymakers – Figure SPM.9

A full and comprehensive description of the methods used in the projections of global mean sea level for the 21st century is provided in the Supplementary Material to Chapter 13 (see Section 13.SM.1). Further plotting details used to produce Figure SPM.9, and the related Figure TS.22 are provided here.

TS.SM.9.1 Projected Global Mean Sea Level Rise

Projections are given from process-based models of global mean sea level rise relative to 1986–2005 for the four emissions scenarios RCP2.6, RCP4.5, RCP6.0 and RCP8.5.

The *likely* range for each RCP timeseries is delimited by the data in files rcpXX_sumlower and rcpXX_sumupper, while the median timeseries is the data in file rcpXX_summid, where 'XX' stands for the respective RCP scenario. These data files are available from the WGI AR5 website www.climatechange2013.org. The coloured vertical bars with horizontal lines for the four RCP scenarios indicate the *likely* ranges and medians for these scenarios as given in Table 13.5 of Chapter 13.

Note that in Figure SPM.9, projected time series are shown only for RCP2.6 and RCP8.5. Figure TS.22 include time series for all four RCP scenarios.

Projected contributions to sea level rise in 2081–2100 relative to 1986–2005 for the four RCP scenarios are provided in Figure TS.21.

TS.SM.10 Notes and Technical Details on the Summary for Policymakers Figure Plotting Global Mean Temperature Increase as a Function of Cumulative Total Global CO_2 Emissions – Figure SPM.10

Figure SPM.10 contains data from CO_2 only simulations and the RCP simulations. This figure is closely derived from TS TFE.8, Figure 1. CO_2 only simulations are represented by grey-shaded patches and thin black lines, RCP data by coloured lines and patches. CMIP5 results are taken from the archive as of March 15, 2013. Note that the thick black line represents the historical time period of the RCP runs.

TS.SM.10.1 Part A – CO_2 Only Runs

The thin black line represents the multi-model mean of the decadal averaged global-mean temperature response of the models listed in Table TS.SM.7 to a global 1% CO_2 only forcing increase as performed as part of CMIP5, as a function of the decadal averaged global-mean diagnosed carbon emissions.

The dark grey patch represents the 90% range surrounding the decadal averaged model response of the CMIP5 models listed in Table TS.SM.7 and is calculated as follows: Diagnosed carbon emissions and temperature response data of the above-defined CMIP5 models (computed as in Gillett et al., 2013) is scaled, respectively, by dividing by the standard deviation over all available decadal-averaged data points for a specific scenario. The 90% range is computed in polar coordinates. The radius stretches along the x-axis (cumulative emissions) and the angle is the one between the slope from (0, 0) to a respective scaled point (cumulative emissions, temperature anomaly) and the x-axis. For each scaled point the radius and angle are computed. A number of n (n = 20) segments are defined by regularly spaced steps along the maximum radius of all available decadal-averaged data points of a specific scenario (scaled as described earlier). From all points that fall within the boundaries of each respective radius segment, the 5th and 95th percentiles in terms of available angles is computed. These percentiles are then assigned to the radius corresponding to the middle of the current radius segment. Each of these mid-segment radii and its corresponding pair of angles are then transformed back to Cartesian coordinates. Finally, the 90% range is drawn by connecting all 5th and 95th percentile points of a specific scenario in a hull.

Table TS.SM.7 | Models that were included in the shown results of the CO2 only 1% increase CMIP5 runs (dark grey patch and thin black line).

Model	Ensemble Member
GFDL-ESM2G	r1i1p1
INM-CM4	r1i1p1
GFDL-ESM2M	r1i1p1
IPSL-CM5B-LR	r1i1p1
BCC-CSM1.1	r1i1p1
MPI-ESM-MR	r1i1p1
IPSL-CM5A-MR	r1i1p1
IPSL-CM5A-LR	r1i1p1
MPI-ESM-LR	r1i1p1
NorESM1-ME	r1i1p1
CESM1(BGC)	r1i1p1
HadGEM2-ES	r1i1p1
MIROC-ESM	r1i1p1
CanESM2	r1i1p1
BNU-ESM	r1i1p1

TS.SM.10.2 Part B – RCP Runs

Data of the RCP runs (coloured lines and patches) is prepared with the same methodology as the data for the CO_2 only runs as described in the previous section. Note that markers show decadal time steps, and that the labels in Figure SPM.10 (and TS TFE.8, Figure 1) denote the cumulative global carbon emissions from 1870 until (but not including) that year (i.e., label 2050 is placed next to the marker of the 2040–2049 decade). The 90% range is computed for n (n = 12) regularly spaced steps along the maximum radius available for each RCP (scaled as described earlier). Available Earth System Models (ESM) for the respective RCP are listed in Table TS.SM.8, available Earth System Models of Intermediate Complexity (EMIC) in Table TS.SM.9.

Following operations are carried out onto the data:

- Decadal means of global-mean temperature change are computed relative to the 1861–1880 base period.
- Emissions from the ESMs for the different scenarios are computed as in Jones et al. (2013).
- Land-use change emission estimated for each RCP are added to all EMICs, and to the ESMs that diagnose fossil-fuel emission only (see Table TS.SM.8). Land-use change emissions are obtained from http://www.pik-potsdam.de/~mmalte/rcps/ for each RCP, respectively. Note that the data for Figure SPM.10 provided at the external sources cited above may be subject to changes in the future by the owners. Furthermore, no guarantee is provided that the web-links cited above remain active.
- Decadal-mean cumulative emissions are computed from cumulative carbon emissions relative to 1870.
- Each RCP range is drawn as long as data is available for all models or until temperatures have peaked. The encompassing range shown in Figure SPM.10 (and TS TFE.8, Figure 1) is constructed by connecting the outer last points of each single RCP range and is filled as long as data are available for all models for RCP8.5. Beyond this point, the range is illustratively extended by further progressing along the radius while keeping the angles fixed at those available at the last point with data from all models for RCP8.5. The fading out of the range is illustrative.

Table TS.SM.8 | Overview of RCP model runs available in the CMIP5 archive, as used in Figure SPM.10 (and TS TFE.8, Figure 1).

Model	Ensemble Member	RCP2.6	RCP4.5	RCP6.0	RCP8.5
BCC-CSM1.1	r1i1p1	x*	x*	x*	x*
CanESM2	r1i1p1	x	x		x
CESM1(BGC)	r1i1p1		x		x
GFDL-ESM2G	r1i1p1	x	x	x	x
GFDL-ESM2M	r1i1p1	x	x	x	x
HadGEM2-CC	r1i1p1		x		x
HadGEM2-ES	r2i1p1	x	x	x	x
INM-CM4	r1i1p1		x*		x*
IPSL-CM5A-LR	r1i1p1	x	x	x	x
IPSL-CM5A-MR	r1i1p1	x	x		x
IPSL-CM5B-LR	r1i1p1		x		x
MIROC-ESM	r1i1p1	x	x	x	x
MIROC-ESM-CHEM	r1i1p1	x	x	x	x
MPI-ESM-LR	r1i1p1	x	x		x
NorESM1-ME	r1i1p1	x	x	x	x

Notes:
* runs do not include explicit land-use change modelling. Models diagnose fossil-fuel and land-use change emissions jointly and therefore do not require adding land-use change emissions.

Table TS.SM.9 | Overview of EMIC RCP model runs from (Eby et al. 2013; Zickfeld et al. 2013), as used in Figure SPM.10 (and TS TFE.8, Figure 1). EMICs output is available from http://www.climate.uvic.ca/EMICAR5.

Model	RCP2.6	RCP4.5	RCP6.0	RCP8.5
Bern3D	x	x	x	x
DCESS	x	x	x	x
GENIE	x	x	x	x
IGSM	x	x	x	x
UVic	x	x	x	x

References

Antonov, J. I., et al., 2010: *World Ocean Atlas 2009*, *Volume 2: Salinity* [Levitus, S. (Ed.)]. NOAA Atlas NESDIS 69, 184 pp.

Bates , N .R ., 2007: Interannual variability of the oceanic CO_2 sink in the subtropical gyre of the North Atlantic Ocean over the last two decades. *J. Geophys. Res. Oceans*, **112**, C09013.

Becker, A., et al., 2013: A description of the global land-surface precipitation data products of the Global Precipitation Climatology Centre with sample applications including centennial (trend) analysis from 1901–present. *Earth Sys. Sci. Data*, **5**, 71–99.

Brown, R. D., and D. A. Robinson, 2011: Northern Hemisphere spring snow cover variability and change over 1922–2010 including an assessment of uncertainty. *Cryosphere*, **5**, 219–229.

Cavalieri, D. J., and C. L. Parkinson, 2012: Arctic sea ice variability and trends, 1979-2010. *Cryosphere*, **6**, 957–979.

Cavalieri, D. J., P. Gloersen, and W. J. Campbell, 1984: Determination of sea ice parameters with the Nimbus-7 SMMR. *J. Geophys. Res. Atmos.*, **89**, 5355–5369.

Church, J. A., and N. J. White, 2011: Sea-Level Rise from the Late 19th to the Early 21st Century. *Surv. Geophys.*, **32**, 585–602.

Comiso, J. C., and F. Nishio, 2008: Trends in the sea ice cover using enhanced and compatible AMSR-E, SSM/I, and SMMR data. *J. Geophys. Res. Oceans*, **113**, C02S07.

Dickson, A.G., C. L. Sabine, and J. R. Christian, J.R., (eds.), 2007: *Guide to best practices for ocean CO_2 measurements*. PICES Special Publication 3, 191 pp.

Domingues, C. M., J. A. Church, N. J. White, P. J. Gleckler, S. E. Wijffels, P. M. Barker, and J. R. Dunn, 2008: Improved estimates of upper-ocean warming and multi-decadal sea-level rise. *Nature*, **453**, 1090–1094.

Dore, J. E., R. Lukas, D. W. Sadler, M. J. Church, and D. M. Karl, 2009: Physical and biogeochemical modulation of ocean acidification in the central North Pacific. *Proc. Natl. Acad. Sci. U.S.A.*, **106**, 12235–12240.

Eby, M., et al., 2013: Historical and idealized climate model experiments: an intercomparison of Earth system models of intermediate complexity. *Clim. Past*, **9**, 1111–1140.

Garcia, H. E., R. A. Locarnini, T. P. Boyer, J. I. Antonov, O. K. Baranova, M. M. Zweng, and D. R. Johnson, 2010: *World Ocean Atlas 2009*, *Volume 3: Dissolved Oxygen, Apparent Oxygen Utilization, and Oxygen Saturation* [Levitus, S. (Ed.)]. NOAA Atlas NESDIS 70, 344 pp.

Gillett, N. P., V. K. Arora, D. Matthews, and M. R. Allen, 2013: Constraining the Ratio of Global Warming to Cumulative CO_2 Emissions Using CMIP5 Simulations. *J. Clim.*, **26**, 6844–6858.

González-Dávila, M., and J. M. Santana-Casiano, 2009: Sea Surface and Atmospheric fCO_2 data measured during the ESTOC Time Series cruises from 1995–2009. Oak Ridge National Laboratory, US Department of Energy, Oak Ridge, Tennessee. http://cdiac.ornl.gov/ftp/oceans/ESTOC_data/.

González-Dávila, M., J. M. Santana-Casiano, J. M. Rueda, and O. Llinás, 2010: Water column distribution of the carbonate system variables in the ESTOC site from 1995 to 2004. *Biogeosciences*, **7**, 3067–3081.

IPCC, 2012: *Managing the Risks of Extreme Events and Disasters to Advance Climate Change Adaptation. A Special Report of Working Groups I and II of the Intergovernmental Panel on Climate Change* [Field, C.B., et al., (eds.)]. Cambridge University Press, Cambridge, UK, and New York, NY, USA, 582 pp.

Ishii, M., and M. Kimoto, 2009: Reevaluation of historical ocean heat content variations with time-varying XBT and MBT depth bias corrections. *J. Oceanogr.*, **65**, 287–299.

Jevrejeva, S., J. C. Moore, A. Grinsted, and P. L. Woodworth, 2008: Recent global sea level acceleration started over 200 years ago? *Geophys. Res. Lett.*, **35**, L08715.

Jones, C., et al., 2013: Twenty-First Century Compatible CO_2 Emissions and Airborne Fraction Simulated by CMIP5 Earth System Models under Four Representative Concentration Pathways. *J. Clim.*, **26**, 4398–4413.

Keeling, C., R. Bacastow, A. Bainbridge, C. Ekdahl, P. Guenther, L. Waterman, and J. Chin, 1976a: Atmospheric Carbon-Dioxide Variations at Mauna-Loa Observatory, Hawaii. *Tellus*, **28**, 538–551.

Keeling, C. D., J. A. Adams, and C. A. Ekdahl, 1976b: Atmospheric Carbon-Dioxide Variations at South Pole. *Tellus*, **28**, 553–564.

Keeling, C. D., S. C. Piper, R. B. Bacastow, M. Wahlen, T. P. Whorf, M. Heimann, and H. A. Meijer, 2001: Exchanges of atmospheric CO_2 and $^{13}CO_2$ with the terrestrial biosphere and oceans from 1978 to 2000. I. Global aspects, SIO Reference Series, No. 01–06. Scripps Institution of Oceanography, San Diego, 88 pp.

Key, R. M., et al., 2004: A global ocean carbon climatology: Results from Global Data Analysis Project (GLODAP). *Glob. Biogeoch. Cycles*, **18**, GB4031.

Le Quéré, C., et al., 2013: The global carbon budget 1959–2011. *Earth Syst. Sci. Data*, **5**, 165–185.

Levitus, S., et al., 2012: World ocean heat content and thermosteric sea level change (0-2000 m), 1955–2010. *Geophys. Res. Lett.*, **39,** L10603.

Locarnini, R. A., et al., 2010: *World Ocean Atlas 2009*, *Volume 1: Temperature* [Levitus, S. (Ed.)]. NOAA Atlas NESDIS 68, 184 pp.

Markus, T., and D. J. Cavalieri, 2000: An enhancement of the NASA Team sea ice algorithm. *IEEE Trans. Geosci. Remote Sens.*, **38**, 1387–1398.

Massonnet, F., T. Fichefet, H. Goosse, C. M. Bitz, G. Philippon-Berthier, M. M. Holland, and P.-Y. Barriat, 2012: Constraining projections of summer Arctic sea ice. *Cryosphere*, **6**, 1383–1394.

Mitchell, T. D., and P. D. Jones, 2005: An improved method of constructing a database of monthly climate observations and associated high-resolution grids. *Int. J. Climatol.*, **25**, 693–712.

Morice, C. P., J. J. Kennedy, N. A. Rayner, and P. D. Jones, 2012: Quantifying uncertainties in global and regional temperature change using an ensemble of observational estimates: The HadCRUT4 data set. *J. Geophys. Res. Atmos.*, **117**, 22.

Nerem, R. S., D. P. Chambers, C. Choe, and G. T. Mitchum, 2010: Estimating Mean Sea Level Change from the TOPEX and Jason Altimeter Missions. *Mar. Geod.*, **33**, 435–446.

Orr, J.C. et al., 2005: Anthropogenic ocean acidification over the twenty-first century and its impact on calcifying organisms. *Nature*, **437**, 681-686.

Orr, J. C., 2011: Recent and future changes in ocean carbonate chemistry. In: *Ocean Acidification* [Gattuso, S.-P., and L. Hansson (eds.)]. Oxford University Press, Oxford, United Kingdom and New York, NY, USA, 352 pp.

Palmer, M. D., K. Haines, S. F. B. Tett, and T. J. Ansell, 2007: Isolating the signal of ocean global warming. *Geophys. Res. Lett.*, **34**, L23610.

Parkinson, C. L., and D. J. Cavalieri, 2012: Antarctic Sea Ice Variability and Trends, 1979-2010. *Cryosphere*, **6**, 871–880.

Ray, R. D., and B. C. Douglas, 2011: Experiments in reconstructing twentieth-century sea levels. *Prog. Oceanogr.*, **91**, 496–515.

Rayner, N. A., et al., 2003: Global analyses of sea surface temperature, sea ice, and night marine air temperature since the late nineteenth century. *J. Geophys. Res. Atmos.*, **108**, 4407.

Schweiger, A., R. Lindsay, J. L. Zhang, M. Steele, H. Stern, R. Kwok, 2011: Uncertainty in modeled Arctic sea ice volume. *J. Geophys. Res. Oceans*, **116**, C00D06.

Smith, D. M., and J. M. Murphy, 2007: An objective ocean temperature and salinity analysis using covariances from a global climate model. *J. Geophys. Res. Oceans*, **112**, C02022.

Thoning, K. W., P. P. Tans, and W. D. Komhyr, 1989: Atmospheric carbon dioxide at Mauna Loa Observatory 2. Analysis of the NOAA GMCC data, 1974-1985. *J. Geophys. Res.*, **94**, 8549–8565.

Vose, R. S., Oak Ridge National Laboratory. Environmental Sciences Division., U.S. Global Change Research Program, United States. Dept. of Energy. Office of Health and Environmental Research., Carbon Dioxide Information Analysis Center (U.S.), and Martin Marietta Energy Systems Inc., 1992: *The global historical climatology network: long-term monthly temperature, precipitation, sea level pressure, and station pressure data.* Carbon Dioxide Information Analysis Center. Available to the public from N.T.I.S., 1 v.

Walsh, J. E., and W. L. Chapman, 2001: 20th-century sea-ice variations from observational data. *Ann. Glaciol.*, **33**, 444–448.

Zickfeld, K., et al., 2013: Long-Term Climate Change Commitment and Reversibility: An EMIC Intercomparison. *J. Clim.*, **26**, 5782–5809.

Please note that all external web-links cited in this document were active at the time of publication, but no guarantee is provided that these links remain active.